

QUANTITATIVE SPECTROSCOPY OF OB-STARS IN THE OPTICAL AND THE INFRARED



Dissertation
an der Fakultät für Physik
der Ludwig-Maximilians-Universität
München

vorgelegt von
Tamara Repolust
aus Wildon

München, 24. März 2005

Erstgutachter: PD Dr. Joachim Puls

Zweitgutachter: Prof. Dr. Harald Lesch

Tag der mündlichen Prüfung: 08. Juli 2005

Contents

List of Figures	xi
List of Tables	xiii
1 Introduction	1
1.1 Massive Stars	1
1.1.1 Mass loss	2
1.1.2 Star Formation	5
1.1.3 Late Evolutionary Stages	7
1.2 Model Atmospheres	8
1.3 Quantitative Optical Spectroscopy	10
1.4 Quantitative Infrared Spectroscopy	13
1.5 Outlook	15
1.6 Outline of the thesis	16
1.6.1 Paper 1: Atmospheric NLTE-Models for the Spectroscopic Analysis of Blue Stars with Winds: II. Line-Blanketed Models	16
1.6.2 Paper 2: Advances in radiatively driven wind models	16
1.6.3 Paper 3: Stellar and wind parameters of Galactic O-stars: The influence of line-blocking and -blanketing	16
1.6.4 Paper 4: Mass-loss and wind-momentum rates of O-type stars: A pure H_{α} analysis accounting for line-blanketing	17
1.6.5 Paper 5: Quantitative H and K band spectroscopy of Galactic OB-stars at medium resolution	17
2 Atmospheric NLTE-Models	23
2.1 Introduction	24
2.2 Basic philosophy of the code	26
2.3 Atomic Data and Metallicity	27
2.4 Background elements: approximate NLTE occupation numbers	28
2.4.1 Selection of levels	29
2.4.2 Ionization equilibrium	29
2.4.3 Excitation	32
Meta-stable levels	32
Subordinate levels	34
2.4.4 Limiting cases	35

2.4.5	Different spin systems	36
2.4.6	Accelerated Lambda Iteration	39
2.4.7	Test calculations	41
2.5	Approximate line-blocking	46
2.5.1	Mean opacities	47
2.5.2	Emissivities	49
2.5.3	Tests/Comparison with WM-Basic	51
2.6	Treatment of inverted levels	56
2.6.1	Treatment of inversions in the Sobolev approximation	56
2.6.2	Treatment of inversions in the comoving frame	57
2.6.3	Tests	58
2.7	Temperature stratification	58
2.8	Comparison with CMFGEN	61
2.9	Model grids	66
2.10	Summary and outlook	68
3	Advances in radiatively driven wind models	77
3.1	Introduction	78
3.2	The WLR for Galactic O-stars: observations and theory	78
3.3	Conclusions: Clumping?	81
4	Stellar and wind parameters of Galactic O-stars	85
4.1	Introduction	86
4.2	The code	87
4.3	The O-star sample	89
4.4	Analysis - General remarks	89
4.5	Comments on individual objects	95
4.5.1	Supergiants	96
4.5.2	Giants	100
4.5.3	Dwarfs	102
4.6	Error Analysis	104
4.6.1	Stellar parameters (cf. Table 4.4)	104
4.6.2	Wind parameters (cf. Table 4.2 and 4.3)	106
4.6.3	Derived Quantities (cf. Table 4.4)	109
4.7	Discussion	110
4.7.1	The effective temperature scale for Galactic O-stars	110
4.7.2	Why lower T_{eff} with blanketed models?	111
4.7.3	The T_{eff} vs. $\log g$ diagram	116
4.7.4	Is there still a mass discrepancy?	118
4.7.5	Wind-momentum rates	121
	Comparison with previous results assuming identical M_V 's	122
	Clumping in the lower wind?	123
4.8	Conclusions and summary	126
4.9	Appendix: Centrifugal correction	129

5	Mass-loss and wind-momentum rates of O-type stars	137
5.1	Introduction	138
5.2	Spectral observations	139
5.3	Sample stars	140
5.4	H $_{\alpha}$ mass-loss rates	143
5.4.1	Input parameters	143
5.4.2	Results	146
	General remarks	146
	Error analysis	147
5.4.3	Comparison with results from a complete analysis	149
5.5	Wind-momentum rates and WLR	151
5.5.1	WLR as function of luminosity class	152
5.5.2	Enlarging the sample	156
5.5.3	WLR as function of profile type	157
5.6	Summary, discussion and conclusions	159
5.6.1	Future work	161
6	Quantitative H and K band spectroscopy of Galactic OB-stars	167
6.1	Introduction	168
6.2	Observations, targets and strategic lines	169
6.3	Model calculations	172
6.3.1	Atomic data and line broadening	172
6.4	Predicted behaviour of strategic lines	173
6.4.1	Hydrogen and He II lines: Influence of Stark broadening	175
6.4.2	He I lines: Influence of NLTE effects	178
6.5	Comparison with results by Lenorzer et al.	179
6.6	Analysis	183
6.6.1	General remarks	183
6.6.2	Fitting strategy and line trends	185
6.6.3	Comments on the individual objects	186
	Dwarfs	186
	Giants	190
	Supergiants	191
6.7	Comparison with optical data	193
6.7.1	Comments on hydrogen collisional cross sections	197
6.8	Summary and conclusions	199

List of Figures

2.1	Ratio of ionization to recombination rate coefficients.	30
2.2	Population of meta-stable levels via excited ones.	33
2.3	Approximate NLTE vs. the exact case.	40
2.4	2. Approximate NLTE vs. the exact case.	42
2.5	Approximate NLTE vs. the results of a solution of the complete rate equations. . . .	43
2.6	As Fig. 2.5, but for model A4045.	44
2.7	Comparison of radiation temperatures of <i>converged</i> models.	46
2.8	FASTWIND vs. WM-Basic.	52
2.9	Comparison of ionizing photon number for the model grid provided by Pauldrach et al. (2001).	53
2.10	Comparison of velocity/density structure for model S30.	54
2.11	Comparison of <i>total</i> photospheric radiative acceleration for model S30 vs. results from an analogous hydrostatic Kurucz-model.	56
2.12	FASTWIND vs. WM-Basic.	60
2.13	Extreme temperature-bump around 22,000 K.	60
2.14	As Fig. 2.12, but for FASTWIND vs. CMFGEN.	61
2.15	As Fig. 2.8, but for FASTWIND vs. CMFGEN.	61
2.16	As Fig. 2.9, but for CMFGEN vs. FASTWIND.	62
2.17	Comparison of strategic H/He lines in the optical for the dwarf-models from the grid by Lenorzer et al. (2004).	64
2.18	Wind-strength parameter Q as an optical depth invariant.	64
2.19	As Fig. 2.17, however for the supergiants from the grid by Lenorzer et al. (2004). . .	65
2.20	Iso-contours of equivalent widths for He I4471, as predicted by FASTWIND.	67
3.1	WLR for Galactic O-stars.	78
3.2	T_{eff} vs. spectral type for Galactic O-stars.	79
3.3	WLR for Galactic O-stars, using line-blanketed models.	80
3.4	Comparison of observed and theoretical wind momenta.	80
3.5	As Fig. 3.3, however classified as function of H_{α} profile type.	82
4.1	Line fits of supergiants with spectral types ranging from O3 to O7.5	96
4.2	As Fig. 4.1, but for spectral types ranging from O7 to O9.7	97
4.3	“Wind lines” of the hotter supergiants as in Fig. 4.1.	99
4.4	“Wind lines” of the cooler supergiants as in Fig. 4.2.	99
4.5	Line fits of the giant sample with spectral types ranging from O5 to O9	101

4.6	“Wind lines” of the giants as in Fig. 4.5.	102
4.7	“Wind lines” of the dwarfs as in Fig. 4.8.	102
4.8	Line fits of the dwarf sample with spectral types ranging from O3 to O9	103
4.9	T_{eff} vs. spectral type for Galactic O-stars (line-blanketed models)	111
4.10	Emergent Eddington flux H_{ν} as function of wavelength.	112
4.11	As Fig. 4.10, but for corresponding radiation temperatures T_{rad}	112
4.12	Ionization fractions of He for the different models from Fig. 4.10, as function of τ_{Ross}	113
4.13	As Fig. 4.11, but with radiation temperatures calculated from mean intensity J_{ν} at $\tau_{\text{Ross}} = 2/3$	114
4.14	As Fig. 4.12, but for ionization ratios He II/He III and He I/He III.	116
4.15	He I 4471 line ($V_{\text{r}} \sin i = 90 \text{ km s}^{-1}$) for all three models from Fig 4.10.	116
4.16	True gravity $\log g_{\text{true}}$ vs. T_{eff} for Galactic O-stars	117
4.17	True gravity $\log g_{\text{true}}$ vs. T_{eff} for Galactic O-stars	117
4.18	The HR diagram for our sample.	118
4.19	Evolutionary vs. spectroscopic masses	119
4.20	Spectroscopic and evolutionary masses of our sample stars with data from Table 4.1	120
4.21	Logarithm of modified wind-momentum rate, $D_{\text{mom}} = \dot{M} v_{\infty} (R_{\star}/R_{\odot})^{0.5}$, vs. $\log(L/L_{\odot})$, for the values derived on the basis of R_{old}	121
4.22	WLR for our sample, using the same M_{V} -values ($\rightarrow R_{\text{old}}$) as in Paper I.	121
4.23	As Fig. 4.22, but with the actual absolute magnitudes from Table 4.1.	124
4.24	WLR of the combined sample from Fig. 4.23.	125
4.25	Geometry used for calculating the centrifugal correction.	130
5.1	Difference in absolute magnitude between our recalculations and the values reproduced by Howarth & Prinja (1989)	141
5.2	Spectral type– T_{eff} and spectral type– $\log g$ relations	144
5.3	Examples of differently shaped H_{α} profiles	146
5.4	Comparison of derived Q -values from our analysis with corresponding data from RPH	151
5.5	Influence of uncertainty in reddening on modified wind-momenta and luminosities	153
5.6	WLR for our sample of Galactic O-type stars	154
5.7	WLR for Galactic O-type stars	156
5.8	As Fig. 5.7, but with regression in dependence of profile type	157
5.9	As Fig. 5.8, but with \dot{M} of class 1 objects (H_{α} in emission) decreased by a factor of 0.48	157
6.1	Comparison of strategic NIR lines for two atmospheric models	174
6.2	Line broadening profile functions for H_{γ} and Br10	176
6.3	Iso-contours of equivalent widths for He I and He II lines	176
6.4	Influence of Stark-broadening for lines with low- and high-lying upper level as a function of gravity	177
6.5	NLTE-departure coefficients for levels of He II.70	178
6.6	Comparison of equivalent widths for NIR hydrogen lines of O-type dwarfs	180
6.7	Comparison of synthetic NIR lines for the grid of O-type dwarfs and supergiants described by Lenorzer et al. (2004)	181
6.8	Equivalent width of Br_{α} as a function of equivalent width invariant Q'	183

6.9	Line fits for hot dwarfs with spectral types ranging from O3 to O7 and cool dwarfs with spectral types ranging from O8 to B2	187
6.10	As Fig. 6.9, but for giants with spectral types ranging from O5 to B9	188
6.11	As Fig. 6.9, but for hot supergiants of spectral type O3 to O7 and cool supergiants of spectral type O9 to B3	192
6.12	Comparison of T_{eff} and $\log g$ derived from the optical and the near-IR	196
6.13	As Fig. 6.12, but for mass-loss rate \dot{M}	197
6.14	Influence of different collisional cross sections for hydrogen	198

List of Tables

4.1	Galactic O-star sample: Stellar and wind parameters adopted (M_V) and derived using FASTWIND	92
4.2	<i>Stars with H_α in emission</i> : Errors in stellar and wind parameters given in Table 4.1	107
4.3	<i>Stars with H_α in absorption</i> : Errors in stellar and wind parameters given in Table 4.1	107
4.4	Parameters and corresponding errors for our sample stars	108
4.5	Coefficients of the WLR obtained in the present investigation compared to the results from Paper I and the theoretical prediction by Vink et al. (2000)	123
5.1	Spectral types and photometric data of the studied stars	142
5.2	Stellar and wind parameters of the O-star sample	148
5.3	Objects with H_α in absorption: variation in derived \dot{M} , for modified β	150
5.4	Coefficients of the WLR obtained for the supergiants of our sample cases A, B, C and D in comparison to results from other investigations	156
5.5	Coefficients of the WLR obtained for Galactic O-stars.	158
6.1	Sample stars and observing data in the H and K band	170
6.2	Comparison of stellar and wind parameters in the optical and the near infrared derived using FASTWIND	194
6.3	Adopted and derived stellar and wind parameters in the infrared for sample IV objects <i>not</i> analyzed in the optical	195

Chapter 1

Introduction

1.1 Massive Stars

Massive stars are important constituents of the Universe and serve as the most important probes for its investigation. They are the production plants for almost all elements heavier than helium. At later evolutionary stages they deliver a significant fraction of their chemically enriched mass back to their environment, by means of stellar winds, eruptions and explosions. Thus, newly produced elements are provided for future generations of stars, their planets, and the possible evolution of life. Massive stars also play a crucial role in the chemical evolution of galaxies as the recycling of processed material influences their ecology. The recycling of these elements is a very efficient process, since the lifetimes of massive stars are very short. Additionally, massive stars contribute enormously to the cosmic evolution because their energetic impact on the parent galaxy is rather violent through their intense radiation and supernova explosions, influencing galaxies from infancy to death and making them the most important sources of energy input in galaxies. In the distant Universe, massive stars dominate the integrated UV-light of very young galaxies (Steidel et al. 1996; Pettini et al. 2000) and at earlier epochs they are the suspected sources of the re-ionization of the Universe (Bromm et al. 2001). At the endpoint of their evolution, they suffer a gravitational collapse and explode as supernovae of type II, Ib, or Ic. Their descendants will emit gamma ray bursts which are associated with a Ic type supernova constituting the most energetic cosmic flashes known (Woosley 1993). Eventually massive stars form black holes and detract matter from the cosmic cycle.

Nearly 20 years ago high mass stars were suspected to have masses up to $\approx 100 M_{\odot}$ (Appenzeller 1987), whereas nowadays the most massive stars are even believed to reach masses of $\approx 150 M_{\odot}$ (Massey 2003). The lower mass limit is commonly accepted to be $8 M_{\odot}$. For initial masses above $8 M_{\odot}$ stars do not have a pre-Main Sequence phase, which means that they already start burning hydrogen while still accreting mass from the proto-stellar gas and dust envelope and/or circumstellar disk and $8 M_{\odot}$ are also found to be the boundary between the initial progenitor mass of white dwarfs and type II supernovae.

Massive stars are the most luminous stellar objects, with luminosities up to a few $10^6 L_{\odot}$, placing most of them at the upper left corner of the Hertzsprung-Russell diagram and being of spectral type O, B and the descendants therefrom. As for their stellar outflow, these stars show direct spectroscopic

evidence of winds throughout their lifetimes above a certain luminosity threshold which corresponds to roughly $10^4 L_{\odot}$ (Abbott 1979). For massive stars in our Galaxy the surface temperatures range between 20,000 K and below 50,000 K (Repolust et al. 2004, i.e., paper 3), depending on mass. In the SMC, for example, even surface temperatures of 55,000 K can be reached (Massey et al. 2004, 2005). Comparing masses and luminosities of these stars, it is possible to derive a relation, the so-called mass-luminosity relation, which scales with $L \propto M^3$ for stars on the Main Sequence implying a much broader range for luminosities than for masses. It also gives us an insight about their lifetimes. Most of the stellar mass consists of hydrogen and the rate at which it is burnt depends on luminosity. Therefore, the lifetime of stars is proportional to $\tau = M/L$. From above, knowing that $L \propto M^3$, we find that $\tau = M^{-2}$, which shows that the most massive stars have the shortest lifetimes. They spend only about 10 million years on the Main Sequence compared to low-mass stars which remain there for about 10^{10} years.

The descendants of hot, massive ($> 30 M_{\odot}$) O and Of stars after the Main Sequence phase are Wolf-Rayet (WR) stars constituting the final stage of massive stellar evolution, after which the star explodes as a supernova. The evolution of massive stars between their Main Sequence and WR phase, is more uncertain, though it is generally assumed that they pass through a short, unstable phase, in which mass loss is quite substantial. This unstable stage is referred to as the Luminous Blue Variable (LBV) phase. During their life, massive stars loose a considerable amount of mass, whereby a large part of this mass is lost during the LBV and WR stage. However, massive stars on the Main Sequence may already suffer substantial mass loss and this is especially relevant for another issue in their evolution concerning the existence of a Red Supergiant (RSG) phase. Whether or not massive stars go through a RSG phase, the number of stars in the blue/red supergiant region, and the variation of their ratio with metallicity is still under debate, but accurate knowledge of mass loss as a function of stellar parameters will help to clarify these questions.

Hot massive stars are known to produce fast, dense, and continuous outflows. These so-called stellar winds can basically be described by two global parameters, the terminal velocity, v_{∞} , and the mass loss rate, \dot{M} , which immensely influence the evolution of massive stars. Hence, these effects must be taken into account when modeling these stars in order to avoid the deduction of erroneous late evolutionary stages. However, the dependency of evolution on mass loss is not well-known as is the dependency of mass loss (on the Main Sequence or at later evolutionary stages) on metallicity, Z (see below). Also stellar rotation affects the rate of mass loss and the interior structure of the stars by means of mixing processes which have been neglected in the past. Our understanding of these processes and their dependence on parameters such as metallicity and angular momentum is still very poor. Further, the presence of “clumping” has severe consequences for the interpretation of observed line profiles, particularly with respect to the derived mass loss rates (Kudritzki & Puls 2000 and references therein). Reliable values of mass-loss rates in relation to the influence of rotation, and the effect of clumping are probably the most intriguing questions at the moment and, thus, worth a closer inspection.

1.1.1 Mass loss

The luminosity of hot massive stars is the key ingredient to the driving of a dense (10^{-6} to $10^{-5} M_{\odot}/\text{yr}$) and fast (v_{∞} up to $3,000 \text{ km s}^{-1}$) outflow lasting a lifetime. The high mass loss imprints unambiguous signatures on the spectral energy distribution and spectral lines received from these objects. In massive stars, the loss of mass occurs by means of radiation pressure exerted onto the

atmospheric material. The radiation pressure from electron scattering of free electrons, which are the main contributors to the continuum opacity, does reduce the local gravity due to their common radial dependence ($1/r^2$), but it is not strong enough to overcome gravity and, hence, cannot explain observed mass loss rates. One also needs to consider the contribution of the Doppler-shifted resonance lines of highly ionized metal lines to the radiative acceleration. The metal lines (together with the radiative force due to continuum opacity) is able to overcome the gravitational well of the star and thus “drive” the stellar wind. Therefore, high luminosities of massive stars result in momentum transfer through the absorption¹ in the resonance metal lines.

The measurements of mass loss rates are model-dependent, and usually determined from the modeling of H_α profiles, the radio, and also UV spectra. From the observational view, the H_α line gives a good indication about the mass lost by stars, although minor problems may arise due to blending with HeII , nebular contamination, or rotational broadening. It is, however, possible to move towards longer wavelengths for mass loss determinations, since hot stars can be observed via the free-free thermal excess caused by stellar winds. Unfortunately, this is only applicable to hot stars with strong winds, since stars with weak winds do not exhibit strong IR excess or radio flux. A comparison of mass loss rates from H_α and IR-radio excess gives well-agreeing results, but it has to be kept in mind that the measurements originate from different regions in the stellar atmosphere, i.e., $\approx 1.5 R_\star$ for H_α and ≈ 50 to $100 R_\star$ for the radio excess, and hence can be used as an excellent tool to determine the stratification of clumping, since both mass loss indicators are sensitive to it.

The best way to discuss the strength of stellar winds is in terms of the wind-momentum luminosity relationship (WLR) (for further details see Puls et al. 1996 and Kudritzki et al. 1999). As winds of hot stars are driven by radiation, the mechanical momentum of stellar outflow should be mainly a function of photon momentum and, hence, depend directly on luminosity such that

$$\log \dot{M} v_\infty R_\star^{0.5} \approx x \log L + D. \quad (1.1)$$

The slope of the observed WLR (modified by $R_\star^{0.5}$) corresponds to the inverse exponent of the line-strength distribution function², $x = 1/\alpha'$.³ The vertical offset D is controlled by the effective number of lines driving the stellar wind. Both parameters depend on spectral type and metallicity (Kudritzki & Puls 2000). The wind-momentum luminosity relationship might allow for an independent determination of extragalactic distances on intermediate scales up to the Virgo/Fornax cluster, among other methods for distance calibrations, i.e., Cepheids and type Ia supernovae (which relies on an empirical calibration by means of a unique relation between the peak luminosity and the width of the light curve).

From the above equation we see that mass-loss is proportional to a certain power of luminosity. This deceptively simply relation, however, hides much of the complication, since α' depends on the effective temperature and Z , which can only be determined by detailed modeling. The physical reason for the change of the slope with T_{eff} is the change in ionization of the elements (because lower ions have more lines) contributing to the radiative line acceleration. For O-type stars the value of α' is \approx

¹The emission component cancels due to the fore-aft symmetry of the emission component.

²The line strength distribution function describes the number of driving lines as a function of their strength, i.e., the density-independent part of their opacity (e.g., Puls et al. 2000).

³Actually, $\alpha' = \alpha - \delta$, where α is the aforementioned exponent and δ (of the order 0.1) accounts for changes in the ionization throughout the wind.

0.6 (Pauldrach et al. 1986 and Kudritzki & Puls 2000), suggesting a luminosity exponent ≈ 1.7 , in agreement with observations. Given the effects of metallicity on the evolution of massive stars, an accurate parameterization of mass-loss across the upper end of the HR-diagram is of great interest. Puls et al. (2000) and Vink et al. (2001) have investigated the theoretical dependence of mass-loss rates on metallicity. Puls et al. (2000) argue that mass-loss should scale approximately as $(Z/Z_{\odot})^{(1-\alpha)/\alpha'}$ with the complication that α and α' will depend on Z as well as on T_{eff} . For $\alpha' = 0.6$, the scaling factor would be $(Z/Z_{\odot})^{0.5}$, which is similar to the result found by Vink et al. (2001). Further observational studies on mass-loss rates would be useful, especially at higher Z . The higher the mass loss the faster the masses decrease. This may sound trivial but the final masses give important clues about the latest evolutionary stages. All stars with initial masses of $\approx 20 M_{\odot}$ and metallicities $\approx Z_{\odot}$ or higher have final masses of $\approx 10 M_{\odot}$. At lower Z , the final masses are higher and the different final masses lead to different types of supernovae.

As an important example, the first stars in our Universe, which constitute the Population III generation, formed out of metal-free gas. Simulations of metal-free star formation indicate that they had high masses (up to $1000 M_{\odot}$) producing a vast amount of UV photons to reionize the Universe. The supernova explosions that ended their lives were responsible for the chemical enrichment of the intergalactic medium with heavy elements (e.g., Ostriker & Gnedin 1996), but also for the termination of the epoch of Population III stars. The efficient and widespread metal-enriched ejecta were mixed into the surrounding gas triggering at some point the transition to lower mass Population II star formation (Bromm & Larson 2004).

Studying stars at different metallicities will also help to understand the decisive role of rotation in combination with stellar evolution, whereby especially the observations and analyses of young stellar populations are crucial for understanding rotation-dependent influences. The effect of stellar rotation and the transport of angular momentum together with rotationally-driven mixing does, indeed, receive increasing attention (Meynet & Maeder 2000). The main effects of rotation comprise structural effects due to the centrifugal force which can produce large distortion at the stellar surface, rotational mixing which is responsible for internal transports of chemical elements and angular momentum by shears and meridional circulation, respectively (Maeder & Meynet 2001), and finally the effect of mass loss enhancement, again, due to the centrifugal acceleration. For example, the mass-loss rate of a rotating $10 M_{\odot}$ -star on the Main Sequence in relation to one with no rotation scales with $\dot{M}_{\text{rot}} \approx 1.5 \dot{M}_{\text{no-rot}}$.

The von Zeipel theorem states that the local radiative flux F of a rotating star is proportional to the local effective gravity g_{eff} . Due to this, a much larger flux and higher T_{eff} is present at the pole than at the equator (Meynet & Maeder 1997). This latitudinal dependence of T_{eff} leads to an asymmetric mass-loss and also to enhanced average \dot{M} rates. Anisotropic mass loss influences the loss of angular momentum such that \dot{M} at the poles removes mass but little angular momentum which in turn influences the evolution of very massive stars with high rotation (Maeder 2002). The projected rotational velocities of O stars are typically $V_r \sin i = 100 \text{ km s}^{-1}$ but can reach values of up to 400 km s^{-1} (Howarth et al. 1997). Mass loss by stellar winds drastically reduces $V_r \sin i$ during evolution because the stellar winds carry away considerable angular momentum and the new surface layers then have a lower $V_r \sin i$ as a result of expansion and redistribution.

The effects of rotation are especially important for rapidly rotating massive stars being most probably also responsible for the production of primary nitrogen (Maeder 2000). In hot stars the studies of mixing focus on helium and CNO. Rapidly rotating OB stars show large surface helium abundances,

whereby the correlation between rotation and mixing found by Herrero et al. (1992) indicates that such stars may follow a completely different evolutionary path than traditional stellar evolution predicts. Evolved O stars, in general, show surface abundances which suggest C and N processing and helium enrichment (e.g., Howarth & Prinja 1989). Rotation also plays an important role in the formation of Wolf-Rayet stars such that a fast rotating star may already enter the WR phase while still burning hydrogen in its core and, thus, skipping the LBV phase and spending more time in the WR phase. All evolutionary studies about rotational effects rely on approximations which allow a one-dimensional treatment, leaving the question if all effects can actually be treated that way.

The final aspect of mass loss-influencing effects is concerned with stellar wind instabilities. Theoretical considerations based on a detailed investigation of radiative line acceleration show that this acceleration is subject to a strong instability, which causes a structured wind. It is now generally accepted that the winds around hot stars have a time-dependent and inhomogeneous structure consisting of shocks, clumps and blobs. The observational evidence for this comes from the presence of black and broad troughs in saturated UV P-Cygni profiles (Lucy 1982a and 1982b) and the X-ray emission of hot stars (e.g., Chlebowski et al. 1989 and references therein). Moreover, some direct evidence for clumping in the outer parts of Wolf-Rayet winds is provided by the observations and analyses of distinct blobs (e.g., Robert & Moffat 1990). Homogeneous smooth winds of O dwarfs predict too strong Nv 1240 and Ov 1371 lines, suggesting that their winds may also be clumped or asymmetric, similar to winds of O supergiants and WR stars (Bouret et al. 2003). Further, the hypothesis is supported by a number of UV analyses. Based on FUSE-observations of Magellanic Cloud stars, Crowther et al. (2002), Massa et al. (2003) and Hillier et al. (2003) found indications that the winds might be clumped, mainly from the behaviour of the PV resonance line (if phosphorus is not strongly under-abundant, as claimed by Pauldrach et al. 1994).

In terms of theory, shocks and wind inhomogeneities are induced by the intrinsic instabilities of radiation driven winds. Illustrated in simple manner, the radiative acceleration is proportional to the *spatial* velocity gradient, $g_{\text{rad}} \propto dv/dr$. Thus, any perturbation will be exponentially amplified, at least in their initial, linear phase. If the velocity is disturbed at an arbitrary point in the wind, $v \rightarrow v + \delta v$, the velocity gradient dv/dr will increase and, hence also the radiative acceleration g_{rad} due to the direct proportionality. Their increase will again influence the velocity perturbation $v + \delta v$ and eventually lead to a runaway situation and to strong reverse shocks, a result that follows from strongly amplified inward propagating waves (Owocki & Rybicki 1984, 1985).

Since mass loss determinations are influenced by clumping and previous theoretical models account for this effect, almost all mass loss rates derived so far might be too high. The presence of clumping would then increase H_α due the ρ^2 -dependence of opacity and, thus, lead to the relation that $\langle \rho^2 \rangle$ is greater than $\langle \rho \rangle^2$ in a structured medium giving a clumping factor of $\langle \rho^2 \rangle / \langle \rho \rangle^2$ that is always greater than 1.⁴ With wrong mass loss predictions, however, it is not possible to calculate realistic stellar and galactic evolutionary models.

1.1.2 Star Formation

Although our knowledge of the physics taking place in stars has enormously increased over the last decades, particularly their early evolutionary phases are still not well understood. These important

⁴The same would be true for the radio-excess, with the corresponding clumping factor present in the outer wind.

phases are normally hidden from our view, since very young massive stars lie deeply embedded in their natal environment of gas and dust. Due to their short lifetimes they spend a significant fraction (\approx up to 20%) of their life in the densest parts of giant molecular clouds. Unfortunately, by the time the central star can be observed in the optical or UV, critical signatures present in the spectra and environment of the star, yielding invaluable information of the formation process, will have disappeared. It is, therefore, important to observe massive stars before their stellar atmospheres have erased chemical and physical evidence tracing their formation mechanism. In order to investigate this long-standing problem, a study of young massive star systems being still embedded in an environment of gas and dust is of great interest.

To understand the formation of massive stars, a first assumption would be to just simply adopt and extend the picture of low mass star formation. The accepted theory of low-mass star formation was founded about 30 years ago by Shu et al. (1987) and starts with slowly rotating molecular cores inside a molecular cloud. The cores are initially supported against gravity by magnetic and turbulent pressure gradients. With the cooling of the cloud a gravitational instability can arise, since as a result the gas pressure in the cloud is decreasing in some areas. It is also possible that atoms accumulate to form molecules, thereby reducing the amount of particles by 1/2 or 1/3 (leading to pressure decrease). Further, due to turbulence within the cloud, the magnetic field counteracting the contraction can drift outwards with time, i.e., ambipolar diffusion, and successively reduce magnetic pressure, or more impulsive events take place such as shock waves. The unstable cloud cores will eventually collapse from inside-out. Typically, the cores that result from fragmentation have masses of the order of 1 to 10 M_{\odot} and sizes of less than 1 pc. This marks the beginning of the next evolutionary phase. The cloud fragment further contracts while matter from the envelope falls in with supersonic velocities onto the central region where a protostar is forming. On impact of the infalling matter a shock front is established, whereby kinetic energy is converted into thermal energy. At 2,000 K H molecules dissociate to atoms using up energy which helped to stabilize the equilibrium condition. The centre of contraction further collapses and the temperature in the core increases. At 10,000 K, H atoms become ionized, resulting in the establishment of a new equilibrium condition and an increase in the gas pressure, thus, making contraction a very slow process. Once the temperature and the density have stabilized, the gravitational pressure directed inwards is about the same as the gas and radiation pressure directed outwards. The protostar establishes hydrostatic equilibrium and contraction is nearly halted. At this point the dynamical evolution of the star stops. The initial radius of the protostar is \approx 5 AU and the protostellar disk (due to conservation of angular momentum) can have dimensions of up to 10^3 AU. The protostar is accreting matter through the disk surrounding it and, hence, gaining mass. The brighter and hotter the star becomes the more surrounding material is dispersed by photon pressure on dust. The star may also develop bipolar outflows along its rotational axis, where matter and angular momentum may be expelled from the stellar system. This bipolar outflow helps to terminate the infall of matter, leaving the protostar and residual disk from which a protoplanetary system may eventually form (Shu et al. 1987).

This formation process entails several difficulties when extended to massive star formation. First of all, the physical properties of clouds undergoing low and high mass star formation are different. Massive stars form in clouds which are warmer, larger, more massive, and which are mainly located in the spiral arms of galaxies. They are thought to form in clusters and associations, whereas low mass stars do not necessarily form in clusters. Low mass stars form in a cooler population of clouds throughout the disk of galaxies, as well as in dark molecular clouds. Further difficulties relate to the fast contraction

times for massive star cores. One of these difficulties arises due to the immense radiation field set up by the growing, fusion-burning central star. The radiation pressure from the young star can reverse the infall of additional gas and ultimately limit the mass that can be directly accumulated onto the star (e.g., Yorke & Kruegel 1977). It is well established that the parent cloud will have some net angular momentum, and this will likely result in the formation of a disk. Theories allowing for accretion of mass from a disk onto a young star have been moderately successful in building high mass stars (e.g., Behrend & Maeder 2001; McKee & Tan 2003). These theories are, however, inadequate to fully resolve the problem of radiation pressure, since it is difficult for massive accretion disks to last long enough to build stars of very high mass ($M_* \approx 50 M_\odot$ or higher). The problem with the radiation pressure has led to the assumption that massive stars cannot form from accretion alone, but instead form from collisions of intermediate mass stars, which are first formed by accretion (Bonnell et al. 1998). The collisional model for star formation can account qualitatively for some of the observational properties of massive stars, such as their tendency to form in the centres of clusters. However, it is difficult to achieve the necessary stellar densities ($> 10^4$ stars pc^{-3} ; Evans 1999) for this process to be efficient. The standard accretion model, recently modified to account for the high pressures and turbulent, nonthermal conditions of massive star forming clumps (Plume et al. 1997) can achieve the high accretion rates necessary to overcome radiation pressure and achieve short formation timescales, $\tau_f \approx 10^5$ yr, in agreement with observations (Nakano et al. 2000). Nearby massive star forming regions show signatures of disks and collimated outflows, suggesting the accretion picture is relevant to the formation of stars with masses up to at least 20 to 30 M_\odot . Further, observations of disks (Shepherd et al. 2001) and jets (Garay et al. 2003) give support to the accretion scenario, but coalescence cannot be ruled out. Given the existence of the two competing hypotheses, the implied dichotomy between accretion and mergers is probably oversimplified, and both types of process may play a role in the formation of massive stars.

1.1.3 Late Evolutionary Stages

Not only does the birth of massive stars lead to vivid discussions, but also their final evolutionary stages are far from being well-understood. Massive stars end their lives in form of supernova explosions, thereby representing both the end and the beginning of stellar evolution. Their debris enriches the interstellar material with heavy nuclei and their kinetic energy helps to trigger further star formation. The explosions are extremely powerful allowing us to measure their distances out to cosmological scales. Moreover, the afterglows of gamma ray bursts (GRB) are thought to be the best probes for the metallicity and ionization state of the intervening intergalactic medium during the epoch of reionization. These events require to understand various physical questions ranging from radiation and neutrino transport to hydrodynamics and turbulent combustion. For all these reasons, the physics of supernovae and gamma ray bursts has to be studied by means of multidimensional hydrodynamical simulations, spectral syntheses, and observations.

Core-collapse supernova explosions are the final stages in the evolution of massive stars. These stars have developed an iron core which becomes gravitationally unstable. The subsequent collapse leads to the formation of a neutron star or a black hole, and in many cases to the ejection of the stellar mantle and envelope in a supernova event. Supernovae of single stars are referred to as type II, Ib or Ic, whereby the last type is associated with an even more violent event, i.e., gamma ray bursts. SNIc result from the explosion of stars without hydrogen and little or no helium which corresponds to a rare category of Wolf-Rayet stars. These so-called WO stars have an excess of C and O with

respect to helium, with $O > C$. Only very massive stars ($\approx 60 M_{\odot}$) with low metallicity can evolve to an oxygen enriched WR star (Maeder et al. 2004). The subsequent SNic explosion show unusual properties like high velocities and energies, asymmetry, and evidence for relativistic motion inferred from its radio afterglow. These afterglows, following cosmic gamma ray bursts, were first discovered in 1997 although the bursts themselves were discovered about 40 years⁵ ago.

The resulting huge energy release of $> 10^{51}$ erg creates a relativistic wind which expands into the medium surrounding the burster. This accelerates electrons to relativistic velocities which then emit synchrotron radiation producing an afterglow. Compared to the short-lived GRBs (which only last seconds) afterglows can be observed over many days, or even months. GRBs and their afterglows are the most luminous electromagnetic phenomena in the Universe. In the high energy bands GRBs should be detectable up to redshifts 20, and if high-redshift GRBs exist an exciting new window into the cosmic dark ages will be opened. Different from quasars and galaxies that fade with increasing redshift, GRB afterglows maintain a roughly constant observed flux for a fixed time lag after the gamma ray trigger. They are, therefore, the best probes of the metallicity and ionization state of the intervening intergalactic medium during the epoch of reionization, which is associated with the pregalactic generation of Population III stars.

Having presented some fascinating aspects of stellar properties and evolution, we will now summarize our most important results of chapters 2 to 6.

1.2 Model Atmospheres

The determination of stellar parameters and wind properties from observed spectra is a very challenging task and difficult to accomplish, since they are not direct observables. We need to rely on stellar atmosphere models, including the hydrodynamic effects of winds, which form the basis for radiative transfer calculations, and compare them to observations. By including lines and continua in the optical and the infrared regime in the analyses we come upon a rather complicated situation. In these cases, the spectral information usually originates simultaneously from the quasi-hydrostatic photospheric layers below the sonic point and from the wind layers above. Thus, *unified model atmospheres* are required (Gabler et al. 1989) which nowadays have become a standard treatment for model atmospheres of hot stars with winds. Unified models are stationary, in non-LTE and in radiative equilibrium. They are spherically extended and comprise the entire sub- and supersonic structure from the pseudo-hydrostatic photosphere to the stellar wind. This enables us to calculate consistent energy distributions, photospheric lines and wind lines, and to treat the multitude of mixed cases, where photospheric lines are contaminated by wind effects.

⁵With the launch of Sputnik 1 by the Russians and the cold war raging, the US began to think about a special commission to ensure a peaceful use of outer space. During the general meeting of the United Nations in December 1959 the first version of an international treaty forbidding all nuclear tests outside the Earth's atmosphere was drafted and in Los Alamos a satellite-borne sensor system to detect illegal nuclear explosions in space was developed. Even though space travel was still in its early days, serious consideration was given to the possibility that the Russians would carry out undetectable nuclear tests at the far side of the Moon. X-rays and gamma radiation emitted in the explosion of a nuclear weapon would indeed be concealed by the Moon, but eventually the expanding cloud from the explosion would sooner or later have to be detected. For this reason the fourth generation of the Vela satellites was launched in April 1967 comprising two identical satellites with 350 kg each in high circular orbits around the Earth at an altitude of 100,000 km. Later that year the first gamma ray burst was detected by Ray Klebesadel and Roy Olsen who picked up a signal very different from that of a nuclear explosion and it was this event which marked the beginning of the scientific studies of gamma ray bursts and their origin (Cambridge University Press, 2002, by G.Shilling).

The analyses carried out in this thesis have been performed by means of non-LTE atmospheres/line formation, utilizing the latest version of FASTWIND (an acronym for Fast Analysis of STellar atmospheres with WINDs; Santolaya-Rey et al. 1997; Herrero et al. 2002; Puls et al. 2005). The code was primarily developed to be highly computationally efficient and tailored for the optical and infrared wavelength regime. FASTWIND has been significantly improved since its first introduction by Santolaya-Rey et al. (1997). It comprises the appropriate treatment of line broadening (i.e., Stark and pressure broadening) which is a prerequisite for the analysis of O-type stars of different luminosity classes covering a variety of wind densities. Moreover, FASTWIND was recently updated to include an approximate treatment of metal line opacity effects, i.e., metal line blocking and blanketing. In order to save computational effort, the resulting metal line opacities are averaged in a suitable way (mean of inverse opacities, in analogy to Rosseland means) over a frequency interval of the order of the wind terminal velocity before the radiation transport is performed. The elements responsible for the effects of line blocking and blanketing are called background elements in contrast to explicit elements which are used as diagnostic tools (e.g., hydrogen and helium, but also C, N, O and others). For the treatment of the metal-line background elements a high accuracy is not necessary and can be approximated as mentioned before, whereas the explicit elements necessitate high precision by means of detailed atomic models. The code meanwhile also allows for the calculation of a consistent temperature stratification in the lower and outer atmosphere, which is particularly important for IR-spectroscopy, since the IR is mainly formed above the stellar photosphere and depends on the run of the electron temperature, T_e .

Apart from FASTWIND, there are, of course, also alternative codes in use, which have been developed for various specific objectives. In particular, these codes are CMFGEN (Hillier & Miller 1998), the Potsdam-group code developed by W.R. Hamann and collaborators (Gräfener et al. 2002), PHOENIX (Hauschildt & Baron 1999), and WM-Basic (Pauldrach et al. 2001) and will be described in more detail in chapter 2. The development of new telescopes and multi-object spectrographs, allowing to observe large samples of stars very efficiently, accentuates the need for fast model atmosphere codes. Since the parameter space investigated for the analysis of only one object comprises the simultaneous derivation of effective temperature T_{eff} , gravity $\log g$, optical depth invariant⁶ $Q = \dot{M}/(R_* v_\infty)^{1.5}$, velocity field parameter β , chemical abundances, and also global background metallicity z , the computational effort needed to calculate a large sample of stellar models is enormous. FASTWIND is able to compute the vast amount of models in a time-saving way (30 min. per model on a 1GHz processor). In the meantime, a number of other analyses have been performed using the present version of FASTWIND (for further details see e.g. Urbaneja et al. 2003; Urbaneja 2004; Massey et al. 2004, 2005).

In chapter 2, we have concentrated on a detailed comparison with results from those two codes which have been used in alternative spectroscopical investigations of OB stars, namely CMFGEN (Hillier & Miller 1998) and WM-Basic (Pauldrach et al. 2001). The new methods have been extensively tested by comparing with results obtained from these two codes, concerning temperature stratification, fluxes, number of ionizing photons and optical⁷ H/He profiles (comparison with CMFGEN only). All three codes predict almost identical temperature structures and fluxes for $\lambda > 400 \text{ \AA}$, whereas at lower wavelengths certain discrepancies are found. Compared to WM-Basic (using an identical line list for the background elements), our supergiant models differ only in the He II continua, where the FASTWIND-

⁶Stellar winds with different combinations of \dot{M} , R_* , and v_∞ but identical Q-parameter give rise to similar profiles (see chapter 2).

⁷IR-lines will be presented in chapter 6, with a similar agreement between FASTWIND and CMFGEN as in the optical.

fluxes are somewhat larger, but still lower than the corresponding fluxes from CMFGEN. Since fluxes and corresponding numbers of ionizing photons react extremely sensitive to subtle model differences in this wavelength regime, we consider any uncritical use of these quantities as being unreliable. For the optical H/He lines, the coincidence between FASTWIND and CMFGEN is remarkable, except for the He I singlets in the temperature range between 36,000 to 41,000 K for dwarfs and between 31,000 to 35,000 K for supergiants, where CMFGEN predicts much weaker singlets. Up to now, the origin of this discrepancy could not be identified, but work is under way to solve this problem.

1.3 Quantitative Optical Spectroscopy

By means of the improved model atmospheres code we began our studies with a first re-analysis of the Galactic O-star sample presented by Puls et al. 1996 as described in chapter 3 and which preceded our detailed investigation of the same sample stars as presented in chapter 4. Such a re-analysis became necessary, since first, this O star sample has originally been analyzed by means of pure H/He models, not including line blanketing effects, whereas our improved code now does account for these effects. Second, from the wind momentum-luminosity equation (Eqn.1.1) we would expect a strict correlation of $\log \dot{M} v_{\infty} R_{\star}^{0.5}$ with $\log L$. In the WLR investigation presented by Puls et al. 1996, however, no unique relation has been found, but instead a clear separation between luminosity class I objects and III/V objects, which is an interesting result as the WLR should be independent of luminosity class. Furthermore, it was found that supergiants follow a very tight relation compared to objects of luminosity classes III and V, whereby the latter exhibit an almost parallel slope until luminosities $\log L/L_{\odot} = 5.3$. Below this value the relation turns off and seems to become much steeper.

Because of this discrepancy between theory and “observations” (remember that the analyses had been performed by means of unblanketed models), we considered a re-analysis to be a good opportunity to re-check i) the *observed* correlation of the WLR with luminosity and ii) to scrutinize the *prediction* of the WLR to depend on luminosity class by means of detailed theoretical simulations (in addition to the alternative theoretical calculations presented by Vink et al. 2000).

As it turned out, the newly derived WLR (based on the material presented in chapter 4) still displays a clear separation between luminosity class I and III/V objects in addition to a larger vertical offset compared to the old WLR derived by Puls et al. 1996. Interestingly, this larger vertical offset is now consistent with the theoretical calculations by Vink et al. 2000 for luminosity class III and V objects. By comparing our result to the detailed theoretical simulations based on self-consistent hydrodynamical wind models by means of WM-basic (Pauldrach et al. 2003) we find, on the one hand, a striking similarity between the two theoretical predictions. This gives us a lot of confidence that the WLR should, indeed, be independent of luminosity class, as both predictions depend on completely independent simulations. On the other hand, theory agrees quite well with observations for non-supergiants (i.e., luminosity class III/V objects), whereas for supergiants an average factor of 3.5 seems to be missing. In other words, the “old” dilemma still exists!

We then have extended our investigation by incorporating a number of Cyg OB2 stars, which have been analyzed by means of FASTWIND as well (cf. Herrero et al. 2002). Although this sample consists almost exclusively of supergiants, the clear separation as a function of luminosity class, which we have confirmed for objects from our sample, is no longer visible. Due to the results we have decided to replot our data (including the Cyg OB2 stars) in a slightly different manner, thereby separating the

sample in terms of the observed H_α profile, i.e., objects with H_α in emission, objects with absorption profiles partly refilled by wind emission, and objects with almost purely photospheric H_α profiles. Classified in this way, it turned out that stars (from the combined sample) with H_α in emission and those with absorption profiles form two distinct WLRs.

From these findings, we suggest that the different WLRs might be a consequence of wind-clumping: The contribution of wind emission to the total profile is significantly different for objects with H_α in absorption compared to object with H_α in emission, since for the former only contributions from the lowermost wind can be seen, whereas for the latter the emission is due to a significant wind volume. Thus, there is the possibility that for these objects we *see* the effects of a clumped wind which would mimic a higher mass-loss rate, as it is most probably the case for Wolf-Rayet winds (e.g., Moffat & Robert 1994). With this suggestion, we do not exclude the presence of clumping in the winds of objects with H_α in absorption. Owing to the low optical depth, however, we simply cannot see it. The principal presence of clumping has never been ruled out for O-star winds, but at least from conventional spectrum analysis methods there was simply no indication that *the H_α forming region* was considerably clumped.

Thus, we asked ourself the question what clumping factor would be required to “unify” the different WLRs with each other and with the theoretical predictions, respectively. In order to investigate this, we have modified the mass-loss rates for all objects with H_α in emission (including the Cyg OB2 stars) to match the WLR of giants/dwarfs as close as possible, assuming that the effective clumping factor in the H_α emitting wind region is similar. The required factor with respect to \dot{M} turned out to be 0.44, corresponding to an effective clumping factor $\langle \rho^2 \rangle / \langle \rho \rangle^2 = 5.2$, i.e., the mass loss rates of stars with H_α in emission would typically be overestimated by a factor of 2.3. Note that the clumping factor and the “mass loss reduction factor” are related by the inverse square of each other, at least if the wind material consists of dense clumps and almost void inter-clump matter.

In summary, there are strong indications that mass-loss analyses of (at least) O-star winds utilizing H_α tend to overestimate the resulting values (by a factor of 2.3 for star with H_α in emission), unless clumping is accounted for or the winds are comparatively thin.

In chapter 4 we present a far more detailed analysis of the same sample of stars as used in chapter 3 (i.e., paper 2) with minor differences in the results, as the results in paper 2 were based on preliminary data. The detailed analysis has been carried out by fitting the photospheric and wind lines of H and He by means of a large sample of spectral subtypes ranging from O2 to O9.5 enabling us to obtain a temperature scale for O supergiants, giants, and dwarfs. We find that the influence of line blanketing redefines the Galactic temperature scale significantly. Supergiants of spectral type O2 to O9.5 are now located between roughly 43,000 K and 30,000 K, whereas dwarfs of spectral type O3 to O9 are located between 47,000 K and 32,000 K. We find a shift towards lower temperatures for all stars in our sample, but we also expected a (moderate) reduction of $\log g^8$, which is found for only about half of the sample stars. For the other half, the gravities remain unaltered or had to be increased in order to obtain a convincing fit.

For those objects, however, where the gravity remained unaltered or had to be increased, we derive a lower helium abundance than found by Herrero et al. (1992). Hence, instead of a reduced gravity, which in these cases is “forbidden” by the hydrogen Balmer lines, we obtained a reduced helium

⁸Note that the values of $\log g$ from Puls et al. 1996 include an approximate correction for wind-effects.

abundance. Thus, the well-known helium discrepancy (Herrero et al. 1992) has considerably been reduced by our analysis using blanketed models (see also Herrero et al. 2002). Note, however, that a large fraction of the sample stars still remains overabundant in He. For these objects, at least the derived range in abundance is consistent with present evolutionary tracks when rotationally induced mixing is accounted for.

Further, we have calculated new spectroscopic masses and compared them with previous results and found, that although the former *mass discrepancy* (Herrero et al., 1992) becomes significantly reduced, a systematic trend for masses below $50 M_{\odot}$ seems to remain: In this range, the spectroscopically derived values are smaller than the “evolutionary masses” by roughly $10 M_{\odot}$.

As for the wind momentum-luminosity relation, we obtain similar results compared to the preliminary ones from paper 2. Although quantitatively different, both the results presented in paper 3 and in paper 2 indicate a clear separation between luminosity class I objects and the III/V objects. Nevertheless, this separation seems to have decreased regarding our new data from the detailed analysis. Including a clumping factor of ≈ 5 can solve this problem, at least by reclassifying the sample in terms of profile type. Of course, we also have to be open to other possibilities which might explain the discrepancies found.

One of the major problems encountered in the analysis in paper 3 is the uncertainty in stellar radius, which originates from uncertain distances and enters quadratically into the values for masses, luminosities and wind-momentum rates. To overcome this uncertainty we decided to consider a sample of stars which is much larger than the one used so far (with the hope that better statistics will help to obtain better constraints). This is what we have investigated in chapter 5 (i.e., paper 4). In this paper, however, we had to proceed differently as only H_{α} spectra were available. Thus, we first had to clarify if a pure H_{α} profile analysis has the potential to provide mass-loss and wind-momentum rates for O-type stars, compatible to those from a state-of-the-art complete spectral analysis. This goal has been attained by comparing the derived mass-loss rates to those determined in paper 3 (via a complete NLTE spectral analysis). To determine \dot{M} and velocity field exponents β , we applied the approximate method developed by Puls et al. (1996). Effective temperatures and gravities needed to perform the H_{α} profile fitting have been obtained via spectral type - T_{eff} and spectral type - $\log g$ calibrations for O stars of luminosity classes I, III and V, based on results of paper 3 and Martins et al. (2002)). Our analysis showed that not only the wind densities but also the WLR derived by means of our approximate approach are in good agreement to the results originating from the complete spectral analysis. In particular, we can confirm the result obtained in paper 3 that the WLR for luminosity class III/V objects strictly follows the theoretical predictions of Vink et al. (2000), while the relation for luminosity class I objects shows a vertical offset. For the combination of our sample with data from the other investigations, we find that with an enhancement factor of ~ 2 for stars with H_{α} in emission the differences in the corresponding WLRs almost vanish and a unique relation can be obtained. This enhancement factor corresponds to an effective clumping factor of 4.3, in agreement with the value previously found in paper 3. From this we deduce that the analysis of the largest O star sample (47 stars) considered so far indicates significant clumping and an overestimate of the present mass loss rate for objects with H_{α} in emission.

1.4 Quantitative Infrared Spectroscopy

By virtue of the star formation scenario described in Sect. 1.1.2 it can be seen that high mass star formation is, indeed, still poorly understood. Our inability to study young, recently formed stellar systems at traditional wavelengths, due to the enormously large extinction, leaves fundamental questions on the nature and evolutionary history of massive star systems unanswered. Molecular gas and dust found in star forming regions allow little or no light to escape at optical wavelengths. The dust, however, becomes more transparent in the infrared (IR) regime. Therefore, well-known observational and modeling techniques have been advanced and extended to near infrared regime. Observations at such wavelengths reveal the hot stellar content of these dust-enshrouded environments like young HII regions in dense molecular clouds, the Galactic centre or massive clusters. Following the substantial progress in ground-based IR instrumentation in the past decade, IR spectroscopy has become a powerful diagnostics for the investigation of hot stars and the stellar winds surrounding them. The first systematic observational studies of OB stars in the H and K band have been performed by e.g., Hanson et al. (1996) providing an important basis for quantitative spectral analysis of early type stars. The modeling of the near-infrared, on the other hand, has been performed mostly for early-type stars with dense winds, e.g., for Wolf-Rayet Stars (Hillier 1982) and for Of/WN stars (Crowther et al. 1995, 1998). For objects with thinner winds (which are of particular interest when aiming at the youngest objects emerging from Ultra-Compact H II regions), no results are available so far, except from a pilot study by Lenorzer et al. (2004) using synthesized spectra. As the ultimate goal is the usage of solely the infrared regime to provide accurate constraints to the characteristics of stars which can only be observed at these wavelengths, it was the second main objective of this thesis to carry out a spectral analysis of stars in the near infrared regime and compare it with results already obtained in the optical. This will allow us to check the extent to which the data derived from the IR are consistent with results obtained from alternative studies in different wavelength bands. We also wanted to test our model atmosphere code FASTWIND (see Sect. 1.2 and paper I) for OB stars in the near infrared, and see if an extended use to these wavelength ranges is feasible. In addition, we gave special attention to those lines which are located in the H and K band, i.e., which can be accessed by *ground-based* instrumentation alone. Note that these lines are mainly formed close to the photosphere, apart from Br_γ and $\text{He II}2.18$, and thus remain uncontaminated by more complex physical processes such as clumping and X-rays, providing rather robust estimates for effective temperatures and gravities. In total, seven lines have been investigated, three from hydrogen, including $\text{Br}10$, $\text{Br}11$ and Br_γ , serving as a diagnostic tool to derive wind-densities, two He I and two He II lines ($\text{He II}1.70$, $\text{He II}2.11$, $\text{He II}1.69$, and $\text{He II}2.18$). For two stars, we could make additional use of $\text{He II}2.05$ (singlet). In particular, $\text{Br}10$ and $\text{Br}11$ give clues on the gravity (if T_{eff} is known), He I and He II define temperature and helium content, and Br_γ can serve as an \dot{M} indicator, at least in principle. In those cases, where only one ionization stage of helium was visible, the determination of Y_{He} becomes problematic, and also the uncertainty for T_{eff} increases. Due to the high quality of our spectra, however, both He II lines were visible for most spectral types.

First we investigated the predicted behaviour of the strategic lines, by means of a large model grid (again, see paper I). Interestingly and in contradiction to what one expects from the optical, almost all photospheric lines in the H and K band (from H, He I and He II) become stronger when the gravity decreases. Concerning H and He II, this is related to the particular behaviour of Stark broadening as a function of electron density, which in the line cores is somewhat different for members of lower and higher series. For the latter, the cores become deeper when the density decreases, and contribute

more to the total line strength than in the optical. Regarding He I, on the other hand, the predicted behaviour is due to some subtle NLTE effects resulting in a stronger overpopulation of the lower level when the gravity decreases, so that the source function becomes weaker and the profile deeper, i.e., stronger. This strong dependence of the profile on the source function is a direct consequence of the IR line formation with $h\nu/kT \ll 1$.

As already mentioned, recently Lenorzer et al. (2004) presented a first calibration of the spectral properties of normal OB stars using near infrared lines. A comparison of the detailed profiles of the strategic lines located in the H and K band as calculated by them with our results has shown that the agreement between the results for the almost purely photospheric lines in the H band is nearly perfect, and also for the K band the comparison turned out to be rather satisfactory. The only important discrepancies concern the He I singlets of the supergiant and dwarf models at intermediate spectral types, a result which was also found in the optical (see Sect. 1.2).

After carrying out the analysis for our sample described above we find that an H/K band analysis is able to derive constraints on the same set of stellar and wind parameters as it is known from the optical, e.g., T_{eff} , $\log g$, Y_{He} and optical depth invariant Q , where the latter yields the mass-loss rate \dot{M} if stellar radius and terminal velocity are known. For cooler objects, when He II is missing, a similar analysis might be possible if He I2.05 is available (due to the almost orthogonal reaction of He I2.05 and He I2.11 on T_{eff} and $\log g$) and the helium content can be adopted, which should be possible for very young objects containing unprocessed material.

For most of our objects, we obtained good fits, except for the line cores of Br $_{\gamma}$ in early O-stars with significant mass-loss. The observations show Br $_{\gamma}$ mostly as rather symmetric emission lines, whereas the models predict a P Cygni type profile with strong absorption. This discrepancy (which also appears in lines synthesized by CMFGEN) might be an indirect effect of clumping. With the derivation of the stellar and wind parameters from the IR, we could compare them to results from previous optical analyses. Overall, the IR results coincide in most cases with the optical ones within the typical errors usually quoted for the corresponding parameters, i.e., an uncertainty in T_{eff} of 5%, in $\log g$ of 0.1 dex and in \dot{M} of 0.2 dex, with lower errors at higher wind densities. In most of the cases where we have found discrepancies beyond these errors, their origin could be easily identified (see chapter 6).

This investigation enables us to constrain the observational requirements to perform such an IR-analysis. Most important is a (very) high S/N (at least for the hotter objects), because most of the lines to be investigated are extremely shallow, and a very good resolution, similar to the one used here (of order 10,000). Only then it is possible to disentangle the line cores from the wings in stellar profiles and to obtain reasonable clues about any contamination due to reduction problems. As for the required set of lines, it is clear that the more lines there are available the better it is for obtaining useful constraints.

The value of a reliable quantitative analysis for hot, massive stars based entirely in the infrared cannot be overstated. Most obvious, it will allow the evaluation of massive star characteristics at an significantly earlier evolutionary stage than has ever been possible before. The influence of disk emission may render the photosphere of some very young massive stars inaccessible. We suspect, however, that among the most massive stars, around mid-O or hotter, the disk will be destroyed well before even near-infrared studies would be feasible due to the very short disk lifetime (Watson & Hanson 1997).

1.5 Outlook

From the above we find that the present status of hot star parameters is not as clear as we would like it to be. Actually, we need to understand a number of additional physical processes and their influence on the derived parameters. Most important are the direct and indirect effects of the line-driven wind instability, i.e., the formation and interaction of clumps and shocks leading to X-ray emission and enhanced EUV-flux in the wind (e.g., Feldmeier et al. 1997; Pauldrach et al. 2001). Although incorporated to some extent into present codes, there are simply too many questions to be answered before we can consider these problems as solved.

Before these effects can be treated in a realistic way, we suggest to primarily rely on diagnostic tools which are least “contaminated”, i.e., to concentrate on weak lines formed in the stellar photospheres (except, of course, the mass-loss indicators which will always be affected by clumping). Future investigations of O-type stars performed by FASTWIND will have to utilize not only H and He but also metal lines, as already incorporated into the analysis of B-stars. Particularly, one of the most important tools will be nitrogen with its strong sensitivity even at higher temperatures where He I begins to fail. Work in this direction is already in preparation.

As previously stated, one of the major implications of our re-analysis of Galactic O stars regards the wind-momentum luminosity relation. A *unification* of the different WLRs is possible by assuming that for those stars with H_α in emission, the derived mass-loss rates are affected by clumping in the lower wind region. For stars with H_α in absorption, on the other hand, this line is formed very close to the photosphere such that clumping effects should not disturb the analysis.

Recently Bouret et al. (2005), however, have investigated the role of wind clumping and its resulting effect on stellar parameters by means of a quantitative analysis of the FUSE and IUE spectra of two Galactic O4-type stars. The authors argue that clumping should start deep in the wind, just above the sonic point, at $v_{\text{clumping}} \approx 30 \text{ km s}^{-1}$. Their results imply that the mass loss rates of *all* O stars need to be significantly revised downward, by a factor of 3 to 7. If this was true, the present evolutionary scenarios of massive stars will drastically be altered.

Other possibilities, however, might also explain the discrepancies found. A combined multi-spectral analysis (UV, optical, IR and radio) based on clumped wind-models and applied to large samples of stars of different spectral type should clarify these questions. With the advent of very large telescopes, the range of quantitative spectroscopy of individual stars can be extended to distant galaxies and multi-aperture or integral-field spectroscopy will allow to observe larger samples very efficiently. Observational campaigns utilizing multi-object spectroscopy like the so-called VLT-FLAMES Survey of Massive Stars (Evans et al. 2005), aiming at the analysis of samples of more than hundred Extragalactic and Galactic objects, will definitely lead to a dramatic increase of our knowledge of hot, massive stars.

1.6 Outline of the thesis

In this section we would like to give an outline of the studies presented within the framework of this thesis.

1.6.1 Paper 1: Atmospheric NLTE-Models for the Spectroscopic Analysis of Blue Stars with Winds: II. Line-Blanketed Models

In this paper we present new or improved methods for calculating NLTE, line-blanketed model atmospheres for hot stars with winds (spectral types A to O), with particular emphasis on fast performance. These methods have been implemented into a previous, more simple version of the model atmosphere code FASTWIND (Santolaya-Rey et al. 1997) and will help us to spectroscopically analyze large samples of massive stars in a reasonable time-scale, using state-of-the-art physics. In particular, we describe our (partly approximate) approach to solve the equations of statistical equilibrium for those elements that are primarily responsible for line-blocking and blanketing, as well as an approximate treatment of the line-blocking itself, which is based on a simple statistical approach using suitable means of line opacities and emissivities. Both methods are validated by specific tests. We comment on our implementation of a consistent temperature structure. A key part of this paper is a detailed comparison with results from two codes used in alternative spectroscopical investigations, namely CMFGEN (Hillier & Miller 1998) and WM-Basic (Pauldrach et al. 2001). Finally, we present suggestions about how to parameterize model-grids for hot stars with winds, with only one additional parameter, the optical depth invariant Q , compared to standard grids from plane-parallel, hydrostatic models.

1.6.2 Paper 2: Advances in radiatively driven wind models

In the next paper we present a first re-analysis of the Galactic O-star sample presented by Puls et al. (1996) by means of NLTE-atmospheres including line blocking and blanketing. In particular, we concentrate on the question concerning the dependence of the wind-momentum luminosity relation (WLR) on luminosity class.

1.6.3 Paper 3: Stellar and wind parameters of Galactic O-stars: The influence of line-blocking and -blanketing

In paper 3 we perform a detailed re-analysis of the Galactic O-star sample from Puls et al. (1996) by means of line-blanketed NLTE model atmospheres in order to investigate the influence of line blocking and blanketing on the derived parameters. The analysis has been carried out by fitting the photospheric and wind lines from H and He. We calculate new spectroscopic masses and compare them with previous results. We discuss the fact that a significant fraction of our sample stars remains over-abundant in He, although the actual values were found to be lower than previously determined. One of the key questions is how the wind-momentum luminosity relation is affected by line blocking and blanketing and see if the derived mass-loss rates of stars with H in emission are affected by clumping.

1.6.4 Paper 4: Mass-loss and wind-momentum rates of O-type stars: A pure H_α analysis accounting for line-blanketing

In paper 4 we study the mass-loss and wind momentum rates of 29 Galactic O-type stars with luminosity classes I, III and V by means of a pure H_α profile analysis and investigate to what extent the results compare to those originating from a state-of-the art, complete spectral analysis. This investigation relies on the approximate method developed by Puls et al. (1996) which we have modified to account for the effects of line blanketing. We derive effective temperatures and gravities needed to obtain quantitative results by means of calibrations based on the spectroscopic NLTE analyses and models of Galactic stars derived in paper 3. Not only do we compare the derived wind densities to those determined in paper 3 for eleven stars in common but we also compare the wind-momentum luminosity relationship (WLR) of the sample stars to those derived by other investigations. Additionally, we investigate the consequences of fine tuning some of the direct and indirect parameters entering the WLR, especially by accounting for different possible values of stellar reddening and distances. At the end of this paper we study the WLR for the largest sample of Galactic O-type stars gathered so far, including an elaborate error treatment.

1.6.5 Paper 5: Quantitative H and K band spectroscopy of Galactic OB-stars at medium resolution

This paper comprises an analysis of 25 Galactic O and early B-stars by means of quantitative H and K band spectroscopy, with the primary goal to investigate to what extent a lone near-IR spectroscopy is able to recover stellar and wind parameters derived in the optical. Most of the spectra have been taken with SUBARU-IRCS, at an intermediate resolution of 12,000, and with a very high S/N, mostly on the order of 200 or better. In order to synthesize the strategic H/He lines, we have used our recent, line blanketed version of FASTWIND (see paper 1). We investigate the predicted behaviour of the strategic lines and see if it is possible to derive the stellar and wind parameters from the IR with the same reliability as from previous optical analyses.

Bibliography

- Abbott, D.C. 1979, in: Proc. IAU Symp. 83, eds. P.S. Conti & C.W.H. de Loore
- Appenzeller, I.N. 1987, in: 'Stabilities in luminous early type stars' p.55-67
- Behrend, R., Maeder, A. 2001, A&A 373, 190
- Bonnell, I.A., Bate, M.R., Zinnecker, H. 1998, MNRAS 298, 93
- Bouret, J.C., Lanz, T., Hillier, D.J. 2003, ApJ 595, 1182
- Bromm, V., Kudritzki, R.P., Loeb, A. 2001, ApJ 552, 464
- Bromm, V., Larson, R.B. 2004, ARA&A 42 79
- Chlebowski, T., Harnden, F.R., Sciortino, S. 1989, ApJ 341 427
- Crowther, P.A., Hillier, D.J., Smith, L.J. 1995, A&A 293, 172
- Crowther P.A., Bohannan, B., Pasquauli, A. 1998, in: Boulder-Munich II, eds. I.D. Howarth, ASP 131, p.38
- Crowther, P.A., Hillier, D.J., Evans, C.J., et. al. 2002, ApJ 579, 774
- Evans II, N.J. 1999 ARA&A 37, 311
- Eversberg, T., Lepine, S., Moffat, A.F.J. 1998, ApJ 494, 799
- Feldmeier, A., Puls, J., Pauldrach, A.W.A. 1997, A&A 322, 878
- Gabler, R., Gabler, A., Kudritzki, R.P., Puls, J., et. al. 1989, A&A 226, 162
- Gräfener, G., Koesterke, L., Hamann, W.-R. 2002, A&A 387, 244
- Hanson, M.M., Conti, P.S., Rieke, M.J. 1996, ApJS 107, 311
- Hauschildt, P.H., Baron, E. 1999, J. Comp. Appl. Math. 109, 41
- Herrero, A., Kudritzki, R.P., Vílchez, J.M., et al. 1992, A&A 261, 209
- Herrero, A., Puls, J., Najarro, F. 2002, A&A 396, 949
- Hillier, D.J. 1982, in: IAUS 99, eds. C.H. de Loore & A.J. Willis, Reidel, Dordrecht, p. 225

- Hillier, D.J., Miller, D.L. 1998, ApJ 496, 407
- Hillier, D.J., Lanz, T., Heap, S.R., et al. 2003, ApJ 588, 1039
- Howarth, I.D., Siebert, K.W., Hussain, G.A.J., et al. 1995, MNRAS 284, 265
- Hubeny, I., Lanz, T. 1995, ApJ 39, 875
- Kudritzki, R.P., Puls, J., Lennon, D.J., et al. 1999, A&A 350, 970
- Kudritzki, R.P., Puls, J. 2000, ARA&A 38, 613
- Leitherer, C., Heckman T.M. 1995, ApJS 96, 9
- Lenorzer, A., Mokiem, M.R., de Koter, A., Puls, J. 2004, A&A 422, 275
- Lucy L.B. 1982 ApJ 255 278 and 286
- Maeder, A. 2000, ARA&A 38, 143
- Maeder, A. 2000, NAR 44, 291
- Maeder, A. 2002, A&A 392, 575
- Maeder, A., Meynet, G. 2000, A&A 38, 143
- Maeder, A., Meynet, G. 2001, A&A 373, 555
- Markova, N., Puls, J., Repolust, T.M., Markov, H. 2004, A&A 413, 693
- Martins, F., Schaerer, D. & Hillier, D.J. 2002, A&A, 382, 999
- Massa, D., Fullerton, A.W., Sonneborn, G., et al. 2003, ApJ 586, 996
- Massey, P. 2003 ARA&A 41, 15
- Massey, P., Kudritzki, R.P., Bresolin, F., et al. 2004, ApJ 608, 1001
- Massey, P., Puls, J., Pauldrach, A.W.A., et al. 2005, in prep. for ApJ
- Meynet, G., Maeder, A. 1997, A&A 321, 465
- Meynet, G., Maeder, A. 2000, A&A 361, 101
- Moffat, A.F.J., Robert, C. 1994, ApJ 421, 310
- Nakano, M., Yamauchi, S., Sugitani, K., et al. 2000, PASJ 52, 437
- Oey, S. 2003, in: Proc. IAU Symp 212, eds. K.A. van der Hucht, A. Herrero & C. Esteban, ASP, p. 620
- Ostriker, J.P., Gnedin, N.Y. 1996, ApJ 472, 63
- Owocki, S.P., Rybicki, G.B. 1984, ApJ 284, 337

- Owocki, S.P., Rybicki, G.B. 1985, *ApJ* 299, 265
- Owocki, S.P. 1991, in: *Proc. 'The Atmospheres of Early Type Stars'*, eds. S. Jeffery & U. Heber, Berlin: Springer Verlag, p.393
- Owocki, S.P., Puls, J. 1999, *ApJ* 510, 355
- Pauldrach, A.W.A., Puls, J., Kudritzki, R.P. 1986, *A&A* 164, 86
- Pauldrach, A.W.A., Hoffmann, T.L., Lennon, M. 2001, *A&A* 375, 161
- Pauldrach, A.W.A., Hoffmann, T.L., Méndez, R. 2003, in *Proc. IAU Symp. 209*, eds. S.Kwok & M.Dopita
- Pettini, M., Steidel, C.C., Adelberger, K.L., et al. 2000, *ApJ* 528, 96
- Plume, R., Jaffe, D.T., Evans, N.J. II, et al. 1997, *ApJ* 476, 730
- Puls, J., Kudritzki, R.P., Herrero, A., et al. 1996, *A&A* 305, 171
- Puls, J., Springmann, U., Lennon, M. 2000, *A&A* 141, 23
- Puls, J., et al. 2003, in: *Proc. IAU Symp 212*, eds. K.A. van der Hucht, A. Herrero & C. Esteban, ASP, p. 61
- Puls, J., Urbaneja, M.A., Venero, R. 2005, *A&A* accepted
- Repolust, T., Puls, J., Herrero, A. 2004, *A&A* 415, 349
- Repolust, T., Puls, J., Hanson, M.M. 2005, submitted
- Robert, C., Moffat, A.F.J. 1990, *ASP Conf. Series Vol. 7*, 271
- Santolaya-Rey, A.E., Puls, J., Herrero, A. 1997, *A&A* 323, 488
- Shu, F.H., Adams, F.C., Lizano, S. 1987, *ARA & A* 25, 23
- Silich, S., Tenorio-Tagle, G. 2001, *ApJ*, 552, 9
- Steidel, C.C., Giavalisco, M., Pettini, M., et al. 1996, *ApJL* 462, L17
- McKee, C.F., Tan, J.C. 2003 *ApJ* 585, 850
- Urbaneja, M.A., Herrero, A., Bresolin, F., et al. 2003, *ApJL* 584, 73
- Urbaneja, M.A. 2004, "B Supergiants in the Milky Way and nearby galaxies: models and quantitative spectroscopy", thesis, University of La Laguna
- Vink, J.S., de Koter, A., Lamers, H.J.G.L.M. 2000, *A&A*, 362, 295
- Vink, J.S., de Koter, A., Lamers, H.J.G.L.M. 2001, *A&A* 369, 574
- Watson, A.M., Hanson, M.M. 1997, *ApJL* 490, 165

Weiss, A., Cassisi, S., Schlattl, H., Salaris, M. 2000 ApJ 533, 413

Woosley, S.E. 1993, A&A 405, 273

Yorke, H. W., Kruegel, E. 1977, A&A 54, 183

Chapter 2

Atmospheric NLTE-Models for the Spectroscopic Analysis of Blue Stars with Winds: II. Line-Blanketed Models

J. Puls, M. A. Urbaneja, R. Venero, T. Repolust, U. Springmann, A. Jokuthy and M. R. Mokiem, A&A, in press

Abstract. We present new or improved methods for calculating NLTE, line-blanketed model atmospheres for hot stars with winds (spectral types A to O), with particular emphasis on a *fast performance*. These methods have been implemented into a previous, more simple version of the model atmosphere code FASTWIND (Santolaya-Rey et al. 1997) and allow to spectroscopically analyze rather large samples of massive stars in a reasonable time-scale, using state-of-the-art physics. Although this updated version of the code has already been used in a number of recent investigations, the corresponding methods have not been explained in detail so far, and no rigorous comparison with results from alternative codes has been performed. This paper intends to address both topics.

In particular, we describe our (partly approximate) approach to solve the equations of statistical equilibrium for those elements which are primarily responsible for line-blocking and blanketing, as well as an approximate treatment of the line-blocking itself, which is based on a simple statistical approach using suitable means for line opacities and emissivities. Both methods are validated by specific tests. Furthermore, we comment on our implementation of a consistent temperature structure.

In the second part, we concentrate on a detailed comparison with results from those two codes which have been used in alternative spectroscopical investigations, namely CMFGEN (Hillier & Miller 1998) and WM-Basic (Pauldrach et al. 2001). All three codes predict almost identical temperature structures and fluxes for $\lambda > 400 \text{ \AA}$, whereas at lower wavelengths a number of discrepancies are found. Particularly in the He II continua, where fluxes and corresponding numbers of ionizing photons react extremely sensitively to subtle differences in the models, we consider any uncritical use of these quantities (e.g., in the context of nebula diagnostics) as being dangerous. Optical H/He lines as synthesized by FASTWIND are compared with results from CMFGEN, obtaining a remarkable coincidence, except for the He I singlets in the temperature range between 36,000 to 41,000 K for dwarfs and between 31,000 to 35,000 K for supergiants, where CMFGEN predicts much weaker lines. Consequences due to these discrepancies are discussed.

Finally, suggestions are presented how to adequately parameterize model-grids for hot stars with winds, with only one additional parameter compared to standard grids from plane-parallel, hydrostatic models.

2.1 Introduction

During the last years, the quantitative spectroscopy of massive stars with winds has made enormous progress due to the development of NLTE (non-local thermodynamic equilibrium) atmosphere codes which allow for the treatment of metal-line blocking and blanketing. With respect to both spectral range (from the extreme ultraviolet, EUV, to the infrared, IR) and metallicity of the analyzed objects (from SMC-abundances to Galactic center stars), a wide range in parameters can now be covered. Presently, five different codes are in use which have been developed for specific objectives, but due to constant improvements they can be applied in other contexts as well. In particular, these codes are CMFGEN (Hillier & Miller 1998), the “Potsdam-group” code developed by W.R. Hamann and collaborators (for a status report, see Gräfener et al. 2002), the “multi-purpose model atmosphere code” PHOENIX (Hauschildt & Baron 1999), WM-Basic (Pauldrach et al. 2001) and FASTWIND, which will be described here (see also Santolaya-Rey et al. 1997 and Herrero et al. 2002 for previous versions).

The first three of these codes are the most “exact” ones, since *all* lines (including those from iron-group elements) are treated in the comoving frame (CMF), which of course is a very time-consuming task. Moreover, since the first two of these codes have originally been designed for the analysis of the very dense winds from Wolf-Rayet stars, the treatment of the photospheric density stratification is approximative (constant photospheric scale-height). For several analyses this problem has been cured by “coupling” CMFGEN with the plane-parallel, hydrostatic code TLUSTY developed by Hubeny & Lanz (1995) (e.g., Bouret et al. 2003).

The multi-purpose code PHOENIX is mainly used for the analysis of supernovae and (very) cool dwarfs, but also a small number of hotter objects have been considered, e.g., the A-type supergiant Deneb (Aufdenberg et al. 2002). Due to this small number a detailed comparison with corresponding results is presently not possible, and, therefore, we will defer this important task until more material becomes available.

In contrast to all other codes which use a pre-described mass-loss rate and velocity field for the wind structure, the model atmospheres from WM-Basic are calculated by actually solving the hydrodynamical equations (with the radiative line-pressure being approximated within the force-multiplier concept, cf. Castor et al. 1975; Pauldrach et al. 1986) deep into the photosphere. Thus, this code provides a more realistic stratification of density and velocity, particularly in the transonic region (with the disadvantage that the slope of the velocity field cannot be manipulated if the wind does not behave as theoretically predicted). Since WM-Basic aims mainly at the prediction of EUV/UV fluxes and profiles, the bound-bound radiative rates are calculated using the in Sobolev approximation (including continuum interactions), which yields “almost” exact results except for those lines which are formed in the transonic region (e.g., Santolaya-Rey et al. 1997). Moreover, line-blocking is treated in an effective way (by means of opacity sampling throughout a first iteration cycle, and “exactly” in the final iterations), so that the computational time is significantly reduced compared to the former three codes.

FASTWIND, finally, has been designed to cope with optical and IR spectroscopy of “normal” stars with $T_{\text{eff}} \gtrsim 8,500 \text{ K}$ ¹, i.e., OBA-stars of all luminosity classes and wind strengths.

Since the parameter space investigated for the analysis of one object alone is large, comprising the simultaneous derivation of effective temperature T_{eff} , gravity $\log g$, wind-strength parameter $Q = \dot{M}/(R_{\star}v_{\infty})^{1.5}$ (cf. Sect. 2.9), velocity field parameter β , individual abundances (most important: helium-abundance Y_{He}) and also global background metallicity z , much computational effort is

¹i.e. molecules do not play any role and hydrogen remains fairly ionized.

needed to calculate the vast amount of necessary models. This is one of the reasons why the samples which have been analyzed so far by both CMFGEN and WM-Basic are not particularly large², comprising typically five to seven objects per analysis (e.g., Hillier et al. 2003; Bouret et al. 2003; Martins et al. 2004 for recent CMFGEN-analyses and Fullerton et al. 2000; Bianchi & Garcia 2002; Garcia & Bianchi 2004 for recent WM-Basic analyses).

The reader may note that although the number of fit-parameters gets smaller when the wind-strength becomes negligible, a certain difference between the results from “wind-codes” and plane-parallel, hydrostatic model atmospheres still remains: More or less independent of the actual mass-loss rate, there will always be an enhanced probability of photon escape from lines in regions close to the sonic point and above, if a super-sonic velocity field is present. A prime example illuminating the consequences of this enhanced escape is the He II ground-state depopulation in O-stars (Gabler et al. 1989), even though it is diminished by line-blocking effects compared to the original case studied by means of pure H/He atmospheres (see also Sect. 2.4.7).

With the advent of new telescopes and multi-object spectrographs, the number of objects which can be observed during one run has significantly increased (e.g., FLAMES attached to the VLT allows for an observation of roughly 120 objects in parallel). An analysis of those samples will definitely result in more reliable parameters due to a more extensive statistics but remains prohibitive unless the available codes are considerably fast.

This was and still is the motivation which has driven the development of FASTWIND. We have always considered a fast performance to be of highest priority. The required computational efficiency is obtained by applying appropriate physical approximations to processes where high accuracy is not needed (regarding the objective of the analysis - optical/IR lines), in particular concerning the treatment of the metal-line background opacities.

Meanwhile, a number of analyses have been performed with our present version of FASTWIND, with significant sample sizes, of the order of 10 to 40 stars per sample (e.g., Urbaneja et al. 2003; Trundle et al. 2004; Urbaneja 2004; Repolust et al. 2004; Massey et al. 2004, 2005). Although the code has been carefully tested and first comparisons with results from CMFGEN and TLUSTY have been published (Herrero et al. 2002), a detailed description of the code and an extensive comparison have not been presented so far. Particularly the latter task is extremely important, because otherwise it is almost impossible to compare the results from analyses performed using different codes and to draw appropriate conclusions. An example of this difficulty is the discrepancy in stellar parameters if results from optical and UV analyses are compared. Typically, UV-spectroscopy seems to result in lower values for T_{eff} than a corresponding optical analysis, e.g., Massey et al. (2005). Unless the different codes have been carefully compared, no one can be sure whether this is a problem related to either inadequate physics or certain inconsistencies within the codes.

This paper intends to answer part of these questions and is organized as follows: In Sect. 2.2 we give a quick overview of the basic philosophy of the code, and in Sect. 6.3.1 we describe the atomic data used as well as our treatment of metallicity regarding the flux-blocking background elements. Sects. 2.4 and 2.5 give a detailed description of our approach to obtain the fast performance desired: Sect. 2.4 details on the approximate NLTE solution for the background elements (which is applied if *no* consistent temperature structure is aimed at), and Sect. 2.5 describes our present method to tackle the problem of line-blocking. Both sections include important tests which have convinced ourselves of the validity of our approach, particularly after a comparison with results from WM-Basic.

²From here on, we will concentrate on the latter two codes because of our objective of analyzing “normal” stars, whereas the “Potsdam”-code has mainly been used to analyze WR-stars.

Sect. 2.6 covers the problem of level inversions and how to deal with them, and Sect. 2.7 comprises the calculation of a consistent temperature structure. In Sect. 2.8, a detailed comparison with results from a grid of CMFGEN models³ is performed, and Sect. 2.9 suggests how to parameterize model-grids adequately and reports on first progress. In Sect. 6.8, finally, we present our summary and an outlook regarding future work.

2.2 Basic philosophy of the code

In the following, we will summarize the basic features of FASTWIND, before we describe in detail the methods used. The first version of the code (unblocked atmosphere/line formation) has been introduced by Santolaya-Rey et al. (1997, hereafter Paper I), and has been significantly improved meanwhile. Let us first mention that we distinguish between two groups of elements, namely the so-called *explicit* ones and the *background* elements.

The explicit elements (mainly H, He, but also C, N, O, Si, Mg in the B-star range, see below) are those which are used as diagnostic tools and are treated with high precision, i.e., by detailed atomic models and by means of CMF transport for the bound-bound transitions. In order to allow for a high degree of flexibility and to make use of any improvements in atomic physics calculations, the code is atomic data driven with respect to these ions, as explained in Paper I: the atomic models, all necessary data and the information on how to use these data are contained in a user supplied file (in the so-called DETAIL input form, cf. Butler & Giddings 1985) whereas the code itself is independent of any specific data.

The background ions, on the other hand, are those allowing for the effects of line-blocking/blanketing. The corresponding data originate from Pauldrach et al. (1998, 2001) and are used as provided, i.e., in a certain, fixed form.

FASTWIND follows the concept of “unified model atmospheres” (i.e., a smooth transition from a pseudo-hydrostatic photosphere to the wind) along with an appropriate treatment of line-broadening (Stark, pressure-) which is a prerequisite for the analysis of O-stars of different luminosity classes covering a variety of wind densities. Particularly and as already described in Paper I, the photospheric density consistently accounts for the temperature stratification and the actual radiation pressure, now by including both the explicit *and* the background elements.

The corresponding occupation numbers and opacities (of the background-elements) can be derived in two alternative ways:

- a) in those cases, where the temperature stratification is calculated by means of NLTE Hopf parameters (see below), we apply an approximate NLTE solution for *all* background elements following the principal philosophy developed by Abbott & Lucy (1985), Schmutz (1991), Schaerer & Schmutz (1994) and Puls et al. (2000), where important features have now been improved (cf. Sect. 2.4). Particularly, the equations of approximate ionization equilibrium have been reformulated to account for the actual radiation field as a function of depth and frequency, and a consistent iteration scheme regarding the coupling of the rate equations and the radiation field has been established to avoid the well-known convergence problems of a pure Lambda Iteration (Sect. 2.4.6).

³as recently calculated by Lenorzer et al. (2004)

- b) In the other case, when the T-stratification shall be calculated from first principles, the complete set of rate equations is solved almost “exactly” for the most abundant background elements (C, N, O, Ne, Mg, Si, S, Ar, Fe, Ni, if not included as explicit ions), employing the Sobolev approximation for the net radiative rates (with actual illuminating radiation field). The remaining background elements, on the other hand, remain to be treated by the approximation as outlined in a).

In order to account for the effects of line-blocking, we use suitable means for the line opacities, averaged over a frequency interval of the order of $1,000 \dots 1,500 \text{ km s}^{-1}$, and appropriate emissivities (Sect. 2.5).

Finally, the temperature stratification can be calculated in two different ways. As long as one is exclusively interested in an optical analysis, the concept of NLTE-Hopf parameters (cf. Paper I) is still sufficient, if the background elements are accounted for in a consistent way, i.e., have been included in the particular models from which these parameters are derived. Since this method is flux-conservative, the correct amount of line-blanketing is “automatically” obtained. Note that for optical depths $\tau_{\text{Ross}} \lesssim 0.01$ a lower cut-off temperature is defined, typically at $T_{\text{min}} = 0.6T_{\text{eff}}$.

Alternatively, the new version of FASTWIND allows for the calculation of a consistent⁴ temperature, utilizing a flux-correction method in the lower atmosphere and the thermal balance of electrons in the outer one (Sect. 2.7). As has been discussed, e.g., by Kubát et al. (1999), the latter method is advantageous compared to exploiting the condition of radiative equilibrium in those regions where the radiation field becomes almost independent on T_e . Particularly for the IR-spectroscopy, such a consistent T-stratification is important, since the IR is formed above the stellar photosphere in most cases and depends critically on the run of T_e in those regions, where our first method is no longer applicable.

2.3 Atomic Data and Metallicity

Explicit elements. In order to obtain reliable results also in the IR, we have significantly updated our H- and He-models compared to those described in Paper I. Our present H and He II models consist of 20 levels each (vs. 10 and 14 in the previous version, respectively), and He I includes levels until $n = 10$, where levels with $n = 8 \dots 10$ have been packed (previous version: 8 levels, packed from 5 \dots 8). Further information concerning cross-sections etc. can be found in Jokuthy (2002). Present atomic models for metals have been accumulated from different sources, mainly with respect to an analysis of B-stars, i.e., for ionization stages II and III, except for Mg (I,II) and Si (II, III, IV). Information on our Si atomic model can be found in Trundle et al. (2004), and on the other metals incorporated so far (C, N, O, Mg) in Urbaneja (2004).

Background elements. The atomic data for background elements originate from Pauldrach et al. (1998, 2001), who have given a detailed description on the various approaches and sources. These data comprise the elements from hydrogen to zinc (except Li, Be, B and Sc which are too rare to affect the background opacity) with ionization stages up to VIII. The number of connecting lines (lower and upper level present in the rate equations) is of the order of 30,000, and the number of lines where only the lower level is present is $4.2 \cdot 10^6$. The former group of lines is used to solve the

⁴Note, however, that non-radiative heating processes might be of importance, e.g., due to shocks.

rate equations, whereas the latter is used to derive the metal-line background opacities (cf. Sect 2.5). In addition to bound-free cross-sections and gf -values, there is also detailed information about the collision-strengths for the most important collisional bound-bound transitions in each ion.

Metallicity. The abundances of the background elements are taken from the solar values provided by Grevesse & Sauval (1998, and references therein)⁵. For different “global” metallicities, $z = Z/Z_{\odot}$, these abundances are scaled proportionally with respect to *mass* ratios, e.g., by 0.2 for the SMC and by 0.5 for the LMC (although these values are certainly disputable, e.g. Massey et al. 2004 and references therein).

A particular problem (independent on the actual value of z) appears in those cases when the He/H ratio becomes non-solar. In this case, we retain the specific relative mass fractions of the other elements, which of course has a significant effect on the *number* ratios. Although this procedure is not quite right, it preserves at least the overall mass fraction of the metals, particularly the *unprocessed* iron group elements, which are most important for the line-blocking. Further comments on the validity of this procedure have been given by Massey et al. (2004). Let us briefly mention a comparison to evolutionary calculations from Schaerer et al. (1993) performed by P. Massey (priv. comm.):

For the 120 M_{\odot} track at $Z = 0.008$ (roughly the LMC metallicity), Z stays essentially unchanged in the core until the end of core H burning, even though the mass fraction of C and N are going up while O is going down: At a number ratio $Y_{\text{He}} = 2$ (i.e., the mass ratio Y has changed from 0.265 to 0.892), the value for Z has changed insignificantly from 0.0080 to 0.0077, and even more interestingly, the mass fraction of the sum of C, N, O, and Ne has essentially changed in the same way (0.0075 to 0.0070), even though the actual mass fraction of N has more than doubled.

2.4 Background elements: approximate NLTE occupation numbers

In order to save significant computational effort, the occupation numbers of the background elements are calculated by means of an approximate solution of the NLTE rate equations. Such an approach has been successfully applied in a variety of stellar atmosphere calculations, e.g., to derive the radiative acceleration of hot star winds (Abbott & Lucy 1985; Lucy & Abbott 1993) and for the spectroscopy of hot stars (Schmutz 1991; Schaerer & Schmutz 1994) and Supernova remnants (Mazzali & Lucy 1993; Lucy 1999; Mazzali 2000). Puls et al. (2000) have used this method for an examination of the line-statistics in hot star winds, by closely following a procedure discussed by Springmann (1997) which in turn goes back to unpublished notes by L. Lucy.

One might argue that such an approximate approach can barely handle all the complications arising from sophisticated NLTE effects. However, in the following we will show that the approximate treatment is able to match “exact” NLTE calculations to an astonishingly high degree, at least if some modifications are applied to the original approach. Moreover, the calculated occupation numbers will *not* be used to synthesize line-spectra, but serve “only” as lower levels for the line-opacities involved in the blocking calculations.

Actually, the major weakness of the original approach is the assumption of a radiation field with *frequency independent* radiation temperatures T_{rad} . Since solely the difference in radiation temperatures at strong ionization edges is responsible for a number of important effects, we have improved upon this simplification by using consistent radiation temperatures (taken from the solution of the

⁵Of course, the user is free to change these numbers.

equations of radiative transfer). As we will see in the following, this principally minor modification requires a number of additional considerations.

2.4.1 Selection of levels

One of the major ingredients entering the approximate solution of the rate equations is a careful selection of participating atomic levels. In agreement with the argumentation by Abbott & Lucy (1985) only the following levels are used:

- the ground-state level
- all meta-stable levels (from equal and different spin systems), denoted by “M”
- all excited levels which are coupled to the ground-state via one single *permitted* transition where this transition is the strongest among all possible downward transitions; in the following denoted as subordinate levels “N”
- all excited levels coupled to one of the meta-stable levels $m \in M$ in a similar way (subordinate levels “S”).

In the above definition, the term “strongest” refers to the Einstein-coefficients A_{ji} . All other levels are neglected, since their population is usually too low to be of importance and cannot be approximated by simple methods.

2.4.2 Ionization equilibrium

In order to allow for a fast and clearly structured algorithm, we allow only for ionizations to and recombinations from the ground-state of the next higher ion, even if this is not the case in reality. Due to this restriction and by summing over all line-processes an “exact” rate equation connecting two neighboring ions is derived which exclusively consists of ionization/recombination processes. In the following, we will further neglect any collisional ionization/recombination processes, which is legitimate in the context considered here, namely in the NLTE-controlled atmospheric regime of hot stars. (In the lowermost, LTE dominated part of the atmosphere, $\tau_R > 2/3$, we approximate the occupation numbers a priori by LTE conditions).

At first, let us consider an ion with only one spin system, e.g., a hydrogenic one. In this case, the ionization equilibrium becomes

$$\sum_i n_i R_{i\kappa} = n_\kappa \sum_i \left(\frac{n_i}{n_\kappa} \right)^* R_{\kappa i} = \sum_i n_i^* R_{\kappa i}, \quad (2.1)$$

with n_i the occupation numbers of the lower ionization stage, n_κ the (ground-state!) occupation number of the higher ion, the asterisks denoting LTE-conditions (at actual electron density, $(n_i/n_\kappa)^* = n_e \Phi(T)$, cf. Mihalas 1975, Sect. 5) and ionization/recombination rate coefficients

$$R_{i\kappa} = \int_{\nu_i}^{\infty} \frac{4\pi J_\nu}{h\nu} a(\nu) d\nu \quad (2.2)$$

$$R_{\kappa i} = \int_{\nu_i}^{\infty} \frac{4\pi}{h\nu} \left(\frac{2h\nu^3}{c^2} + J_\nu \right) e^{-h\nu/kT_e} a(\nu) d\nu. \quad (2.3)$$

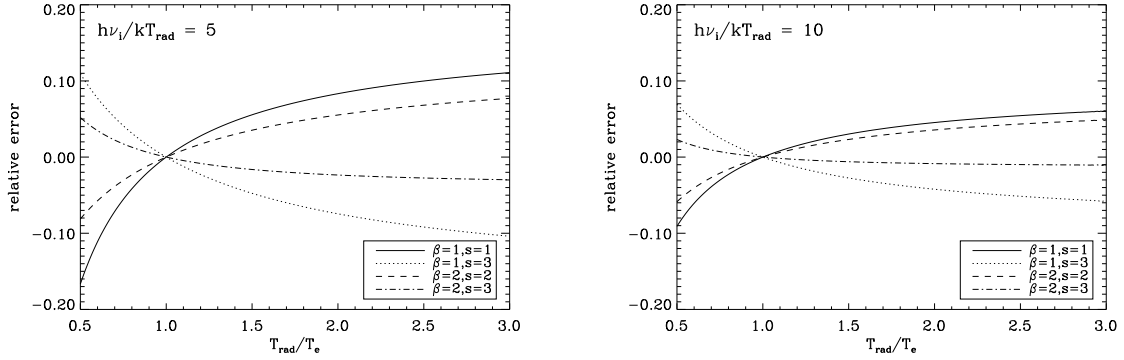


Figure 2.1: Ratio of ionization to recombination rate coefficients: Relative error between “exact” ratios (Eq. 2.12) and approximate ones (Eq. 2.15, with $\beta = 1$ and $s = 2$) as a function of T_{rad}/T_e , for different combinations of (β, s) . The error decreases for even higher ionization energies.

J_ν is the mean intensity, $a(\nu)$ the ionization cross-section and all other symbols have their usual meaning. Once more, within our above approximation (ionization to ground state only), Eq. 2.1 is “exact” and does not depend on any assumption concerning the bound-bound processes (radiative or collisional; optically thick or thin) since the corresponding rates drop out after summation.

By introducing the recombination coefficient α_i defined in the conventional way,

$$n_\kappa n_e \alpha_i = n_i^* R_{\kappa i}, \quad (2.4)$$

the ionization equilibrium can be reformulated

$$\sum_i n_i R_{i\kappa} = n_\kappa n_e \sum_i \alpha_i, \quad (2.5)$$

and we extract all quantities referring to the ground-state of the lower ion,

$$n_\kappa n_e = \frac{1}{\sum_i \alpha_i} n_1 R_{1\kappa} \left(1 + \frac{\sum_{i>1} n_i R_{i\kappa}}{n_1 R_{1\kappa}} \right). \quad (2.6)$$

Finally, inserting the ground-state recombination coefficient α_1 (cf. Eq. 2.4) on the *rhs*, we obtain the ionization equilibrium expressed as the ratio of two neighboring ground-states,

$$\frac{n_\kappa}{n_1} = \left(\frac{n_\kappa}{n_1} \right)^* \frac{R_{1\kappa}}{R_{\kappa 1}} \frac{\alpha_1}{\sum_i \alpha_i} \left\{ 1 + \sum_{i \in M, N, S} \frac{n_i}{n_1} \frac{R_{i\kappa}}{R_{1\kappa}} \right\}. \quad (2.7)$$

Note that this ratio depends on the radiation field, the actual electron density and temperature and on the *excitation* within the lower ion, which will be discussed in the next subsection. Note also that all what follows is “only” a simplification of this equation.

So far, our derivation and the above result are identical to previous versions of the approximate approach. From now on, however, we will include the frequency dependence of the radiation field. To this end, we describe the ionization cross-sections by the *Seaton-approximation* (Seaton 1958), which is not too bad for most ions,

$$a(\nu) = a_i \left(\beta \left(\frac{\nu_i}{\nu} \right)^s + (1 - \beta) \left(\frac{\nu_i}{\nu} \right)^{s+1} \right). \quad (2.8)$$

Writing the mean intensity as $J_\nu(r) = W(r) B_\nu(Trad(\nu, r))$ with dilution factor W and neglecting the stimulated emission in the recombination integral (valid for all important ionization edges), we obtain (radial dependence of all quantities suppressed in the following)

$$R_{i\kappa} = \frac{8\pi W}{c^2} \left(\frac{kT_{r,i}}{h} \right)^3 a_i \mathcal{F}(x_{r,i}; \beta, s) \quad (2.9)$$

$$R_{\kappa i} = \frac{8\pi}{c^2} \left(\frac{kT_e}{h} \right)^3 a_i \mathcal{F}(x_{e,i}; \beta, s) \quad (2.10)$$

with $x_{r,i} = h\nu_i/kT_{r,i}$, $x_{e,i} = h\nu_i/kT_e$ and

$$\mathcal{F}(x; \beta, s) = \beta x^s \Gamma(3-s, x) + (1-\beta) x^{1+s} \Gamma(2-s, x). \quad (2.11)$$

We have assumed $Trad(\nu) =: T_{r,i}$ to be constant over the decisive range of the ionizing continuum $\nu \gtrsim \nu_i$, since only those frequencies close to the edge are relevant. In other words, each transition is described by a *unique* radiation temperature. In the above equation, the incomplete Gamma-function $\Gamma(a, x)$ has been generalized to include also negative parameters, $a \leq 0$. The ratio of ground-state ionization/recombination rate coefficients is thus given by

$$\frac{R_{1\kappa}}{R_{\kappa 1}} = W \left(\frac{T_{r,1}}{T_e} \right)^3 \frac{\mathcal{F}(x_{r,1}; \beta, s)}{\mathcal{F}(x_{e,1}; \beta, s)}, \quad (2.12)$$

i.e., is independent of the actual value of the cross-section at the threshold, a_i . Although this expression is rather simple, it requires the somewhat time-consuming evaluation of the incomplete Gamma-functions. To keep things as fast as possible, we generally use the parameter set ($\beta = 1, s = 2$) instead of the actual parameters which results in a particularly simple function \mathcal{F} ,

$$\mathcal{F}(x; 1, 2) = x^2 \exp(-x). \quad (2.13)$$

Note that these parameters do *not* correspond to the hydrogenic cross-section, which would be described by $s = 3$. Using this parameter set, the ionization/recombination rates simplify to

$$\begin{aligned} R_{i\kappa} &= \frac{8\pi W}{c^2} \left(\frac{kT_{r,i}}{h} \right)^3 a_i \nu_i^2 e^{-h\nu_i/kT_{r,i}} \\ R_{\kappa i} &= \frac{8\pi}{c^2} \left(\frac{kT_e}{h} \right)^3 a_i \nu_i^2 e^{-h\nu_i/kT_e}, \end{aligned} \quad (2.14)$$

and the ratio $R_{1\kappa}/R_{\kappa 1}$ becomes

$$\frac{R_{1\kappa}}{R_{\kappa 1}} = W \frac{T_{r,1}}{T_e} \exp \left[-\frac{h\nu_1}{k} \left(\frac{1}{T_{r,1}} - \frac{1}{T_e} \right) \right]. \quad (2.15)$$

We have convinced ourselves that this approximation leads to acceptable errors of the order of 10%, cf. Fig. 2.1. Furthermore, we define the following quantities, where ζ is just the ratio of ground-state to total recombination coefficient,

$$\frac{\alpha_1}{\sum_i \alpha_i} = \zeta, \quad \sum_{i \in M(N,S)} \frac{n_i}{n_1} \frac{R_{i\kappa}}{R_{1\kappa}} \equiv C_{M(N,S)}. \quad (2.16)$$

Let us point out that any ratio α_i/α_j (particularly, the case $j = 1$ and thus ζ) is independent of the temperature and depends exclusively on atomic quantities, namely cross-section, transition frequency and statistical weight, a fact which follows from Eqs. 2.4 and 2.14:

$$\frac{\alpha_i}{\alpha_j} = \left(\frac{n_i}{n_j}\right)^* \frac{R_{\kappa i}}{R_{\kappa j}} = \left(\frac{n_i}{n_j}\right)^* \frac{a_i}{a_j} \left(\frac{\nu_i}{\nu_j}\right)^2 \exp\left[-\frac{h(\nu_i - \nu_j)}{kT_e}\right] = \frac{a_i}{a_j} \left(\frac{\nu_i}{\nu_j}\right)^2 \frac{g_i}{g_j}. \quad (2.17)$$

Collecting terms, our approximate ionization equilibrium finally reads

$$\begin{aligned} \frac{n_\kappa}{n_1} &= \left(\frac{n_\kappa}{n_1}\right)^* W \frac{T_{r,1}}{T_e} \exp\left[-\frac{h\nu_1}{k} \left(\frac{1}{T_{r,1}} - \frac{1}{T_e}\right)\right] \times \zeta (1 + C_N + C_M + C_S) = \\ &= \left(\frac{n_\kappa}{n_1}\right)^*_{T_{r,1}} W \sqrt{\frac{T_e}{T_{r,1}}} \zeta (1 + C_M + C_N + C_S), \end{aligned} \quad (2.18)$$

where the second variant uses the LTE ratio evaluated at actual electron-density and radiation temperature of the ionizing continuum.

2.4.3 Excitation

The remaining step concerns the term in the bracket above, i.e., the approximate calculation of the excitation inside the lower ion (which, of course, is also required in order to calculate the partition functions). For consistency, frequencies (energies) are still defined with respect to the ionization threshold, i.e., line frequencies have to be calculated from $\nu_{ij} = \nu_i - \nu_j > 0$ instead of the usual definition (upper - lower) which would refer to excitation energies.

Meta-stable levels

We begin with the occupation numbers of meta-stable levels which can be populated via excited levels or via the continuum (see also Abbott & Lucy 1985).

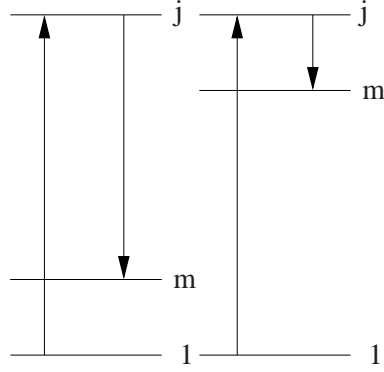
Population via excited levels. Denoting the excited level by j , considering the fact that this excited level is fed by the ground state (otherwise it would not exist in our level hierarchy) and neglecting collisional processes, the population can be approximated by

$$\frac{n_m}{n_1} = \frac{W \left(\frac{n_j}{n_1}\right)^*_{T_{r,1j}}}{W \left(\frac{n_j}{n_m}\right)^*_{T_{r,mj}}}, \quad m \in M \quad (j \in N > m) \quad (2.19)$$

(see also Eq. 2.26 with $\delta \approx 0$), where the dilution factor cancels out. In the following, we have to distinguish between two cases: the meta-stable level lies either close to the ground-state or close to the excited level, cf. Fig. 2.2.

Case a: low lying meta-stable level. The transition frequencies of both transitions are fairly equal, $\nu_{1j} \approx \nu_{mj}$, i.e., $T_{r,1j} \approx T_{r,mj}$, and we find

$$\frac{n_m}{n_1} \approx \frac{g_m}{g_1} \exp\left(-\frac{h\nu_{1m}}{kT_{r,1j}}\right) = \left(\frac{n_m}{n_1}\right)^*_{T_{r,1j}}. \quad (2.20)$$



$$\nu_{1j} \approx \nu_{mj}, T_{r,1j} \approx T_{r,mj} \quad \nu_{mj} < \nu_{1j} \approx \nu_{1m}, T_{r,1j} \approx T_{r,1m}$$

Figure 2.2: Population of meta-stable levels via excited ones (see text).

Note that the population is controlled by the radiation field $T_{r,1j}$, i.e., from frequencies much larger than the “excitation energy”, ν_{1m} .

Case b: high lying meta-stable level. Now we have $\nu_{mj} < \nu_{1j} \approx \nu_{1m}$,

$$\frac{n_m}{n_1} \approx \frac{g_m}{g_1} \exp\left(-\frac{h\nu_{1j}}{kT_{r,1j}}\right) \approx \frac{g_m}{g_1} \exp\left(-\frac{h\nu_{1m}}{kT_{r,1m}}\right) = \left(\frac{n_m}{n_1}\right)^*_{T_{r,1m}}. \quad (2.21)$$

and the population depends on the radiation field at (or close to) the excitation energy.

Population via continuum. The third case comprises a population via the continuum which will only be treated in a crude approximation, where a correct evaluation will be given later (Sect. 2.4.5). If we neglect for the moment the influence of any meta-stable and excited levels, we find from Eq. (2.18) with $\zeta \rightarrow 1$, $C_{N(M,S)} \rightarrow 0$

$$\frac{n_m}{n_1} = \frac{\left(\frac{n_\kappa}{n_1}\right)}{\left(\frac{n_\kappa}{n_m}\right)} \approx \frac{\left(\frac{n_\kappa}{n_1}\right)^*_{T_{r,1}} T_{r,1}}{\left(\frac{n_\kappa}{n_m}\right)^*_{T_{r,m}} T_{r,m}} \sqrt{\frac{T_{r,m}}{T_{r,1}}} = \frac{g_m}{g_1} \frac{T_{r,1}}{T_{r,m}} \exp\left[-\frac{h}{k} \left(\frac{\nu_1}{T_{r,1}} - \frac{\nu_m}{T_{r,m}}\right)\right]. \quad (2.22)$$

Note that all three cases converge to the *identical* result

$$\frac{n_m}{n_1} \rightarrow \left(\frac{n_m}{n_1}\right)^*_{T_{rad}} \quad \text{for } T_{rad} = \text{const} \quad (2.23)$$

which is quoted by Abbott & Lucy (1985).

In order to continue our calculation of C_M , we find from Eqs. 2.14 and 2.17

$$\frac{R_{m\kappa}}{R_{1\kappa}} = \frac{T_{r,m}}{T_{r,1}} \frac{\alpha_m}{\alpha_1} \frac{g_1}{g_m} \exp\left[-\frac{h}{k} \left(\frac{\nu_m}{T_{r,m}} - \frac{\nu_1}{T_{r,1}}\right)\right]. \quad (2.24)$$

Multiplying by n_m/n_1 we find that for the three cases Eqs. 2.20, 2.21 and 2.22

$$\left(\frac{n_m R_{m\kappa}}{n_1 R_{1\kappa}} \right)_{m \in M} = \begin{cases} \frac{\alpha_m}{\alpha_1} \frac{T_{r,m}}{T_{r,1}} \exp \left[-\frac{h}{k} \left(\frac{\nu_m}{T_{r,m}} - \frac{\nu_1}{T_{r,1}} + \frac{\nu_{1m}}{T_{r,1j}} \right) \right] \\ \frac{\alpha_m}{\alpha_1} \frac{T_{r,m}}{T_{r,1}} \exp \left[-\frac{h}{k} \left(\frac{\nu_m}{T_{r,m}} - \frac{\nu_1}{T_{r,1}} + \frac{\nu_{1m}}{T_{r,1m}} \right) \right] \\ \frac{\alpha_m}{\alpha_1}, \end{cases} \quad (2.25)$$

respectively. As mentioned before, the result for the third case (population over continuum) is only a crude approximation, which is also evident from the fact that it depends only on atomic quantities but not on any radiation temperature.

Subordinate levels

Due to our definition of subordinate levels their population can be approximated by a two-level-atom Ansatz (between ground-state $j = 1$ and subordinate level $i \in N$ or between meta-stable level $j \in M$ and subordinate level $i \in S$), such that the population can be expressed by

$$\frac{n_i}{n_j} = W(1 - \delta) \left(\frac{n_i}{n_j} \right)_{T_{r,ij}}^* + \delta \left(\frac{n_i}{n_j} \right)_{T_e}^*, \quad i \in N(S), \quad j \in 1(M) \quad (2.26)$$

where δ is the parameter expressing the competition between thermalization ($\delta \rightarrow 1$) and local escape (in Sobolev approximation),

$$\delta = \frac{\epsilon}{\epsilon(1 - \beta) + \beta}. \quad (2.27)$$

ϵ is the usual LTE parameter in a two-level atom,

$$\epsilon = \frac{C_{ji}}{A_{ji} + C_{ji}}, \quad (2.28)$$

with collisional de-excitation rate C_{ji} and Einstein-coefficient A_{ji} . β is the local escape probability in Sobolev approximation,

$$\beta = \frac{1}{2} \int_{-1}^1 \frac{1 - e^{-\tau_S(\mu)}}{\tau_S(\mu)} d\mu, \quad (2.29)$$

and the illuminating radiation field is approximated by

$$\beta_c I_c = \frac{1}{2} \int_{\mu_*}^1 I_c(\mu) \frac{1 - e^{-\tau_S(\mu)}}{\tau_S(\mu)} d\mu \approx W B_\nu(T_{r,ij}) \beta. \quad (2.30)$$

Note, that our approximation (2.26) neglects any coupling to the continuum inside the resonance zone. By means of Eq. (2.17), the individual terms comprising C_N can be calculated from

$$\begin{aligned} \left(\frac{n_i}{n_1} \frac{R_{i\kappa}}{R_{1\kappa}} \right)_{i \in N} &= \frac{\alpha_i}{\alpha_1} \frac{T_{r,i}}{T_{r,1}} \exp \left[-\frac{h}{k} \left(\frac{\nu_i}{T_{r,i}} - \frac{\nu_1}{T_{r,1}} \right) \right] \times \\ &\times \left[W(1 - \delta_{1i}) \exp \left(-\frac{h\nu_{1i}}{kT_{r,1i}} \right) + \delta_{1i} \exp \left(-\frac{h\nu_{1i}}{kT_e} \right) \right] \end{aligned} \quad (2.31)$$

whereas the components of C_S are described by

$$\begin{aligned} \left(\frac{n_i}{n_1} \frac{R_{i\kappa}}{R_{1\kappa}} \right)_{i \in S} &= \left(\frac{n_m}{n_1} \right)_{m \in M} \cdot \left(\frac{n_i}{n_m} \frac{R_{i\kappa}}{R_{1\kappa}} \right)_{i \in S} = \\ &= \left(\frac{n_m}{n_1} \frac{g_m}{g_1} \right) \times \frac{\alpha_i}{\alpha_1} \frac{T_{r,i}}{T_{r,1}} \exp \left[-\frac{h}{k} \left(\frac{\nu_i}{T_{r,i}} - \frac{\nu_1}{T_{r,1}} \right) \right] \times \\ &\times \left[W(1 - \delta_{mi}) \exp \left(-\frac{h\nu_{mi}}{kT_{r,mi}} \right) + \delta_{mi} \exp \left(-\frac{h\nu_{mi}}{kT_e} \right) \right] \end{aligned} \quad (2.32)$$

(with (n_m/n_1) taken from Eqs. 2.20, 2.21 and 2.22, respectively). Obviously, the population of subordinate levels is controlled by at least three different radiation temperatures (ionization from the considered level, ionization from the connected lower level and excitation due to line processes).

2.4.4 Limiting cases

In the following, we will consider some limiting cases which have to be reproduced by our approach.

Constant radiation temperature, no collisional excitation are the assumptions underlying the description by Springmann (1997) and Puls et al. (2000) on the basis of Lucy's unpublished notes. With $Trad = \text{const}$, meta-stable levels are populated via

$$\left(\frac{n_m}{n_1} \frac{R_{m\kappa}}{R_{1\kappa}} \right)_{m \in M} = \frac{\alpha_m}{\alpha_1} \quad (\nu_m - \nu_1 + \nu_{1m} = 0!), \quad (2.33)$$

independent of the actual feeding mechanism. With $\delta = 0$ (only radiative line processes), we thus obtain for the population of subordinate levels (both $i \in N$ and $i \in S$!)

$$\left(\frac{n_i}{n_1} \frac{R_{i\kappa}}{R_{1\kappa}} \right)_{i \in N,S} = W \frac{\alpha_i}{\alpha_1}. \quad (2.34)$$

Thus, for constant radiation temperatures, it does not play any role how the meta-stable levels are populated, and whether subordinate levels are connected to the ground-state or to a meta-stable level. Only the corresponding recombination coefficient is of importance and the fact that subordinate levels suffer from dilution (since they are fed by a diluted radiation field), whereas for meta-stable levels this quantity cancels out (cf. Abbott & Lucy 1985). In total, our simplified ionization equilibrium then becomes

$$\frac{n_\kappa}{n_1} = \left(\frac{n_\kappa}{n_1} \right)_{T_{\text{rad}}}^* W \sqrt{\frac{T_e}{T_{\text{rad}}}} \zeta \left(1 + \sum_{i \in M} \frac{\alpha_i}{\alpha_1} + W \sum_{i \in N,S} \frac{\alpha_i}{\alpha_1} \right). \quad (2.35)$$

If we define η as the fraction of recombination coefficients for all meta-stable levels,

$$\eta = \frac{\sum_{i \in M} \alpha_i}{\sum_i \alpha_i} \quad (2.36)$$

we find

$$\sum_{i \in M} \frac{\alpha_i}{\alpha_1} = \frac{1}{\zeta} \frac{\sum_{i \in M} \frac{\alpha_i}{\alpha_1}}{\sum_i \frac{\alpha_i}{\alpha_1}} = \frac{\eta}{\zeta} \quad (2.37)$$

and

$$\sum_{i \in N, S} \frac{\alpha_i}{\alpha_1} = \frac{1 - \eta - \zeta}{\zeta}, \quad (2.38)$$

and the ionization equilibrium can be described in a very compact way,

$$\frac{n_\kappa}{n_1} = \left(\frac{n_\kappa}{n_1} \right)_{T_{\text{rad}}}^* W \sqrt{\frac{T_e}{T_{\text{rad}}}} (\zeta + \eta + W(1 - \eta - \zeta)), \quad (2.39)$$

which indeed is the result of the previous investigations mentioned above. If we further prohibit all ionizations from meta-stable and subordinate levels, i.e. allow for

Ionization/recombination only from and to the ground-state, we find with $\zeta = 1$ and $\eta = 0$

$$\begin{aligned} \frac{n_\kappa}{n_1} &= \left(\frac{n_\kappa}{n_1} \right)_{T_{\text{rad}}}^* W \sqrt{\frac{T_e}{T_{\text{rad}}}} = \\ &= \frac{2g_\kappa}{g_1} \frac{1}{n_e} \left(\frac{2\pi m_e k T_{\text{rad}}}{h^2} \right)^{3/2} \exp\left(-\frac{h\nu_1}{k T_{\text{rad}}}\right) W \sqrt{\frac{T_e}{T_{\text{rad}}}}, \end{aligned} \quad (2.40)$$

which is a well-known result and also valid for the case where all lines are optically thick and in detailed balance, e.g., Abbott (1982). The

LTE-case is recovered independently from the specific values of ζ and η in the lowermost atmosphere, when the dilution factor approaches unity, $W = 1$, and the radiation field becomes Planck, $T_{\text{rad}} \rightarrow T_e$. In this case, the ionization balance becomes

$$\frac{n_\kappa}{n_1} = \left(\frac{n_\kappa}{n_1} \right)_{T_e}^* (\zeta + \eta + (1 - \eta - \zeta)) = \left(\frac{n_\kappa}{n_1} \right)_{T_e}^* \quad (2.41)$$

and for the excitation we have

$$\frac{n_i}{n_1} = \left(\frac{n_i}{n_1} \right)_{T_e}^*, \quad i \in M, N, S. \quad (2.42)$$

2.4.5 Different spin systems

The last problem to overcome is the presence of different spin systems, a problem already encountered for He I. Our approximation is to consider the different systems as completely decoupled (except if strong inter-combination lines are present, see below), since a coupling via collisional inter-combination is effective only at high densities (i.e., in or close to LTE, which is treated explicitly in our procedure anyway).

Then for each of the separate multiplets, the ionization equation can be calculated independently. The different subsystems are defined in the following way

- the first subsystem includes all levels coupled to the ground-state plus those meta-stable levels fed from higher lying (subordinate) levels (case a/b in Sect. 2.4.3). In this way, we include

also systems of different spin which are connected to the ground-state system via *strong* inter-combination lines, a condition which is rarely met. In total, the ground-state subsystem includes the levels $i \in 1, N, M', S'$, where M' comprises all case a/b meta-stable levels and S' those excited levels which are coupled to M' . For reasons of convenience, we will denote this set of levels by $(1, N')$.

- a second group of j subsystems comprises
 - systems of different spin decoupled from the ground-state;
 - “normal” meta-stable levels populated via continuum processes (poorly approximated so far) and excited levels coupled to those.

Both groups can be treated in a similar way and are also identified in a similar manner, namely from the condition that the lowest state of these systems is meta-stable and *not fed* from higher lying levels. Each subsystem comprises the “effective” ground state $m_j \in M''$ (either different spin or fed by continuum) and coupled levels, $i \in S''_j$.

Once more, j is the number of meta-stable levels per ion which are *not* fed by higher lying levels. Note that for a *single* spin-system with meta-stable levels, there are now $1 + j$ different subsystems if j continuum fed meta-stable levels were present. Note also that by using this approach we neglect a possible coupling of two or more non-ground-state multiplets via strong inter-combination lines, if there were any.

Because of the assumed decoupling, for each subsystem we can write down the appropriate ionization equation. For the ground-state system, we have

$$\frac{n_\kappa}{n_1} = \left(\frac{n_\kappa}{n_1} \right)_{T_{r,1}}^* W \sqrt{\frac{T_e}{T_{r,1}}} \zeta_1 (1 + C_{N'}) \quad (2.43)$$

$$\zeta_1 = \frac{\alpha_1}{\sum_{(1, N')} \alpha_i}, \quad C_{N'} = \sum_{i \in N'} \frac{n_i}{n_1} \frac{R_{i\kappa}}{R_{1\kappa}} \quad (2.44)$$

where, again, N' comprises the “old” levels $\in N, M'$ and S' . Note the difference between ζ_1 and ζ from Eq. 2.16.

For each of the j additional subsystems, we obtain in analogy

$$\frac{n_\kappa}{n_{m_j}} = \left(\frac{n_\kappa}{n_{m_j}} \right)_{T_{r,m_j}}^* W \sqrt{\frac{T_e}{T_{r,m_j}}} \frac{\alpha_{m_j}}{\alpha_1} \zeta_{m_j} (1 + C_{S''_j}) \quad (2.45)$$

$$\zeta_{m_j} = \frac{\alpha_1}{\sum_{(m_j, S''_j)} \alpha_i}, \quad C_{S''_j} = \sum_{i \in S''_j} \frac{n_i}{n_{m_j}} \frac{R_{i\kappa}}{R_{m_j\kappa}} \quad (2.46)$$

and S''_j comprises all levels coupled to m_j . The individual components of $C_{N'}$ and $C_{S''_j}$ are calculated as described in Sect. 2.4.3. Dividing Eq. 2.43 by Eq. 2.45, we find for the ratios (n_{m_j}/n_1) (required, e.g., for calculating the partition functions),

$$\frac{n_{m_j}}{n_1} = \frac{(n_\kappa/n_1)_{T_{r,1}}^*}{(n_\kappa/n_{m_j})_{T_{r,m_j}}^*} \sqrt{\frac{T_{r,m_j}}{T_{r,1}}} \frac{\alpha_1 \zeta_1}{\alpha_{m_j} \zeta_{m_j}} \left(\frac{1 + C_{N'}}{1 + C_{S''_j}} \right), \quad (2.47)$$

or, explicitly written,

$$\frac{n_{m_j}}{n_1} = \frac{g_{m_j} T_{r,1}}{g_1 T_{r,m_j}} \exp \left[-\frac{h}{k} \left(\frac{\nu_1}{T_{r,1}} - \frac{\nu_{m_j}}{T_{r,m_j}} \right) \right] \frac{\alpha_1 \zeta_1}{\alpha_{m_j} \zeta_{m_j}} \left(\frac{1 + C_{N'}}{1 + C_{S_j''}} \right). \quad (2.48)$$

The last equation is the “correct approximation” for continuum fed meta-stable levels. On the one hand, if the ion consists of the ground-state plus a number of meta-stable levels alone, we would have $C_{N'} = C_{S_j''} = 0$, $\zeta_1 = 1$ and $\zeta_{m_j} = \alpha_1/\alpha_{m_j}$. In this case, Eq. 2.48 and Eq. 2.22 would give identical results, which shows that both approaches are consistent under the discussed conditions. But as already pointed out, Eq. 2.22 is highly approximative if a variety of levels are involved, and the occupation numbers should be calculated according to Eq. 2.48 always.

The major difference to our former approach (one spin system only) is the following: In approach “one”, the ground-state population, n_κ/n_1 , is affected by *all* meta-stable levels, whereas in approach “two” only those meta-stable levels have an influence which are coupled to the ground-state system via higher levels.

Constant radiation temperature, no collisional excitation. Concerning the limiting case where $Trad = \text{const}$ and $\delta = 0$, Eq. 2.39 remains valid if we account for the different “normalization”, i.e., if we replace ζ by ζ_1 and include only those meta-stable levels into η which are populated via excited levels:

$$\frac{n_\kappa}{n_1} = \left(\frac{n_\kappa}{n_1} \right)_{T_{\text{rad}}}^* W \sqrt{\frac{T_e}{T_{\text{rad}}}} (\zeta_1 + \eta_1 + W(1 - \eta_1 - \zeta_1)) \quad (2.49)$$

with

$$\zeta_1 = \frac{\alpha_1}{\sum_{(1,N')} \alpha_i}, \quad \eta_1 = \frac{\sum_{i \in M'} \alpha_i}{\sum_{(1,N')} \alpha_i}. \quad (2.50)$$

Inside the individual sub-systems we then obtain

$$\frac{n_\kappa}{n_{m_j}} = \left(\frac{n_\kappa}{n_{m_j}} \right)_{T_{\text{rad}}}^* W \sqrt{\frac{T_e}{T_{\text{rad}}}} (\zeta' + W(1 - \zeta')), \quad \zeta' = \frac{\alpha_{m_j}}{\alpha_1} \zeta_{m_j} \quad (2.51)$$

which immediately indicates the correct thermalization for $W = 1$ and $Trad \rightarrow T_e$. After dividing Eq. 2.49 by 2.51, we find for the population of (n_{m_j}/n_1) in the same limit

$$\frac{n_{m_j}}{n_1} = \frac{g_{m_j}}{g_1} \exp \left(-\frac{h\nu_{1m_j}}{kTrad} \right) \left(\frac{\zeta_1 + \eta_1 + W(1 - \eta_1 - \zeta_1)}{\zeta' + W(1 - \zeta')} \right). \quad (2.52)$$

This expression reveals two things. First, we obtain the correct population in LTE when $W \rightarrow 1$. Second, the difference to our crude approximation in Sect. 2.4.3 becomes obvious: The quasi-LTE ratio (2.23) has to be multiplied by the last factor in the above equation to obtain consistent populations. This factor (which can be lower or larger than unity) becomes unity only when $W \rightarrow 1$ (i.e., in the lower atmosphere) or for $\zeta_1 = \zeta' = 1$, i.e., in those cases where only ground-state and meta-stable levels are present, as already discussed above.

2.4.6 Accelerated Lambda Iteration

To overcome the well-known problems of the Lambda-iteration when coupling the rate-equations with the equation of radiative transfer, we apply the concept of the Accelerated Lambda Iteration (ALI, for a review see Hubeny 1992) to obtain a fast and reliable convergence of the solution. Since our rate-equations have been formulated in a non-conventional way and since the radiation field is expressed in terms of local, frequency-dependent radiation temperatures, the procedure has to be modified somewhat, and we will describe the required re-formulations as follows (for a comparable implementation see also de Koter et al. 1993).

At first, assume that only *one* bound-free opacity is present, i.e., the radiation-field is controlled by the opacity of the considered transition i (no overlapping continua present). In this case, the usual ALI formulation for the mean intensity J_ν^n at iteration cycle n is given by

$$\begin{aligned} J_\nu^n &\rightarrow J_\nu^{n-1} + \Lambda_\nu^*(S_i^n - S_i^{n-1}) \\ &= \Delta J_\nu + \Lambda_\nu^* S_i^n \quad \text{with} \quad \Delta J_\nu = J_\nu^{n-1} - \Lambda_\nu^* S_i^{n-1}, \end{aligned} \quad (2.53)$$

where S_i is the continuum source-function for transition i and Λ_ν^* the corresponding Approximate Lambda Operator (ALO), calculated in parallel with the solution of the continuum transfer⁶ following the method suggested by Rybicki & Hummer (1991, Appendix A).

Substituting this expression into the rate equations, we find for the corresponding *effective* ionization/recombination rate coefficients

$$R_{i\kappa} \rightarrow \int_{\nu_i}^{\infty} \frac{4\pi a_\nu}{h\nu} \Delta J_\nu d\nu \quad (2.54)$$

$$R_{\kappa i} \rightarrow \int_{\nu_i}^{\infty} \frac{4\pi a_\nu}{h\nu} \left(\frac{2h\nu^3}{c^2} (1 - \Lambda_\nu^*) + \Delta J_\nu \right) e^{-h\nu/kT_e} d\nu, \quad (2.55)$$

i.e., the problematic, optically thick part of the radiation field has been canceled analytically. Neglecting again stimulated emission (the ΔJ_ν -term in the recombination rate coefficient above), approximating $S_i^{n-1} = B_\nu/b_i^{n-1}$ with Planck-function B_ν and NLTE-departure coefficient b_i^{n-1} , and using the radiation temperature at the threshold, $T_{\text{rad},i}$ along with Seaton parameters $\beta = 1$, $s = 2$, we have in analogy to Eq. 2.14

$$\begin{aligned} R_{i\kappa} &\rightarrow \frac{8\pi}{c^2} a_i \nu_i^2 \left\{ W \frac{kT_{\text{r},i}^{n-1}}{h} e^{-h\nu_i/kT_{\text{r},i}^{n-1}} - \frac{\Lambda_\nu^*}{b_i^{n-1}} \frac{kT_e}{h} e^{-h\nu_i/kT_e} \right\} \\ &:= R_{i\kappa}^{n-1} - R'_{i\kappa} \end{aligned} \quad (2.56)$$

$$R_{\kappa i} \rightarrow \frac{8\pi}{c^2} \frac{kT_e}{h} a_i \nu_i^2 e^{-h\nu_i/kT_e} (1 - \Lambda_\nu^*) := R_{\kappa i} - R'_{\kappa i}. \quad (2.57)$$

In those cases where an overlapping continuum is present, i.e., if different transitions contribute to the opacity, the ALO has to be modified according to

$$\Lambda_\nu^* \rightarrow \beta_i(\nu) \Lambda_\nu^* \quad \text{with} \quad \beta_i = \frac{\chi_i(\nu)}{\chi_{\text{tot}}(\nu)}. \quad (2.58)$$

χ_i is the opacity of the considered transition, χ_{tot} the total opacity and β_i is assumed to be constant between two subsequent iterations (cf. Paper I). Let us mention explicitly that the opacities used for

⁶including the pseudo-continua from the multitude of overlapping lines, cf. Sect. 2.5

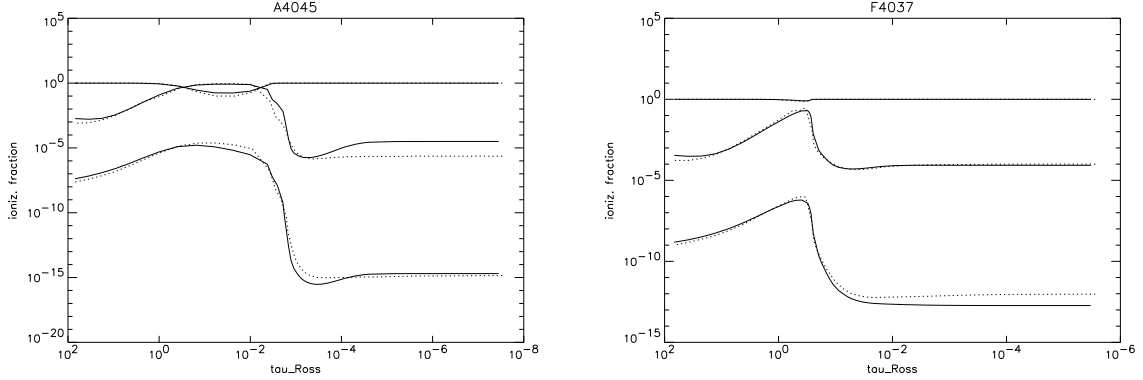


Figure 2.3: Approximate NLTE vs. the exact case: He ionization fractions (from top to bottom: He III, He II, He I) for pure H/He atmospheric models at $T_{\text{eff}}=40,000$ K (left panel: dwarf with $\log g=4.5$ and thin wind; right panel: supergiant with $\log g=3.7$ and thick wind). Bold: exact solution for helium; dotted: He in approximate NLTE (see text).

the radiative transfer are calculated from their *actual* Seaton parameters (β, s) , whereas the uniform values $(\beta = 1, s = 2)$ are applied “only” to evaluate the approximate ionization/recombination rates.

Since the Lambda Iteration fails only in the optically thick case, we apply the ALI-scheme exclusively for ground state transitions. Thus, by substituting the effective rate coefficients $R_{1\kappa}$ and $R_{\kappa 1}$ into Eqs. 2.4, 2.5, we have

$$\frac{n_{\kappa}}{n_1} = \left(\frac{n_{\kappa}}{n_1} \right)^* \frac{R_{1\kappa}}{R_{\kappa 1}} \frac{1 - \frac{R'_{1\kappa}}{R_{1\kappa}} + \sum_{i \in N'} \frac{n_i}{n_1} \frac{R_{i\kappa}}{R_{1\kappa}}}{1 - \frac{R'_{\kappa 1}}{R_{\kappa 1}} + \sum_{i \in N'} \left(\frac{n_i}{n_1} \right)^* \frac{R_{\kappa i}}{R_{\kappa 1}}}. \quad (2.59)$$

Using, again, Eq. 2.17 and the definitions given in (2.44), we finally obtain

$$\frac{n_{\kappa}}{n_1} = \left(\frac{n_{\kappa}}{n_1} \right)^* \frac{R_{1\kappa}}{R_{\kappa 1}} \zeta_1 (1 + C_{N'}) \frac{1 - \frac{1}{1 + C_{N'}} \frac{R'_{1\kappa}}{R_{1\kappa}}}{1 - \zeta_1 \frac{R'_{\kappa 1}}{R_{\kappa 1}}}. \quad (2.60)$$

In the case of $\Lambda_{\nu}^* \equiv 0$ (implying $R'_{1\kappa} = R'_{\kappa 1} = 0$), we immediately recover the original result, Eq. 2.43, since

$$\left(\frac{n_{\kappa}}{n_1} \right)^* \frac{R_{1\kappa}}{R_{\kappa 1}} = \left(\frac{n_{\kappa}}{n_1} \right)_{T_{r,1}} W \sqrt{\frac{T_e}{T_{r,1}}} \quad (2.61)$$

by means of Eq. 2.15. If, on the other hand, the ALO is significant (i.e., close to unity), we find

$$\frac{R'_{1\kappa}}{R_{1\kappa}} = \frac{\Lambda_{\nu}^*}{W b_1^{n-1}} \frac{T_e}{T_{r,1}^{n-1}} \exp \left[-\frac{h\nu_1}{k} \left(\frac{1}{T_e} - \frac{1}{T_{r,1}^{n-1}} \right) \right] \quad (2.62)$$

$$\frac{R'_{\kappa 1}}{R_{\kappa 1}} = \Lambda_{\nu}^*. \quad (2.63)$$

Thus, the reformulated ALI-scheme collapses to a simple correction of the original equation (2.43)

for the ground-state population,

$$\begin{aligned} \frac{n_\kappa}{n_1} &= \frac{n_\kappa}{n_1} (\Lambda_\nu^* \equiv 0) \cdot C_A(T_{r,1}^{n-1}, b_1^{n-1}), \quad \text{with factor} \\ C_A &= \frac{1 - \frac{\Lambda_\nu^*}{(1 + C_{N'})Wb_1^{n-1}} \frac{T_e}{T_{r,1}^{n-1}} \exp \left[-\frac{h\nu_1}{k} \left(\frac{1}{T_e} - \frac{1}{T_{r,1}^{n-1}} \right) \right]}{1 - \zeta_1 \Lambda_\nu^*}. \end{aligned} \quad (2.64)$$

The consistency of this scheme is easily proven, because after convergence we would get (cf. Eq. 2.43)

$$\begin{aligned} \frac{1}{b_1} &= \left(\frac{n_1^*}{n_1} \right) = \frac{n_\kappa}{n_1} \left(\frac{n_1}{n_\kappa} \right)^* \\ &= W \frac{T_{r,1}}{T_e} \exp \left[-\frac{h\nu_1}{k} \left(\frac{1}{T_{r,1}} - \frac{1}{T_e} \right) \right] \zeta_1 (1 + C_{N'}), \end{aligned} \quad (2.65)$$

so that the “ALO-correction factor” C_A becomes unity. Throughout the iteration the correction factor can take values smaller or larger than unity, leading to a fast and reliable convergence.

2.4.7 Test calculations

In order to check the accuracy of our approximate approach, we will present two different test calculations. The first test aims at a clean investigation of the methods outlined above, unaffected by additional complications such as line-blocking/blanketing. To this end, we have computed a pure H/He atmosphere at $T_{\text{eff}} = 40,000$ K, for two different sets of parameters: the first model (A4045 with $\log g = 4.5$) corresponds to a dwarf with thin wind, the second (F4037 with $\log g = 3.7$) to a supergiant with thick wind.⁷

For both models we have calculated an “exact” solution as described in Paper I, namely by solving for the H/He occupation numbers from the complete rate equations, with all lines in the CMF and a temperature stratification calculated from NLTE Hopf-parameters. In order to test our approach, we calculated two additional models, with an exact solution for hydrogen only, whereas helium has been treated by means of our approximate approach. (In the standard version of our code, helium is always treated exactly.)

Fig. 2.3 shows the very good agreement of the resulting ionization fraction for helium in both cases. The small differences at large optical depths (i.e., for LTE conditions) are due to the different atomic models for helium used in both the exact and the approximate solution. (The data-base applied to the approximate solution comprises a lower number of levels for both He I and He II, so that the partition functions are somewhat smaller than in the exact case, and consequently also the ionization fractions. The occupation numbers of the levels *in common* are identical though).

Most intriguing is the excellent agreement of the He II ground state departure coefficient as a function of depth (Fig. 2.4, upper panel). The crucial feature is the depopulation of the He II ground-state close to the sonic point, which is a sophisticated NLTE-effect arising in unified model atmospheres and depends on a delicate balance between the conditions at the He II ground-state, the $n = 2$ ionization edge and the He II Ly $_{\alpha}$ line (which in itself depends on the radiation field at 303 \AA and the escape probabilities), cf. Gabler et al. (1989). The comparison between exact and approximate solution shows clearly that our approach, accounting for frequency dependent radiation temperatures and important line transitions, is actually able to cope with such complicated problems.⁸

⁷Concerning the nomenclature of our models, cf. Sect. 2.9

⁸Actually, it was this feature that motivated us to refrain from frequency independent radiation temperatures, since a first

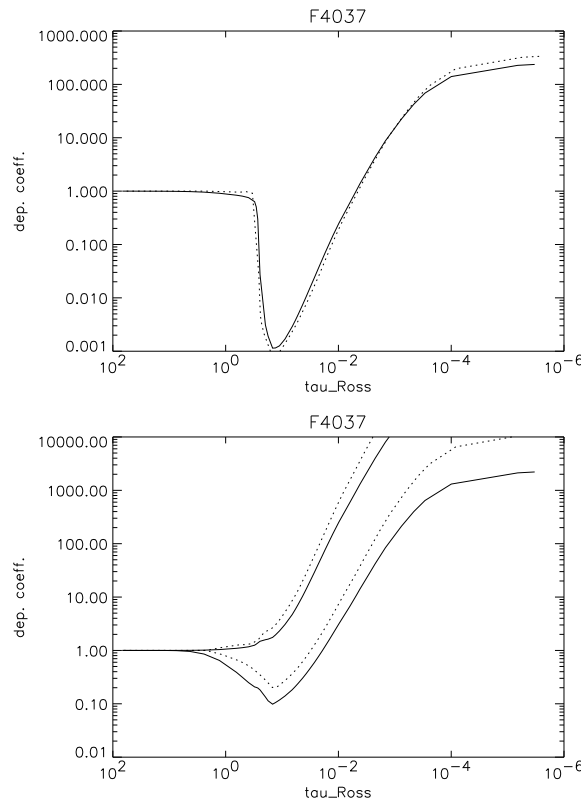


Figure 2.4: Approximate NLTE (dotted) vs. the exact case (bold): He departure coefficients for model F4037. Upper panel: He II ground-state departure coefficient. Lower panel: He I triplet and singlet “ground”-states (upper and lower curves, respectively).

In the lower panel of the figure, we have displayed the “ground”-state departure coefficients of He I, for the triplet and singlet system (upper and lower curves, respectively). Although the precision is not as excellent as for the He II ground-state, one has to consider that He I at 40,000 K is an extremely rare ion, and that the major features (depopulation of the singlet ground-state, no depopulation for the triplet ground-state) are reproduced fairly well.

The second test investigates the behaviour of the metals. We compare the results from the approximate method with results from an “almost” exact solution, for model F4037. As we will see in Sect. 2.7, the introduction of a consistent temperature structure calculated in parallel with the solution of the rate equations forced us to consider the most important elements (in terms of their abundance) in a more precise way than described so far, at least if we calculate the temperature from the electron thermal balance. In this case it is extremely important that the occupation numbers from *all* excited levels are known to a high precision in order to account for the cooling/heating by bound-bound collisions in a concise way. Unfortunately, this latter constraint cannot be fulfilled by our approximate method, simply because not all excited levels are considered, and small deviations from the exact solution (which are negligible for the effects of line-blocking, see below) can have disastrous effects on the total cooling/heating rates.

comparison using the latter simplification gave extremely unsatisfactory results.

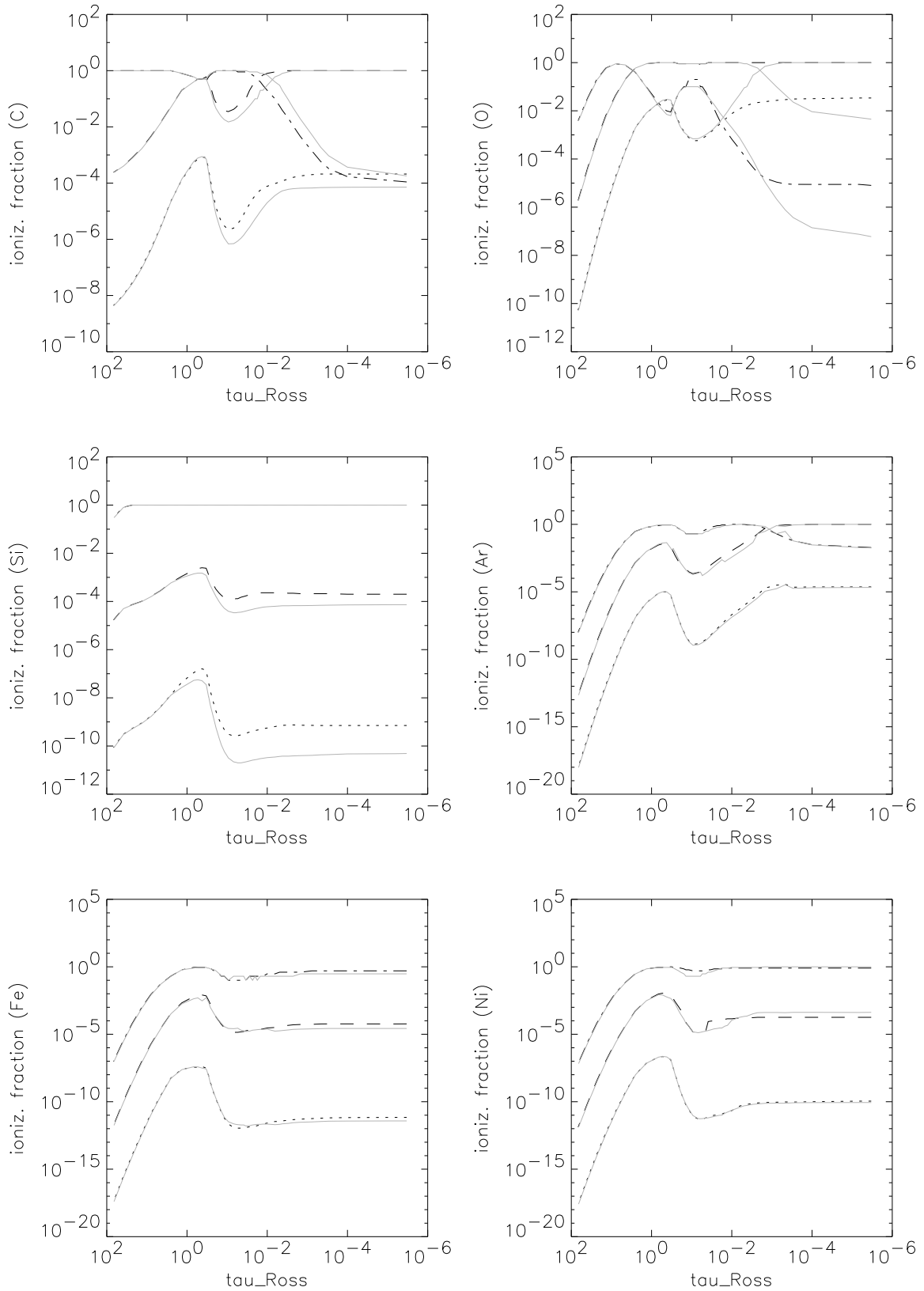


Figure 2.5: Approximate NLTE (grey) vs. the results of a solution of the complete rate equations, using Sobolev line transfer (black): ionization fractions of important metals for model F4037. Displayed are the ionization stages III, IV, V (dotted, dashed and dashed-dotted, respectively).

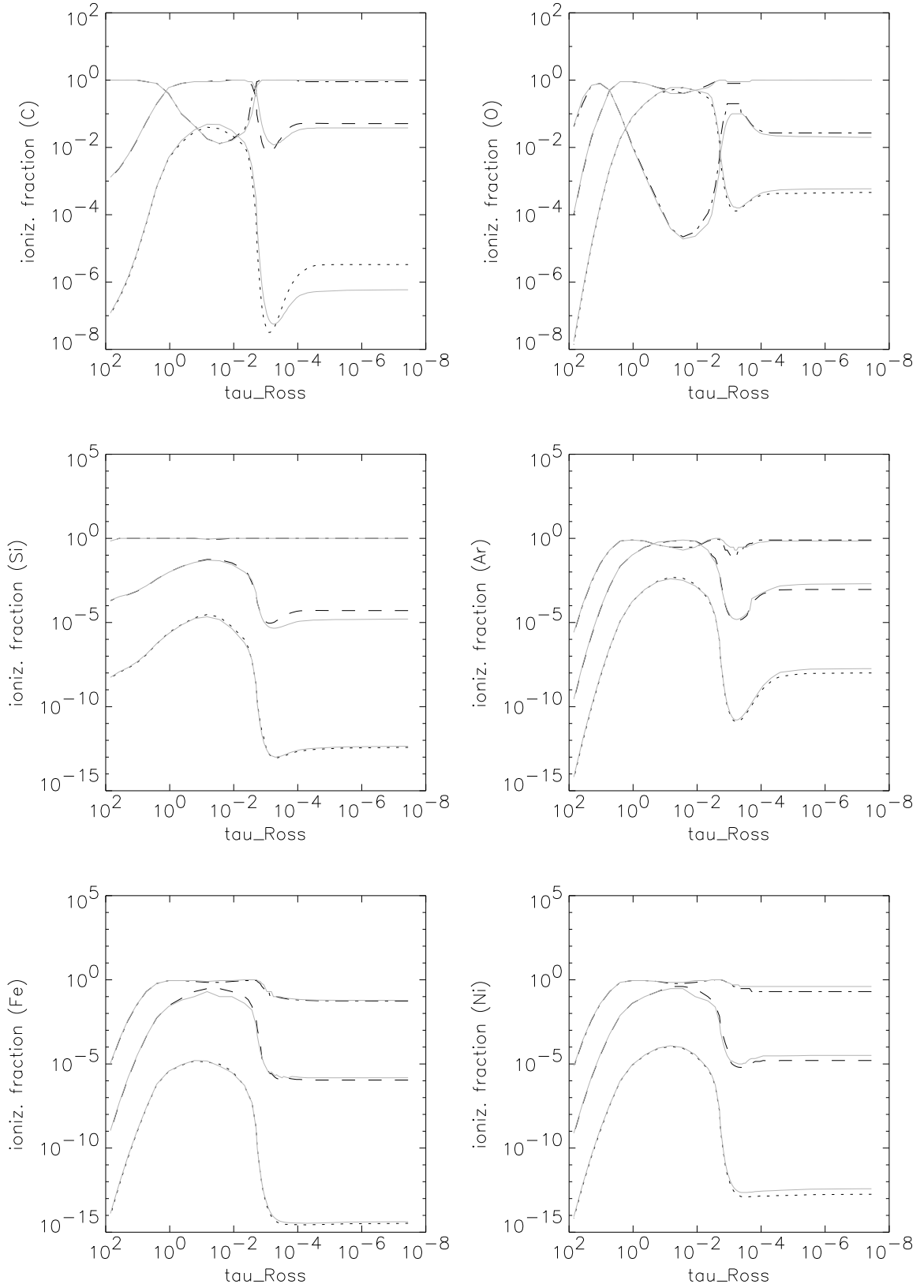


Figure 2.6: As Fig. 2.5, but for model A4045.

Thus, for the most abundant elements the complete set of rate-equations has to be solved for in any case, and this solution (which uses a Sobolev line transfer, cf. Sect. 2.7) is compared with our approximate one in Fig. 2.5, for the ionization stages III to V of some important metals, namely C, O, Si, Ar, Fe and Ni. Note that the comparison includes the effects of line-blocking on the radiation field, where this radiation field has been calculated either from the exact occupation numbers or from the corresponding approximate values, respectively. Our comparison demonstrates three important points.

- The transition between LTE and NLTE (taking place at $\tau_{\text{Ross}} > 2/3$ in our approximate approach) is described correctly.
- The approximate treatment works particularly well for elements with complex electronic structure (Ar, Fe, Ni), i.e., our treatment of meta-stable levels is reasonable.
- If there are differences, they occur predominantly in the outer wind.

In almost all considered cases, the principal run of the approximate ionization fractions agrees reasonably or even perfectly well with the exact result. The only exception is oxygen where the major/minor stages (IV/III) appear reversed in the outer wind (no problems have been found for nitrogen and neon which are not displayed here). These differences in the outer wind (see also C and Si) are partly due to two effects. On the one hand, our approach becomes questionable in those cases when *all* line transitions are optically thin so that the two-level-atom approach fails to describe the excitation-balance of subordinate levels. If only this effect were responsible this would imply (as suggested by our referee) that the discrepancy should become worse for thinner winds. Thus, we performed a similar comparison for model A4045, which has a considerably lower wind density than model F4037, by a factor of almost 100. The corresponding ionization fractions are shown in Fig. 2.6. Note that the transition point between photosphere and wind is located at lower values of τ_{Ross} , compared to model F4037, due to the weaker wind. Interestingly, the discrepancies between approximated and “exact” ionization fractions in the outer wind have remained at the same level as for model F4037, and in the case of oxygen the situation is almost perfect now. Consequently, the effect discussed above cannot be responsible alone for the observed discrepancy, and we attribute it to a combination of various ingredients inherent to our approximative approach. For our models, however, this is of minor importance, since we are not aiming at a perfect description of the occupation numbers in the outer wind unless we actually need it, i.e., when a consistent temperature structure shall be derived. In this latter case, the occupation numbers are calculated exactly anyway.

Different occupation numbers influence the radiation field, which in turn influences the occupation numbers, and so on. This is the second process which might affect our final approximate solution. Fig. 2.7 compares the emergent fluxes (expressed as radiation temperatures) for the converged models of F4037, calculated by both alternative approaches.

Due to the excellent agreement between the ionization fractions in the line/continuum forming part of the atmosphere, also the fluxes agree very well. The maximum differences, located between 200 to 400 Å, are of the order of $\pm 1,000$ K, which translates to a typical difference in population of ± 0.15 dex in the outer wind.

Globally, however, the differences in flux are so small that we can consider the two results as equivalent. Thus, the radiation field calculated in parallel with the line-blocking background elements is insensitive to the chosen approach (exact vs. approximate occupation numbers) which primarily differs in the precision (and presence) of subordinate levels.

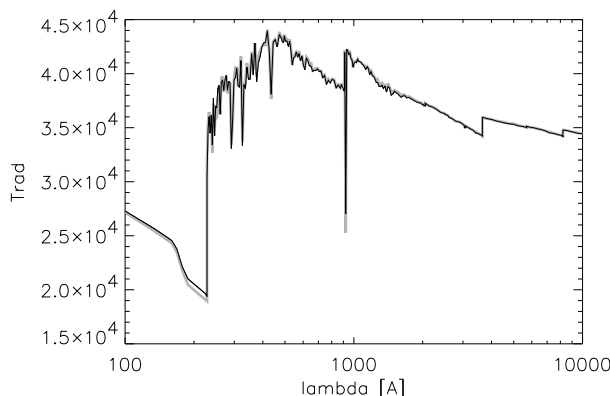


Figure 2.7: As Fig. 2.5. Comparison of radiation temperatures of *converged* models.

2.5 Approximate line-blocking

The most time-consuming part in the computation of *realistic* stellar atmospheres is the calculation of the radiation field, realizing the multitude of overlapping⁹ lines with considerable opacity (see also the discussion by Puls & Pauldrach 1990 and Pauldrach et al. 2001).

For CMFGEN as well as for the wind-code developed by the Potsdam group (for a recent status report, see Gräfener et al. 2002), this problem has been tackled by performing a comoving-frame solution for the *complete* EUV/UV range. Obviously, this approach is very time-consuming. A quick calculation shows that the number of frequency points which must be treated is of the order of 900,000, if a range between 200 and 2,000 Å and a typical resolution of 0.8 km s^{-1} is considered (i.e., ten points covering a thermal width of 8 km s^{-1}).

In the approach followed by WM-Basic, on the other hand, an observer's frame solution is performed which requires "only" a couple of thousand frequency points to be considered. The conservation of work, however, immediately implies that in this case a lot of time has to be spent on the resolution of the resonance zones of the overlapping lines, a problem which is avoided a priori in a CMF calculation.

In order to solve the problem on a minimum time-scale, both a Monte-Carlo solution¹⁰ (e.g., Schaerer & Schmutz (1994); Schaerer & de Koter (1997)), and a *statistical* approach are feasible:

Since the number of metal lines to be treated is very large, the information about the exact position of individual lines inside a (continuum transfer) frequency grid interval becomes less important for obtaining a representative mean background. As shown by Wehrse et al. (1998), the *Poisson Point Process* is well suited to describe such a line ensemble, particularly because it is very flexible and can be described by relatively few parameters.

The additional introduction of a *Generalized Opacity Distribution Function* by Baschek et al. (2001) serves two purposes. First, additional analytical insight is given into the effects of the vast amount of blocking lines on the mean opacity in differentially moving media with line overlap. Second, it is a fast tool to derive such mean backgrounds numerically. In particular, it is able to

⁹both in the observer's and in the comoving frame

¹⁰which becomes costly as well if a detailed description of all possible interactions between radiation field and plasma is accounted for.

“solve problems that have been inaccessible up to now as e.g. the influence of very many, very weak lines”(Baschek et al. 2001), and to describe the transition from a static to a moving configuration, since it is equally efficient in both cases.

In our opinion, this approach is very promising, and work adapting and applying the corresponding method is presently under way in our group. Since it will take some time to finalize this approach (the most cumbersome problem is the formulation of consistent emissivities), we have followed a somewhat simplified approach in the mean time, which relies on similar arguments and has been developed by carefully comparing with results from “exact” methods, mostly with the model grid calculated with WM-Basic as described by Pauldrach et al. (2001).

Again, the principal idea is to define suitably averaged quantities which represent a mean background and which can be calculated easily and fast. The multitude of lines will be approximated in terms of a pseudo continuum (split into a “true” absorption and a scattering component), so that the radiative transfer can be performed by means of a standard continuum solution, for relatively few frequency points (see below). Strongest emphasis has been given to the requirement that any integral quantity calculated from the radiation field (such as the photo-integrals) has to give good approximations compared to the exact case, because these quantities (and not the frequential ones) are most decisive for a correct description of the level populations and, in turn, for the blocked radiation field.

2.5.1 Mean opacities

To this end, we define a “coarse grid” with spacing $2Nv_{\text{th}}^{\text{m}}$, where v_{th}^{m} is a typical thermal velocity (say, of oxygen) including micro-turbulence, and $2N$ is an integer of the order of 100. (The reason to define here $2N$ instead of N will soon become clear.) Under typical conditions, this grid has a resolution of 1,000-1,500 km s⁻¹ and is used to calculate appropriate averaged opacities. With respect to a simplified approach, a mean constructed in analogy to the Rosseland mean is perfectly suited, i.e., an average of the *inverse* of the opacity,

$$\frac{1}{\langle \chi^{\text{tot}} \rangle} =: \frac{\int_{2Nv_{\text{th}}^{\text{m}}} \frac{d\nu}{\chi_{\nu}^{\text{tot}}}}{\int_{2Nv_{\text{th}}^{\text{m}}} d\nu}, \quad (2.66)$$

since it has the following advantageous properties:

- a) if no lines are present, the pure continuum opacity is recovered
- b) if one frequency interval is completely filled with non-overlapping, strong lines *of equal strength*, also the average opacity approaches this value, whereas
- c) in those cases when the interval has “gaps” in the opacity, these gaps lead to a significant reduction of the mean, i.e., allow for an appropriate escape of photons. Note that any *linear* average has the effect that *one* strong line alone (of typical width $2v_{\text{th}}^{\text{m}}$) would give rise to a rather large mean opacity (just a factor of N weaker than in case b) and, thus, would forbid the actual escape.
- d) Finally, the average according to Eq. 2.66 is consistent with the standard Rosseland mean in the lowermost atmosphere (as long as $\partial B_{\nu}/\partial T$ is roughly constant over one interval), i.e., it

is consistent with the diffusion approximation applied as a lower boundary condition in the equation of (continuum) radiative transfer.

Because of the large number of contributing lines (typically $5 \cdot 10^5$ (O-type) to 10^6 (A-type) lines if only ions of significant population are considered¹¹), the calculation of this mean has to be fast.

First, assume that any velocity field effects (leading to Doppler-shift induced line overlaps) are insignificant, i.e., assume a thin wind, so that line blocking is essential only in the subsonic regions of the wind. The generalization in order to approximate line-overlap in the wind will be described later on.

Instead of evaluating the “exact” profile function, for each line we use a box car profile of width $2v_{\text{th}}^m$. The frequential line opacity is, thus, given by

$$\chi_L(\nu) = \begin{cases} \chi_L & \text{for } \nu_0 + \Delta\nu_D \leq \nu \leq \nu_0 - \Delta\nu_D \\ 0 & \text{else} \end{cases} \quad (2.67)$$

$$\chi_L = \frac{1}{2\Delta\nu_D} \frac{\pi e^2}{m_e c} g f \frac{n_l}{g_l}, \quad \Delta\nu_D = \frac{\nu_0 v_{\text{th}}^m}{c}, \quad (2.68)$$

where stimulated emission has been neglected again. Due to this definition, at least the frequency-integrated line opacity is correctly recovered. The *coarse* frequency grid is now divided into N sub-intervals of width $\Delta\nu = 2\Delta\nu_D$. Inside each of these sub-intervals (“channels”) we sum up any line opacity which has appropriate rest-wavelength. Insofar, we account (approximatively) for any *intrinsic* (i.e., not wind-induced) line overlap. Inside each channel i , we thus have a (total) frequential opacity

$$\chi_{\nu,i}^{\text{tot}} = \sum_j \chi_{Lj} + \chi_\nu^{\text{cont}}, \quad \chi_\nu^{\text{cont}} = \chi_\nu^{\text{c,true}} + \sigma_e \quad (2.69)$$

if lines j are located inside channel i and the continuum opacity is assumed to be constant inside each coarse grid interval. $\chi_\nu^{\text{c,true}}$ is the contribution by true absorption processes, and σ_e the contribution by electron scattering. After replacing the integrals by appropriate sums and since all channels have the same width, the mean opacity (on the coarse grid) is simply given by

$$\frac{1}{\langle \chi^{\text{tot}} \rangle} \approx \frac{\sum_{i=1}^N \frac{\Delta\nu}{\chi_{\nu,i}^{\text{tot}}}}{\sum_{i=1}^N \Delta\nu} = \frac{1}{N} \sum_{i=1}^N \frac{1}{\chi_{\nu,i}^{\text{tot}}}. \quad (2.70)$$

For later purposes we split this mean opacity into the contribution from lines and continuum, respectively, where the line-contribution is given by

$$\langle \chi_L \rangle = \frac{N}{\sum_i \frac{1}{\chi_{\nu,i}^{\text{tot}}}} - \chi_\nu^{\text{cont}} \quad (2.71)$$

and we have

$$\langle \chi^{\text{tot}} \rangle = \langle \chi_L \rangle + \chi_\nu^{\text{cont}}. \quad (2.72)$$

Note that both mean opacities, $\langle \chi_L \rangle$ and $\langle \chi^{\text{tot}} \rangle$, are frequency dependent as a function of coarse grid index. In accordance with our reasoning from above, Eq. (2.71) implies that

¹¹Remember, that our present data base comprises $4.2 \cdot 10^6$ lines in total.

- a) if $\chi_{Lj} = 0$ for *all* lines inside one interval, the correct result $\langle \chi_L \rangle = 0$ is obtained
- b) if the same *total* line opacity $\chi_L(\nu)$ is present inside *each channel*, this value will also be obtained for the mean, $\langle \chi_L \rangle = \chi_L(\nu)$.
- c) if only one (strong) line is present, the mean line opacity is given by $\langle \chi_L \rangle \approx \chi^{\text{cont}}/(N - 1)$, i.e., it will be much smaller than the continuum opacity, since most of the flux can escape via the $(N - 1)$ unblocked channels (according to our present assumption that Doppler-induced line overlap is negligible).

Finally, let us point out that the opacities constructed in this way are used also to calculate the photospheric line pressure, in analogy to the description given in Paper I (Eq. 3), however including the line contribution (cf. Fig. 2.11).¹²

2.5.2 Emissivities

In order to calculate the corresponding emissivities, we assume that each transition can be described by means of a two-level atom, where the *lower* occupation number is known from the solution (“exact” or approximate) of the rate equations.¹³

Although this assumption is hardly justified for (weak) recombination lines, it is a fair representation for most of the stronger transitions arising from either the ground-state or a meta-stable level, particularly if the level population itself is calculated from a multi-level atom.

It might be argued that the two-level atom approach is superfluous for those *connecting* transitions which are calculated from an exact NLTE solution, since the occupation numbers for both levels and, thus, the source-functions are already known. The maximum number of these lines is of the order of 30,000, and therefore much lower than the total number of lines we are using for our line-blocking calculations (cf. Sect. 6.3.1). For the latter transitions, however, only the lower level is present in the atomic models, so that the corresponding source-functions have to be approximated in any case.

Moreover, treating all lines (including the connecting transitions) in a two-level way has the additional advantage that the contribution of scattering and thermal processes can be easily split, which allows to simulate their impact by means of a pseudo-continuum, so that the standard continuum transfer can be applied without any modification.

To keep things simple and as fast as possible and to be in accordance with our assumption of box car profiles, we replace the scattering integral inside the two-level source-function by mean intensities, i.e., we write

$$S_L = \rho J_\nu + \delta B_\nu, \quad \rho = 1 - \delta, \quad (2.73)$$

where δ has been defined in Eq. 2.27 and is evaluated for the line-specific thermalization parameter and escape probability. The total source-function (in channel i , before averaging) is then given by

$$S_{\nu,i} = \frac{\eta_\nu^{\text{c,true}} + \sigma_e J_\nu + \sum_j \chi_{Lj} (\rho_j J_\nu + \delta_j B_\nu)}{\chi_\nu^{\text{cont}} + \sum_j \chi_{Lj}}, \quad (2.74)$$

¹²In our present version of FASTWIND we allow for deviations from the generalized Kramer-law (Paper I, Eq. 2) by simply including these deviations as correction-factors into the atmospheric structure equations. This method becomes important for models at rather cool temperatures when hydrogen and background-metals are recombining (and become ionized again) in photospheric regions, which usually leads to some deviations from the above (power-) law.

¹³Note that this approach is equivalent to the typical assumption made if deriving the radiation field via Monte-Carlo simulations.

with $\eta_\nu^{\text{c,true}}$ being the thermal component of the continuum emissivity. Note that the frequential line-opacity χ_{Lj} includes the “profile function” $(2\Delta\nu_D)^{-1}$, cf. Eq. 2.67.

In the following, we will investigate how to average the above quantities in order to be consistent with our definition of $\langle\chi^{\text{tot}}\rangle$ and $\langle\chi_L\rangle$. With respect to the equation of transfer, which will be finally solved on the coarse grid, we find that after integration over the subgrid-channels

$$\frac{1}{\langle\chi^{\text{tot}}\rangle} \frac{d}{dz} \langle I_\nu \rangle = \langle S_\nu \rangle - \langle I_\nu \rangle, \quad (2.75)$$

with z being the depth variable along the impact parameter p in the usual (p, z) -geometry. Strictly speaking, the first term in the above equation (i.e., the mean inverse opacity) is given by

$$\frac{1}{\langle\chi^{\text{tot}}\rangle} = \frac{\int \frac{1}{\chi_\nu} \frac{d}{dz} I_\nu d\nu}{\int \frac{d}{dz} I_\nu d\nu} \quad (2.76)$$

(where the denominator is equivalent to $d/dz \langle I_\nu \rangle$, and all integrals extend over the range $2Nv_{\text{th}}^{\text{m}}$), i.e., a different definition applies when compared to the corresponding quantity in Eq. 2.66. Our crucial approximation is to equate both definitions, i.e., inside each coarse grid cell (of width $\approx 1,000 \dots 1,500 \text{ km s}^{-1}$) we assume that

$$\int \frac{1}{\chi_\nu} \frac{d}{dz} I_\nu d\nu / \int \frac{d}{dz} I_\nu d\nu \approx \int \frac{d\nu}{\chi_\nu} / \int d\nu.$$

Let us frankly admit that this approximation can be justified only if a) the spatial gradient of the specific intensity is a slowly varying function of frequency (i.e., deep in the atmosphere) or b) the opacities are similar for *most* of the sub-channels, i.e., either no lines are present at all or the (summed) line-opacities do not vary too much. Additionally and most important, this approximation still works in those cases when only a couple of channels are populated by large opacities and the rest is filled by a weak background due to the inverse relation between opacity and intensity: On the lhs, the high opacity channels do not contribute to the fraction because of the correspondingly low intensities in both the nominator and the denominator, whereas on the rhs these channels drop out at least in the nominator because of the low value of $1/\chi$.

There are, of course, a number of cases where the above approximation is only poor. With respect to the results presented below and since we are *not* aiming at a perfect, highly resolved description of the radiation field in the line-blocking EUV/UV regime, the errors introduced by the above approximation (and the following one, which is of similar quality) are acceptable though.

In order to proceed with appropriate expressions for the emissivity, the mean source-function, $\langle S_\nu \rangle$, is given by

$$\langle S_\nu \rangle = \frac{\eta_\nu^{\text{c,true}}}{\langle\chi^{\text{tot}}\rangle} + \left(\frac{\sigma_e}{\langle\chi^{\text{tot}}\rangle} + \left\langle \frac{\sum_j \chi_{Lj} \rho_j}{\chi_\nu^{\text{tot}}} \right\rangle \right) \langle J_\nu \rangle + \left\langle \frac{\sum_j \chi_{Lj} \delta_j}{\chi_\nu^{\text{tot}}} \right\rangle B_\nu, \quad (2.77)$$

where the Planck-function B_ν is assumed to be constant within one macro-grid interval. For those averages which are multiplied by $\langle J_\nu \rangle$, we have employed an approximation similar to the one discussed above. If we, finally, denote the opacity dependent means of the third and fourth term by f_{nth} and f_{th} , respectively (i.e., *non-thermal/thermal*), the equation of radiative transfer for the averaged quantities

becomes

$$\begin{aligned} \frac{1}{\langle \chi^{\text{tot}} \rangle} \frac{d}{dz} \langle I_\nu \rangle &= \\ &= \frac{\eta_\nu^{\text{c,true}} + (\sigma_e + \langle \chi^{\text{tot}} \rangle f_{\text{nth}}) \langle J_\nu \rangle + \langle \chi^{\text{tot}} \rangle f_{\text{th}} B_\nu}{\langle \chi^{\text{tot}} \rangle} - \langle I_\nu \rangle, \end{aligned} \quad (2.78)$$

and can be solved in the conventional way (pure continuum transport). The resulting quantities for the radiation field are to be understood as average quantities, in the sense that integral quantities such as $\int J_\nu d\nu$ or $\int H_\nu d\nu$ are described correctly, at least in most cases. The coefficients f_{th} and f_{nth} can be calculated by summing over the sub-channels,

$$f_{\text{th}} = \frac{1}{N} \sum_i \frac{(\sum_j \chi_{Lj} \delta_j)_i}{(\chi_\nu^{\text{cont}} + \sum_j \chi_{Lj})_i} \quad (2.79)$$

$$f = f_{\text{th}} + f_{\text{nth}} = \frac{1}{N} \sum_i \frac{(\sum_j \chi_{Lj})_i}{(\chi_\nu^{\text{cont}} + \sum_j \chi_{Lj})_i} < 1! \quad (2.80)$$

$$f_{\text{nth}} = f - f_{\text{th}}, \quad (2.81)$$

and after some simple algebraic manipulations, the following relation is obtained:

$$\langle \chi_L \rangle = \langle \chi^{\text{tot}} \rangle (f_{\text{th}} + f_{\text{nth}}). \quad (2.82)$$

With this equation it is easy to show that the mean source-function (2.77) allows for a correct thermalization, if $\eta_\nu^{\text{c,true}} \rightarrow \chi_\nu^{\text{c,true}} B_\nu$ and $\langle J_\nu \rangle \rightarrow B_\nu$. In this case, the mean source-function becomes $\langle S_\nu \rangle = B_\nu$, q.e.d.

We now need to incorporate the effects of the velocity field into our approach. Due to the method to average the opacity, we cannot simply shift the lines with respect to the stellar frame: Consider, e.g., one strong line to be present without any other interfering lines. In “reality” and in the observer’s frame, the absorption part of this line becomes broader as a function of velocity, i.e., the larger the velocity the more flux is blocked (of course, a significant part is reemitted due to scattering). If we simply shift our line(s) as a function of velocity, almost nothing would happen, since, as shown above, the mean opacity/radiation field remains almost unaffected by one strong line, due to the possible escape via the (N-1) unblocked sub-channels. Thus, in order to simulate the physical process, we proceed in a different way: When the velocity shift becomes larger than twice the average “thermal” width (including micro-turbulence), we combine (in proportion to the local velocity) more and more subchannels to increase the relative weight of the line in the mean opacity. In particular, the line width (more precisely, the width of the sub-channels) is set to the value

$$\Delta\nu = \max(2\Delta\nu_D, \frac{v(r)}{\lambda_0}). \quad (2.83)$$

Although this procedure is highly approximative, it allows to deal with the effects of “line-shadowing” and prevents any premature escape of photons when the lines begin to overlap.

2.5.3 Tests/Comparison with WM-Basic

Before we test our approximate approach by comparing with alternative calculations, let us mention two important consistency checks we have performed.

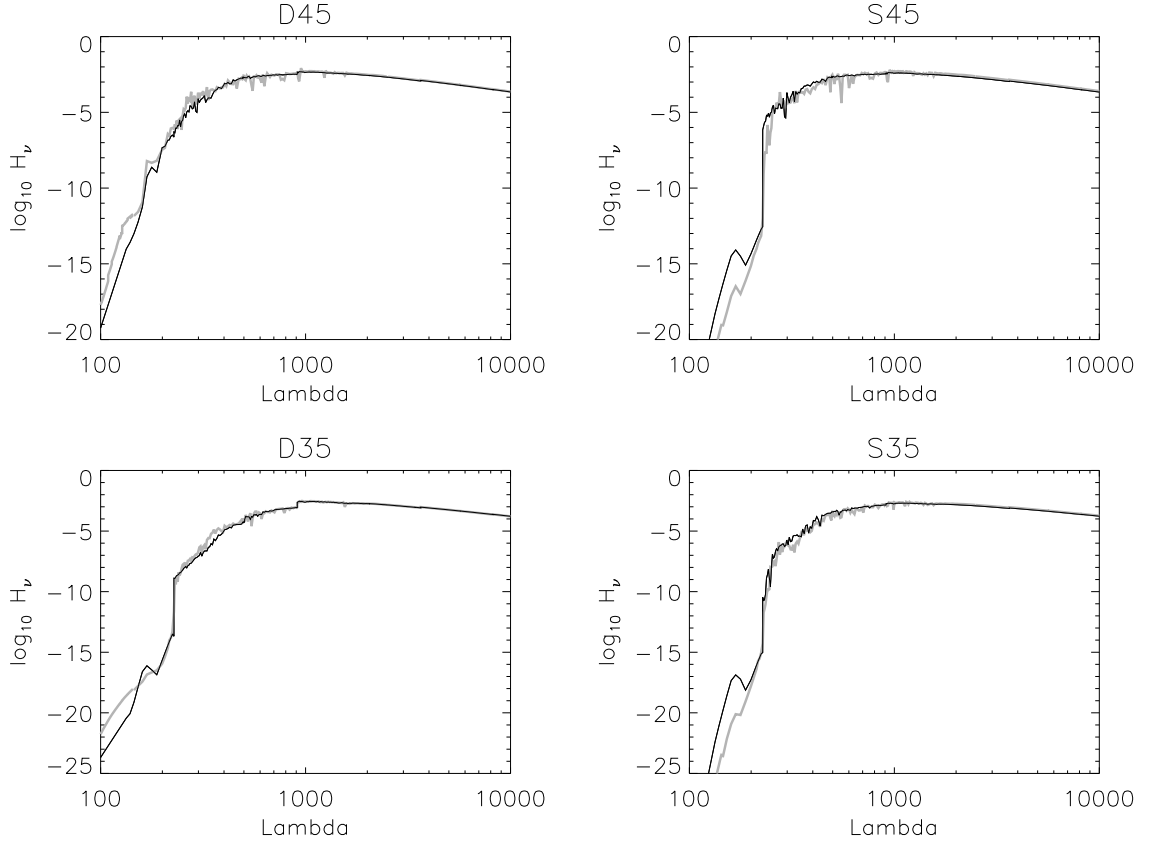


Figure 2.8: FASTWIND vs. WM-Basic (grey): comparison of emergent fluxes for two dwarf and two supergiant models at 35 and 45 kK (for parameters, cf. Pauldrach et al. 2001). In order to allow for a meaningful comparison, the high resolution frequency grid provided by WM-Basic has been re-mapped while keeping the corresponding flux-integrals conserved.

- a) The calculated models (and spectral energy distributions/line profiles) are, almost, independent of the actual value of coarse grid cells, N , at least if varied within a reasonable range. (We checked for values between $0.5N$ to $2N$, for $N = 60$.)
- b) As long as the IR/radio-range is not considered, our simpler models with a temperature-structure calculated from Hopf-parameters and *all* background elements in approximate NLTE agree very well with complex models including a consistent T-structure. This check verifies analyses performed with previous versions of FASTWIND, e.g., Herrero et al. (2002) and Repolust et al. (2004).

In the following, we will compare the fluxes from our models with those calculated by WM-Basic by means of the O-star grid presented by Pauldrach et al. (2001)¹⁴. These tests should give reasonable agreement, since both codes use the same atomic data base for the background-elements. A comparisons with results from CMFGEN will be discussed later on.

¹⁴available via <http://www.usm.uni-muenchen.de/people/adi/Models/Model.html>

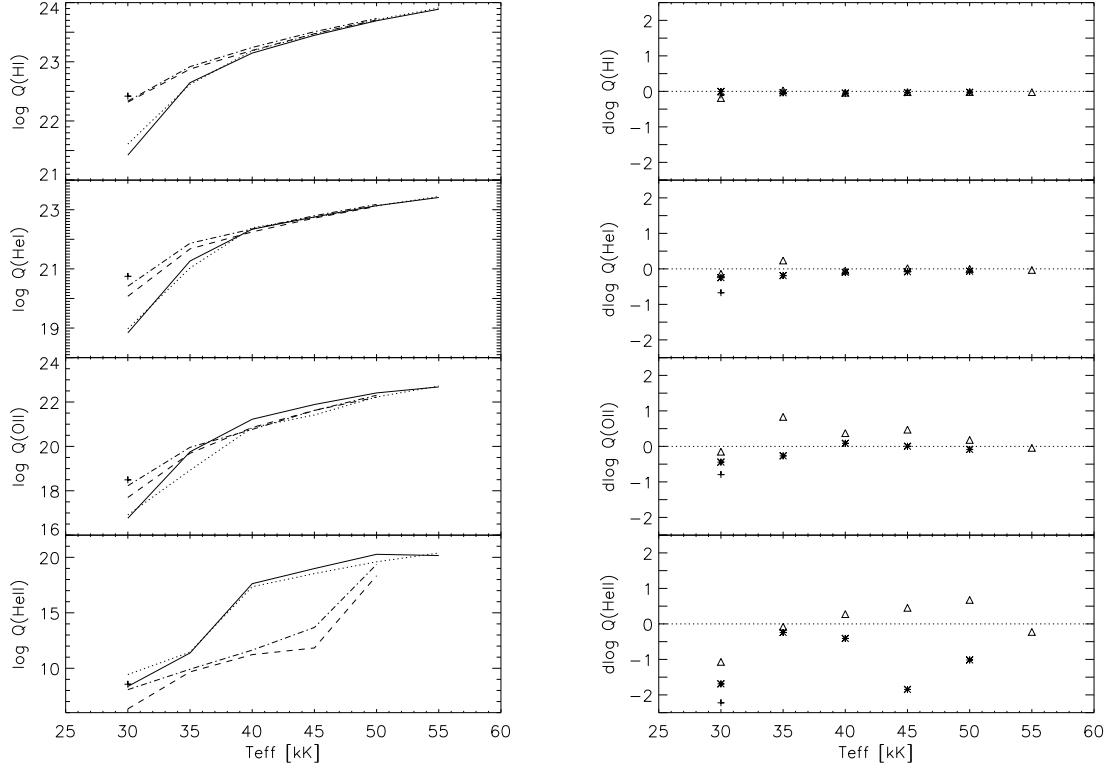


Figure 2.9: Comparison of ionizing photon number for the model grid provided by Pauldrach et al. (2001). Left panel: logarithm of Zanstra-integrals, $\log Q_x$, see Eq. 2.84, for H I, He I, O II, and He II: Bold/dashed: dwarfs/supergiants as calculated by WM-Basic; dotted/dashed-dotted: results from FASTWIND. Right panel: ratio of corresponding Zanstra integrals, $\Delta \log Q_x = \log Q_x^{\text{WMB}} - \log Q_x^{\text{FW}}$ (WMB: WM-Basic, FW: FASTWIND), for dwarfs (triangles) and supergiants. For the supergiant model at 30,000 K (“S30”), we have used the FASTWIND model *without* photospheric line-pressure in both figures. The corresponding results for the “correct” model, i.e., including photospheric line-pressure, are indicated by the + sign (see text).

The parameters of the corresponding models (calculated without X-rays) can be found in Pauldrach et al. (2001, Table 5). Our models have been constructed as closely as possible to the approach inherent to WM-Basic, i.e., including a consistent temperature stratification (which will be described in Sect. 2.7) and Sobolev line-transfer. For the velocity-field, we have used $\beta = 0.9$, which results in a stratification very close to the one predicted by WM-Basic (see below). The computation time on a 2 GHz processor machine is of the order of 15 to 20 minutes per model (typically 40 to 50 iteration cycles for a final convergence below 0.003 in *all* quantities, if the temperature is updated each 2nd cycle).

The grid comprises 6 “dwarfs” and 5 “supergiants” in the range between 30... 55 kK (“D30”... “D55” and “S30”... “S50”, respectively), and we have concentrated on the grid with solar abundances, in order to deal with more prominent effects related to line-blocking/blanketing. Fig 2.8 compares the emergent fluxes for some typical cases, two dwarf and two supergiant models at 35

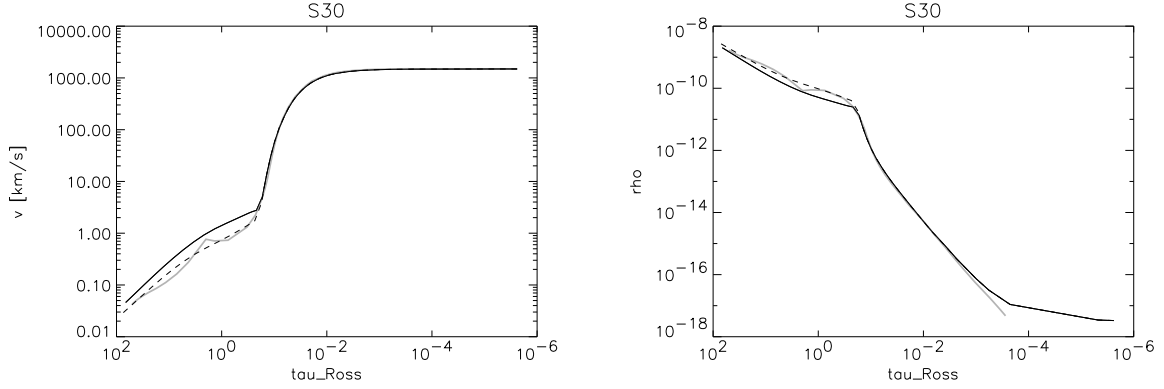


Figure 2.10: Comparison of velocity/density structure for model S30. Grey: WM-Basic; bold/dashed: FASTWIND with/without photospheric line-pressure, respectively.

and 45 kK. In order to allow for a meaningful comparison, we have re-mapped the high resolution frequency grid provided by WM-Basic while keeping the corresponding flux-integrals conserved.

Overall, the agreement is rather good; in particular, the range above 400 Å is reproduced very well, except for some strong absorption/re-emission features which are missing in our mean-opacity approach. We have convinced ourselves that in all cases also the IR-fluxes (not displayed here) agree perfectly, i.e., the IR flux-excess induced by the wind is reproduced equally well in both codes. Major differences are “only” present in two regions: most models differ in fluxes below 200 Å, although the strength of He II Lyman-jump itself is very similar. Mostly, this problem is related to the enormous bound-free opacity provided by OIV (and FeV or CIV for the hotter or cooler objects, respectively) leading to an optically thick wind from the outermost radius point on (in our case, $R_{\max} = 120R_{\star}$), so that the flux is rather badly defined in this frequential region. As we will see from a comparison with models calculated with CMFGEN (Figs. 2.15), these models predict a third alternative for $\lambda < 200$ Å, and even the Lyman-jump is different. As a result, we consider the ionizing fluxes in this wavelength range as not particularly reliable. Moreover, the influence of X-rays becomes decisive, implying that any tool for nebula diagnostics should use these numbers only with care.

The second inconsistency is found in the region between 300 to 400 Å. Although this range poses no problem for supergiants, the flux-blocking predicted by FASTWIND for *dwarfs between 35 to 45 kK* is larger than calculated by WM-Basic, with a maximum discrepancy around 35 kK. The reader might note that CMFGEN again produces somewhat different results in this range: Agreement with WM-Basic is found for dwarfs, whereas the fluxes emitted from supergiants are larger compared to both FASTWIND and WM-Basic.

This dilemma becomes particularly obvious if we consider the corresponding Zanstra-integrals,

$$Q_x = \int_{\nu_x}^{\infty} \frac{H_{\nu}}{h\nu} d\nu, \quad (2.84)$$

which are proportional to the emitted number of ionizing photons. In the left panel of Fig. 2.9, we compare the logarithm of Q_x , evaluated for H I, He I, O II and He II, whereas the corresponding ratios, $\Delta \log Q_x = \log Q_x^{\text{WMB}} - \log Q_x^{\text{FW}}$ (WMB: WM-Basic, FW: FASTWIND), are displayed in the right panel. Obviously both codes predict the same numbers in the hydrogen Lyman and in the He I continuum. As already discussed, the situation is much less satisfactory for the He II continuum, where

the differences are particularly significant for supergiants. Note, however, that the principal dependence of Q_{HeII} on spectral type and luminosity class, which shows the largest variation throughout the spectrum (lower left panel), is much more consistent than one might expect on basis of the right panel alone. In the OII continuum ($\lambda < 352 \text{ \AA}$), finally, the differences for the dwarfs at intermediate spectral type are evident.

Note that in this wavelength range the line-density is very large, and differences in the treatment of the weakest background opacities might explain the established disagreement. An argument in support of this hypothesis is given by the fact that FASTWIND recovers the results by WM-Basic perfectly if a line-list is used which has significantly less (overlapping) weaker lines in the considered interval. For a final statement, however, more tests are certainly required. Note that a comparison with CMFGEN addressing this point will not solve the problem, since the number of lines included in this code is mostly lower than described here, because CMFGEN uses only those lines where the occupation numbers of *both* levels are known, in contrast to our approach which uses also lines where the upper level is lying too high to be included into the rate equations.

One last point we would like to mention concerns model S30. In a first comparison, we immediately encountered the problem that particularly this model provided fluxes which showed significantly less agreement at all frequencies than the other models (indicated by the plus-signs in Fig. 2.9). Comparing the models themselves, it turned out that temperature, density and velocity structure showed a severe mismatch in photospheric regions (cf. Fig. 2.10, grey vs. black curves). After some tests, we found that both models agree well if the photospheric line pressure is neglected in FASTWIND (grey vs. dashed curves in Fig. 2.10). Most likely, this problem is related to the treatment of the line pressure in WM-Basic. Whereas the continuum forces are calculated from correctly evaluated opacities, the line pressure, independent of location, is calculated in terms of the force-multiplier concept, utilizing the Sobolev approximation. Particularly, $g_{\text{rad}}^{\text{line}} \propto t^{-\alpha}$, with “depth parameter” $t \propto \rho/(dv/dr)$. Thus, g_{rad} decreases rapidly in photospheric regions when the density is large and the velocity gradient small.

In those cases where the (static) line pressure is non-negligible in photospheric regions, the chances are high that the above approximation leads to a too large effective gravity, i.e., too high densities. Actually, this problem is already known for a long time and has been discussed in fair detail in Pauldrach et al. (1986, particularly Fig. 6c). The reason that this problem occurs only in S30 results from fact that the Eddington factor is considerably higher than for almost all other models ($\Gamma = 0.52$). Insofar, the photospheric line pressure has much more impact than for models with either high gravity or low Γ . Moreover, at an effective temperature of 30 kK, FeIV with its enormous number of lines spread throughout the spectrum is the dominant (or almost dominant) ionization stage in the “middle” photosphere, thus, contributing a much larger amount of static line pressure than for hotter temperatures, where FeV or even FeVI are contributing.

Note that we have also compared our (cooler) models (from our grids as described in Sect. 2.9 and from additional A-star models) with corresponding Kurucz models, where in most cases a very good agreement regarding the photospheric radiative acceleration has been found, e.g., Fig. 2.11. Only for models cooler than 9,000 K a mismatch becomes obvious, where “our” radiation pressure is too low, due to a number of missing FeII lines in the optical (improvements under way!).

In order to allow for a meaningful comparison concerning our approximate line-blocking, in Fig. 2.9 we have used the results from our S30 model *without* photospheric line-force, whereas the results from the “actual” model (including $g_{\text{rad}}^{\text{line}}$) are indicated by “+”. Independently, however, Fig. 2.10 (left panel) also shows the validity of our treatment of the transition zone from photosphere to wind (cf. Paper I), since in this region both velocity fields agree perfectly. (Remember that WM-Basic

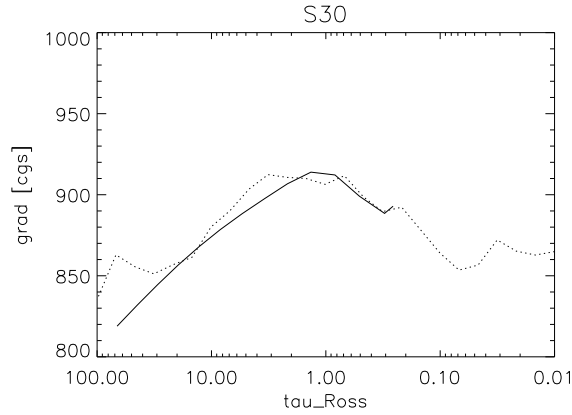


Figure 2.11: Comparison of *total* photospheric radiative acceleration for model S30 (bold) vs. results from an analogous hydrostatic Kurucz-model (dotted). Note that the gravitational acceleration for this model is 1000 cm s^{-2} , i.e., the radiative acceleration is very close to this value and, thus, of extreme importance (cf. Fig. 2.10). The deviations at largest depths are due to the fact that this model becomes (spherically) extended in the lowermost photosphere, an effect which cannot be treated in a plane-parallel approach (cf. Paper I).

solves the hydrodynamical equations in a consistent way).

2.6 Treatment of inverted levels

One of the more complex problems when solving the coupled equations of statistical equilibrium and radiative transfer is the presence of population inversions, which often occur in the outermost layers of hot expanding stellar atmospheres. The amount of the overpopulation (i.e., $n_u/g_u > n_l/g_l$) is usually small, but even in this case it invokes a number of problems concerning the solution of the radiative transfer equation. Particularly with respect to the usual concept of using source functions, a problem occurs in the transition zone between “normal” population and overpopulation, where the source function formally diverges. In addition, factors like $\exp(-\tau)$ may produce numerical problems for $\tau < 0$. In a number of codes, this problem is “solved” by setting the upper level into LTE with respect to the lower one or by other approximations. Since level inversions are particularly present between levels responsible for IR-lines and since FASTWIND aims at a reliable solution also in these cases, we cannot afford such approximations and have to solve the “exact” case which in turn has an influence on the degree of overpopulation itself. In this section, we briefly describe how we have solved the problem in FASTWIND both with respect to the Sobolev approach and within the CMF-transport.

2.6.1 Treatment of inversions in the Sobolev approximation

Since the Sobolev approach uses only *local* quantities, a divergence of the source function is not possible, except for the extremely unlikely case that upper and lower populations, normalized to the appropriate statistical weight, are numerically identical. Thus, we can retain the standard concept (optical depth and source function) and follow the approach described in Taresch et al. (1999): In

case of a level inversion, the interaction function $U(\tau_S, \beta_P)^{15}$ is split into two parts in order to avoid numerical problems,

$$\bar{U} = U_1 + U_2, \quad \text{with} \quad U_1 = 1 - \beta. \quad (2.85)$$

β is the usual escape probability in Sobolev approximation (Eq. 2.29), which for the case of inversion is given by

$$\beta = \frac{\exp|\tau_S| - 1}{|\tau_S|} \quad (2.86)$$

and U_2 has been described in Taresch et al. (1999, Eq. A13).

For $|\beta_P| \rightarrow \infty$, i.e., dominating continuum, U_2 approaches zero. In the case of dominant line processes, on the other hand, and $\tau_S < 0$, U_2 approaches $(\beta - 1)$ and \bar{U} goes to zero. Thus, we recover the “classical” result by Sobolev, where the influence of continua has been neglected.

In our approach, we have significantly extended the grid used by Taresch et al. (1999) from which U_2 is calculated by means of interpolation. Due to the different behaviour of this function in different regions of the (τ_S, β_P) plane, (four) different tables with different degrees of resolution have been calculated. The boundaries of the complete grid comprise the area between $-6 \leq \log|\tau_S| < 2.8$ and $-6 \leq \log|\beta_P| < 6$. Beyond the boundaries, U_2 is calculated analytically (by either considering the appropriate limits or using a first order expansion). In particular, it turns out that

$$U_2 = 0.5|\tau_S|, \quad \log|\tau_S| < -6 \quad \text{independent of } \beta_P \quad (2.87)$$

$$U_2 = \beta - 1, \quad \log|\beta_P| < -6 \quad \text{independent of } \tau_S \quad (2.88)$$

$$U_2 = \frac{1}{\sqrt{2\pi|\beta_P|}}, \quad \log|\beta_P| > 6, \quad \log|\tau_S| > -6 \quad (2.89)$$

and the limits for large $\log|\tau_S| > 2.8$ and $-6 \leq \log|\beta_P| \leq 6$ result from appropriate extrapolations from the pre-calculated tables.

2.6.2 Treatment of inversions in the comoving frame

In the CMF solution, the problem of source-function divergence is inevitable when a population inversion occurs and the standard formalism is used. Even if the local quantities are not diverging, there will be an implicit divergence just between the two depth-points before and at the beginning of overpopulation, which, due to the applied discretization, will not be handled consistently. To avoid this problem, it is more suitable to work directly with emissivities and opacities rather than with optical depths and source functions. Thus, in the case of inversion, we solve the two coupled equations of radiative transfer in the comoving frame according to

$$\frac{\partial u}{\partial z} - \frac{\partial v}{\partial x} = -\chi v \quad (2.90)$$

$$\frac{\partial v}{\partial z} - \frac{\partial u}{\partial x} = \eta - \chi u, \quad (2.91)$$

where u and v are the usual Feautrier variables, x is the frequency measured from the center of the line in Doppler width units, and z is the depth variable along the impact parameter. The opacity is $\chi = \chi_c(z) + \chi_L(z, x)$ and the emissivity is $\eta = \eta(z, x)$.

¹⁵which describes the interaction between line and continuum processes, where τ_S is the Sobolev optical depth and β_P the ratio of continuum to line opacity in a frequency interval corresponding to the thermal Doppler width, cf. Hummer & Rybicki (1985); Puls & Hummer (1988).

In order to discretize the equations with respect to z and x , a fully implicit scheme is used. As was shown by Mihalas et al. (1975, Appendix B) this method is *unconditionally* stable.

2.6.3 Tests

A number of tests have been performed concerning both the Sobolev and the CMF implementations. Most importantly, we have also tested models where the above discretization of the CMF equations with respect to z has been used for *all* transitions, not only for the “inverted” ones, and found satisfactory agreement with our standard implementation using a discretization with respect to τ .

After convincing ourselves that the algorithms are working in principal, we have tested our improved methods by comparing them with older results (where in case of inversion the upper level and the line source function were set to zero). This comparison has been performed for the O-star grid described in the previous section. The results were very satisfying, and a number of convergence problems originating from the older treatment of inverted populations are no longer present.

The differences in the resulting H/He line profiles (both in the optical and in the IR) turned out to be rather small, since for our grid parameters these lines are formed below those regions where the inversion sets in. However, we like to point out that a consistent treatment might be important for winds with more extreme mass-loss rates and for a number of metallic IR transitions with an inversion already occurring in photospheric regions.¹⁶

2.7 Temperature stratification

As has been previously mentioned, the present version of FASTWIND allows for the calculation of a consistent temperature stratification, utilizing a flux-correction method in the lower wind and the thermal balance of electrons (cf. Kubát et al. 1999) in the outer part.¹⁷ The region where both methods are connected is somewhat dependent on mass-loss, but typically lies at $\tau_{\text{Ross}} = 0.5$. Although the implementation of this method is straightforward, and the contribution of individual processes have been discussed in fair detail by Drew (1985, 1989), three points are worth mentioning.

In order to calculate the appropriate heating/cooling rates resulting from collisional bound-bound transitions, the population of excited levels is as important as the population of ground and meta-stable ones. This can readily be seen from the fact that the *net* heating rate from a collisional transition between lower level l and upper level u can be expressed as

$$Q_{ul} - Q_{lu} = (n_u C_{ul} - n_l C_{lu}) h\nu_{lu} = n_l C_{lu} h\nu_{lu} \left(\frac{b_u}{b_l} - 1 \right), \quad (2.92)$$

with collisional rates C_{ul} and NLTE departure coefficients b_l, b_u . Thus, the *ratio* of departure coefficients controls whether a certain transition heats or cools the plasma and its deviation from unity controls the degree of energy transfer: Heating results from transitions with an upper level being overpopulated with respect to the lower one, and cooling vice versa. Thus, the occupation numbers of *all* ionic levels have to be known with some precision, and we have to modify our approach when the electron thermal balance is used to calculate the temperature profile. The approximate NLTE solution as described in Sect. 2.4 simply does *not* yield the required occupation numbers of excited levels

¹⁶a typical example is the SiIV IR transition $4d\ ^2D^e - 4f\ ^2F^o$

¹⁷Note that adiabatic cooling resulting from wind expansion is presently neglected in our models (work under way).

(except those which are directly connected to the ground or meta-stable level), and any brute force approximation would give incorrect heating/cooling rates.

To overcome this dilemma we incorporated a detailed solution of the statistical equilibrium at least for those elements with large contributions to the net heating rates (positive or negative). After some experiments it turned out that the inclusion of the most abundant background elements C, N, O, Ne, Mg, Si, S, Ar, Fe, Ni (plus the explicit elements, of course) is sufficient to stabilize the results. For these elements then, the complete rate-equations are solved with line transitions treated in Sobolev approximation, whereas for the remaining ones the approximate NLTE solution is employed.

The second point to be mentioned regards the flux-conservation of the final models. The conventional approach to calculate the energy balance, formulated in terms of radiative equilibrium, satisfies this constraint by construction, at least in principle. (Most numerical codes, including CMFGEN and FASTWIND, calculate mean intensity and flux on different grids, which somewhat destroys the coupling between radiative equilibrium and flux conservation). On the other hand, our formulation in terms of the electron thermal balance is decoupled from the latter requirement, at least regarding any *explicit* dependence. Note, however, that there is an implicit coupling via the rate equations, assuring that the constraints of electron thermal balance and radiative equilibrium are physically equivalent (cf. Hillier & Miller 1998 and Hillier 2003, where further discussion concerning both methods and their correspondance is given). Insofar, we can use the achieved flux-conservation as an almost independent tool to check whether our models have been constructed in a consistent way. In most of the cases considered so far we have found a perfect conservation, but in the worst cases (below 5% of all models) a violation up to 1.5% is possible.

The third point to be discussed is mainly relevant for our specific approach of modeling stellar atmospheres. Presently, and in accordance with the majority of similar codes, we do *not* update the photospheric density stratification once it has been calculated. Since the photospheric structure equations are solved for the gas-pressure P and the density is calculated from the ratio P/T , the density is only as good as the initial “guess” for the temperature stratification. Moreover, an implicit dependence of the final temperature distribution on this initial guess is created.

Thus, it is still important to obtain a fair approximation for the latter quantity, which in our models is accomplished via the corresponding NLTE Hopf-parameters (see Paper I) which have to account for line-blanketing effects. Meanwhile, we have accumulated a large set of these parameters from our model-grid calculations (and, for cooler temperatures, from corresponding Kurucz-models). If, on the other hand, the initial (photospheric) temperature stratification were not appropriate, both occupation numbers and line profiles would be affected from the erroneous density (although the flux would be conserved, see above).

In Fig. 2.12 we show some of our results in comparison with results calculated by means of WM-Basic, a code which also uses the electron thermal balance. Obviously, the differences are tiny and visible only for the temperature bumps of supergiants, which are predicted to be more prominent by WM-Basic. Note, however, that our solution is more consistent with the results from CMFGEN (see Fig. 2.14), which will be presented in the next section.

Comparing the computation time of models with and without consistent temperature structure, we find a typical difference of a factor of two. Interestingly, the number of iterations becomes only moderately larger (because of the fast convergence of the temperature when using the electron thermal balance, see Kubát et al. 1999), and most of the additional time is spent for solving the NLTE equations for the important back-ground elements.

We finish this section with an interesting finding and warning. After having calculated a large

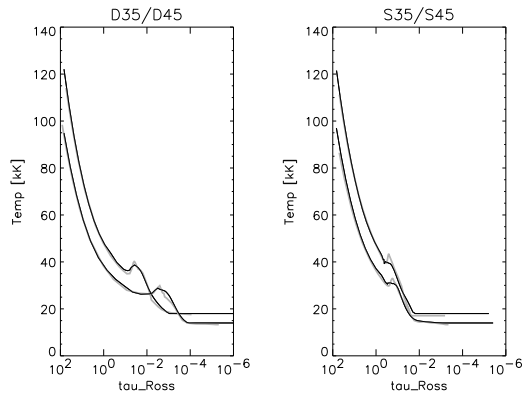


Figure 2.12: FASTWIND (bold) vs. WM-Basic (grey): comparison of temperature stratification for some of the models described in Sect. 2.5.3.

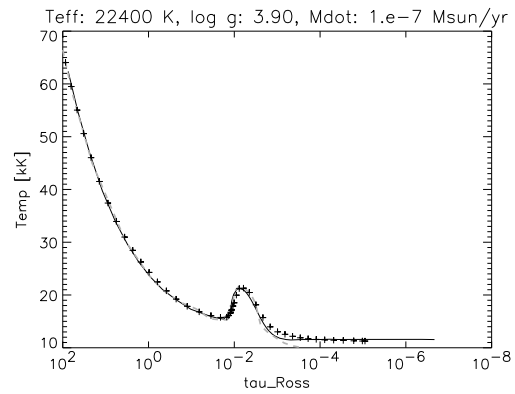


Figure 2.13: Extreme temperature-bump around 22,000 K: FASTWIND (bold) vs. WM-Basic (grey, dashed) and CMFGEN (crosses). See text.

number of models with our code, in certain domains of T_{eff} we have found temperature bumps of *extreme* extent. In contrast to “normal” bumps (arising from line-heating in the outer photosphere) which are of the order of 2,000 K or less for O-stars (Fig. 2.12), corresponding values at lower effective temperatures might reach 5,000 K, as shown for an exemplary dwarf-model at $T_{\text{eff}} = 22,400$ K in Fig. 2.13.

We like to stress the fact that this behaviour has been confirmed by calculations performed by means of WM-Basic and CMFGEN, kindly provided by T. Hoffmann and F. Najarro on our request. This finding (identical results for an unexpected and somewhat strange effect) allows for two conclusions. First, the effect is “real”, at least in terms of the applied physics (see below), and second, the results from different codes using different techniques are strongly converging, which is very promising and allows for an increasing trustworthiness of the results themselves.

After some investigations, it turned out that the feature under discussion originates from bound-bound heating by CIII¹⁸ (which is a major ion at these temperatures), contributed by few transitions connected to the ground-state (singlet), to the meta-stable level (lowermost triplet state) and the transition between ground and meta-stable level at roughly 1909 Å. Note that the latter transition has been identified to be of significant importance for the energy-balance in the wind of P Cyg, in that case as a cooling agent (cf. Drew 1985, Fig. 3). In our case, however, the CIII ground-state is strongly underpopulated in the transonic region (because of the same effect under-populating the He II ground-state in hot stars, cf. Gabler et al. 1989), so that the bracket in Eq. 2.92 becomes very large and the heating-rate enormous, also because of the large collisional strengths of these transitions. If, on the other hand, the contributions by CIII are neglected at all, a temperature bump of only moderate size is created.

The lesson we learn from this exercise is two-fold. First, only a couple of lines (from one ion) can lead to a considerable heating in stellar atmospheres, at least theoretically. Since this heating takes place in the outer photosphere it will have a significant effect on the spectra, and we can check this prediction observationally. However, we have also to consider that the degree of heating (i.e., the extent of the temperature bump) depends strongly on the corresponding collision strengths of the

¹⁸at this specific temperature, bumps at other temperatures originate from different ions, e.g., helium.

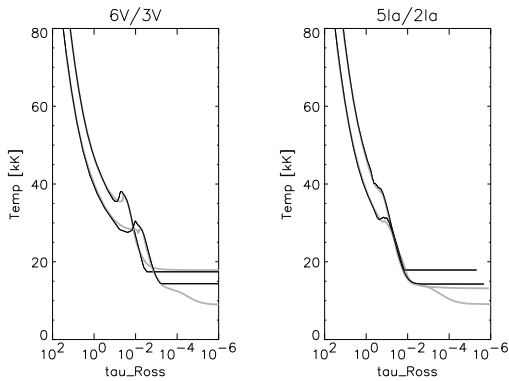


Figure 2.14: As Fig. 2.12, but for FASTWIND (bold) vs. CMFGEN (grey, dashed). The stellar parameters are similar to the models displayed in Fig. 2.12, with $T_{\text{eff}}(6V) = 35861$ K, $T_{\text{eff}}(3V) = 43511$ K, $T_{\text{eff}}(5Ia) = 35673$ K and $T_{\text{eff}}(2Ia) = 44642$ K. CMFGEN results from the model grid as calculated by Lenorzer et al. (2004).

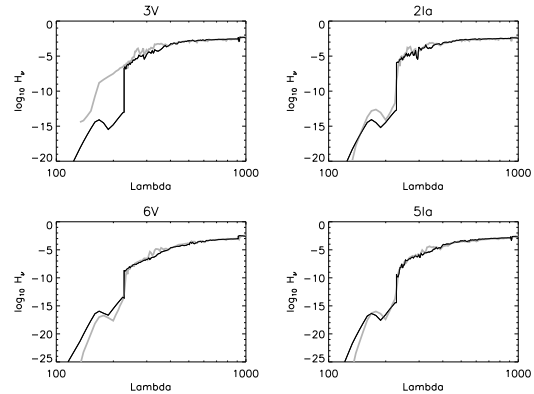


Figure 2.15: As Fig. 2.8, but for FASTWIND vs. CMFGEN (grey). Effective temperatures as in Fig. 2.14. Only the EUV part is plotted, at larger wavelength the results are extremely similar.

responsible transitions (as a function of temperature), and before relying on our results we have to carefully check for possible uncertainties.¹⁹

2.8 Comparison with CMFGEN

In this section, we will compare the results from our models with corresponding results from CMFGEN, with particular emphasis on the optical H/He profiles which cannot be compared to results from WM-Basic, due to lack of comoving frame transport and adequate line-broadening. For this purpose, we have used the CMFGEN-simulations by Lenorzer et al. (2004), who have provided a grid of dwarf, giant and supergiant models (no clumping) in the O-/early B-star range. The corresponding FASTWIND models have been calculated with identical parameters, and the explicit elements (H/He) have been treated with comoving frame transport. Thus, the only “physical” difference in both calculations concerns the photospheric density stratification, which is approximated by a constant scale-height in CMFGEN, but described consistently by FASTWIND (cf. Sect. 2.5).

The corresponding temperature profiles are displayed in Fig. 2.14, for two dwarf and two supergiant models with parameters similar to our comparison with WM-Basic. Remember that the temperature structure is derived from radiative equilibrium in CMFGEN, whereas FASTWIND uses the thermal balance of electrons in the outer atmosphere. Overall, the differences are small, and the extent of the temperature bumps are comparable. The only disagreement is found in the outer wind, where FASTWIND uses an artificial cut-off ($T_{\text{min}} = 0.4 T_{\text{eff}}$) in order to prevent numerical problems at lower effective temperatures. We have convinced ourselves that this cut-off has no further consequences for the models as described here, which neglect adiabatic cooling in the outer wind anyway.

Fig. 2.15 compares the corresponding EUV-fluxes, in analogy to Fig. 2.8. As already discussed

¹⁹Note that even some of the hydrogen collision strengths have been revised recently, cf. Przybilla & Butler (2004).

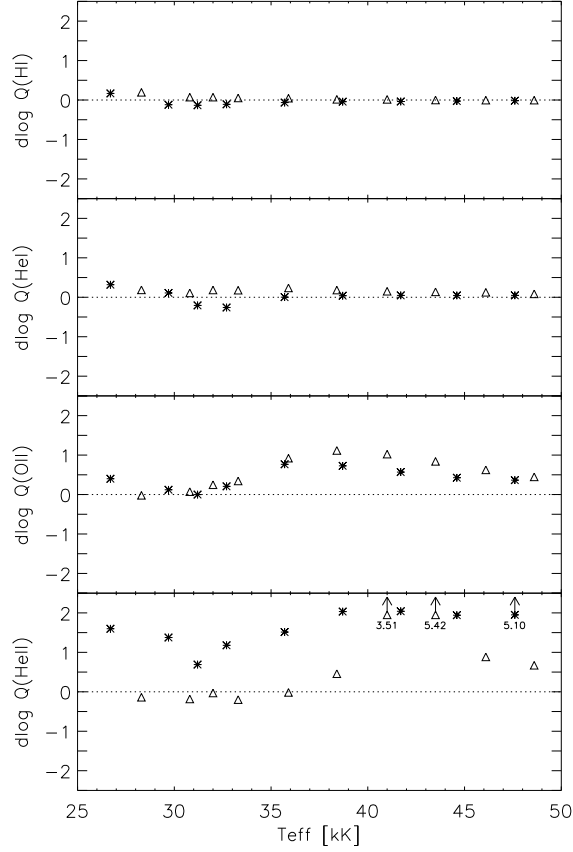


Figure 2.16: As Fig. 2.9, right panel, but for CMFGEN vs. FASTWIND (positive values result from Zanstra-integrals being larger in CMFGEN). Triangles: dwarfs; asterisks: supergiants. Note that the x-axis extends only until $T_{\text{eff}} = 50,000$ K. The three objects denoted by arrows in the lowermost panel (He II) correspond to the dwarf models ‘3V’ and ‘4V’ and the supergiant model ‘1Ia’, respectively. The resulting differences for $\Delta \log Q_{\text{HeII}}$ are given beneath the arrows.

in Sect. 2.5.3, the largest differences occur in the He II-continua. This effect can be seen even clearer in Fig. 2.16, lowermost panel. Regarding the supergiants, the deviation is contrary to our comparison with WM-Basic: The WM-Basic He II-fluxes were mostly lower than those from FASTWIND, whereas the CMFGEN-fluxes are larger, particularly at the edges, so that the corresponding Zanstra integrals become larger as well. Thus, the FASTWIND results for Q_{HeII} lie roughly in the middle of the results from CMFGEN and WM-Basic, at least for the supergiants. Again, we like to point out the extreme sensitivity of the model predictions in this frequential range and warn the reader about any uncritical use of corresponding results, e.g., with respect to nebula modeling.

Regarding the dwarf models, both codes give more or less identical results for the He II-continua for $T_{\text{eff}} < 36,000$ K, whereas at hotter temperatures extreme differences are found for the two models at $T_{\text{eff}} = 41,000$ K and $43,500$ K, respectively. In contrast to both our predictions and those from

WM-Basic the CMFGEN-models do not show any He II-edge at all, cf. Fig. 2.15, model “3V”.

Concerning the OII-continua (actually, for the complete range within $300 \text{ \AA} < \lambda < 400 \text{ \AA}$), the hotter models ($T_{\text{eff}} > 35,000 \text{ K}$) show a higher flux-level in CMFGEN, for both the supergiants and the dwarfs. We have already commented on this problem in Sect. 2.5.3 and speculated that this behaviour is related to missing line-opacity. (OII itself plays no role at these temperatures). Of course, we cannot exclude a problem in our approximate treatment of line-blocking. Finally, and in accordance with the comparison with WM-Basic, the agreement of the H I - and He I-continua is almost perfect.

Figs. 2.17 and 2.19 are now the most interesting plots in this section, displaying the strategic H/He lines in the optical (CMFGEN-profiles in grey). Regarding the dwarfs, the agreement of almost all lines is excellent. The only differences are found for the line cores of He II4686, which are shallower in CMFGEN at almost all temperatures, and for the He I singlets for models ‘4V’ to ‘6V’ with T_{eff} lying in the range between 41,000 K and 36,000 K, respectively. (Note that for model ‘4V’ He I4387 agrees well whereas He I4922 and He I6678 differ). Most prominent are the differences for models ‘5V’ and ‘6V’ (the same is true for the giant models not displayed here), where all singlet lines predicted by CMFGEN are almost a factor of two smaller in equivalent width than those predicted by FASTWIND. Most interestingly, however, the triplet lines agree perfectly throughout the grid.

So far, the origin of this discrepancy could not be identified; particularly, the atomic data used (incl. broadening functions) are very similar, and also the ionizing continua (important for the singlet-formation) agree very well, as shown above. One might speculate that there is a connection to the flux differences around the He II resonance line at 304 \AA or to possible discrepancies at the He I resonance line(s), but this has to be checked carefully (investigations under way). Further comments on this discrepancy will be given after we have discussed the results for the supergiants.

The corresponding profiles are displayed in Fig. 2.19, upper panel. There, the situation is somewhat different from the dwarf case. At first, we note that the deviations of the He I singlets are not as extreme as before. Significant disagreement is found only for He I4922 and 6678 (no problem for He I4387) in model “5Ia” (36,000 K), where these singlets are weak anyway. For model “6Ia” the differences are moderate, much less than the factor of two in equivalent width encountered above. Noticeable differences are found for other lines though. At first, the hydrogen Balmer line wings predicted by CMFGEN are much stronger, which would lead to lower gravities if an analysis of observed spectra were performed. Second, both H_{α} and He II4686 show stronger wind emission which would lead to lower mass-loss rates compared to FASTWIND. Note however that the wind emission in both lines is a strongly increasing function of mass-loss (e.g., Puls et al. 1996), and an analysis of observed spectra would result in \dot{M} -difference not exceeding the 20 to 30% level.

The difference in the Balmer line wings points to a problem mentioned above, namely the assumption of a constant photospheric scale height in CMFGEN. In order to obtain an impression in how far this approximation (as well as the somewhat artificial transition from photosphere to wind) has an influence on the resulting models and profiles, Lenorzer et al. (2004) have calculated an additional set of “low-gravity” supergiants, where the gravity has been lowered by typically 0.1 to 0.2 dex (model series “_lg”) with respect to their “standard” grid of supergiants. Due to this manipulation, at least part of the effect of photospheric radiation pressure g_{rad} is accounted for (although this quantity is *not* constant throughout the photosphere), since the profiles provide a measure of the *effective* gravity (i.e., $g_{\text{grav}} - g_{\text{rad}}$) alone.

In Fig. 2.19, lower panel, we compare the FASTWIND profiles (identical to those from the upper panel, since our “high gravity” models *do* include the photospheric g_{rad}) with these low-gravity models calculated by CMFGEN. Consequently, the photospheric densities should be much more similar

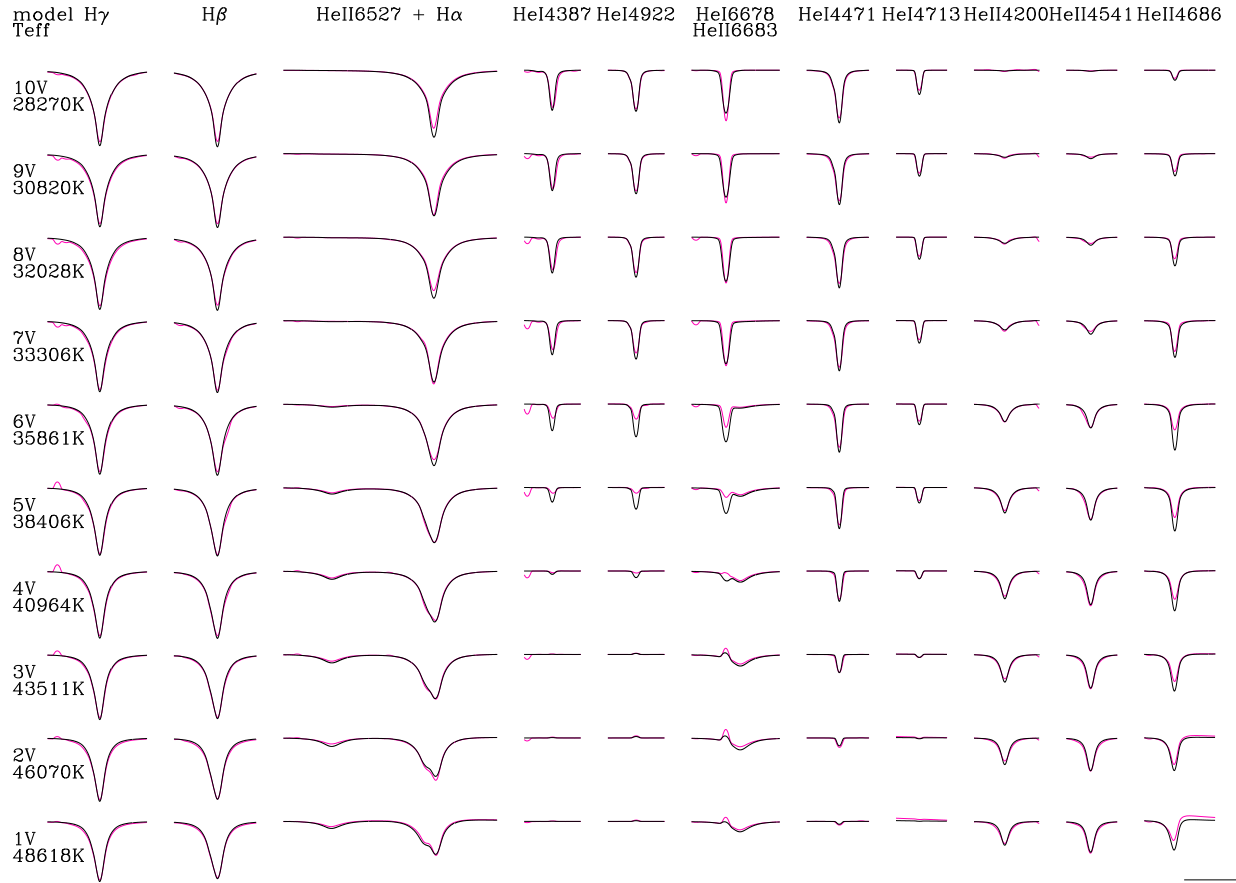


Figure 2.17: FASTWIND (black) vs. CMFGEN (grey): Comparison of strategic H/He lines in the optical for the dwarf-models from the grid by Lenorzer et al. (2004). For both models, the lines have been degraded to a resolution of 10,000 and rotationally broadened with $v \sin i = 80 \text{ km s}^{-1}$. He I $\lambda\lambda$ 4387, 4922 and 6678 are singlet lines, and He I $\lambda\lambda$ 4471 and 4713 are triplets. The horizontal and vertical lines in the bottom right corner indicate the scale used and correspond to 20 \AA in wavelength and 0.5 in units of the continuum, respectively (extending from 0.65 to 1.15).



Figure 2.18: Wind-strength parameter Q as an optical depth invariant: H/He profiles for the model of α Cam as determined by Repolust et al. (2004), with $\dot{M} = 6.04 \cdot 10^{-6} M_{\odot}/\text{yr}$ and $R_{\star} = 32.5 M_{\odot}$. Overplotted in grey are the corresponding profiles for a model with identical Q -parameter (Eq. 6.1) but different mass-loss rate and radius ($\dot{M} = 3.3 \cdot 10^{-6} M_{\odot}/\text{yr}$ and $R_{\star} = 21.7 M_{\odot}$).

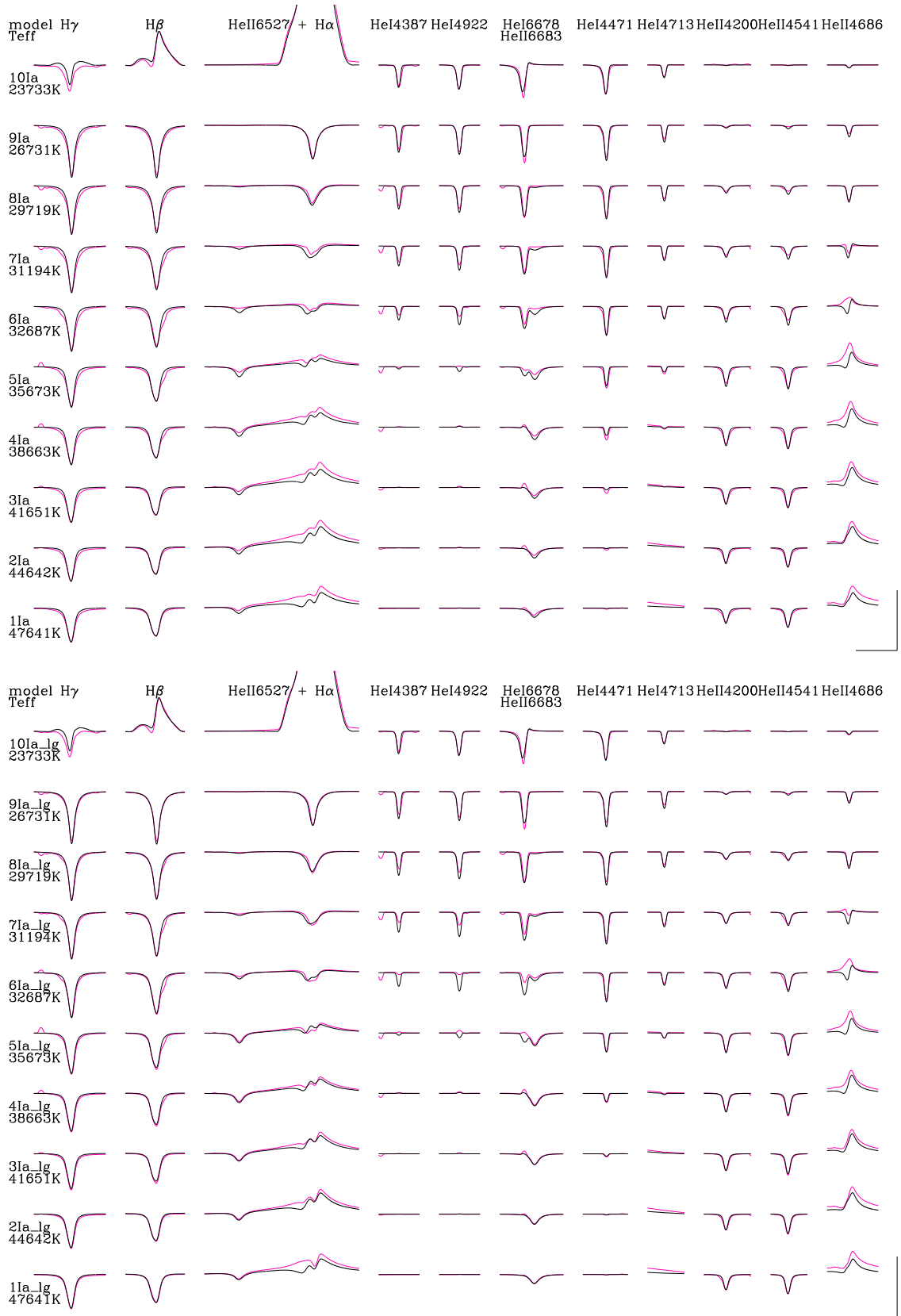


Figure 2.19: As Fig. 2.17, however for the supergiants from the grid by Lenorzer et al. (2004). Upper panel: CMFGEN models with “standard” gravities. Note that the differences in the wings of the Balmer lines and in the H α -emission almost vanish if our results are compared to the “low gravity” CMFGEN models in the lower panel (see text).

than in the previous case, at least in those regions where the Balmer line wings are formed. Indeed, the differences in H_γ and H_β have now vanished, and also the H_α emission is very similar, except for the hottest models on the blue side of the profile. In some cases, the discrepancy for He II 4686 has become weaker as well. The He I triplets have not changed (they seem to be almost independent on the photospheric density in CMFGEN), whereas a strong influence on the He I singlets is found. In the “critical” temperature region, they have become significantly weaker, and a strong discrepancy also for the low-gravity model ‘6Ia_lg’ is present again, by the same degree as we have found for the dwarfs.

In summary, we find a very good agreement with the optical spectra from CMFGEN if the problem of different density stratifications is accounted for. The only disturbing fact is the strong difference in the He I singlets for dwarfs between 36,000 to 41,000 K and for supergiants between 31000 to 35,000 K.

Although it is presently not clear which profiles are “correct” or whether the truth lies in the “middle”, we like to point out the following. In our analyses of Galactic O-stars (Repolust et al. 2004), no problems were found to match both the observed singlet and triplet lines in dwarfs. Concerning the supergiants, we actually met a problem for almost *all* stars cooler than O6, namely the well-known “generalized dilution effect” (see the discussion and references in Repolust et al. 2004). Briefly, we could fit all He I lines (singlets and triplets) in parallel with the He II lines, except for He I 4471 (triplet) which was predicted to be too weak. One might argue that this is a symptom of generally incorrect He I lines, and speculate that this problem is related to the inconsistency seen here. Assuming that the He I-singlets produced by FASTWIND are erroneous it might then be possible to fit all He I singlets and the λ 4471 triplet at cooler temperatures. In this case, however, we (and CMFGEN!) would meet the problem that the other triplet lines would be too strong and the He II lines too weak!

Presently, there is no other way out of this dilemma than to perform a number of detailed comparisons, with respect to both the models and the observations. Since the actual problem concerns the *ratio* of triplet to singlet lines and the problem is most pronounced for dwarfs, it should be possible to find a solution by comparing the theoretical predictions for this ratio (in terms of equivalent widths) as a function of T_{eff} vs. the observed ratio as a function of spectral type for a large sample of stars. Such work is in progress now.

2.9 Model grids

As already outlined in Sect. 2.1, the parameter space to be investigated for the analysis of one object alone is large and almost prohibitive for the *detailed* analysis of very large samples of stars which have recently been collected (e.g., by means of the multi-object spectrograph FLAMES). Alternatively, a somewhat coarser analysis by means of the “traditional” model-grid method is still applicable if an appropriate grid can be constructed. In this section, we will give some suggestions for this objective and report on first progress.

Although the presence of a wind introduces a large number of additional parameters to be considered in a fine fit (\dot{M} , v_∞ , β and R_\star), there is a fortunate circumstance which allows for the construction of such model-grids with only *one* more parameter compared to grids from hydrostatic, plane-parallel models, at least if we do not aim at the analysis of specific (UV) resonance lines.

As has been shown by, e.g., Puls et al. (1996, see also Schmutz et al. 1989; de Koter et al. 1998 for diversifications), the wind-emission from recombination dominated transitions (so-called ρ^2 -lines)

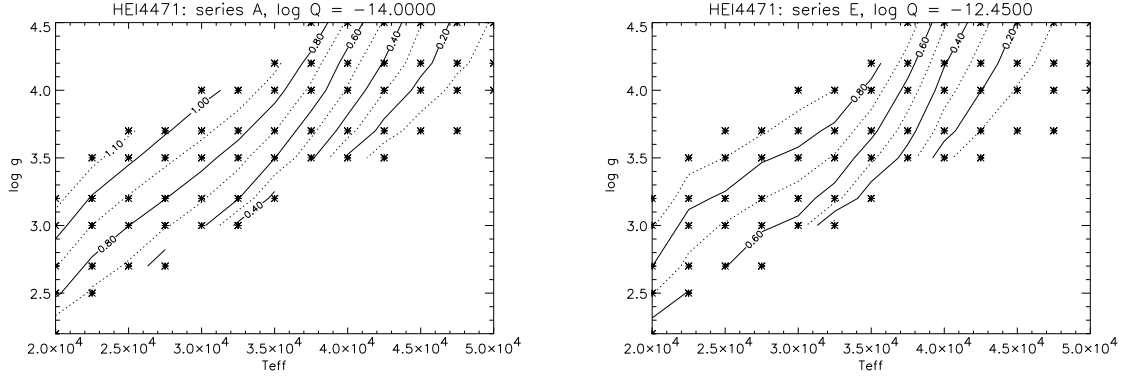


Figure 2.20: Iso-contours of equivalent widths for He I4471, as predicted by FASTWIND, using results from our model-grid with Helium abundance $Y_{\text{He}} = 0.1$ and solar metallicity for background elements. Left: negligible wind. Right: typical O-supergiant wind. Note the effect of wind-emission, shifting the iso-contours to the left. The locations of the corresponding models are indicated by asterisks.

remains rather unaffected from the specific choice of the individual values of \dot{M} , v_{∞} and R_{\star} as long as the wind-strength parameter Q (also denoted as the “optical depth invariant”),

$$Q = \frac{\dot{M}}{(v_{\infty} R_{\star})^{\frac{3}{2}}}, \quad (2.93)$$

does not vary. In this case then, most of the other lines also preserve their shape. An example is given in Fig. 2.18, where we have varied the mass-loss rate of a model of α Cam (cf. Repolust et al. 2004) by a factor of two (and accordingly the radius by $2^{1.5}$) without almost any effect on the resulting H/He spectrum.

This behaviour (i.e., spectrum and emergent fluxes depend almost exclusively on Q and not on its individual constituents) follows from the fact that

- ρ^2 -dependent line processes (e.g., recombination lines and resonance lines from ions one stage below the major one²⁰) scale with Q in the wind regime,
- the wind density scales with $\dot{M}/(v_{\infty} R_{\star}^2)$ (continuity equation), and
- (resonance) lines from major ions scale with $\dot{M}/(v_{\infty}^2 R_{\star})$, e.g. Hamann (1981).

Thus, the common power of “1.5” with respect to v_{∞} and R_{\star} used in Q , which refers to the scaling of ρ^2 lines, is also the best compromise to deal with the other physical parameters affecting a stellar model (most importantly, the line-blocking which depends both on density and line opacity).

Exploiting this knowledge, we have constructed a set of nine model-grids for the analysis of H/He profiles with three different helium abundances, $Y_{\text{He}} = 0.1, 0.15$ and 0.2 , and three different background metallicities, $z = 1.0, 0.5$ and 0.2 (cf. Sect. 6.3.1), respectively. Each grid with given helium abundance and metallicity is three-dimensional with respect to the parameters T_{eff} , $\log g$ and $\log Q$, and the grid-spacing is roughly equidistant. The individual values for parameters incorporated into $\log Q$ (which are actually needed to calculate a specific model) and additional ones have been assumed according to present knowledge:

²⁰e.g., SiIV in most hot stars

- R_\star from “empirical” values, as a function of spectral type (T_{eff}) and luminosity class ($\log g$).
- v_∞ as a function of photospheric escape velocity v_{esc} ,

$$v_\infty = C(T_{\text{eff}}) \cdot v_{\text{esc}}, \quad (2.94)$$

in accordance with the results collected by Kudritzki & Puls (2000).

- Velocity exponent β from empirical values (see also Kudritzki & Puls 2000 and references therein), with $\beta = 0.9$ (as a compromise) for O-stars and increasing values towards later types.
- \dot{M} from $\log Q$, R_\star and v_∞ as specified above.
- micro-turbulence $v_{\text{turb}} = 15 \text{ km s}^{-1}$ throughout the grid as a compromise between O and B stars.

Our present grids comprise the range $20,000 \text{ K} \leq T_{\text{eff}} \leq 50,000 \text{ K}$ with $\Delta T_{\text{eff}} = 2,500 \text{ K}$, $\log g$ between $2.2 \leq \log g \leq 3.2$ at $T_{\text{eff}} = 20,000 \text{ K}$ and $4.0 \leq \log g \leq 4.5$ at $T_{\text{eff}} = 50,000 \text{ K}$.

The position of all models can be inferred from Fig. 2.20. With respect to $\log Q$ we have used values with $-14.0 \leq \log Q \leq -11.4$ ($\Delta \log Q = 0.35$ in most cases), where the lowest value corresponds to an almost negligible wind and the highest one to almost Wolf-Rayet conditions.

The denotation is such that we specify a letter for the wind density (“A” to “H”, with densities $\log Q = -14.0, -13.5, -13.15, -12.8, -12.45, -12.1, -11.75, -11.4$, respectively, if \dot{M} is calculated in M_\odot/yr , v_∞ in km s^{-1} and R_\star in R_\odot). Effective temperature and gravity are denoted by two ciphers each. Thus, model “E2730” refers to $\log Q = -12.45$, $T_{\text{eff}} = 27,500 \text{ K}$ and $\log g = 3.0$. Typical O-type supergiants correspond to series “E”, and typical B-type supergiants to series “D”.

For all these models we have calculated H/He profiles and equivalent widths in the optical and the IR. Thus, by simply over-plotting observed vs. simulated spectra one finds an immediate guess for the parameters T_{eff} , $\log g$, Y_{He} and wind-strength if the background metallicity is specified and the theoretical profiles have been convolved accounting for rotational broadening and resolution. In this way, the coarse analysis of one star is possible within a couple of minutes and might be fine-tuned by calculating specific models (particularly with respect to β if inferable from the emission line shapes).

In addition, a plot of various iso-contours of calculated equivalent widths gives deeper insight into certain dependencies. As an example, Fig. 2.20 shows the effect of wind emission on He I 4471. Further examples, particularly with respect to the spectral type classification criterium of O-star, $\log W' = \log(\text{ew}_{4471}) - \log(\text{ew}_{4541})$, are given in Massey et al. (2005).

We intend to make these grids publicly available in the near future when the problem regarding the He I singlets has been solved.

2.10 Summary and outlook

In this paper we have described all updates applied to our previous version of FASTWIND (Paper I), regarding the approximative treatment of metal line-blocking/blanketing and the calculation of a consistent temperature structure.

The problem of line-blocking has been tackled in two steps. First, the occupation numbers of back-ground elements are calculated by an approximative solution of the corresponding equations of statistical equilibrium with the option that the most abundant elements are treated almost “exactly”, i.e., by means of the Sobolev transport for line processes. Compared to alternative approaches (cf.

Sect. 2.4) our method allows for the treatment of different spin systems, radially and frequency dependent radiation temperatures and a consistent ALI-iteration scheme. We have tested our solutions by comparing the approximative results with results from exact solutions and have not found any major discrepancies.

The occupation numbers derived in this way are subsequently used to calculate the line-blocked radiation field, again, in an approximative way. To this end, we have formulated suitable means for the opacities (in analogy to Rosseland means but for frequency intervals not larger than $1,000 \dots 1,500 \text{ km s}^{-1}$) and emissivities (two-level-atom approach), and the resulting pseudo-continuum of overlapping lines is treated by means of a conventional continuum radiative transfer. Specific problems inherent in our approach (regarding a rigorous statistical description) have been pointed out and might lead to inaccurate solutions in a few cases. Investigations to improve our approach are presently under way in our group, as discussed in Sect. 2.5.

Our new version of FASTWIND allows for the calculation of a consistent temperature structure by applying a flux-correction method in the lower atmosphere and the electron thermal balance in the outer one. Regarding optical H/He lines, no major differences have been found compared to our previous NLTE Hopf-function method (cf. Paper I and Repolust et al. 2004).

Due to the approximations applied and as intended, the performance of our code is very fast. The total computational time (starting all models from scratch) is of the order of 30 minutes on a PC with a 2 GHz processor if only H and He lines are considered as explicit ions, whereas the inclusion of other elements (e.g., Urbaneja 2004) into the “explicit” treatment requires additional 5 to 10 minutes each.

The new methods have been extensively tested by comparing with results from WM-Basic and CMFGEN, concerning temperature stratification, fluxes, number of ionizing photons and optical²¹ H/He profiles (comparison with CMFGEN only).

We have highlighted the importance of photospheric line-pressure, which is incorporated into the FASTWIND models and neglected in the standard version of CMFGEN, if not coupled to the plane-parallel code TLUSTY (see Sect. 2.1). Particularly, we have found indications that the use of the Sobolev approximation (within the force-multiplier concept) in WM-Basic can lead to an underestimate of this quantity, as already predicted by Pauldrach et al. (1986). On the other hand, the density/velocity stratification resulting from our approach (smoothly connecting the quasi-static photosphere and a β -law wind) agrees surprisingly well with the hydrodynamic structure as calculated from a consistent solution if β is not too different from the “canonical” value of $0.8 \dots 1.0$.

All three codes predict almost identical temperature structures and fluxes for $\lambda > 400 \text{ \AA}$, whereas at lower wavelengths certain discrepancies are found. Compared to WM-Basic (using an identical line list for the background elements), our *supergiant* models differ only in the He II continua, where the FASTWIND-fluxes are somewhat larger, but still lower than the corresponding fluxes from CMFGEN. Since fluxes and corresponding numbers of ionizing photons react extremely sensitive to subtle model differences in this wavelength regime, we consider any uncritical use of these quantities as being dangerous.

Major discrepancies are also found in the range $300 \text{ \AA} < \lambda < 400 \text{ \AA}$, i.e., in the OII continuum and at the He II304 resonance line. Compared to both WM-Basic and CMFGEN, our *dwarf* models produce less flux in this region (more blocking or less re-emission), whereas the *supergiant* models of FASTWIND and WM-Basic agree very well. The supergiant models of CMFGEN, on the other hand,

²¹IR-lines will be presented in a forthcoming paper (Repolust et al., in prep. for A&A), with a similar agreement between FASTWIND and CMFGEN as for the optical ones.

show much less blocking which might point to some missing opacity. Again, we like to stress that the H I and He I continua agree very well in all three codes.

For the optical H/He lines, the coincidence between FASTWIND and CMFGEN is remarkable, except for the He I singlets in the temperature range between 36,000 to 41,000 K for dwarfs and between 31,000 to 35,000 K for supergiants, where CMFGEN predicts much weaker singlets. Up to now, the origin of this discrepancy could not be identified, but work is under way to solve this problem.

Although it is reassuring that the different codes agree well with respect to most of their predictions, this is only part of the story. One particularly disturbing fact concerns the present mismatch between the parameters obtained from an analysis in the optical and the UV, respectively. In the majority of cases, the UV gives lower effective temperatures, i.e., of the order of 2,000 to 4,000 K, if one compares the analyses of Galactic stars performed by Bianchi & Garcia (2002) and Garcia & Bianchi (2004) with results from Repolust et al. (2004) (WM-Basic vs. FASTWIND) and the corresponding work for Magellanic Cloud stars by Hillier et al. (2003) and Bouret et al. (2003) (partly including also the optical range) with the results from Massey et al. (2004, 2005) (CMFGEN vs. FASTWIND). (Interestingly, the work by Crowther et al. 2002 (CMFGEN) indicates higher temperatures for MC supergiants than derived by Massey et al. 2005.)

Part of this discrepancy (if combined UV/optical analyses are compared) might be related to the He I singlet vs. triplet problem as discussed above. Note, however, that this would account only for discrepancies in certain domains of the T_{eff} space and would typically result in maximum differences of the order of 2,000 K, as has been found from a number of test calculations performed by one of us (J.P.) and F. Najarro (using CMFGEN), which will be reported on in a forthcoming publication. Moreover, the temperature scale for O-type dwarfs as derived by Martins et al. (2002) using CMFGEN and concentrating on the classification criterium He I 4471 (triplet) vs. He II 4541 is actually 1,000 to 2,000 K *hotter* than the calibration by Repolust et al. (2004).

In a recent paper, Martins et al. (2004) have discussed the uncertainties in T_{eff} which is obtained by relying on different diagnostic tools in the UV, analyzing four SMC-N81 dwarfs of spectral types O6.5 to O8.5. From the specific values derived from the UV-color index, the ionization balance of O IV/V and Fe IV/V and the N V 1238/1242 and C III 1426/1428 doublets, respectively, they quote a typical uncertainty of $\pm 3,000$ K in T_{eff} , which might easily account for part of the discrepancies with the optical.

Unfortunately, it is rather difficult to compare the differences obtained so far in a strict one-to-one case, simply because the corresponding samples hardly overlap. In particular, a large fraction of the objects which have been analyzed by means of CMFGEN are somewhat extreme, comprising either supergiants with (very) dense winds (Crowther et al. 2002) or dwarfs with very thin winds (Martins et al. 2004). The analysis of SMC stars by Bouret et al. (2003), on the other hand, covers only a sample of 6 dwarfs, in contrast to the larger sample by Massey et al. (2004, 2005), and, therefore, it is not clear in how far selection effects do play a role. Finally, it is interesting to note that at least for one object in common, the O4 I(f) star ζ Pup (HD 66811), the different analyses give almost identical results (Crowther et al. 2002, Repolust et al. 2004 and Pauldrach et al., in prep. for A&A, analyzing the UV by means of WM-Basic).

Thus, we conclude that the present status of hot star parameters is not as clear as we would like it to be. Actually, we need to understand a number of additional physical processes and their influence on the derived parameters. Most important are the direct and indirect effects of the line-driven wind instability, i.e., the formation and interaction of clumps and shocks leading to X-ray emission and enhanced EUV-flux in the wind (e.g., Feldmeier et al. 1997; Pauldrach et al. 2001).

Although incorporated to some extent into present codes, there are simply too many questions to be answered before we can consider these problems as solved. To give only two examples: We do not know the spatial distribution of the “clumping factor”, and also the X-ray emission is only on the verge of being understood (e.g., Kramer et al. 2003; Oskinova et al. 2004).

Before these effects can be treated in a realistic way, we suggest to primarily rely on diagnostic tools which are least “contaminated”, i.e., to concentrate on weak lines formed in the stellar photospheres (except, of course, the mass-loss indicators which will always be affected by clumping). Future investigations of O-type stars performed by FASTWIND will have to utilize not only H and He but also metal lines, as already incorporated into the analysis of B-stars (cf. Sect 2.1). Particularly, one of the most important tools will be nitrogen with its strong sensitivity even at higher temperatures where He I begins to fail. Work in this direction is under way.

Acknowledgements:

We like to thank a number of colleagues for their enduring willingness to discuss problems and provide assistance. The most important colleague in this respect was and is Dr. Keith Butler, the living compendium in atomic physics, since without his support it would have been extremely difficult to finish this project. Particular thanks to Dr. Adi Pauldrach for providing his atomic data base (tailored for WM-Basic). Many thanks also to Drs. Paco Najarro and Tadziu Hoffmann for performing a number of test calculations with CMFGEN and WM-Basic, respectively, and their stimulating discussions concerning NLTE-effects. Finally, we would like to thank Drs. Phil Massey and Alex de Koter for valuable comments on the manuscript.

M.A.U. acknowledges financial support for this work by the Spanish MCyT under project PNAYA2001-0436, R.V. acknowledges support from the University of La Plata by a FOMEC grant (Pr. 724/98), and T.R. gratefully acknowledges financial support in form of a grant by the International Max-Planck Research School on Astrophysics (IMPRS), Garching.

Bibliography

- Abbott, D.C. 1982, ApJ 259, 282
- Abbott, D.C., Lucy, L.B. 1985, ApJ 288, 679
- Aufdenberg, J. P., Hauschildt, P. H., Baron, E., et al. 2002, ApJ 570, 344
- Baschek, B., v. Waldenfels, W., Wehrse, R. 2001, A&A 371, 1084
- Bianchi, L., Garcia, M. 2002, ApJ 581, 610
- Bouret, J.-C., Lanz, T., Hillier, D. J., et al. 2003, ApJ 595, 1182
- Butler K., Giddings J.R., 1985, Coll. Comp. Project No. 7 (CCP7), Newsletter 9, London, p. 7
- Castor, J., Abbott, D.C., Klein, R.I. 1975, ApJ 195, 157
- Crowther, P.A., Hillier, D.J., Evans, C.J., et. al. 2002, ApJ 579, 774
- de Koter, A., Schmutz, W., Lamers, H.J.G.L.M. 1993, A&A 277, 561
- de Koter, A., Heap, S.R., Hubeny, I. 1998, ApJ 509, 879
- Drew, J. 1985, MNRAS 217, 867
- Drew, J. 1985, ApJS 71, 267
- Feldmeier, A., Puls, J., Pauldrach, A.W.A. 1997, A&A 322, 878
- Fullerton, A.W., Crowther, P.A., De Marco, O., et al. 2000, ApJ 538 L43
- Gabler, R., Gabler, A., Kudritzki, R.P., Puls, J., et. al. 1989, A&A 226, 162
- Garcia, M., Bianchi, L. 2004, ApJ 606, 497
- Gräfener, G., Koesterke, L., Hamann, W.-R. 2002, A&A 387, 244
- Grevesse, N., Sauval, A.J. 1998, SSR 85, 161
- Hamann, W.-R. 1981, A&A 100, 169
- Hauschildt, P.H., Baron, E. 1999, J. Comp. Appl. Math. 109, 41
- Herrero, A., Puls, J., Najarro, F. 2002, A&A 396, 949

- Hillier, D.J. 2003, ASPC 288, 199
- Hillier, D.J., Miller, D.L. 1998, ApJ 496, 407
- Hillier, D.J., Lanz, T., Heap, S.R., et al. 2003, ApJ 588, 1039
- Hubeny, I. 1992, in “The Atmospheres of Early-Type Stars”, eds. U. Heber & C.S. Jeffery, Springer, Berlin, p. 377
- Hubeny, I., Lanz, T. 1995, ApJ 39, 875
- Hummer, D.G., Rybicky, G.B. 1985, ApJ 293, 258
- Jokuthy, A. 2002, “Infrared spectrum analysis of hot stars”, Diploma thesis, University Munich
- Kramer, R.H., Cohen, D.H., Owocki, S.P. 2003, ApJ 592, 532
- Kubát, J., Puls, J., Pauldrach, A.W.A. 1999, A&A 341, 587
- Kudritzki, R.P., Puls, J. 2000, ARA&A 38, 613
- Lenorzer, A., Mokiem, M.R., de Koter, A., Puls, J. 2004, A&A 422, 275
- Lucy, L.B. 1999, A&A 345, 211
- Lucy, L.B., Abbott, D.C. 1993, ApJ 405, 738
- Martins, F., Schaerer, D., Hillier, D.J. 2002, A&A 382, 999
- Martins, F., Schaerer, D., Hillier, D.J., et al. 2004, A&A 420, 1087
- Massey, P., Kudritzki, R.P., Bresolin, F., et al. 2004, ApJ 608, 1001
- Massey, P., Puls, J., Pauldrach, A.W.A., et al. 2005, in prep. for ApJ
- Mazzali, P.A., Lucy, L.B. 1993, A&A 279, 447
- Mazzali, P.A. 2000, A&A 363, 705
- Mihalas, D. 1975, “Stellar atmospheres”, 2nd edition, Freeman, San Francisco
- Mihalas, D., Kunasz, P.B., Hummer, D.G. 1975, ApJ 202, 465
- Oskinova, L.M., Feldmeier, A., Hamann, W.-R. 2004, A&A 422, 675
- Pauldrach, A.W.A., Puls, J., Kudritzki, R.P. 1986, A&A 164, 86
- Pauldrach, A.W.A., Lennon, M., Hoffmann, T.L., et al. 1998, in: Boulder-Munich Workshop II, PASP conf. series 131, ed. I. Howarth, p. 258
- Pauldrach, A.W.A., Hoffmann, T.L., Lennon, M. 2001, A&A 375, 161
- Przybilla, N., Butler, K. 2004, ApJ 609, 1181

- Puls, J., Hummer, D.G. 1988, A&A 191, 87
- Puls, J., Kudritzki, R.P., Herrero, A., et al. 1996, A&A 305, 171
- Puls, J., Pauldrach, A.W.A. 1990, in: Proc. Boulder Munich Workshop, ed. C. Garmany, PASPC 7, p. 202
- Puls, J., Springmann, U., Lennon, M. 2000, A&A 141, 23
- Repolust, T., Puls, J., Herrero, A. 2004, A&A 415, 349
- Rybicki, G.B., Hummer, D.G. 1991, A&A 245, 171
- Santolaya-Rey, A.E., Puls, J., Herrero, A. 1997, A&A 323, 488 (Paper I)
- Schaerer, D., Schmutz, W. 1994, A&A 288, 231
- Schaerer, D., de Koter, A. 1997, A&A 322, 598
- Schaerer, D., Meynet, G., Maeder, A., Schaller, G. 1993, A&AS 98, 523
- Schmutz, W., 1991, in: Stellar Atmospheres: Beyond Classical Models, eds. Crivellari, L., Hubeny, I., and Hummer, D.G., NATO ASI Series C Vol.341, Kluwer, Dordrecht, p.191
- Schmutz, W., Hamann, W.-R., Wessolowski, U. 1989, A&A 210, 236
- Seaton, M. 1958, MNRAS 118, 504
- Springmann, U. 1997, “On the theory of radiation driven winds of Wolf-Rayet stars”, thesis, University Munich
- Taresch, G., Kudritzki, R.P., Hurwitz, M., et al. 1999, A&A 321, 531
- Trundle, C., Lennon, D.J., Puls, J., et al. 2004, A&A 417, 217
- Urbaneja, M.A. 2004, “B Supergiants in the Milky Way and nearby galaxies: models and quantitative spectroscopy”, thesis, University of La Laguna
- Urbaneja, M.A., Herrero, A., Bresolin, F., et al. 2003, ApJL 584, 73
- Wehrse, R., von Waldenfels, W., Baschek, B. 1998, JQSRT 60, 963

Chapter 3

Advances in radiatively driven wind models

*J. Puls, T. Repolust, T. L. Hoffmann, A. Jokuthy, R. O. J. Venero
IAU Symp. 212, 61, “A Massive Star Odyssey: From Main Sequence To Supernova” edited
by Karel A. van der Hucht, Artemio Herrero and César Esteban, ASP, 2003.*

Abstract. We report on a re-analysis of the Galactic O-star sample presented by Puls et al. (1996) by means of NLTE-atmospheres including line-blocking/blanketing. In particular, we concentrate on the question concerning the dependence of the wind-momentum luminosity relation (WLR) on luminosity class. Owing to the line-blanketing, the derived effective temperatures become significantly lower when compared to previous results, whereas the so-called “modified wind-momentum rates” remain roughly at their former values. Therefore, we obtain a new WLR for O-stars. By comparing these “observational” results with new theoretical predictions and simulations, we conclude that the H_α forming region for objects with H_α in emission might be considerably clumped and thus a larger mass-loss rate than actually present is mimicked. We suggest that the previously found dependence of the WLR on luminosity class is an artefact.

3.1 Introduction

One of the major results from the analyses of radiation driven hot star winds is the empirical finding that their (modified) wind momentum rate can be expressed as a simple function of stellar luminosity,

$$\log \dot{M} v_{\infty} R_{\star}^{0.5} \approx x \log L + D. \quad (3.1)$$

In terms of theory, the slope of this relation corresponds to the inverse exponent of the so-called line-strength distribution function (modified for ionization effects), i.e., $x = 1/\alpha'$. The vertical offset D is controlled by the effective number of lines driving the wind. Both parameters depend on spectral type and metallicity (for details, see Kudritzki & Puls 2000 and references therein).

Once having been carefully calibrated, the wind momentum luminosity relation (WLR) will allow for an independent determination of extragalactic distances on intermediate scales (up to Virgo/Fornax cluster distances), utilizing spectra of A-type supergiants taken with 10m-class telescopes.

While considerable progress, with respect to such a calibration, has been obtained in recent years, a number of questions became evident which so far prohibit a deeper understanding of some of the empirical findings. As an important example, we like to mention the problem of a much lower wind-momentum rate of mid-type B-supergiants compared to other spectral types (cf. Kudritzki et al. 1999).

In order to clarify these questions and to allow for an updated view of the present status quo, we have begun a re-investigation of already published data, with respect to both the “observed” values and the theoretical predictions, on basis of up-to-date model atmosphere codes including *line-blocking and blanketing*. In the following, we will report on first results from these investigations.

3.2 The WLR for Galactic O-stars: observations and theory

In Fig. 3.1, we display the starting point of all follow-up investigations, namely the WLR for Galactic O-stars, as presented by Puls et al. (1996). Interestingly, no unique relation had been found; instead, a

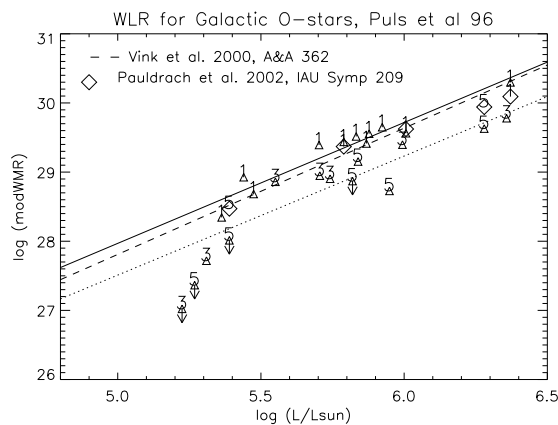


Figure 3.1: WLR for Galactic O-stars (cf. Puls et al. 1996), in comparison with recent theoretical predictions (dashed: Vink et al; diamonds: simulations by Pauldrach et al., for the same stellar parameters as derived by observations). Numbers correspond to luminosity class, arrows indicate upper limits for the modified wind-momentum rate (mWMR), and the lines result from linear regression to l.c. I and III/V objects, respectively.

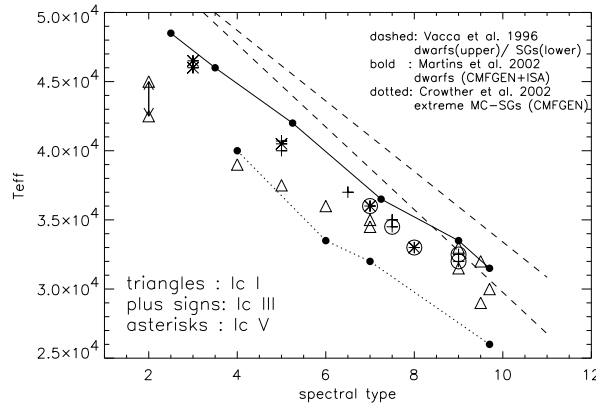


Figure 3.2: T_{eff} vs. spectral type for Galactic O-stars (line-blanketed models, this analysis), compared to similar investigations and results from unblanketed models. The entries at O2 correspond to HD93129A (recently detected binarity status, with $\Delta m \approx 0.5$, E. Nelan & N. Walborn, priv. comm.), displaying upper and lower limits for T_{eff} . Circles enclose extremely fast rotators with $V_r \sin i \geq 300$ km/s.

clear separation between luminosity class I objects and the rest (here: III and V) seems to be apparent. The most obvious interpretation would be that the effective number of driving lines is a function of luminosity class. A comparison with recent theoretical predictions, however, indicates that this is not probable. While originating from completely different approaches, the simulations by both Vink, de Koter, & Lamers (2000, Monte-Carlo simulation, with \dot{M} resulting from global energy conservation) and Pauldrach, Hoffmann, & Méndez (2002, self-consistent, line-blanketed wind models) predict a unique relation which is located in between the two “observed” ones. Actually, this uniqueness had previously been found in more simplified theoretical calculations, cf. Puls et al. (1996).

One has to keep in mind that the stellar/wind parameters entering Fig. 3.1 had been derived from pure H/He models, and that an influence of line-blanketing effects is more than likely. In order to exclude this potential source of uncertainty from further argumentation about “observed” relation(s) (nevertheless, dependent on the underlying physical assumptions) and possible contradictions with theory, we have begun to re-investigate the situation by means of line-blanketed models which have recently become available.

For this purpose we have used FASTWIND (Santolaya-Rey, Puls, & Herrero 1996) which has been updated for an approximative treatment of line-blocking/blanketing by us (for a brief description and first applications, cf. Herrero, Puls, & Najarro 2002). This code follows the philosophy of performing appropriate physical approximations allowing for a very fast computational time. Note that even the re-analysis of our first Galactic O-star sample required the calculation of 350 models.

The code has been carefully tested, by comparison with results from alternative, fully blanketed codes presently available (e.g., with CMFGEN (Hillier & Miller 1998), TLUSTY (Hubeny & Lanz 1995) and WM-basic (Pauldrach, Hoffmann, & Lennon 2001)). Part of these tests have already been discussed by Herrero et al. (2002), and additional material will be published elsewhere.

For our re-analysis, we have used the spectra described in Herrero et al. (1992) and Puls et al. (1996) and performed detailed line fits to the Hydrogen Balmer lines (α to ϵ), HeI and HeII, including λ 4686 (strongly wind-contaminated) and those He-lines neighbouring H_α . Details will be presented in Repolust et al. (2002, in prep.).

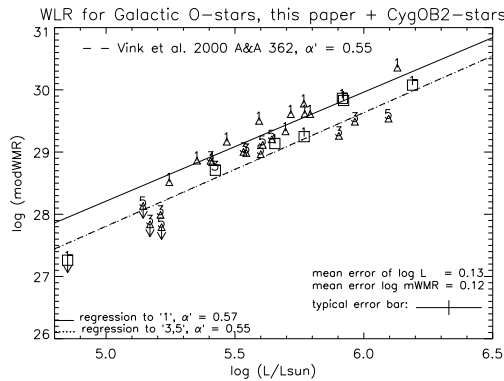


Figure 3.3: WLR for Galactic O-stars, using line-blanketed models, including results from Herrero et al. (2002) for CygOB2 stars (squares).

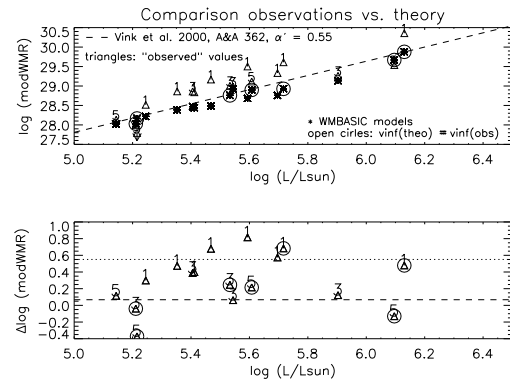


Figure 3.4: Comparison of observed and theoretical wind momenta. Upper panel: absolute values; lower panel: difference of logarithmic wind momenta. Lines indicate the mean difference with respect to l.c. I and for the rest, corresponding to (average) factors of 3.5 and 1.1, respectively (see text).

In Fig. 3.2, we display our new spectral type vs. T_{eff} relation. For dwarfs, the influence of line-blanketing is slightly larger than found by Martins, Schaerer, & Hillier (2002) in a comparable investigation (utilizing model-grids), whereas our effective temperatures of supergiants are somewhat hotter than derived by Crowther et al. (2002) for *extreme* MC objects. (Extreme objects are rare in our sample.) Note that the entry at O4 corresponds to ζ Pup, for which we have derived the same value (39,000 K) as indicated by Crowther et al. Compared to the latest calibration by Vacca, Garmany, & Shull (1996), utilizing pure H/He atmospheres, the differences are of the order of 4,000 to 8,000 K in the earliest types and become minor around B0.

Whereas the effective temperatures decrease significantly, the influence of line-blanketing on the derived stellar radius and \dot{M} is marginal, since the optical fluxes (used by us to determine R_*) are similar to those from unblanketed models at their “older”, higher T_{eff} (flux-conservation!) and since the influence of the reduced electron temperature on H_α is weak. Thus, compared to results from unblanketed models, the luminosities of the earliest types become significantly reduced and remain roughly constant around O9, whereas the “old” modified wind momentum rates are preserved. The resulting WLR is displayed in Fig. 3.3 (triangles only). Compared to Fig. 3.1, two points become apparent. First, the separation between l.c. I objects and the rest is still present. Second, the vertical offset is much larger (equal momenta at lower L), so that the “theoretical” WLR from Vink et al. is now consistent with the “observed” WLR for non-supergiants.

For most of the analyzed objects, we have additionally calculated self-consistent wind models by means of WM-basic. This was done for the stellar parameters derived in this study and without fine-tuning, i.e., without X-rays and leaving all metals at solar abundance. The results, compared to both the WLR by Vink et al. and the “observed” wind momenta, is shown in Fig. 3.4. On the one hand, the similarity between the two theoretical predictions is striking. On the other hand, theory agrees quite well with observations for non-supergiants, whereas for supergiants an average factor of 3.5 seems to be missing. A closer inspection (possible only for self-consistent hydrodynamical models) shows that just a part of the models (indicated by circles) is able to reproduce the observed terminal velocity,

whereas the rest reveals a mismatch of the order of a factor of two (theory too low). The reason for this mismatch is still unclear, particularly since the (effective) gravities can be derived with rather narrow error bars of order $\pm 0.1 \dots 0.15$ dex.

Corresponding UV-spectra have been calculated for all models, for both the “observed” and the self-consistent wind-parameters, in order to obtain an additional constraint on the wind-density by comparing them to the observed (IUE) spectra. Although we have not undertaken a detailed analysis so far, some preliminary conclusions are already possible. Considering the global ionization balance, we find no contradiction with our “new” temperature scale. On the other hand, without inclusion of X-rays, C IV is almost always saturated, thus prohibiting any further conclusions. N V in “cooler” stars (below 35,000 K) is much too weak without X-rays, and P V reacts very sensitively to variations of \dot{M} (cf. also Crowther et al. 2002) which is also true (and well known) for Si IV. Considering in particular the subset of models where the self-consistent terminal velocity agrees with the observed one, we find an interesting behaviour: For those objects where the observed and the theoretical mass-loss rates do not agree, Si IV favours the “observed” one, whereas the lines formed close to the photosphere (mainly Fe, Ni) seem to be consistent with a lower value.

In order to gain insight into whether the apparent problems are related to our spectroscopic analysis or to the theoretical simulations, the observed WLR for CygOB2 stars (which should be free of errors related to relative distances) has been included in Fig. 3.3. Note that this WLR has been derived with the same code as applied in the present investigation (cf. Herrero et al. 2002 and this volume). Although this sample consists almost exclusively of supergiants, the clear separation as a function of luminosity class, which we have confirmed for objects from our sample, is no longer visible. On the contrary, only two objects, namely the most extreme supergiants in the CygOB2 sample, follow the “upper” WLR, whereas the derived values for all other objects are consistent with our WLR for l.c. III/V stars.

Guided by this perception, we have replotted our data (including the Cyg OB2 stars) in a slightly different manner, as shown in Fig. 3.5. In this plot, we have reclassified our sample in terms of the observed H_α profile: Class 1 comprises those objects with H_α in emission, class 3 designates objects with an absorption profile partly refilled by wind emission, and class 5 comprises objects with almost purely photospheric H_α profiles. Classified in this way, a unique trend, now also for the CygOB2 stars, becomes visible: *Stars with H_α in emission and those with refilled absorption profiles form two distinct WLRs.*

3.3 Conclusions: Clumping?

The difference between the new class 1 and 3 objects is, of course, given by the different contribution of wind-emission to the total profile. In class 3 objects, only contributions from the lowermost wind can be seen, whereas in class 1 objects the emission is due to a significant volume of the wind, out to $1.5 R_\star$ in extreme cases (cf. Puls et al. 1996). Thus, there is the possibility that for these objects we *see* the effects of a *clumped* wind, which would mimic a higher mass-loss rate, as is most probably the case for Wolf-Rayet winds. Note that we do not exclude the presence of clumping in the intermediate/outer wind for class 3 objects, but owing to the low optical depth we simply cannot see it, in contrast to the case of class 1 objects where we observe the emission from a larger volume.

Actually, the principal presence of clumping has never been ruled out for O-star winds; however, there was simply no indication that *the H_α forming region* was considerably clumped (see the discus-

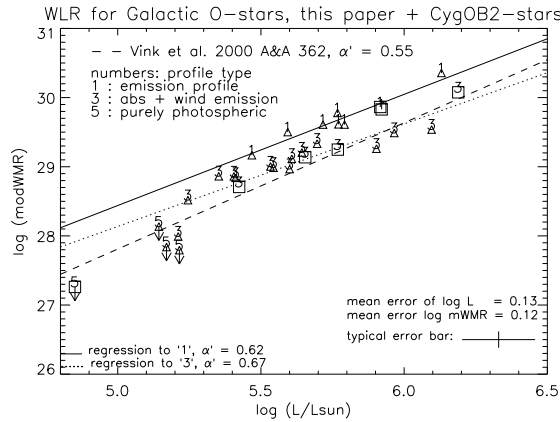


Figure 3.5: As Fig. 3.3, however classified as function of H_α profile type (see figure and text).

sion in Puls et al.). Our new perspective is the result of a re-analysis of old data with improved models. In addition, recent theoretical considerations (e.g., Owocki & Puls 1999 and references therein; Feldmeier, Puls, & Pauldrach 1997) do not prohibit such a relatively deep-seated clumped region. Interestingly, time-series analyses of HeII 4686 from ζ Pup by Eversberg, Lepine, & Moffat (1998) have revealed “outward moving inhomogeneities”, from regions near the photosphere out to $2 R_*$.

Our hypothesis of seeing the effects of clumping at work is supported by three further facts. First, our hypothesis is consistent with the behaviour of the synthetic SiIV line described above, since this line reacts similarly to H_α (being a ρ^2 dependent line in O-stars). Second, for five out of the seven “class 1” objects from our sample, those synthetic Balmer lines formed in or close to the photosphere (H_γ and H_δ) show too much wind emission in their cores, and would require at least a factor of 1.5 less mass-loss in order to be consistent with observations (cf. also Herrero et al. 2002). Third, if we reduce the mass-loss rates of our class 1 objects by a factor of 0.42, these objects would perfectly fit the WLR for class 3, in accordance with theoretical expectations. Such a factor would correspond to an average clumping factor of 5.7, which is not too different from the values found in the case of Wolf-Rayet stars. Note also that a recent simulation for the atmosphere of ζ Pup by G. Gräfener (priv. comm.), including clumping, was able to simultaneously reproduce the UV and optical spectrum, for a mass-loss rate of *half* the value derived from our unclumped models. This finding is perfectly consistent with our conclusions stated above.

In summary, there are strong indications that mass-loss analyses of (at least) O-star winds utilizing H_α tend to overestimate the resulting values, unless clumping is accounted for or the winds are comparatively thin. Of course, we also have to be open to other possibilities which might explain the discrepancies found here. A combined multi-spectral analysis (UV, optical and IR) based on clumped wind-models and applied to large samples of stars of different spectral type should clarify these questions. Taking the recent advances in radiation driven wind models into account, this task has now become feasible.

Acknowledgements:

This investigation has been supported in part by the German *DLR* under grant RD-RX-50 OR 9909 2 and by the *International Max-Planck Research School at the Ludwig-Maximilians-Universität, Munich*.

Bibliography

- Crowther, P.A., Hillier, D.J., Evans, C.J., et. al. 2002, ApJ 579, 774
- Feldmeier, A., Puls, J., Pauldrach, A.W.A. 1997, A&A 322, 878
- Eversberg, T., Lepine, S., Moffat, A.F.J. 1998, ApJ 494, 799
- Herrero, A., Kudritzki, R.P., Vílchez, J.M., et al. 1992, A&A 261, 209
- Herrero, A., Puls, J., Najarro, F. 2002, A&A 396, 949
- Hillier, D.J., Miller, D.L. 1998, ApJ 496, 407
- Hubeny, I., Lanz, T. 1995, ApJ 39, 875
- Kudritzki, R.P., Puls, J. 2000, ARA&A 38, 613
- Kudritzki, R.P., Puls, J., Lennon, D.J., et al. 1999, A&A 350, 970
- Martins, F., Schaerer, D., Hillier, D.J. 2002, A&A 382, 999
- Owocki, S.P., Puls, J. 1999, ApJ 510, 355
- Pauldrach, A.W.A., Hoffmann, T.L., Lennon, M. 2001, A&A 375, 161
- Pauldrach, A.W.A., Hoffmann, T.L., Méndez, R. 2003, in Proc. IAU Symp. 209, eds. S.Kwok & M.Dopita, in press
- Puls, J., Kudritzki, R.P., Herrero, A., et al. 1996, A&A 305, 171
- Puls, J., et al. 2003, in: Proc. IAU Symp 212, eds. K.A. van der Hucht, A. Herrero & C. Esteban, ASP, p. 61
- Santolaya-Rey, A.E., Puls, J., Herrero, A. 1997, A&A 323, 488
- Vacca, W.D., Garmany, C.D., Shull, M. 1996, ApJ 460, 914
- Vink, J.S., de Koter, A., Lamers, H.J.G.L.M. 2000, A&A, 362, 295

Chapter 4

Stellar and wind parameters of Galactic O-stars: The influence of line-blocking and -blanketing

T. Repolust, J. Puls, A. Herrero, A&A 415, 349

Abstract. We have re-analyzed the Galactic O-star sample from Puls et al. (1996) by means of line-blanketed NLTE model atmospheres in order to investigate the influence of line-blocking/blanketing on the derived parameters. The analysis has been carried out by fitting the photospheric and wind lines from H and He. In most cases we obtained a good fit, but we have also found certain inconsistencies which are probably related to a still inadequate treatment of the wind structure. These inconsistencies comprise the line cores of H_γ and H_β in supergiants (the synthetic profiles are too weak when the mass-loss rate is determined by matching H_α) and the “generalized dilution effect” (cf. Voels et al. 1989) which is still present in He I 4471 of cooler supergiants and giants.

Compared to pure H/He plane-parallel models we found a decrease in effective temperatures which is largest at earliest spectral types and for supergiants (with a maximum shift of roughly 8,000 K). This finding is explained by the fact that line-blanketed models of hot stars have photospheric He ionization fractions similar to those from unblanketed models at higher T_{eff} and higher $\log g$. Consequently, any line-blanketed analysis based on the He ionization equilibrium results in lower T_{eff} -values along with a reduction of either $\log g$ or helium abundance (if the reduction of $\log g$ is prohibited by the Balmer line wings). Stellar radii and mass-loss rates, on the other hand, remain more or less unaffected by line-blanketing.

We have calculated “new” spectroscopic masses and compared them with previous results. Although the former *mass discrepancy* (Herrero et al., 1992) becomes significantly reduced, a systematic trend for masses below 50 M_\odot seems to remain: The spectroscopically derived values are smaller than the “evolutionary masses” by roughly 10 M_\odot . Additionally, a significant fraction of our sample stars stays over-abundant in He, although the actual values were found to be lower than previously determined.

Also the wind-momentum luminosity relation (WLR) changes because of lower luminosities and almost unmodified wind-momentum rates. Compared to previous results, the separation of the WLR as a function of luminosity class is still present but now the WLR *for giants/dwarfs* is consistent with theoretical predictions.

We argue that the derived mass-loss rates of stars with H_α in emission are affected by clumping in the *lower* wind region. If the predictions from different and independent theoretical simulations (Vink et al. 2000; Pauldrach et al. 2003; Puls et al. 2003a) that the WLR should be independent of luminosity class were correct, a typical clumping factor $\langle \rho^2 \rangle / \langle \rho \rangle^2 \approx 5$ should be derived by “unifying” the different WLRs.

4.1 Introduction

The understanding of massive stars and their evolution is not only fundamental to *stellar* astrophysics but it also provides insights into a variety of other processes. Massive star winds (with parameters depending on evolutionary stage and environment) are crucial for the chemical and dynamical evolution of galaxies through their input of energy, momentum, and nuclear processed material into the interstellar medium (e.g., Leitherer & Heckman 1995; Silich & Tenorio-Tagle 2001; Oey 2003). In the distant Universe, massive stars dominate the integrated UV-light of very young galaxies (Steidel et al. 1996; Pettini et al. 2000); even earlier they are the suspected sources of the re-ionization of the Universe (Bromm et al. 2001).

Thus, by observing and analyzing massive stars we can (in principle) provide the numbers required to tackle these problems. Moreover, we can address a number of ensuing questions which are of great interest and might have significant consequences for our general understanding. Present efforts, for example, concentrate on the physics of rotation (with respect to both the interior structure by means of mixing processes and the exterior structure by modifying the wind morphology, e.g. Maeder & Meynet 2000 and references therein), the influence of time-dependent processes (see below) and the so-called wind-momentum luminosity relation (WLR) which might become an independent tool to derive extragalactic distances on an intermediate scale (up to the Virgo and Fornax cluster).

This knowledge is mainly derived from the analysis of stellar spectra which in turn requires adequate atmospheric models. For this purpose sophisticated model atmosphere codes have been developed in the last decade, e.g., Hubeny & Lanz (1995), Santolaya-Rey et al. (1997, “FASTWIND”), Hillier & Miller (1998), Pauldrach et al. (2001) and Gräfener et al. (2002) which incorporate detailed atomic models and improved numerical techniques. These models offer us the opportunity to derive rather realistic stellar parameters and provide insight into the chemical composition of stars. Additionally, the latter four codes allow for an investigation of important wind properties such as mass-loss rates, wind terminal velocities and velocity structures.

Considering that the actual value of the mass-loss rate has a significant influence on massive star evolution¹, the derived mass-loss rates need to be known to a level of precision better than a factor of two; otherwise, evolutionary calculations relying on these numbers could become completely erroneous.

Although such a precision is feasible (at least differentially, cf. Kudritzki & Puls 2000 and references therein), the situation looks different on an absolute scale. Most important in this sense is the fact that stellar rotation (e.g., Maeder & Meynet 2000a), the intrinsic instability of the line-driving mechanism (Owocki, Castor & Rybicki, 1988; Feldmeier, 1995; Owocki & Puls, 1999) and their interaction (Owocki, 1999) are able to produce non-spherical and inhomogeneous structures, observationally evident, e.g., from X-ray emission and line profile variability. Unless we completely understand these structures, we cannot be entirely sure about the “average” properties of stellar winds like mass-loss rates and ionizing fluxes. At least in the case of WR-stars, the presence of clumping has severe consequences for the interpretation of observed line profiles, particularly with respect to the derived mass-loss rates, e.g., Moffat & Robert (1994); Schmutz (1997).

Not only do present mass-loss rates remain somewhat uncertain but also the basic stellar parameters of O-stars are subjected to a number of uncertainties. Using plane-parallel NLTE-models, Herrero et al. (1992) have presented discrepancies in masses and helium abundances of O-stars, derived from

¹Note that, e.g., for O-stars the product of typical mass-loss rate times hydrogen burning life-time is a significant fraction of total mass.

either evolutionary tracks or spectroscopy. It was suggested that these discrepancies could be reduced by accounting for rotational mixing in the evolutionary calculations (which partly turned out to be true, Meynet & Maeder 2000) and/or by including the effects of mass-loss and sphericity into the atmospheric models.

The latter deficiency was corrected when so-called unified model atmospheres became available (Gabler et al., 1989). On the basis of these models, Puls et al. (1996) introduced an approximate method to obtain mass-loss estimates for a large sample of Galactic and Magellanic Cloud O-stars. As a “by-product”, this analysis provided the basis for the wind-momentum luminosity relationship of hot stars (Kudritzki et al., 1995).

There is, however, one additionally important effect that could not be treated at that time: the influence of line-blocking/blanketing which should significantly affect the analysis, mainly with respect to the temperature scale as a function of spectral type. With the present generation of atmospheric model codes this task has now become feasible.

Recently Martins et al. (2002) have presented such a new temperature scale for massive O *dwarfs* that is actually considerably lower than the one found by Vacca et al. (1996) (based on plane-parallel, pure H/He model atmospheres) as a result of strong metal line blanketing. Crowther et al. (2002) have presented an analysis of four supergiants in the LMC and SMC with similar but stronger trends, and Herrero et al. (2002) have analyzed seven Cyg OB2 stars by means of the latest, line-blanketed version of FASTWIND.

In view of the important role of hot stars and their winds, a re-analysis of the O-star sample by Puls et al. (1996) is urgently required, particularly because this sample still comprises the basic data set for O-star mass-loss rates and corresponding WLRs.

In the present paper we will first concentrate on the Galactic sub-sample and on a detailed spectral analysis of the corresponding stars and then comment on peculiarities, problems and uncertainties, mainly on the basis of a differential comparison with previous results from unblanketed models. Preliminary results of our investigation have already been published in Puls et al. (2003a).

The remainder of this paper is organized as follows. In Sect. 4.2 we briefly outline the characteristics of the code used, followed by a description of our Galactic sample in Sect. 4.3. Sect. 4.4 comprises general remarks on our procedure and summarizes the basic results of our analysis in Table 4.1. In Sect. 4.5, we comment in detail on our individual objects and in Sect. 4.6 we present an elaborated error analysis. In Sect. 4.7 we discuss the implications of our investigation: First, we consider the relation between effective temperature vs. spectral type and gravity vs. effective temperature in view of the new results. We then explain the differences in the results from blanketed and unblanketed models in fair detail and comment on the status quo of mass and helium discrepancies outlined above and present an updated view of the WLR for Galactic O-type stars. Finally, Sect. 4.8 comprises further conclusions and a summary of this work.

4.2 The code

In order to investigate the influence of line-blocking/blanketing on T_{eff} , and subsequently on the other stellar and wind parameters, we have begun to re-analyze the O-star sample compiled by Puls et al. (1996, in the following Paper I). As outlined above, in the present paper we will concentrate on the Galactic objects of this sample, where the analysis will be performed by means of NLTE-atmospheres/line formation, utilizing the latest version of FASTWIND (an acronym for Fast Analysis

of STellar atmospheres with WINDs; Herrero et al. 2002; Santolaya-Rey et al. 1997). This code, allowing for the simultaneous computation of photospheric and wind lines, has the enormous advantage of being very fast (roughly 30 min/model on any 1 GHz processor), enabling us to calculate the vast amount of models required. This computational efficiency is obtained by applying appropriate physical approximations to certain processes where high accuracy is not needed (regarding the objective of the analysis - optical lines!), in particular for the treatment of the metal-line background opacities.

The code comprises the concept of “unified model atmospheres” (i.e., the smooth transition from a pseudo-hydrostatic photosphere to a wind) along with an appropriate treatment of line-broadening which is a prerequisite for the analysis of O-stars of different luminosity classes covering a variety of wind densities.

The approximations underlying the treatment of metal line blocking/blanketing will be described in detail by Puls et al. (2003b, in prep). In summary, the calculation of the required NLTE metal opacities (bound-bound, bound-free, and free-free) follows the principal philosophy presented by Abbott & Lucy (1985), Schmutz (1991), Schaerer & Schmutz (1994) and Puls et al. (2000) and important details have now been improved upon. Particularly, the equations of approximate ionization equilibrium have been re-formulated to account for the actual radiation field as a function of depth at *all* ionization edges, and a consistent iteration scheme regarding the coupling of the rate equations and the radiation field has been established to avoid the well-known convergence problems of a pure Lambda Iteration. For the calculation of the effects of line-blocking, we used suitable means for the line opacities, averaged over a frequency interval of the order of ν_∞ , while flux conservation (line-blanketing!) is obtained by incorporating the concept of NLTE-Hopf parameters (cf. Santolaya-Rey et al. 1997) in a consistent way.

The code has carefully been tested by comparison with results from alternative, fully blanketed codes presently available. On the one hand, we have compared our blanketed fluxes with those from the model-grid² provided by Pauldrach et al. (2001, WMBasic), and found very good agreement in almost all cases. Some of the complementary tests, on the other hand, have already been discussed by Herrero et al. (2002, see also Urbaneja et al. 2003). As an example for stars with negligible winds, the analysis of 10 Lac (O9 V) resulted in an excellent fit at temperatures lower than those obtained from unblanketed models, and the derived parameters completely agree with those obtained by Hubeny et al. (1998) using TLUSTY. With respect to CMFGEN, direct as well as indirect tests have been performed. As an example of direct tests, Herrero et al. (2002) have compared the emergent fluxes resulting from FASTWIND and CMFGEN for a model of Cyg OB2 #7 (O3 If*), and again found remarkable agreement between both codes for this hot supergiant with strong wind. Unpublished indirect tests (Najarro, priv.com.) concern an alternative combined UV/optical analysis, performed for a part of the Cyg OB2 objects from Herrero et al. (2002) by means of CMFGEN. For two objects (Cyg OB2 #4 (O7 III ((f))) and #10 (O9.5 I) excellent agreement in all derived parameters was obtained, whereas for two other objects (Cyg OB2 #11 (O5 If*) and #8A (O5.5 I(f)) somewhat cooler temperatures (and accordingly also lower mass-loss rates) have been derived. The origin of this inconsistency (the only one arising so far) is still unclear and will be analyzed in a forthcoming investigation. Note, however, that an independent CMFGEN analysis of ζ Pup (O4 I(f)) performed by Crowther et al. (2002) resulted in very similar parameters as found in the present work (cf. Sect. 4.7.1).

²comprising six supergiants and six dwarfs between 30,000 and 50,000 K, see also
<http://www.usm.uni-muenchen.de/people/adi/Models/Model.html>

4.3 The O-star sample

For our re-analysis we have used the spectra described by Herrero et al. (1992) and Puls et al. (1996). The H_α observations of the core sample of Galactic O-stars were taken from Herrero et al. (1992) and Herrero (1993) and were carried out with the 2.5m Isaac Newton telescope at the Observatory of El Roque de los Muchachos in La Palma in July and October 1989 and in August 1992. The blue observations needed to derive photospheric parameters were obtained during the same runs with an additional one in September 1991. Note however that the blue and red spectra were not taken simultaneously. For a specific observational run, all red spectra were obtained during *one night*, whereas the blue spectra were collected during the remaining nights.

The Intermediate Dispersion Spectrograph (IDS) was used with the 1800 V grating along with the 235 mm camera yielding a spectral resolution of 0.8 \AA FWHM along with a measured S/N ratio of ≈ 300 and a spectral resolution of 0.6 \AA FWHM along with a S/N ratio ranging from 150 to 200 for the red and the blue observations, respectively. The reduction of the data was made following standard procedures (using various packages such as IRAF, FIGARO (Shortridge, 1987), Midas etc.) comprising bias subtraction, flat field division, spectrum extraction, wavelength calibration and continuum rectification.

The above data is supplemented by additional O3 stars located in the Carina nebula and some further well-observed stars such as ζ Pup and α Cam. The data for the Carina stars (HD 93129A, HD 93128, HD 93250, and HD 303308) were obtained in December 1992 using the ESO New Technology Telescope (NTT) and the EMMI spectrograph covering the wavelength ranges 3920 - 4380, 4300 - 4750 and 6300 - 6800 \AA at a resolution of 0.9, 0.95 and 1.1 \AA , respectively. The measured S/N ratio was found to be of the order of ≈ 200 .

Furthermore, additional red spectrograms of HD 207198, and HD 209975 were obtained with a similar instrumental setup as described by Herrero et al. (1992) and Herrero (1993).

The blue spectra of α Cam were taken from Lennon et al. (1992), and the red ones from Lennon et al. (1993).

The data for ζ Pup (blue and red), finally, was taken from Bohannan et al. (1990), where further information of the observational material and data reduction procedures may be found.

For all spectra we used the rectifications provided by the corresponding observers. Note, however, that particularly the region around the “new” He I/He II lines in the red band (see below) suffers from some problems in rectification, since this region has not been considered in detail before. Nevertheless, we have refrained from any “re-rectification” and have commented on the problem when present.

In total the sample consists of 24 Galactic O-stars as listed in Table 4.1 covering luminosity class I, III, and V objects.

4.4 Analysis - General remarks

Before presenting the detailed results of our analysis, we would like to remark on certain aspects concerning our procedure.

Micro-turbulence. As is well known, the inclusion of an adopted micro-turbulent velocity into the profile-functions can diminish certain discrepancies between the He I singlet and triplet lines in the B-

and late O-star regime (cf. Smith & Howarth 1998 and the discussion below), whereas for hotter O-stars micro-turbulence has (almost) no effect on the analysis (Villamariz & Herrero, 2000). Following these results, for almost all stars later than O6 (regardless of their luminosity class) we adopted a v_{turb} of 10 km s^{-1} as a reasonable compromise. At spectral type O6, our analysis of HD 210839 (1c I) indicated that such a micro-turbulence is still needed, whereas for HD 217086 (O7V), the inclusion of v_{turb} did not change our results. Since both stars turned out to lie at $T_{\text{eff}} = 36000 \text{ K}$, we conclude this temperature to be an upper limit where micro-turbulence plays a role and is actually needed. For all stars hotter than O6, we adopted $v_{\text{turb}} = 0$, in agreement with the results from Villamariz & Herrero (2000).

Distances/Radii. It has recently been proposed that distances to open clusters derived from HIPPARCOS observations might be systematically smaller than photometric ones (de Zeeuw et al., 1999). If this was confirmed, we would require a new calibration of absolute magnitudes in the upper part of the HR diagram. However, since present data is still scarce, we have systematically adopted photometric distances for stars belonging to OB associations (collected from different sources in the literature) to avoid an additional bias in our data.

Nevertheless, we still have to consider the runaway or field stars in the sample. Four of them have measured HIPPARCOS parallaxes (ESA 1997) with not too large errors: HD 66811 (ζ Pup), HD 210839 (λ Cep), HD 24912 (ξ Per) and HD 149757 (ζ Oph). In these cases, however, we have to consider the uncertainty in the derived absolute magnitudes introduced by the Lutz-Kelker effect (Lutz & Kelker 1973). Only ζ Oph has a relative error that allows a standard correction of the Lutz-Kelker effect and we adopt the value derived from the measured parallax and the correction provided by Koen (1992). We have reduced the 90% confidence limits provided by Koen to the usual standard deviation for our errors.

The relative error in the parallax of ζ Pup is slightly beyond the limit for which the standard Lutz-Kelker correction can be applied. We have estimated the correction using Fig. 2 in Oudmajer et al. (1998) and have found that the resulting value agrees well with existing calibrations of absolute magnitude versus spectral classification (e.g., Massey 1998 or Walborn 1972). Therefore, we have adopted this resulting value and corresponding uncertainty (i.e., $\pm 0.43 \text{ mag}$ which is larger than the uncertainty adopted for most of the stars).

We have performed the same exercise for λ Cep, but the resulting value did not comply with current calibrations. We preferred the absolute magnitude from spectroscopic parallaxes given in the literature, in particular the value provided by Garmany & Stencel (1992) since its agreement with existing calibrations is better. Additionally, we adopted a larger uncertainty in absolute magnitude, $\pm 0.5 \text{ mag}$.

ξ Per has the largest relative error in the measured parallax and the absolute magnitudes found in the literature do not match its spectral classification (Humphreys 1978; de Zeeuw et al. 1999; Hoogerwerf et al. 2001). Therefore, we adopt a value from the calibrations by Massey (1998) and Walborn (1972).

For HD 30614 (α Cam), finally, we have used the absolute magnitude taken from the calibration by Walborn (1972).³

Compared to the “old” values from Paper I, the “new” absolute magnitudes remain almost un-

³For a more thorough discussion concerning the problem of distances and magnitudes, we refer the reader to Markova et al. (2003).

changed (typical modifications are of the order of $\pm 0.1 \dots 0.15$ mag) except for the following cases: ξ Per, α Cam and HD 209975 have become brighter by 0.4, 0.9 and 0.7 mag, respectively, whereas HD 217086 has become fainter by 0.4 mag.

From these M_V -values, stellar radii have been calculated following the procedure outlined by Kudritzki (1980) and Herrero et al. (1992):

$$5 \log R_\star = 29.58 + (V_{\text{theo}} - M_V), \quad (4.1)$$

$$V_{\text{theo}} = -2.5 \log \int_{\text{filter}} 4H_\lambda S_\lambda d\lambda, \quad (4.2)$$

where H_λ is the *theoretical* Eddington flux from the calculated models (in units of $[\text{erg s}^{-1} \text{ cm}^{-2} \text{ \AA}^{-1}]$) and S_λ is the spectral response of the photometric system.

The input radii used as starting values for our atmospheric models were taken from Paper I and have been calculated from the “old” M_V -values provided by Herrero et al. (1992) and Paper I. Since the inclusion of line blocking/blanketing changes the theoretical fluxes (cf. Sect. 4.7.2) and since we have adopted somewhat different values for M_V (see above), the radii change accordingly which has been accounted for in the calculation of the final models. Even for the largest modifications of M_V , the changes in radius remain below 25%, except for α Cam, with an increase in radius by 50%, cf. Table 4.1.

Note that in Table 4.1 all radius-dependent quantities such as luminosity, mass and mass-loss rate refer to the stellar radii calculated from the M_V -values as described above (“ R_\star ”), since we regard these values as superior to the “older” ones. However, we additionally provide stellar radii calculated from the “old” M_V -values (“ R_{old} ”). Hence, L, M, \dot{M}, \dots can easily be rescaled (e.g., Sect. 4.7.5), accounting for the fact that a strictly differential comparison with earlier analyses is one of the primary objectives of the present work.

Projected rotational velocities. As a first guess we have used the values provided in Paper I (except for HD 210839 = λ Cep, where the value given (i.e., 100 km s^{-1}) is a miss-print and should read 200 km s^{-1}). However, in 9 out of 24 cases our analysis (including additional He I lines) indicated somewhat different values, which we used instead of the original ones. Except for the two stars in Carina, HD 93250 and HD 303308, where we had to increase $V_r \sin i$ from 100 to 130 km s^{-1} , these corrections are below 20%. Compared to the elaborate analyses by Penny (1996) and Howarth et al. (1997) using cross-correlation techniques based on UV observations, our results agree very well in most cases. With respect to the values presented by Penny (1996) we find an average ratio of the derived projected rotational velocities of 1.03 ± 0.10 (mean absolute deviation: ± 0.08), and with respect to the values from Howarth et al. (1997) an analogue comparison results in 1.02 ± 0.15 (mean absolute deviation: ± 0.11). The only real difference has been found in the case of HD 93129A, for which Howarth et al. (1997) claim a value of 180 km s^{-1} , compared to 130 km s^{-1} in this work. Note, however, that the value provided by Penny (1996), 143 km s^{-1} , agrees much better with our analysis for this star.

Mass-loss rates have exclusively been derived from H_α . In so far, the consistency (present or absent) of the synthetic and observed He II 4686 line allows to check the accuracy of our code (see below).

Table 4.1: Galactic O-star sample: Stellar and wind parameters adopted (M_V) and derived using FASTWIND. T_{eff} in kK, R_* in R_\odot , $V_r \sin i$ and v_∞ in km s^{-1} , M_* in M_\odot , L in L_\odot , \dot{M} in $10^{-6} M_\odot/\text{yr}$ (terminal velocities v_∞ from Paper I). HD 93129A and HD 303308 have recently been detected as binary systems but they are treated here as single stars (see text). Bold face numbers denote β -values which could be derived with high precision from emission profiles. Stars with absorption profiles were fitted with an assumed value of $\beta = 0.80$. R_{old} is the stellar radius resulting from our new models which was calculated by means of the “old” M_V values from Paper I (not tabulated here).

Star	Sp.Type	M_V	T_{eff}	$\log g$	$\log g_{\text{true}}^{2)}$	R_*	Y_{He}	$V_r \sin i$	v_∞	$\log L$	M_*	\dot{M}	β	R_{old}
HD 93129A ¹⁾	O2 If*	-6.74	42.5	3.70	3.71	(22.5)	0.10	130	3200	(6.17)	(94.8)	(26.30)	0.80	(21.4)
HD 93128	O3 V ((f))	-5.24	46.5	4.00	4.01	10.4	0.10	100	3100	5.66	39.8	2.64	0.85 ³⁾	10.2
HD 93250	O3 V ((f))	-6.14	46.0	3.95	3.96	15.9	0.10	130	3250	6.01	83.3	3.45	0.90 ³⁾	17.6
HD 66811	O4 I(f)	-6.32	39.0	3.55	3.59	19.4	0.20	220	2250	5.90	53.9	8.80	0.90	16.8
HD 303308 ¹⁾	O4 V ((f ⁺))	-5.29	41.0	3.90	3.91	(11.5)	0.075	120	3100	(5.53)	(39.0)	(1.63)	0.80	(12.6)
HD 14947	O5 If ⁺	-5.94	37.5	3.45	3.48	16.8	0.20	140	2350	5.70	30.7	8.52	0.95	18.1
HD 15558	O5 III(f)	-6.27	41.0	3.80	3.81	18.2	0.10	150	2800	5.93	78.7	5.58	0.80	19.4
HD 193682	O5 III(f)	-5.55	40.0	3.60	3.65	13.1	0.20	200	2800	5.60	27.9	1.73	0.80	12.3
HD 15629	O5 V ((f))	-5.50	40.5	3.70	3.71	12.8	0.08	90	3200	5.60	30.4	1.28	0.80	12.8
HD 210839	O6 I(n) fp	-6.40	36.0	3.55	3.58	21.1	0.10	200	2250	5.83	62.2	6.85	1.00	20.2
HD 190864	O6.5 III(f)	-5.29	37.0	3.55	3.57	12.3	0.15	105	2500	5.41	20.3	1.39	0.80	14.2
HD 192639	O7 Ib (f)	-6.10	35.0	3.45	3.47	18.7	0.20	125	2150	5.68	37.5	6.32	0.90	19.6
HD 193514	O7 Ib (f)	-6.15	34.5	3.30	3.32	19.3	0.10	105	2200	5.68	28.2	3.48	0.80	19.7
HD 24912	O7.5 III(n)((f))	-5.50	35.0	3.50	3.56	14.0	0.15	220	2450	5.42	26.1	1.08	0.80	11.6
HD 203064	O7.5 III:n ((f))	-5.74	34.5	3.50	3.60	15.7	0.10	300	2550	5.50	35.9	1.41	0.80	14.1
HD 217086	O7 V n	-4.50	36.0	3.50	3.72	8.6	0.15	350	2550	5.05	14.2	≤ 0.23	0.80	10.4
HD 13268	ON8 V	-4.77	33.0	3.25	3.48	10.3	0.25	300	2150	5.05	11.7	≤ 0.26	0.80	11.4
HD 210809	O9 Iab	-6.20	31.5	3.10	3.12	21.2	0.14	100	2100	5.60	21.7	5.30	0.90	21.2
HD 207198	O9 Ib	-5.80	33.0	3.45	3.46	16.6	0.12	80	2150	5.47	29.0	1.79	0.80	14.5
HD 30614	O9.5 Ia	-7.00	29.0	2.97	2.99	32.5	0.10	100	1550	5.83	37.6	6.04	1.15	21.5
HD 209975	O9.5 Ib	-6.41	32.0	3.20	3.22	22.9	0.10	100	2050	5.69	31.4	2.15	0.80	16.5
HD 18409	O9.7 Ib	-5.58	30.0	2.95	3.04	16.3	0.14	150	1750	5.29	10.6	1.02	0.85 ³⁾	15.7
HD 191423	O9 III:n*	-5.24	32.5	3.35	3.60	12.9	0.20	400	1150	5.23	24.6	≤ 0.41	0.80	12.7
HD 149757	O9 V	-4.35	32.0	3.65	3.85	8.9	0.17	400	1550	4.87	20.2	≤ 0.18	0.80	8.2

¹⁾ component of binary system.

²⁾ $\log g$ including centrifugal correction (see text).

³⁾ denotes those absorption profiles for which there are indications that β differs from 0.80 (see text).

Velocity law for thin winds. In case of thin winds, i.e., H_α in absorption, it is (almost) impossible to derive the exponent of the velocity-law, β , in the wind. In this case, we usually adopted the “theoretical” value $\beta = 0.8$ (cf. Pauldrach et al. 1986), but performed a rigorous error analysis concerning the possibility that other values are present (cf. Sect. 4.6). For some stars with H_α in absorption, we actually found indications of values different from $\beta = 0.8$. These special cases are described in our comments on individual objects (Sect. 4.5) and also indicated in Table 4.1 - the summarized results of our analysis.

Summary of results. This table comprises the HD number, spectral classification, “new” absolute magnitude, effective temperature T_{eff} , “measured” gravity $\log g$, “true” gravity $\log g_{\text{true}}$ (including the centrifugal correction, cf. Sect. 4.6), stellar radius R_\star (see above), the luminosity L , the helium abundance (by number) $Y_{\text{He}} = N(\text{He})/N(\text{H})$, projected rotation velocity $V_r \sin i$, terminal velocity v_∞ , mass M_\star , mass-loss rate \dot{M} and, as mentioned above, the derived or adopted value of β . Furthermore, we provide also the stellar radii as calculated from the M_V -values from Paper I, R_{old} .

The spectral classification used is the one adopted by Herrero et al. (1992) except for those objects for which a re-classification of luminosity class has been proposed. The main purpose of this re-classification was to reduce the scatter of physical parameters (e.g., gravity) within a given luminosity class and to adopt consistent absolute magnitudes. Since in the present work we make no use of any parameters calibrated against luminosity class (except for the absolute magnitude of α Cam), a re-classification is not necessary. Therefore, we prefer to maintain the classification based on purely morphological aspects. Note, however, that some stars might have physical parameters that deviate from those obtained using calibrations.

Moreover, according to Walborn et al. (2002), HD 93129A and HD 303308 (prior to knowing that the two stars were binaries; see Nelan et al. 2003, in prep.) have been revised to O2 If* and O4 V((f⁺)), respectively.

The final fits for our sample stars are plotted in Figs. 4.1 to 4.7. Figs. 4.1, 4.2, 4.5 and 4.8 display the fits of those lines which are preferentially formed in the photosphere, whereas Figs. 4.3, 4.4, 4.6 and 4.7 comprise the “wind lines”, H_α (along with He II 6527) and He II 4686.

Strategic lines. For the photospheric lines we display the hydrogen Balmer lines H_β and H_γ (H_δ and H_ϵ are absent in most of our spectra since they lie at the far edge of the short wavelength range), the He I singlets $\lambda\lambda 4387, 4922$, the He I triplets $\lambda\lambda 4471, 4713$ (He I 4026 again is absent in most cases) and the He II lines $\lambda\lambda 4200, 4541$. Additionally, we have included those He lines neighboring H_α , namely He II 6404 and He II 6683/He I 6678.

In former analyses mainly two He II lines, He II $\lambda\lambda 4200$ and 4541 ($n = 4 \rightarrow 11$ and $n = 4 \rightarrow 9$) have been used to derive the stellar parameters, since He II 4686, on many occasions, is affected by severe wind emission which could not be synthesized from plane-parallel models. Moreover, He II 4686 depends strongly on the behaviour of the He II resonance line at 303\AA , which in turn reacts sensitively to the details of line-blocking (as all other He II resonance lines do).

Since the present code can deal with both winds and line-blocking, this line has now been included and serves as an ideal tool to indirectly check the accuracy of the calculated line-blocking in the EUV.

Moreover, as already mentioned, we have included the He lines located blue- and redwards of H_α into our analysis, providing additional constraints and information on the sensitivity to small parametric changes and thus allowing to check the consistency of our assumptions and results. In particular, we added the two He II lines at 6404Å and 6527Å bluewards of H_α with corresponding transitions $n = 5 \rightarrow 15$ and $n = 5 \rightarrow 14$, respectively. Redwards of H_α we included He II 6683 ($n = 5 \rightarrow 13$) which is blended with He I 6678. The latter line belongs to the singlet system with lower level ($2p^1P^0$) and upper level ($3d^1D$).

Before beginning to comment on the individual objects, we would like to point out some general behaviour of the fitted lines.

Line cores of photospheric Balmer lines. For almost all luminosity class I objects from our sample with $T_{\text{eff}} > 35,000$ K, the synthetic Balmer lines formed in or close to the photosphere (H_γ and H_δ , where present, along with H_β) show too much wind emission in their cores if H_α fits (cf. Fig. 4.1, in particular ζ Pup). In these cases, it turned out that it is impossible (within the standard assumptions of our model) to obtain a consistent fit for *all* Balmer lines at a given mass-loss rate. This finding, however, is not completely new, cf. Herrero et al. (2000, 2002). Reversing our *modus operandi* we obtain well fitted line cores but rather poor H_α profiles if we reduce \dot{M} by a factor of typically 1.5 - 2.

On the other hand, for those supergiants with $T_{\text{eff}} \leq 35,000$ K we either obtain a good fit quality for all Balmer lines or (in two cases) H_γ and/or H_β show too little wind emission in their cores.

“Generalized dilution effect”. Another prominent feature found in class I to III objects is the presence of the so-called “generalized dilution effect”.

“Historically”, this effect expresses the strengthening of the He I absorption lines with decreasing effective temperature (see Voels et al. 1989 and references therein) and has been invoked to explain certain deviations between synthetic line profiles from *plane-parallel* models and observations in cool O-supergiants: in this spectral range, one usually finds that a number of synthetic He I lines are considerably weaker than the observations, whereas this effect is most prominent for He I 4471.

The conventional explanation assumes that the lower levels of the corresponding transitions, $2^3S, 2^1S, 2^3P$, and 2^1P become overpopulated (with decreasing degree of overpopulation) because of the dilution of the radiation field in the (lower) wind. Note that the NLTE departure coefficients scale with the inverse of the dilution factor, since the ionization rates are proportional to this quantity (less ionization from a diluted radiation field), whereas the recombination rates remain unaffected.

Once more, this explanation is based on principal theoretical considerations, without any direct proof by actual simulations accounting for an extended atmosphere.

From the results of our simulations (which now include such a treatment), however, it is obvious that there still might be something missing in the above interpretation. In particular He I 4471 is still too weak in cooler supergiants, even if we account for a significant micro-turbulence (see above). Again, this finding is supported by previous investigations from Herrero et al. (2000, 2002).

Another consequence of the above theoretical scenario would be the following: For each of the lower He I levels under consideration, the lines belonging to *one* series should become less affected by the dilution of the radiation field with decreasing oscillator strength, since the line is formed at increasingly greater depths.

This would imply, e.g., that He I 6678 with lower level 2^1P (larger oscillator strength but less overpopulated lower level) should approximately be as strongly affected by dilution as He I 4471 (with lower level 2^3P). From our results, however, we can see that also this prediction does not hold if checked by simulations. A typical example is α Cam: Although He I 4471 is too weak, He I 6678 can perfectly be fitted.

At least for all other lines investigated, the prediction seems to hold. The weakest transitions in each series, i.e., the He I 4713 triplet line and the He I 4387 singlet line, give very good line fits and the same is true for He I 4922.

Hence, the only line with prominent generalized dilution effect (we keep this denotation) is He I 4471 and cannot be reproduced by our code even if line-blocking/blanketing is included. Similarly, it is rather improbable that a too large wind emission in the line core (as found for the blue Balmer lines) is the reason for this “defect”, since this problems seems to be present only in hotter supergiants. For the cooler ones, where He I 4471 is too weak, the line cores of all other lines are equally well described.

Thus, the actual origin of the dilution effect in He I 4471 is unclear, although a tight relation to either luminosity and/or the presence of a (strong) wind seems to be obvious: dwarfs do not suffer from this effect, no matter if early or late type dwarfs, as can be seen from the almost perfect fit quality of He I 4471 in these cases (Fig. 4.8).

On the other hand, all O-type class I and III objects between O6 and O9.5 show too weak He I 4471, whereas stars earlier than O6 behave like class V objects, i.e., they pose no problem.

The boundary for the onset of the dilution effect, however, is difficult to determine. Our model calculations of HD 210839 (O6 I(n) fp) which constitutes an upper boundary for the effect in class I objects reveal that a decrease in T_{eff} or β along with corresponding changes in \dot{M} helps to improve the H_γ , H_β and He I 4471 line fits, whereas the good fit quality for the other lines is lost in this case. The situation is similar for HD 190864 (O6.5 III(f)). No matter which sensible parametric alterations we applied, there were hardly any changes in He I 4471.

From these experiments, we estimate the upper boundary for the presence of the dilution effect to lie somewhere between O6 and O6.5 for class I and III objects.

It cannot be excluded, of course, that the discussed effect is a deficiency of the present version of FASTWIND. Combined UV/optical CMFGEN analyses by Crowther et al. (2002) and Hillier et al. (2003) for LMC/SMC supergiants do actually reproduce the strength of He I 4471 in parallel with the other lines, but the number of objects analyzed is still too low to allow for firm conclusions. Nevertheless, we are aware of the fact that a consistent calculation of the temperature structure (also in the outer wind) might be relevant for the formation of the He I 4471 line cores, particularly in the parameter space under consideration; since a new version of FASTWIND will include such a consistent temperature stratification, we will be able to report on any changes due to this improvement in forthcoming publications.

4.5 Comments on individual objects

In the following section we will give specific comments on peculiarities, problems and uncertainties for each individual object, starting with the hottest of each luminosity class and ordered according to derived T_{eff} .

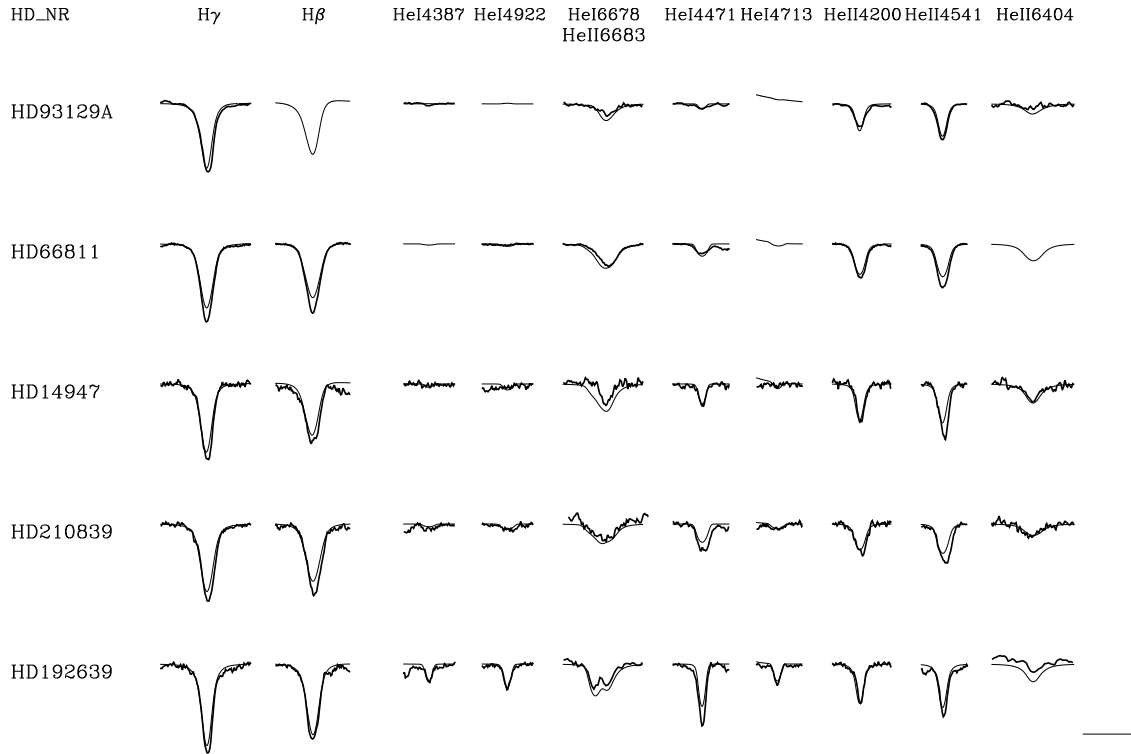


Figure 4.1: Line fits of supergiants with spectral types ranging from O3 to O7.5, ordered according to derived T_{eff} . The horizontal and vertical lines in the bottom right corner indicate the scale used and correspond to 20 Å in wavelength and 0.5 in units of the continuum, respectively (extending from 0.75 to 1.25.)

4.5.1 Supergiants

HD 93129A. The re-analysis of this object reveals a T_{eff} of 42,500 K (compared to $T_{\text{eff}} = 50,500$ K from Paper I) which constitutes the most significant change in T_{eff} found throughout the course of this investigation. The upper temperature limit lies at 45,000 K where the wings in the He II lines start to become too strong. Before a final statement concerning the effective temperature can be given, the nitrogen spectrum will have to be synthesized, of course.

The value of β has been constrained to 0.8 and the helium abundance to $Y_{\text{He}} = 0.1$. A larger helium abundance can be excluded since an increase in Y_{He} would yield too strong absorption troughs. The reader may note that this object was recently confirmed as a binary with a separation of 60 mas (Nelan et al. 2003, in prep.), where the components have been found to be similar with respect to their spectral types and masses. Thus, the observed spectrum might be significantly contaminated and the results of our analysis are somewhat artificial (especially concerning all radius dependent quantities such as mass, luminosity and mass-loss rate. If we assume that both components were actually identical, the values for radius, luminosity, mass and mass-loss rate given in Table 4.1 would have to be scaled by a factor of $2^{-1/2}$, $1/2$, $1/2$ and $2^{-3/4}$, respectively, in order to obtain the corresponding values for *one* component.) Note, however, that the deduced reduction in T_{eff} (as a consequence of severe

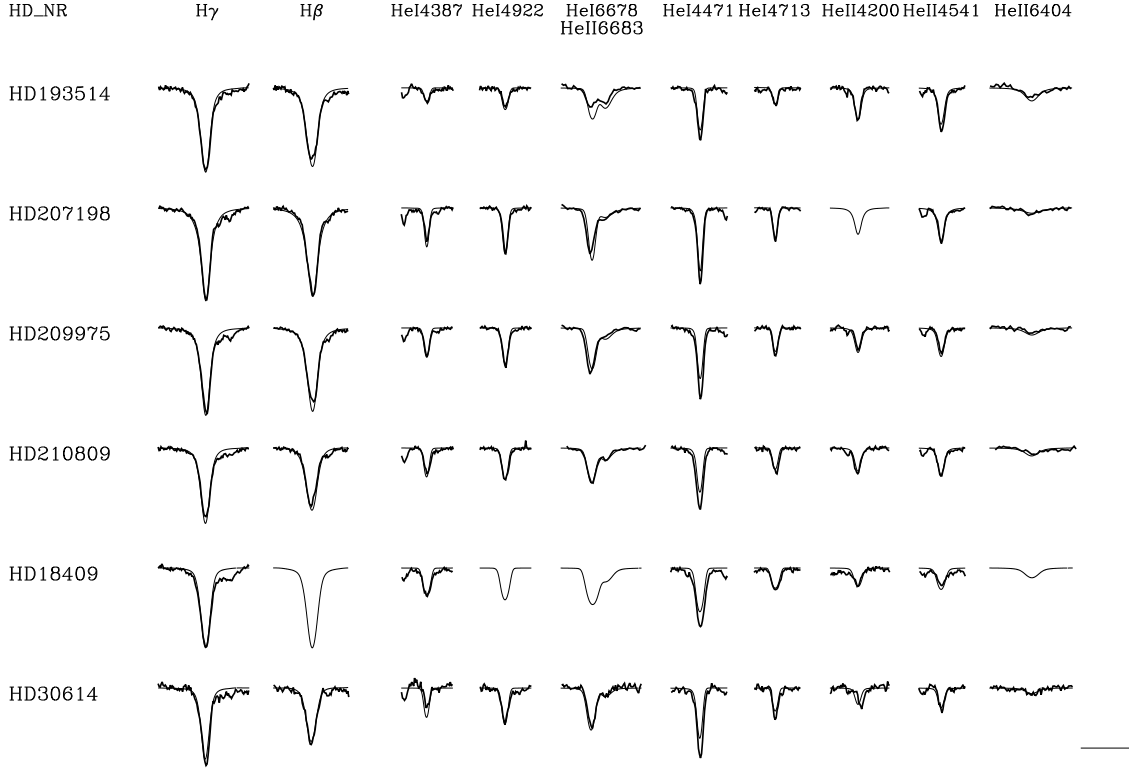


Figure 4.2: As Fig. 4.1, but for spectral types ranging from O7 to O9.7

line-blanketing) sounds reasonable and gives some clue about what would happen if the object were a single star.

Since the value for $V_r \sin i$ claimed by Howarth et al. (1997) significantly exceeds the value deduced by us (cf. Sect. 4.4), we have also determined an upper limit for this value. In order to obtain synthetic spectra consistent with the observations, this limit turned out to be 150 km s^{-1} , very close to the alternative value provided by Penny (1996).

HD 66811 (ζ Pup). For this star, as already discussed, the line cores of H_γ and H_β become too strongly filled in by wind emission if we use the mass-loss rate derived from a fit of H_α . In this case, we have concentrated on the red wing of H_α since the blue wing is known to be problematic (see also Paper I). In particular, the (strong) blue absorption trough cannot be reproduced by our models. It might be speculated whether this feature is related to an aspherical wind which should be present because of the large value of $V_r \sin i$ and which is supported by spectropolarimetric analyses carried out by Harries & Howarth (1996).

Compared to the results from Paper I, \dot{M} needed to be increased from 6.0 to $8.8 \cdot 10^{-6} M_\odot/\text{yr}$, mainly because β had to be reduced from 1.15 to 0.90 .

A lower limit for the mass-loss rate of $7.4 \cdot 10^{-6} M_\odot/\text{yr}$ can be inferred if we try to reproduce the line cores of H_γ , H_β and He II 4541; in this case, H_α and He II 4686 become much too weak,

of course. From these limits, however, it might be possible to derive tight constraints concerning the possibility of wind clumping (see Sect. 4.7.5).

Although the fit quality for He II 4200 is good, He II 4541 (with same lower level) appears too weak. The discrepancy between these two lines (which is evident also for the next two stars, HD 14947 and λ Cep) has already been discussed by Herrero et al. (1992, 2000) for plane-parallel and unified model atmospheres without line-blocking/blanketing, respectively. The inclusion of the latter effects does not resolve the problem. Interestingly, it seems to occur only in those cases where the line cores of H_γ and H_β are too weak.

HD 14947. The overall fit quality is good, but again no optimum solution for the line cores of the blue Balmer lines could be obtained. In order to match the profile shape of He II 4686, β had to be increased by 0.25 and \dot{M} to be decreased by 25% (from $8.5 \cdot 10^{-6} M_\odot/\text{yr}$ to $6.4 \cdot 10^{-6} M_\odot/\text{yr}$), compared to the values derived from H_α .

Since He I 4471 is the only He I line with considerable strength, the ionization equilibrium (and thus the effective temperature) remains somewhat uncertain, due to missing additional constraints.

The apparent discrepancy between the predicted and observed line profile of He II 6683 is partly due to an erroneous rectification.

HD 210839 (λ Cep). This star, as ζ Pup, is known to be a fast rotator with a projected rotational speed of $V_r \sin i = 200 \text{ km s}^{-1}$. Also the fit quality is very similar to ζ Pup: We find the same line core problems in H_γ and H_β and no possibility to obtain the observed P Cygni shape in H_α (again aspherical wind?). Note that HD 210839 is the first star with observable dilution effect. Note also that the rather large uncertainty in M_V (due to the distance problem discussed in Sect. 4.4) leads to correspondingly large error bars in $\log L$, \dot{M} and related quantities.

HD 192639. Our re-analysis gives a rather consistent fit of both the Balmer lines and the weak He I lines, with exception of the strong dilution effect observed in He I 4471.

For this star, we found the most striking discrepancy between theoretical prediction and observation in He II 4686, where theory predicts strong emission but a weak P Cygni shaped profile is observed instead. In order to fit this line appropriately, it would be necessary to decrease the mass-loss rate by more than 50% (from $\dot{M} = 6.3 \cdot 10^{-6} M_\odot/\text{yr}$ to $\dot{M} \approx 2.8 \cdot 10^{-6} M_\odot/\text{yr}$.) Note that this star has parameters and profiles similar to λ Cep. The latter is known to be strongly variable (cf. Herrero et al. 2000) and, thus, it might be possible that also for HD 192639 the apparent mismatch of H_α and He II 4686 might be partly related to wind variability: As pointed out in Sect. 4.3, the blue and red spectra have not been taken simultaneously, but with a temporal offset larger than the typical wind flow time which is of the order of a couple of hours.

The apparent bad fit of He II 6404 is solely due to an erroneous rectification.

HD 193514. The presence of a wind is evident from He II 4686 showing a weak emission. By comparing the star to HD 192639 which is of same spectral type with similar values for T_{eff} and $\log g$, we can see that the H_α line in the case of HD 193514 is in absorption, whereas in the case of HD 192639 it is in emission. Accordingly, the derived mass-loss rate for HD 193514 has half the value of HD 192639.

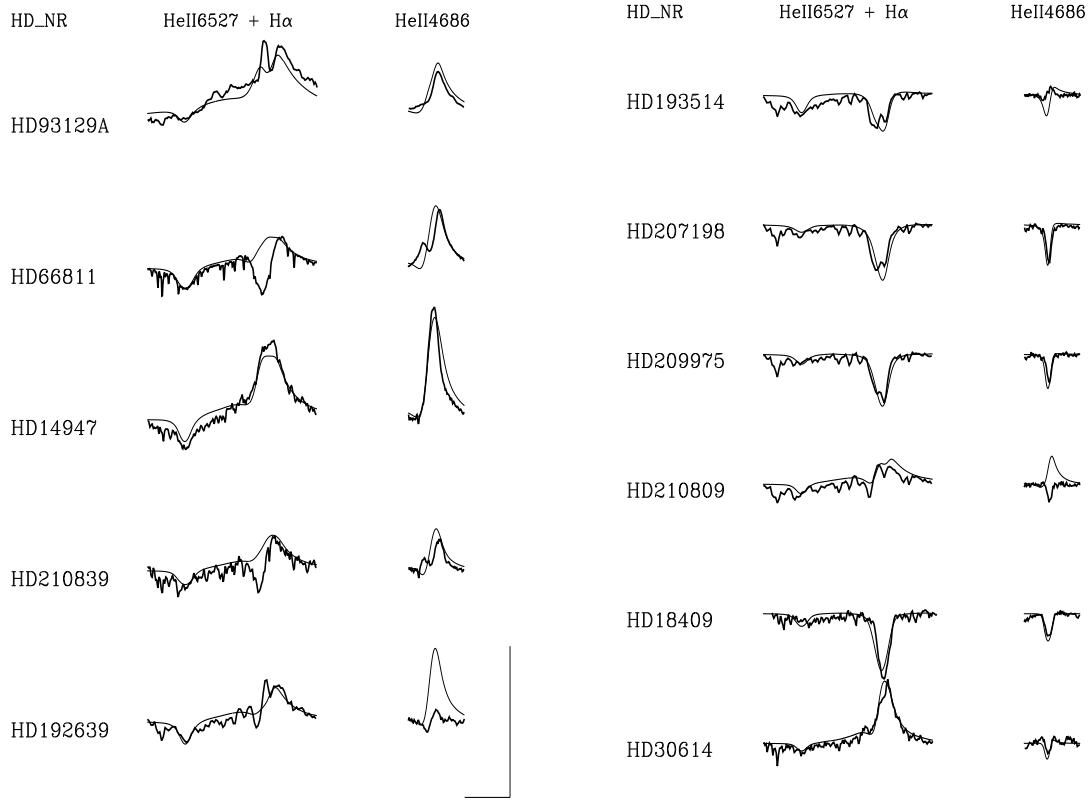


Figure 4.3: “Wind lines” of the hotter supergiants as in Fig. 4.1.

Figure 4.4: “Wind lines” of the cooler supergiants as in Fig. 4.2.

HD 207198. The fit quality for this sample star is very good (except for a small dilution effect in He I 4471), so no further comment is necessary.

HD 209975. The spectrum and line fit is very similar to HD 207198 and also the parameters deduced lie close together. Compared to HD 207198, this star has a slightly lower T_{eff} along with a 0.25 dex lower value for $\log g$. Note that the dilution effect in He I 4471 is considerably stronger.

HD 210809. For this star, the synthetic H_γ and H_β profiles are slightly too strong in *absorption*, in contrast to all cases encountered so far.

He II 4686 reveals a huge difference between theoretical prediction and observation. The theoretical emission feature as shown in Fig. 4.4 is similar to the one observed in HD 192639 (but not as prominent). In this temperature range, the line reacts strongly to small changes in temperature. Around a critical temperature of $T_{\text{eff}} = 30,000$ K, He II 4686 switches from absorption to emission, i.e., at that temperature we would be able to fit the line perfectly. Nevertheless, we have retained the higher value (31,500 K) since this value gives a more consistent fit concerning the remaining lines.

This discrepancy which points to some possible problems in our treatment of line-blocking around 303 Å (or could be also related to wind variability) will be accounted for in our error analysis when discussing the error bars for T_{eff} .

HD 18409. This star comprises a similar problem as found in HD 203064 and ξ Per (see below): The photospheric value of $V_r \sin i = 150 \text{ km s}^{-1}$ has to be reduced to $V_r \sin i = 80 \text{ km s}^{-1}$ in the case of H_α . Although this line is in absorption, we favor a value of $\beta = 0.85$ which improves the fit quality of the wings of H_α and He II 4686 moderately.

HD 30614 (α Cam). The effects of line blocking on T_{eff} are rather weak, and in order to obtain a convincing fit we had to decrease the helium abundance from $Y_{\text{He}} = 0.2$ to $Y_{\text{He}} = 0.10$. β turned out to be slightly larger than derived in Paper I (1.15 compared to 1.10). Note that the value derived for T_{eff} , 29,000 K, is identical to the value obtained via a UV-analysis performed by Pauldrach et al. (2001, WMBasic).

4.5.2 Giants

HD 15558. The line fits obtained are in good agreement with the observations and especially the Balmer lines give a consistent fit. T_{eff} was reduced by $\approx 13\%$ to 41,000 K, whereas the other parameters remained more or less at their old values (except for the rotational velocity which had to be adapted from 120 km s^{-1} to 150 km s^{-1}).

The rather small discrepancy between theoretical prediction and observation in the case of He II 4686 can be removed by increasing \dot{M} from $5.6 \cdot 10^{-6} M_\odot/\text{yr}$ to $6.5 \cdot 10^{-6} M_\odot/\text{yr}$.

HD 193682. As can be seen in Fig. 4.6, the red wings of H_α and of He II 4686 do not fit the observations perfectly, but constitute the best compromise concerning the overall fit quality of the spectrum.

The rotational speed $V_r \sin i$ was found to be 200 km s^{-1} , although with a value of 180 km s^{-1} an improved fit quality of the H_α line could be achieved.

Compared to the values from Paper I (which relied on the analysis by Herrero et al. 1992), the helium abundance, Y_{He} , needed to be drastically decreased, from 0.43 to 0.20. This reduction (obtained by requiring a comparable fit quality for all lines) is mainly a consequence of the reduction of T_{eff} by 5,000 K and the inclusion of the additional He lines in our analysis as described above.

HD 190864. The re-analysis gives a consistent fit for the Balmer lines and all He I and He II lines with exception of the dilution effect observed in He I 4471. Although T_{eff} had to be reduced by 4,000 K to 37,000 K, $\log g$ remained at its old value. Again, the helium abundance needed to be decreased, in this case from 0.2 to 0.15. A value of $\beta = 0.8$ was already suggested in Paper I, and also the differences in the derived mass-loss rates are negligible.

HD 203064. is an extremely rapid rotator with $V_r \sin i = 300 \text{ km s}^{-1}$ which is clearly visible in the broadened line profiles as shown in Fig. 4.5. The theoretical predictions agree well with the observations apart from the dilution effect in He I 4471.

The star behaves prototypical for a number of giants (and the supergiant HD 18409) with large values of $V_r \sin i$: Whereas H_γ and H_β reveal a consistent fit, only the line cores of H_α and He II 4686

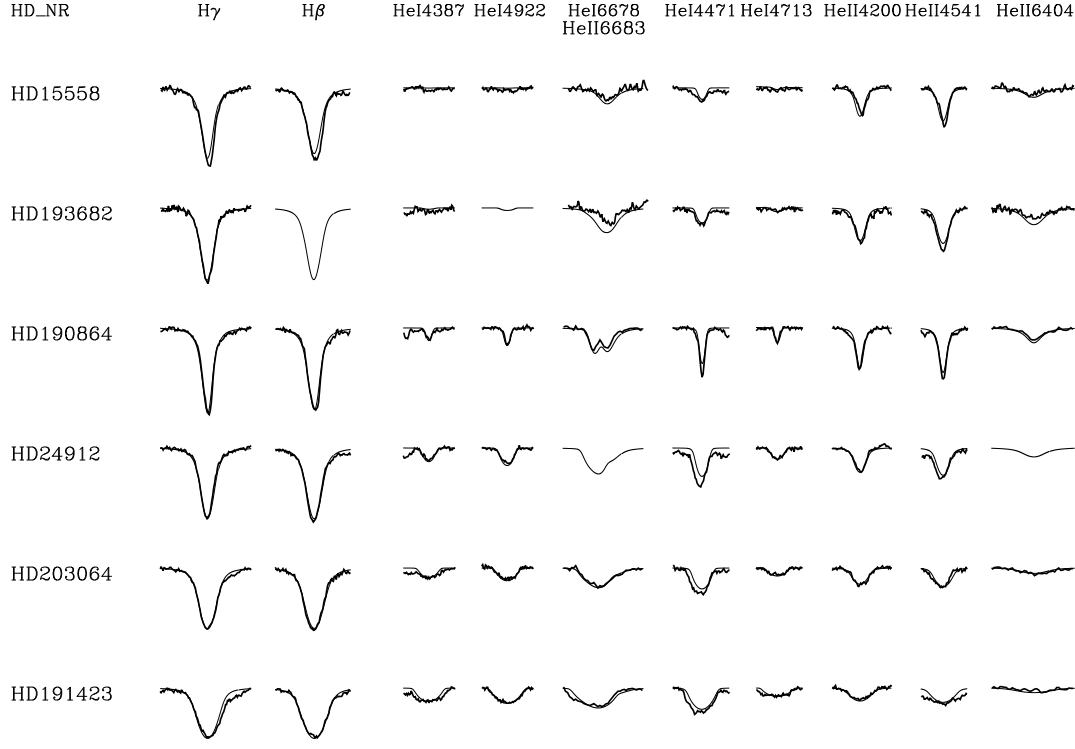


Figure 4.5: Line fits of the giant sample with spectral types ranging from O5 to O9, ordered according to derived T_{eff} .

are in agreement with the observations. The wings of both lines, however, are too narrow compared to the photospheric rotational speed and would be much more consistent if we used a lower value of 190 km s^{-1} (cf. Paper I and Sect. 4.8).

HD 24912 (ξ Per). The fit quality is good, with the exception of He I 4471 which apart from the generalized dilution effect also comprises a small error in rectification. Photospheric lines display a projected rotational speed of $V_r \sin i = 220 \text{ km s}^{-1}$, while H_α indicates a much lower value, $\lesssim 100 \text{ km s}^{-1}$ (for further comments see Paper I).

HD 191423. together with HD 149757 are the fastest rotators in the whole sample with a projected rotational speed of $V_r \sin i = 400 \text{ km s}^{-1}$. As for the previous two stars, the wings of H_α are too narrow compared to H_γ and H_β , corresponding to an “effective” value of 300 km s^{-1} .

Line blanketing leads to a reduction in T_{eff} by 1,500 K, and the mass-loss rate had to be increased by nearly a factor of two (from $\dot{M} = 0.2 \cdot 10^{-6} M_\odot/\text{yr}$ to $\dot{M} = 0.4 \cdot 10^{-6} M_\odot/\text{yr}$). Note that the profile points to a disk like structure as discussed in Paper I.

The derived helium abundance is larger than the one obtained by Villamariz et al. (2002, $Y_{\text{He}} = 0.14$). In essence, this difference is mainly due to the lower micro-turbulent velocity adopted by us.

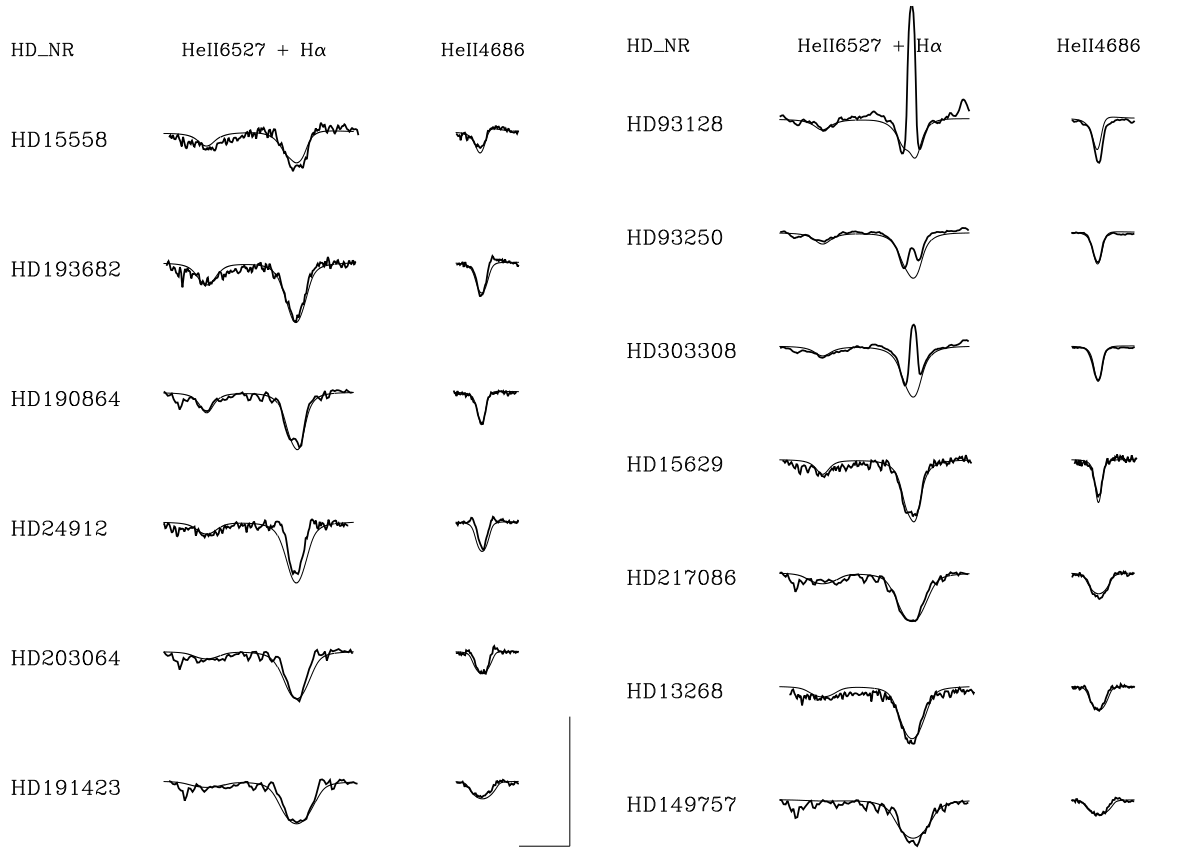


Figure 4.6: “Wind lines” of the giants as in Fig. 4.5.

Figure 4.7: “Wind lines” of the dwarfs as in Fig. 4.8.

4.5.3 Dwarfs

HD 93128. The H_{α} line cores of all dwarfs in our sample, which are located in Carina (HD 93128, HD 93250 and HD 303308), are contaminated by nebula emission which makes the determination of \dot{M} a somewhat difficult task. For HD 93128, we derive a mass-loss rate of $2.65 \cdot 10^{-6} M_{\odot}/\text{yr}$ which is roughly a factor of two higher than the value obtained in Paper I. This value is an upper limit (the lower one is given in the next section) and has been used to calculate the final model. Line-blanketing leads to a decrease in T_{eff} from 52,000 K to 46,500 K without changing $\log g$. With $\beta = 0.85$ we were able to improve the fit of the wings of H_{α} , although this procedure turned out to be rather difficult due to the contamination by nebula emission.

HD 93250. The profiles are generally very similar to HD 93128, although HD 93250 seems to be less affected by line-blanketing effects. We had to reduce T_{eff} to 46,000 K (from the older value of 50,500 K), again with no changes in $\log g$. \dot{M} is decreased by $1.4 \cdot 10^{-6} M_{\odot}/\text{yr}$ to $3.5 \cdot 10^{-6} M_{\odot}/\text{yr}$, for a value of $\beta = 0.90$ which resulted from a compromise between the fit of the line core and the wings of both H_{α} and He II 4686.

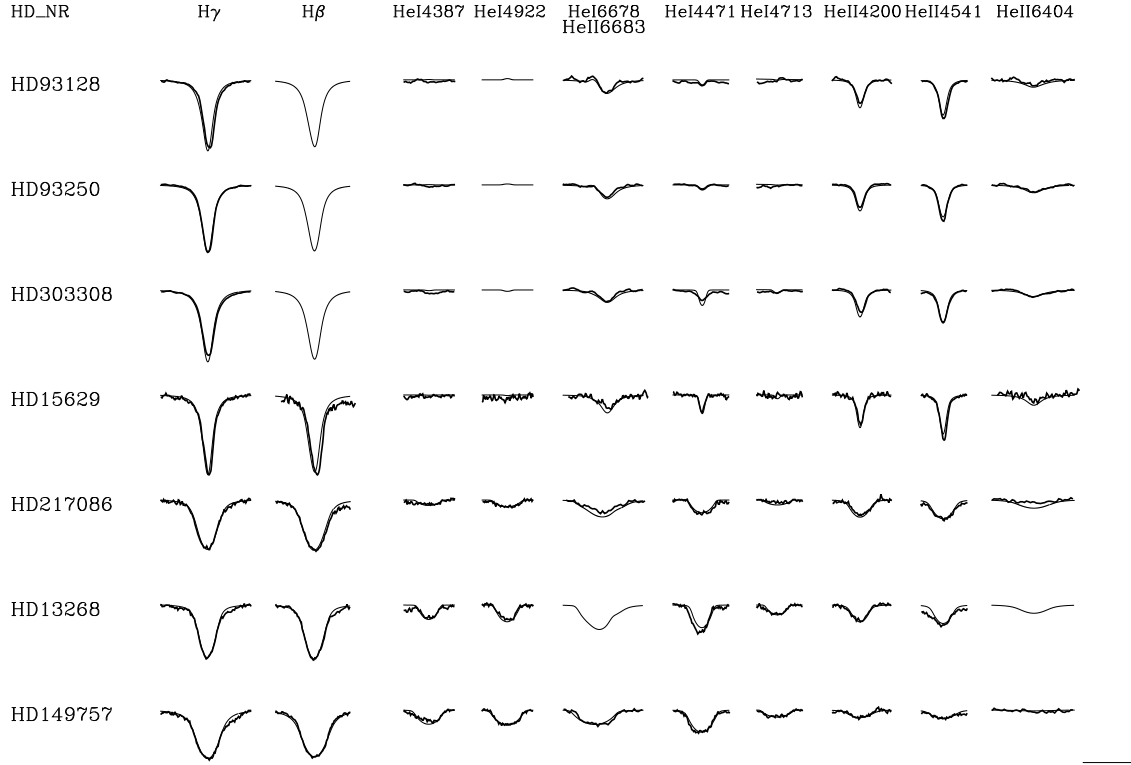


Figure 4.8: Line fits of the dwarf sample with spectral types ranging from O3 to O9, ordered according to derived T_{eff} .

HD 303308. For this sample star we had to apply a relatively large T_{eff} -correction of 7,000 K (to 41,000 K) along with a change in $\log g$ of 0.15 dex (to 3.90). \dot{M} is slightly reduced, whereas the rotational speed had to be increased from 100 km s^{-1} to 120 km s^{-1} . Interestingly, our model calculations display an under-abundance in helium, $Y_{\text{He}} = 0.075$. The star is a “very likely” binary with a separation of approximately 14 mas (Nelán et al. 2003, in prep.), implying that the results might be somewhat artificial. However, from the rather good fit quality of the profiles, the contamination brought about by the companion seems to be negligible.

HD 15629. For this star, T_{eff} needed to be decreased quite drastically, from 47,000 K to 40,500 K with an appropriate adjustment of $\log g$ to 3.70. The mass-loss rate is moderate ($\dot{M} = 1.3 \cdot 10^{-6} M_{\odot}/\text{yr}$) but almost twice as high as deduced in Paper I. The fit quality is generally good, and we confirm the helium deficiency to be $Y_{\text{He}} = 0.08$ as found in Paper I and by Herrero et al. (2000).

HD 217086. For both the Balmer and the He I lines we obtain a very good fit quality, but there are still small discrepancies for He II 6683 and He II 6404 which constitutes a problem in other sample stars as well. However, usually they occur only in stars with low rotational speed. HD 217086 is a fast rotator with $V_{\text{r}} \sin i = 350 \text{ km s}^{-1}$ and exhibits very broad line profiles as shown in Fig. 4.8 and

Fig. 4.7. According to Paper I there is a difference in the photospheric and the “effective” rotational velocity of 85 km s^{-1} which could not be confirmed in our present analysis. The upper limit for the mass-loss rate was found to be $0.23 \cdot 10^{-6} \text{ M}_{\odot}/\text{yr}$ for an adopted $\beta = 0.80$.

HD 13268. Although being a fast rotator with $V_r \sin i = 300 \text{ km s}^{-1}$, the photospheric value, again, applies to the H_{α} profile (in contrast to the findings from Paper I). For the mass-loss rate only an upper limit of $0.26 \cdot 10^{-6} \text{ M}_{\odot}/\text{yr}$ can be given, for an adopted value of $\beta = 0.80$. The enhanced helium abundance $Y_{\text{He}} = 0.25$, as given in Paper I, was retained giving the best compromise especially in the case of $\text{He II } 4541$ which is still slightly too weak.

HD 149757 (ζ Oph). finally, is a very fast rotator ($V_r \sin i = 400 \text{ km s}^{-1}$), but also here the photospheric lines and H_{α} display the same broadening, i.e., the discrepancy found in Paper I could not be confirmed. We obtained a mass-loss rate of $0.18 \cdot 10^{-6} \text{ M}_{\odot}/\text{yr}$ as an upper limit. This value was used for our final model calculation and is considerably higher than previously determined, where \dot{M} was found to be $\approx 0.03 \cdot 10^{-6} \text{ M}_{\odot}/\text{yr}$. Moreover, the “old” helium abundance of $Y_{\text{He}} = 0.19$ could be slightly decreased to 0.17 giving a very good fit quality as displayed in the corresponding figures.

4.6 Error Analysis

In the following section we will discuss the errors estimated (and derived) for the parameters given in Table 4.1 which will be needed for our further analysis.

4.6.1 Stellar parameters (cf. Table 4.4)

Effective temperatures. The formal errors in T_{eff} , estimated from the quality of the helium line fits, generally lie between $\pm 1,000 \text{ K}$ and $\pm 1,500 \text{ K}$ (Table 4.2 to 4.3, cf. also Herrero et al. 1992, 2002) with two exceptions: The upper temperature limit for HD 93129A (neglecting its binary status) lies at $45,000 \text{ K}$, in contrast to the temperature of our final, best-fitting model at $42,500 \text{ K}$. Although somewhat artificial, we will not discard this star from our analysis for the sake of completeness and assume ΔT_{eff} to be of the order of $\pm 2,500 \text{ K}$. The second case with larger error bars in T_{eff} constitutes HD 210809 for which we also adopt an error of $\pm 2,500 \text{ K}$, due to the dilemma concerning $\text{He II } 4686$ (cf. Sect. 4.5). Since we found the critical temperature, where this line switches from absorption to emission, to be located at $T_{\text{eff}} = 30,000 \text{ K}$ (compared to $T_{\text{eff}} = 31,500 \text{ K}$ for our final model), we added this additional uncertainty in our model (i.e., $1,500 \text{ K}$) to the usual error of $1,000 \text{ K}$.

Gravities. The errors in the derived $\log g$ -values, $\Delta \log g$, were consistently taken to be ± 0.10 due to the rather good fit quality of the Balmer line wings. It has to be noted, however, that these values are “only” *effective* values, contaminated by the centrifugal forces present due to rotation. In order to obtain the “true” gravities needed to calculate the masses, one has to apply a “centrifugal correction”. This has previously been done by Herrero et al. (1992) and Vacca et al. (1996), who argued that the centrifugal acceleration averaged over the stellar disk can be approximated by the projected centrifugal velocity,

$$\langle g_{\text{cent}} \rangle = \frac{\langle (V_{\text{rot}} \sin \theta)^2 \rangle}{R_{\star}} \approx \frac{(V_{\text{rot}} \sin i)^2}{R_{\star}}, \quad (4.3)$$

where θ is the stellar co-latitude. However, in neither of these publications this expression has been actually *derived*, and we could not find such a derivation anywhere. Since such a derivation is inevitable, especially with respect to a thorough error analysis, we decided to calculate the desired centrifugal correction from first principles. In Appendix A, we have outlined the solution of the problem, and it turned out (neglecting any distortion of the stellar radius) that Eq. 4.3 is correct, and that the underlying errors (originating mostly from statistical arguments) can be summarized by

$$\frac{\Delta\langle g_{\text{cent}} \rangle^2}{\langle g_{\text{cent}} \rangle^2} \approx \left(\frac{\Delta R_\star}{R_\star} \right)^2 + \left(\frac{\Delta f}{f} \right)^2, \text{ with} \quad (4.4)$$

$$\frac{\Delta f}{f} \approx \frac{3}{4 \pm \sqrt{5} - 1} \approx {}^{+0.61}_{-0.23}, \quad (4.5)$$

assuming that the projected rotational velocities can be measured with high precision. Since

$$g_{\text{true}} = g + \langle g_{\text{cent}} \rangle,$$

the total error of the “true” gravity follows from

$$(\Delta \log g_{\text{true}})^2 \approx \frac{(g \Delta \log g)^2 + (\langle g_{\text{cent}} \rangle \Delta \log \langle g_{\text{cent}} \rangle)^2}{g_{\text{true}}^2}, \quad (4.6)$$

with

$$\Delta \log \langle g_{\text{cent}} \rangle = \log \left(1 + \frac{\Delta \langle g_{\text{cent}} \rangle}{\langle g_{\text{cent}} \rangle} \right) \approx \frac{\Delta \langle g_{\text{cent}} \rangle}{\langle g_{\text{cent}} \rangle} \log e. \quad (4.7)$$

Remarkably, the error in $\log g_{\text{true}}$ is of the same order as the adopted error for $\log g$, i.e., 0.1 (and sometimes even smaller), since the true gravity can become considerably larger than the effective value due to the centrifugal correction, whereas the error with respect to this correction remains rather low.

Helium abundance. The model calculations of both HD 303308 and HD 15629 show an under-abundance in helium of $Y_{\text{He}} = 0.075$ and $Y_{\text{He}} = 0.08$, respectively. Due to the good fit quality of the He I and He II lines (see Figs. 4.8 and 4.7) and the low values found for Y_{He} , only small variations are possible. We, therefore, estimate an error of not more than $\Delta Y_{\text{He}} = +0.02 / -0.01$. In the case of HD 303308 the formal under-abundance might be easily explained by its binarity, i.e., by a possible contamination from the companion, but in the case of HD 15629 the situation is different. For this star we found the same value as determined by Herrero et al. (1992), although we have used a completely different code and accounted for line-blocking/blanketing. Since it would be very difficult to justify such an under-abundance in physical terms, we refrain from any explanation and will keep this star in mind as an objective for further investigations.

For stars with “normal” helium abundance (i.e., $Y_{\text{He}} = 0.10$), the fit quality is good and suggests an error of $\Delta Y_{\text{He}} = \pm 0.02$.

For objects with slightly increased values in Y_{He} (i.e., $Y_{\text{He}} = 0.12$ to 0.15), we deduced an error in helium abundance of $\Delta Y_{\text{He}} = \pm 0.03$ which is consistent with the values given by Herrero et al. (2002). The last “group” of stars are those for which we found a definite over-abundance in helium, i.e., $Y_{\text{He}} = 0.20$ to 0.25 . The error estimate is the same as before, namely $\Delta Y_{\text{He}} = \pm 0.03$. Even for HD 13268 with the highest abundance found throughout our analysis ($Y_{\text{He}} = 0.25$), we estimate an error of the same order, since the fit quality is extremely good.

Radii. As is well known, one of the largest sources of error concerning any *derived* parameter (mass, luminosity and mass-loss rate, see below) *for Galactic objects* comprises the uncertainty in the stellar radius due to uncertain distances or absolute visual magnitudes M_V , respectively. For a thorough discussion we refer the reader to Markova et al. (2003); in the present investigation we adopt a general uncertainty of $\Delta M_V = \pm 0.3$ as a representative value for all our objects. Although the individual $1\text{-}\sigma$ values are different and smaller in most cases, we adopt this value in view of the different sources from which our data is derived. The only exceptions are ζ Pup and λ Cep, for which larger uncertainties (± 0.43 and ± 0.5 mag) are adopted, as explained in Sect 4.4.

Since we calculate the stellar radius from both M_V and theoretical model fluxes (Eq. 4.1) and since $H_\lambda \approx B_\lambda(T_{\text{rad}}) \propto T_{\text{eff}}$ in the V-band (Sect. 4.4), the corresponding error is given by

$$\begin{aligned}\Delta \log R_\star &\approx 0.2 \sqrt{(\Delta M_V)^2 + (2.5 \Delta \log T_{\text{eff}})^2}, \\ \Delta \log T_{\text{eff}} &= \log \left(1 + \frac{\Delta T_{\text{eff}}}{T_{\text{eff}}} \right).\end{aligned}\tag{4.8}$$

With the above estimates for ΔM_V and ΔT_{eff} , the error in the stellar radius is dominated by the uncertainty in M_V and is of the order of $\Delta \log R_\star \approx \pm 0.06$, i.e., roughly 15 %.

4.6.2 Wind parameters (cf. Table 4.2 and 4.3)

All terminal velocities, v_∞ , which have been taken from Paper I, were found to be subjected to an uncertainty of approximately 10% as shown by Haser (1995). Here and in the following, we will neglect this uncertainty with respect to its influence on the derived mass-loss rate.

In order to address the errors in the wind-parameters \dot{M} and β (which are intimately coupled), we first have to consider the fact that any line-fit to H_α does not allow to specify \dot{M} itself, but only the quantity Q , as extensively discussed in Paper I,

$$Q = \frac{\dot{M}}{R_\star^{1.5}}\tag{4.9}$$

The logarithmic error of this quantity can be calculated from the uncertainty in \dot{M} at a *given* value for R_\star , i.e.,

$$\Delta \log Q = \log \left(1 + \frac{\Delta \dot{M}}{\dot{M}} \right)_{R_\star = \text{const}}\tag{4.10}$$

Remember that any change of R_\star leads to an identical fit if \dot{M} is adapted in such a way that Q remains constant.⁴

Thus, before we calculate the total error in mass-loss rate which depends on both the error in Q and in R_\star via

$$\Delta \log \dot{M} = \sqrt{(\Delta \log Q)^2 + \left(\frac{3}{2} \Delta \log R_\star\right)^2},\tag{4.11}$$

we have to consider the errors in Q alone. For this purpose, we distinguish between two cases:

⁴Except for objects which lie close to the Eddington-limit, where the actual value of R_\star has a direct impact on the photospheric structure.

Table 4.2: *Stars with H_α in emission*: Errors in stellar and wind parameters given in Table 4.1. ΔT_{eff} in kK, $\Delta\beta$ adopted as ± 0.1 , $\Delta\log Q_1$ is the error in Q -value due to uncertainties in H_α line fit, $\Delta\log Q_2$ is the error in Q -value arising from uncertainties in T_{eff} and $\Delta\log Q_t$ is the total error. All values have to be preceded by a \pm sign.

Star	ΔT_{eff}	$\Delta\log Q_1$	$\Delta\log Q_2$	$\Delta\log Q_t$
HD 93129A	2.5	0.02	.04	0.047
HD 66811	1.5	0.02	.03	0.035
HD 14947	1.5	0.02	.03	0.036
HD 210839	1.5	0.04	.03	0.051
HD 192639	1.5	0.03	.035	0.045
HD 210809	2.5	0.04	.065	0.075
HD 30614	1.0	0.04	.03	0.049

Table 4.3: *Stars with H_α in absorption*: Errors in stellar and wind parameters given in Table 4.1. Notation and units as in Table 4.2, except for the adopted uncertainty in β and the corresponding uncertainty in \dot{M} (for stellar radii from Table 4.1, see text). The upper and lower limits of \dot{M} (in units of $10^{-6}M_\odot/\text{yr}$) correspond to the lower and upper limits of β , respectively. The listed errors in T_{eff} and $\log Q_2$ (cf. Table 4.2) have to be preceded by a \pm sign.

Star	ΔT_{eff}	$\Delta\beta$	\dot{M}_1^-	\dot{M}_1^+	$\Delta\log Q_2$	$\Delta\log Q_t$
HD 93128	1.5	$+0.15$ -0.15	1.59	3.70	0.023	$+0.15$ -0.22
HD 93250	1.5	$+0.10$ -0.10	2.58	3.87	0.023	$+0.05$ -0.13
HD 303308	1.5	$+0.20$ -0.10	1.35	2.00	0.027	$+0.09$ -0.09
HD 15558	1.5	$+0.20$ -0.10	3.84	6.31	0.027	$+0.06$ -0.16
HD 193682	1.5	$+0.20$ -0.10	0.94	2.16	0.028	$+0.10$ -0.27
HD 15629	1.0	$+0.20$ -0.10	0.85	1.55	0.018	$+0.08$ -0.18
HD 190864	1.0	$+0.20$ -0.10	0.97	1.85	0.020	$+0.13$ -0.16
HD 193514	1.5	$+0.20$ -0.10	2.90	4.16	0.033	$+0.08$ -0.09
HD 24912	1.0	$+0.20$ -0.10	0.74	1.29	0.022	$+0.08$ -0.17
HD 203064	1.0	$+0.20$ -0.10	0.94	1.77	0.022	$+0.10$ -0.18
HD 217086	1.0	$+0.20$ -0.10	≤ 0.05	≤ 0.33	0.021	$+0.17$ -0.68
HD 13268	1.0	$+0.20$ -0.10	≤ 0.12	≤ 0.34	0.024	$+0.13$ -0.33
HD 207198	1.0	$+0.20$ -0.10	1.29	2.33	0.024	$+0.12$ -0.14
HD 209975	1.0	$+0.20$ -0.10	1.55	2.28	0.025	$+0.04$ -0.14
HD 18409	1.5	$+0.15$ -0.15	0.74	1.54	0.040	$+0.18$ -0.14
HD 191423	1.0	$+0.20$ -0.10	≤ 0.28	≤ 0.46	0.024	$+0.06$ -0.17
HD 149757	1.0	$+0.20$ -0.10	≤ 0.04	≤ 0.25	0.024	$+0.14$ -0.65

Table 4.4: Parameters and corresponding errors for our sample stars. For errors in T_{eff} and $\log Q$, see Table 4.2, 4.3. All quantities are given in the same units as in Table 4.1. D_{mom} denotes the modified wind-momentum rate (Eq. 4.14) and is given in cgs-units. Note that all values quoted for HD 93129A and HD 303308 may (strongly) suffer from a possible contamination by a companion. Only the values for T_{eff} , $\log g$, Y_{He} and Q (which are more or less independent of V) might be considered to be of correct order of magnitude.

Star	$\log g_{\text{true}}$	$\Delta \log g_{\text{true}}$	R_*	ΔR_*	Y_{He}	ΔY_{He}	$\log L$	$\Delta \log L$	M_*	ΔM_*	$\log \dot{M}$	$\Delta \log \dot{M}$	$\log D_{\text{mom}}$	$\Delta \log D_{\text{m}}$
HD93129A	3.71	+0.10 -0.10	22.5	+3.4 -3.0	0.10	± 0.02	6.17	+0.16 -0.16	94.8	+41.3 -28.8	-4.58	+0.10 -0.10	30.40	+0.14 -0.14
HD93128	4.01	+0.10 -0.10	10.4	+1.5 -1.3	0.10	± 0.02	5.66	+0.13 -0.13	39.8	+17.2 -12.0	-5.58	+0.17 -0.24	29.22	+0.19 -0.26
HD93250	3.96	+0.10 -0.10	15.9	+2.4 -2.1	0.10	± 0.02	6.01	+0.13 -0.13	83.3	+36.0 -25.1	-5.46	+0.11 -0.16	29.45	+0.14 -0.18
HD66811	3.59	+0.09 -0.09	19.4	+4.3 -3.5	0.20	± 0.03	5.90	+0.18 -0.19	53.9	+30.8 -19.5	-5.06	+0.13 -0.13	29.74	+0.18 -0.18
HD303308	3.91	+0.10 -0.10	11.5	+1.7 -1.5	0.075	+0.02 -0.01	5.53	+0.14 -0.14	39.0	+16.8 -11.7	-5.79	+0.13 -0.13	29.03	+0.16 -0.16
HD14947	3.48	+0.10 -0.09	16.8	+2.5 -2.2	0.20	± 0.03	5.70	+0.14 -0.14	30.7	+13.1 -9.2	-5.07	+0.10 -0.10	29.71	+0.13 -0.13
HD15558	3.81	+0.10 -0.10	18.2	+2.7 -2.4	0.10	± 0.02	5.93	+0.14 -0.14	78.7	+33.8 -23.7	-5.25	+0.11 -0.19	29.62	+0.14 -0.21
HD193682	3.65	+0.09 -0.09	13.1	+2.0 -1.7	0.20	± 0.02	5.60	+0.14 -0.14	27.9	+11.7 -8.2	-5.76	+0.14 -0.28	29.04	+0.16 -0.30
HD15629	3.71	+0.10 -0.10	12.8	+1.9 -1.7	0.08	+0.02 -0.01	5.60	+0.13 -0.13	30.4	+13.1 -9.1	-5.89	+0.12 -0.20	28.96	+0.15 -0.22
HD210839	3.58	+0.09 -0.09	21.1	+5.5 -4.4	0.10	± 0.02	5.83	+0.21 -0.21	62.2	+41.5 -24.9	-5.16	+0.16 -0.16	29.65	+0.21 -0.21
HD190864	3.57	+0.10 -0.10	12.3	+1.8 -1.6	0.15	± 0.03	5.41	+0.13 -0.13	20.3	+8.7 -6.1	-5.86	+0.16 -0.18	28.88	+0.18 -0.20
HD192639	3.47	+0.10 -0.10	18.7	+2.8 -2.4	0.20	± 0.03	5.68	+0.14 -0.14	37.5	+16.1 -11.2	-5.20	+0.10 -0.10	29.57	+0.14 -0.14
HD193514	3.32	+0.10 -0.10	19.3	+2.9 -2.5	0.10	± 0.02	5.68	+0.14 -0.14	28.2	+12.1 -8.5	-5.46	+0.12 -0.13	29.33	+0.15 -0.16
HD24912	3.56	+0.09 -0.09	14.0	+2.1 -1.8	0.15	± 0.03	5.42	+0.13 -0.13	26.1	+10.9 -7.6	-5.97	+0.12 -0.19	28.80	+0.15 -0.21
HD203064	3.60	+0.09 -0.08	15.7	+2.3 -2.0	0.10	± 0.02	5.50	+0.13 -0.13	35.9	+14.9 -10.3	-5.85	+0.13 -0.20	28.95	+0.16 -0.22
HD217086	3.72	+0.10 -0.08	8.6	+1.3 -1.1	0.15	± 0.03	5.05	+0.13 -0.13	14.2	+6.3 -4.0	≤ -6.64	+0.19 -0.68	≤ 28.03	+0.21 -0.69
HD13268	3.48	+0.11 -0.08	10.3	+1.5 -1.3	0.25	± 0.03	5.05	+0.13 -0.13	11.7	+5.2 -3.3	≤ -6.59	+0.16 -0.34	≤ 28.05	+0.18 -0.36
HD210809	3.12	+0.10 -0.10	21.2	+3.3 -2.8	0.14	± 0.03	5.60	+0.18 -0.19	21.7	+9.4 -6.6	-5.28	+0.12 -0.12	29.51	+0.15 -0.15
HD207198	3.46	+0.10 -0.10	16.6	+2.5 -2.2	0.12	± 0.03	5.47	+0.13 -0.13	29.0	+12.5 -8.7	-5.75	+0.15 -0.17	28.99	+0.17 -0.19
HD30614	2.99	+0.10 -0.10	32.5	+4.8 -4.2	0.10	± 0.02	5.83	+0.13 -0.14	37.6	+16.1 -11.2	-5.22	+0.10 -0.10	29.53	+0.14 -0.14
HD209975	3.22	+0.10 -0.10	22.9	+3.4 -3.0	0.10	± 0.02	5.69	+0.13 -0.13	31.4	+13.4 -9.4	-5.67	+0.10 -0.17	29.12	+0.13 -0.19
HD18409	3.04	+0.09 -0.09	16.3	+2.5 -2.1	0.14	± 0.03	5.29	+0.15 -0.15	10.6	+4.4 -3.1	-5.99	+0.20 -0.17	28.66	+0.22 -0.19
HD191423	3.60	+0.11 -0.08	12.9	+1.9 -1.7	0.20	± 0.03	5.23	+0.13 -0.13	24.6	+11.2 -7.0	≤ -6.39	+0.11 -0.19	≤ 28.03	+0.14 -0.22
HD149757	3.85	+0.10 -0.08	8.9	+1.3 -1.1	0.17	± 0.03	4.87	+0.13 -0.13	20.2	+8.8 -5.7	≤ -6.75	+0.17 -0.66	≤ 27.72	+0.19 -0.66

- *Stars with H_α in emission* (cf. Table 4.2). \dot{M} and β are fit parameters and determined from the H_α profile itself (for specified R_\star). The influence of β on the profile shape (specifically on the central emission peak and also on the part where the wings start to form) is so large that it can be determined in parallel with the mass-loss rate. In this case, we adopt $\Delta\beta = \pm 0.1$; the corresponding error in the mass-loss rate, which directly translates into the corresponding error in the Q -value, $\Delta\log Q_1$, has been estimated from the requirement that within these errors the fit quality of H_α should remain reasonable. Note, however, that the uncertainty in mass-loss rate (Q -value) depends also on the error in effective temperature, ΔT_{eff} , because of the accompanying change in the ionization/excitation equilibrium of hydrogen. The corresponding error, $\Delta\log Q_2$, has been estimated using Eqns. (48, 49) in Paper I which covers this effect.⁵ The total error arising from both effects (line-fit and ΔT_{eff}), $\Delta\log Q_t$, follows from the usual error propagation assuming both error sources to be independent. From the results presented in Table 4.2, the typical (total) error in $\log Q$ (which would also be the total error in $\log \dot{M}$ if the radius were known to high precision) is of the order of 0.05 dex, i.e., 12%. Only for HD 210809, the error is of the order of 20% mainly because of the larger uncertainty in T_{eff} (see above).
- *Stars with H_α in absorption* (cf. Table 4.3). For stars with absorption profiles a different approach has to be applied since β can no longer be derived from the profile shape (with exception of a few cases which we have commented on in the previous section). Instead, it has to be adopted from theoretical considerations, and we used $\beta = 0.8$ as discussed in Sect. 4.4. Note that the derived mass-loss rate (actually the derived Q -value) is valid only for this specific value and that the dependence of Q on β is much stronger for absorption than for emission type profiles (cf. Fig. 15 in paper I). Thus, in order to obtain reliable error estimates for Q , we varied β within reasonable limits and deduced, for a specified value of R_\star , the corresponding upper and lower boundaries of the mass-loss rate from the fit to the observed profiles.

Generally, \dot{M} will become smaller if β is increased and vice versa. In particular, we have varied β typically by (+0.2/-0.1) to obtain i) a conservative lower limit for \dot{M} and ii) to exclude β values below 0.7 (which are difficult to justify theoretically). Only in those case where we were able to constrain β due to additional arguments (cf. Sect. 4.5), the “allowed range” of β could be (moderately) reduced. The specific values chosen for β_{min} and β_{max} as well as the errors in \dot{M} estimated in such a way are listed in Table 4.3. Together with the small influence of ΔT_{eff} , we obtain typical uncertainties in $\Delta\log Q_t$ between 0.1 to 0.2 dex, i.e., of the order of 25... 60%, which indicates the lower quantity of the derived mass-loss rates if H_α is in absorption (cf. Paper I and Kudritzki & Puls 2000).

For stars with extremely low mass-loss rates, where only an upper limit of \dot{M} could be deduced (HD 217086, HD 13268, HD 191423 and HD 149757), the same procedure has been applied, such that the derived limiting values, \dot{M}^+ and \dot{M}^- , are also only upper limits. Note the extreme uncertainty in \dot{M} for HD 217086 and HD 149757.

4.6.3 Derived Quantities (cf. Table 4.4)

So far, we have considered the errors for the quantities which can actually be “measured” from a spectroscopic analysis, i.e., T_{eff} , $\log g_{\text{eff}}$, Y_{He} , Q and, to a lesser extent, $\log g_{\text{true}}$, β , and R_\star . In the

⁵In order to account for the effects of line-blanketing incorporated in the present work, we have used $T_{\text{rad}} \approx 0.9 T_{\text{eff}}$, cf. Sect. 4.7.2

following, we briefly summarize the errors in the *derived* quantities which are needed for our further interpretation in order to assess the achieved accuracy. All values are presented in Table 4.4.

At first, the error in luminosity is given by

$$\Delta \log L \approx \sqrt{(4 \Delta \log T_{\text{eff}})^2 + (2 \Delta \log R_{\star})^2} \quad (4.12)$$

and results in $\Delta \log L \approx \pm 0.14$, i.e., the influence of the error in R_{\star} is somewhat larger than that in T_{eff} . The error in mass,

$$\Delta \log M \approx \sqrt{(\Delta \log g_{\text{true}})^2 + (2 \Delta \log R_{\star})^2} \quad (4.13)$$

is rather large and suffers, again, from the uncertainty in radius. The error in \dot{M} is found from the errors in $\log Q$ and in $\log R_{\star}$ (Eq. 4.11). Finally, the modified wind-momentum rate, D_{mom} , is given by

$$D_{\text{mom}} = \dot{M} v_{\infty} \left(\frac{R_{\star}}{R_{\odot}} \right)^{0.5} = Q v_{\infty} \left(\frac{R_{\star}}{R_{\odot}} \right)^2, \quad (4.14)$$

where the corresponding error has to be calculated from the second equality, since Q (and not \dot{M}) is the actual fit quantity. The typical errors in $\log D_{\text{mom}}$ are of the same order as the errors in $\log L$ which will result in a more or less quadratic error box when plotting the wind-momentum luminosity relation.

4.7 Discussion

4.7.1 The effective temperature scale for Galactic O-stars

Our analysis was carried out using a large sample of spectral subtypes ranging from O2 to O9.5 enabling us to obtain a temperature scale for O supergiants, giants, and dwarfs. Fig. 4.9 displays our current calibration of T_{eff} vs. spectral type for Galactic O-type stars. From this plot, we conclude that the influence of line-blanketing redefines this temperature scale significantly. Supergiants of spectral type O2 to O9.5 are now located between roughly 43,000 K and 30,000 K (if we assume that the effective temperature of HD 93129A is not too wrong), whereas dwarfs of spectral type O3 to O9 are located between 47,000 K and 32,000 K.

Our results indicate a somewhat larger influence of line-blocking on the effective temperature of dwarfs than found by Martins et al. (2002) in a comparable investigation utilizing model grids. Typically, our temperatures are lower by 1,000 to 2,000 K. One has to note, however, that a significant number of our objects are fast rotators, which might be affected by gravity darkening (e.g., Cranmer & Owocki 1995; Petrenz & Puls 1996) and hence appear cooler than their non-rotating counterparts.

Moving from dwarfs to supergiants (the temperatures of giants lie in between), we can see that our temperature scale is somewhat *hotter* than the scale derived by Crowther et al. (2002, line-blanketed models using CMFGEN). The differences are marginal at spectral type O4 but increase towards later types, where the discrepancy is of the order of 4,000 K. It should be mentioned though that the accomplished analysis and results obtained by Crowther et al. (2002) comprised extreme Magellanic Clouds objects, whereas in our sample such extreme objects are rare. Thus, it can be speculated that the derived effective temperatures are lower just because of the extreme wind-density of the objects analyzed (see below). Note also that the lower entry at O4 corresponds to ζ Pup. For this star (which

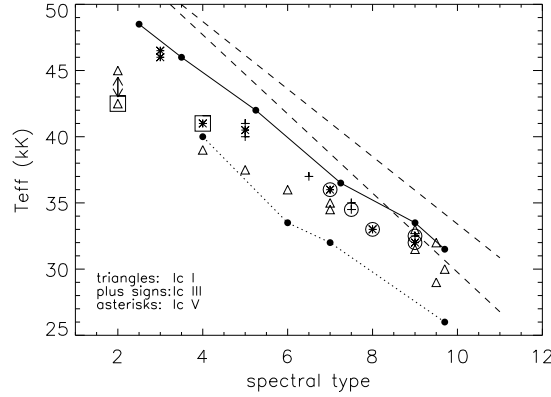


Figure 4.9: T_{eff} vs. spectral type for Galactic O-stars (line-blanketed models, this analysis), compared to similar investigations and results from unblanketed models. The dashed lines denote the results obtained by Vacca et al. (1996, plane-parallel, unblanketed models), where the upper and lower relation correspond to dwarfs and supergiants, respectively. The results obtained by Martins et al. (2002) are displayed by the bold line and corresponds to dwarfs (using CMFGEN+ISA). The dotted line corresponds to extreme supergiants in the Magellanic Clouds (as derived by Crowther et al. 2002 using CMFGEN). The rectangles at O2 and O4 correspond to HD 93129A and HD 303308, respectively (both stars are binary systems; see Nelan et al. 2003), whereas the arrow indicates upper and lower limits of T_{eff} for HD 93129A. Circles enclose extremely fast rotators with $V_r \sin i \geq 300 \text{ km s}^{-1}$.

has a much more typical wind-density), the results of both analyses (ours and the one performed by Crowther et al.) agree perfectly, with a derived value for $T_{\text{eff}}=39,000 \text{ K}$.

Compared to the latest T_{eff} -spectral type calibrations published by Vacca et al. (1996), which is based on plane-parallel, pure H/He model atmospheres, the differences are of the order of 4,000 K to 8,000 K at earliest spectral types and become minor around B0, as also shown in Fig. 4.9. In the following, we will discuss the origin of these differences in considerable detail.

4.7.2 Why lower T_{eff} with blanketed models?

As mentioned above, the inclusion of line-blanketing effects reduces the effective temperature scale significantly, when compared to the results from pure H/He models without winds (and, to a lesser extent, when compared to the results from pure H/He models *with* winds, cf. Herrero et al. 2002). As we will see in the next section, the gravities become smaller as well, at least in the typical case. On the other hand, the values for R_* and \dot{M} remain roughly at their “old” values, so that we can anticipate a significantly modified wind-momentum luminosity relation, due to the decrease in luminosity. Thus, we find severe effects concerning all problems related to T_{eff} as function of spectral type (and luminosity class, due to the additional impact of mass-loss), and in the following we will investigate the question *why* the stars “become cooler” in more detail.

A simple answer to this question has been given in a variety of publications dealing with line-blocking/blanketing (cf. Sect. 6.1), and we will briefly summarize the major aspects.

Due to the presence of the multitude of metal-lines in the EUV, the flux is depressed (“blocked”)

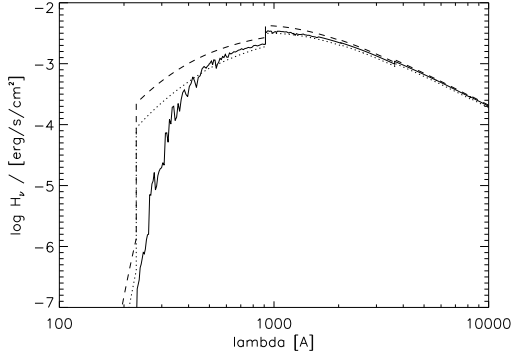


Figure 4.10: Emergent Eddington flux H_ν as function of wavelength. Solid line: Current model of HD 15629 (O5V((f)) with parameters from Table 4.1 ($T_{\text{eff}}=40,500$ K, $\log g=3.7$, “model 1”). Dotted: Pure H/He model without line-blocking/blanketing and negligible wind, at same T_{eff} and $\log g$ (“model 2”). Dashed: Pure H/He model, but with $T_{\text{eff}}=45,000$ K and $\log g=3.9$ (“model 3”).

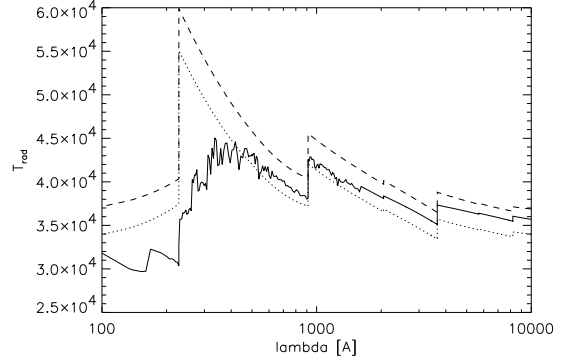


Figure 4.11: As Fig. 4.10, but for corresponding radiation temperatures T_{rad} . The radiation temperature of the blanketed model 1 (solid lines) in the V-band and close to H_α is roughly $0.9 T_{\text{eff}}$.

in this regime, compared to a metal-line-free model. Since the *total* flux, however, has to be conserved the flux blocked by the lines will emerge at other frequencies. This is the case in regions where only a few lines are present, i.e., at longer wavelengths, resulting in an increase of the optical flux.

This can readily be seen in Figs. 4.10 and 4.11, where we compare the results from a prototypical example (our current model of HD 15629 (O5V((f)), $T_{\text{eff}}=40,500$ K, $\log g=3.7$, hereafter “model 1”) with those from a pure H/He model (with negligible wind) at the same effective temperature and gravity (“model 2”). Note in particular that the radiation temperature in the V-band (and close to H_α) is given by $T_{\text{rad}} \approx 0.9 T_{\text{eff}}$ ⁶, compared to the values of $0.75 \dots 0.8 T_{\text{eff}}$ for pure H/He models (Paper I). Thus, the ratio of the emergent fluxes longwards and shortwards from the flux maximum increases due to line-blocking/blanketing.

The process responsible for achieving this flux increase at longer wavelengths is line-blanketing. Due to the *blanket* of metal-lines above the continuum-forming layer, a significant fraction of photons is scattered back (or emitted in the backwards direction), such that the number density of photons (\propto mean intensity J_ν) below this blanket is larger compared to the line-free case. These photons are (partially) thermalized, and the (electron-) temperature (around $10^{-2} \lesssim \tau_{\text{Ross}} \lesssim 2$) increases. Since the emergent flux is proportional to the source-function at $\tau_\nu = 2/3$ (Eddington-Barbier), and since the NLTE-departure coefficients for the excited levels of hydrogen are close to unity for hot stars (note that the optical continuum is dominated by hydrogen bf-processes), an increase in temperature directly translates into an increase of the optical flux.

Thus, if we determined effective temperatures from optical continuum fluxes (concerning the failure of such a method, see Hummer et al. 1988), the reduction of T_{eff} would be easily explained:

Line-blanketed models have optical fluxes similar to those from unblanketed models at higher T_{eff} .

⁶This result roughly holds for all spectral types considered here.

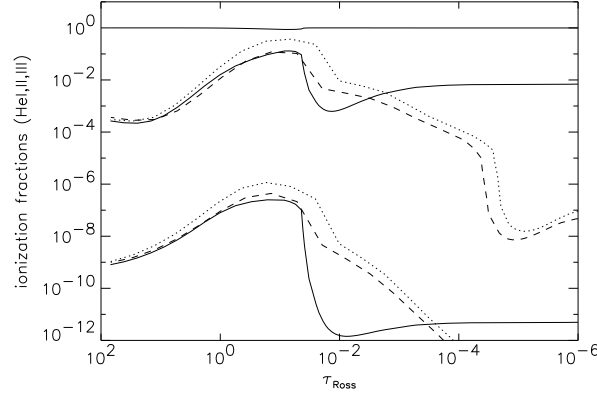


Figure 4.12: Ionization fractions of He for the different models from Fig. 4.10, as function of τ_{Ross} . From top to bottom: He III (blanketed model only), He II and He I, respectively. Note that the fractions for our current blanketed model (solid) coincide with the fractions for the *hotter*, unblanketed one (dashed).

Although the actual analysis of T_{eff} for hot stars depends on the helium ionization equilibrium (see below), the above finding allows us to understand why the derived stellar radii remain almost unaltered: Since we “measure” these radii from a comparison of M_V (which of course is independent of the model) with theoretical model fluxes in the V-band (cf. Eq. 4.1), where the latter depend almost linearly on the corresponding T_{rad} (Rayleigh-Jeans regime), the ratio between “old” and new radii can be approximated by

$$\frac{R_{\star}^{\text{new}}}{R_{\star}^{\text{old}}} \approx \frac{0.9 T_{\text{eff}}^{\text{new}}}{0.8 T_{\text{eff}}^{\text{old}}}$$

and is close to unity in any case, since $T_{\text{eff}}^{\text{new}} < T_{\text{eff}}^{\text{old}}$.

A closer inspection. As just pointed out, the actual determination of T_{eff} for hot stars exploits the sensitivity of the He I/He II ionization equilibrium on temperature. Figure 4.12 shows the corresponding ionization fractions for model 1 and 2 (compare with Fig. 3 in Herrero et al. 2002), as well as the results for a hotter, pure H/He model (again with negligible wind) at $T_{\text{eff}}=45,000$ K and $\log g=3.9$ (dashed curve, “model 3”). In the formation region of *photospheric* lines ($\tau_{\text{Ross}} \lesssim 5 \cdot 10^{-2}$, onset of wind at lower values), the ionization fractions of both He I and He II are similar for model 1 and 3; in contrast, model 2 produces significantly more He I and He II:

Line-blanketed models of hot stars have photospheric He ionization fractions similar to those from unblanketed models at higher T_{eff} (and higher $\log g$, see below).

The final question then is: What determines the displayed behaviour of the ionization fractions? If we concentrated on Fig 4.11, this behaviour would remain unclear. In model 1, the emergent flux shortwards of the He II-Lyman-edge is lowest. In so far, we would erroneously conclude that this model has the *highest* population of He II (at least, regarding the ground-state), in contrast to what is displayed in Fig. 4.12.⁷ We have to remember, however, that the ionization equilibrium is controlled by the

⁷The reason that model 1 has the lowest emergent flux is given by the fact that for this model the He II continuum becomes optically thick already in the wind, since the He II population is larger there, compared to the other models.

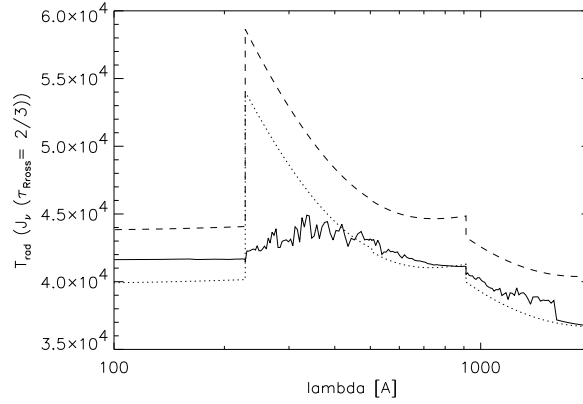


Figure 4.13: As Fig. 4.11, but with radiation temperatures calculated from mean intensity J_ν at $\tau_{\text{Ross}} = 2/3$. Note the difference in the He II Lyman continuum ($\lambda < 229 \text{ \AA}$). Whereas the Lyman-*flux* is lowest for the blanketed model (Fig. 4.11), the corresponding mean intensities lie in between the results of both unblanketed H/He models.

balance between ionization (dependent on the local photon-density) and recombination (dependent on the local electron temperature and density).

Thus, in order to understand the run of ionization, we have to consider the mean intensity, plotted in Fig. 4.13 as corresponding radiation temperature ($J_\nu := B_\nu(T_{\text{rad}}(\nu))$ for a depth of $\tau_{\text{Ross}} = 2/3$). Most important and in contrast to Fig. 4.11 (*emergent flux*) is the fact that the mean intensities shortwards of the He II Lyman edge are now ordered in the following sequence (from lowest to highest values): model 2, 1 and 3, i.e., the results for the blanketed model lie in between the results of the unblanketed ones. This is true not only for $\tau_{\text{Ross}} = 2/3$, but also for the complete photosphere, and it is also true for the run of the electron temperature, lying in between the temperature stratifications for model 2 and 3 due to the effects of line-blanketing as discussed above.

It is well known that the ionization balance (or more correctly, the ratio between the ground state occupation numbers of ion k and ion $k + 1$) can be approximated by (e.g., Abbott & Lucy 1985; Puls et al. 2000)

$$\frac{n_{1,k}}{n_{1,k+1}} = n_e \sqrt{\frac{T_{\text{rad}}}{T_e}} \left(\frac{n_{1,k}}{n_{1,k+1} n_e} \right)^*_{T_{\text{rad}}}$$

with n_e being the actual electron-density and T_{rad} being the radiation temperature at the ionization edge. The bracket denotes the corresponding LTE-value evaluated at T_{rad} ⁸. Without those constants which are identical for a specific ion, we have

$$\begin{aligned} \frac{n_1(\text{He II})}{n(\text{He III})} &\propto \frac{n_e}{T_{\text{rad}}(229 \text{ \AA}) \sqrt{T_e}} \exp \left(\frac{1.4388 \cdot 10^8}{229 \cdot T_{\text{rad}}(229 \text{ \AA})} \right) \\ \frac{n_1(\text{He I})}{n(\text{He III})} &\propto \frac{n_e}{T_{\text{rad}}(504 \text{ \AA}) \sqrt{T_e}} \exp \left(\frac{1.4388 \cdot 10^8}{504 \cdot T_{\text{rad}}(504 \text{ \AA})} \right) \frac{n_1(\text{He II})}{n(\text{He III})} \end{aligned} \quad (4.15)$$

⁸Actually, this expression needs to be modified by a factor containing certain branching ratios with respect to ordinary and metastable levels, which in the following is of no concern.

Using these approximations, we have convinced ourselves in Fig. 4.14 that the similarity of the He ionization equilibrium for model 1 and 3 as well as the larger population of He I and He II for model 2 can be explained by three facts:

- i) the run of the electron temperatures, where the values for the blanketed model lie in between the ones for the unblanketed models (back-warming);
- ii) the run of the radiation temperatures, which are rather similar to T_e (continua optically thick in the photosphere!), although somewhat higher⁹.
- iii) the higher electron density n_e for model 3, because of the higher gravity in this case ($\log g=3.9$ vs. $\log g=3.7$). If we had compared models with identical gravities, model 3 would have yielded the highest ionization degree, which is just compensated because of the increased recombination due to the higher electron density.

In summary, the He ionization equilibrium of our blanketed model 1 and the hotter, unblanketed model 3 are similar because of backwarming (increasing T_e and, thus, T_{rad} at the edges in model 1) and because of the higher gravity in model 3 (increasing the photospheric recombination).

Fig. 4.15 finally displays the corresponding profiles for He I 4471. Obviously, the results for model 1 and 3 are indistinguishable, whereas model 2 produces a much stronger profile. Thus, a spectroscopic analysis of hot stars, based on the He ionization equilibrium and performed by means of blanketed models, will usually result in parameters at lower T_{eff} and lower $\log g$, compared to an analysis utilizing pure H/He models.

The parameters derived from He I, of course, have to consistently produce the other (optical) lines from hydrogen and He II. Since for hotter stars the He II lines $\lambda\lambda$ 4200, 4541 are preferentially fed by recombination from He III (which remains the dominant ion with and without blocking), they remain almost unaffected by temperature variations and react mainly (but weakly) on gravity (cf. the corresponding sequence of He II lines in Fig. 4.8). On the other hand, the hydrogen Balmer lines remain fairly unaltered if temperature and gravity are changed in parallel, which needs to be done in any case if He I is to be preserved.

It is hence possible to obtain line-fits of almost equal quality from blanketed and unblanketed models, if the former have lower T_{eff} and $\log g$ than the latter. For physical reasons we prefer the former, implying that we have to accept a re-calibration of stellar parameters as a function of spectral type.

In the following we will see that there is also another possibility: If the hydrogen lines “forbid” a decrease in gravity, we might be able to obtain a fit at lower T_{eff} and *equal* $\log g$, but with a *reduced* helium abundance. This reduction then compensates for the increase of the He I fraction, which otherwise could be obtained only by a decrease in $\log g$. The He II lines must allow for such a reduction, which is possible in certain domains of the $(T_{\text{eff}}, \log g)$ -plane.

From these results it becomes also clear why the T_{eff} correction for supergiants is larger than for dwarfs. Supergiants have a stronger wind due to a larger luminosity. At first glance, one might speculate that the major effect is an increased backwarming effect due to an increased wind-albedo (cf. Hummer 1982; Voels et al. 1989): the “blanket” becomes denser because of the increase in line opacity and the velocity shift in the wind. However, in most cases this effect is minor compared to the

⁹Because of the usual effect that for ground states and close to the surface, $J_\nu > B_\nu(T)$, and the additional increase of J_ν due to back-scattered photons from above in case of the blanketed model 1

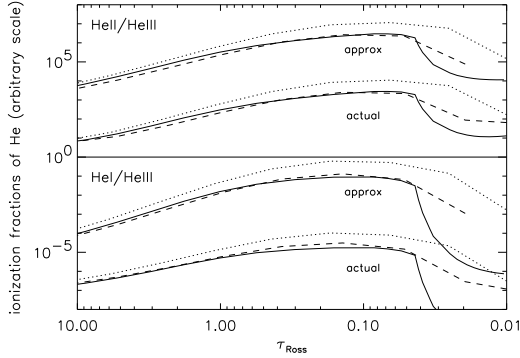


Figure 4.14: As Fig. 4.12, but for ionization ratios He II/He III (upper panel) and He I/He III (lower panel). Both panels show the actual ratios for all three models as well as the ratios as approximated by Eq. 4.15, using mean intensities *at* the ionization edge. The offset between all four arrays of curves is arbitrary. Obviously, the approximation is a good representation for the actual situation (see text.)

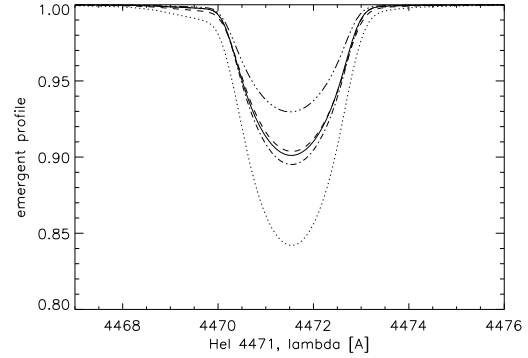


Figure 4.15: He I 4471 line ($V_r \sin i = 90 \text{ km s}^{-1}$) for all three models from Fig 4.10. Whereas the profiles model 1 and model 3 coincide, model 2 produces a much stronger line (see also Fig. 4.12). The dashed-dotted profile results from a model similar to our current blanketed one, but with negligible mass-loss. Obviously, the presence or absence of a *weak* wind (model 1 has a mass-loss rate of $1.3 \cdot 10^{-6} M_{\odot}/\text{yr}$) has no effect on the temperature analysis. The weakest profile shows the influence of a strong wind: the underlying model again is similar to model 1, but with a mass-loss rate of $7.5 \cdot 10^{-6} M_{\odot}/\text{yr}$.

influence of the wind itself. In a dense wind, the line cores are formed in the wind, and particularly He I is significantly filled in by wind emission (Fig. 4.15). Thus, a larger correction to even lower T_{eff} is required to match the observations, compared to an analysis based on wind-free models.

One last comment: Not only T_{eff} and \dot{M} have an influence on the effect of line-blocking, but also $\log g$, particularly for dwarfs. Since with increasing $\log g$ the photospheric density increases, the recombination rates of the metal-ions become enhanced, which results in a higher population of the lower ionization states. Less ionized metals have a more complex level structure whose more numerous lines then enhance the blocking and blanketing effect.

4.7.3 The T_{eff} vs. $\log g$ diagram

Figs. 4.16 and 4.17 show the spectroscopist's view of the Hertzsprung-Russel diagram, namely $\log g$ vs. T_{eff} , which is independent of any uncertainty in the distance. Compared to the results from Paper I, a shift towards lower temperatures can be observed for all stars in our sample as indicated by the displacement vectors, which is in agreement with the results from above. As shown, we would also expect a (moderate) reduction of $\log g^{10}$, which is found for only 14 out of 24 sample stars. For eight stars, the gravities remain unaltered, and for two stars, HD 24912 and HD 207198 (luminosity class III and I, respectively), we actually had to increase $\log g$ in order to obtain a convincing fit.

If we consider those objects in more detail where the gravity remained at its old value (or had to

¹⁰Note that the values of $\log g$ from Paper I include an approximate correction for wind-effects.

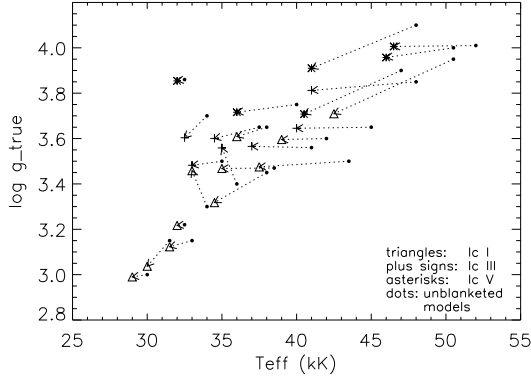


Figure 4.16: True gravity $\log g_{\text{true}}$ vs. T_{eff} for Galactic O-stars (this work) compared to the results from Paper I (unblanketed models, gravity corrected for wind effects and centrifugal forces). A shift towards lower temperatures can be observed for all stars in our sample, as indicated by the displacement vectors in the $T_{\text{eff}}\text{-}\log g$ plane; 14 out of 24 stars had to be shifted towards lower $\log g$, 8 objects preserved their “old” value and for two objects we had to increase the gravity (see text).

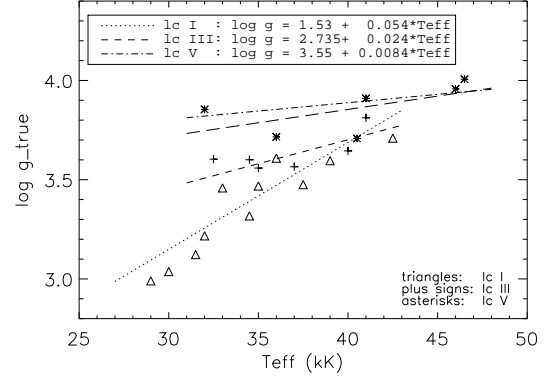


Figure 4.17: True gravity $\log g_{\text{true}}$ vs. T_{eff} for Galactic O-stars (this work) compared to the calibrations provided by Markova et al. (2003), evaluated in the $T_{\text{eff}}\text{-}\log g$ plane. Although almost all results agree within the typical error bars $\Delta T_{\text{eff}} \approx \pm 1,500$ K and $\Delta \log g \approx \pm 0.1$, the “outliers” HD 217086 (O7Vn, fast rotator) and HD 15629 (O5V((f))) might indicate a steeper relation for dwarfs, as indicated by the long-dashed line, $\log g = 3.32 + 0.013 \cdot T_{\text{eff}}$, T_{eff} in kK (see text).

be increased), it turns out that for 9 of the 12 objects we derived a lower helium abundance than found by Herrero et al. (1992). These cases, thus, comprise the alternative stated above: Instead of a reduced gravity, which in these cases is “forbidden” from the hydrogen Balmer lines, we obtained a reduced helium abundance. Therefore, the well-known helium discrepancy has considerably been reduced by our analysis using blanketed models (see also Herrero et al. 2002).

Fig. 4.17 again displays our new $\log g$ vs. T_{eff} diagram for Galactic O-stars, but now we compare the results to a recent calibration implicitly provided by Markova et al. (2003), who have partly used the results described in the present paper. In particular, the plot serves as a consistency check, because Markova et al. derived two independent calibrations, T_{eff} vs. spectral type and $\log g_{\text{true}}$ vs. spectral type. Since their calibrations are based on a linear model (with all its caveats, particularly for extreme supergiants), it is possible to combine both and to derive a calibration for $\log g$ vs. T_{eff} . This is what we have done in Fig. 4.17, where also the corresponding coefficients have been tabulated as a function of luminosity class.

In the case of class I and III objects, also this new combination agrees with our results: almost all objects are within the typical error bars $\Delta T_{\text{eff}} \approx \pm 1,500$ K and $\Delta \log g \approx \pm 0.1$, even if we include the “problematic” object HD 207198 mentioned above (this object, however, together with λ Cep, does lie above the general trend).

It should be noted that some of the stars studied have deliberately been excluded from the analysis performed by Markova et al. (2003). Not only were the two binaries HD 93129A and HD 303308 discarded but also the fast rotators (e.g., HD 217086 and HD 13268).

Nevertheless, the quality of the comparison performed is rather good with exception of the class

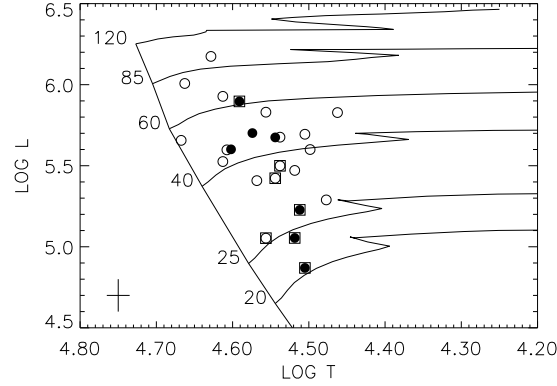


Figure 4.18: The HR diagram for our sample. Filled symbols indicate stars with He abundances higher than $Y_{\text{He}} = 0.17$ and open squares mark the rapid rotators with $V_r \sin i$ higher than 200 km s^{-1} . Evolutionary tracks for non-rotating stars are taken from Schaller et al. (1992).

V objects. For this luminosity class, Markova et al. have included the results obtained by Martins et al. (2002) into their calibrations. These results are based on an analysis of model-grids and on a different code (CMFGEN), which might lead to a certain inconsistency. The comparison of our results with the calibration now indicates a steeper relation, if we do not exclude the “outliers” HD 217086 and HD 15629 (both with $\log g \approx 3.7$). For both stars, the fit quality is very good, making an error in the spectroscopically derived $\log g$ very unlikely). To account for this problem, we have added an alternative regression based on our results only (along with the corresponding coefficients), denoted by the long-dashed line in Fig. 4.17.

If we assume, on the other hand, that the regression by Markova et al. were correct, the mismatch could be explained by means of an under-estimate of the true gravity, at least for HD 15629 ($V_r \sin i = 90 \text{ km s}^{-1}$) in case it were a fast rotator seen pole-on (Eq. 4.5). For HD 217086, however, this possibility can most probably be excluded, since it is a fast rotator with only a small error in the centrifugal correction.

In conclusion, the $\log g$ vs. T_{eff} calibration for l.c.V objects remains somewhat uncertain, whereas for l.c.I/III stars no obvious problems are visible.

4.7.4 Is there still a mass discrepancy?

Fig. 4.18 shows the position of our objects in the HR Diagram, where different symbols have been used to mark objects with large He abundances or rotational velocities.

A comparison with the data from Paper I using the same absolute magnitudes (which would slightly modify the entries in Fig. 4.18) reveals two major differences which are explained by the new, lower temperatures and subsequently by the lower luminosities (remember that the radii are very similar).

First, lower masses are derived for the most massive stars, even if we include the binary components in Carina. In Paper I, progenitor masses in excess of $120 M_{\odot}$ and actual masses in excess of $100 M_{\odot}$ were derived for the most massive stars, whereas in our present work all stars have progenitor masses and actual masses below $100 M_{\odot}$.

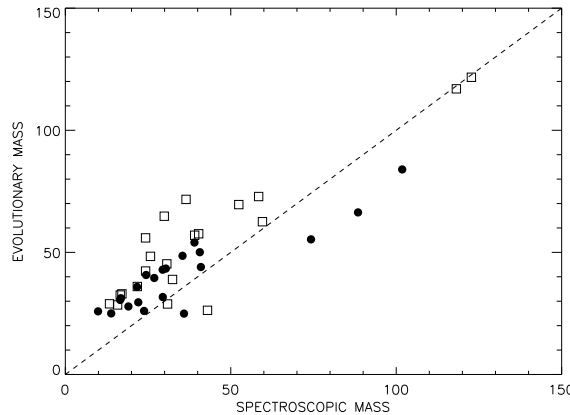


Figure 4.19: Evolutionary vs. spectroscopic masses obtained in Paper I (open squares) and in the present work (filled circles), using the same absolute magnitudes ($\rightarrow R_{\text{old}}$).

Second, all of our stars are clearly separated from the ZAMS except HD 93128, although we have another five stars classified as dwarfs. This offset in effective temperature cannot be explained by distance uncertainties, unless they have been seriously overestimated (which would then pose a problem for HD 93128). A similar effect has been found in the data set analyzed by Herrero et al. (1992), although they have used different evolutionary models and there were no sample stars as young as HD 93128. Investigating the evolutionary tracks, this star would have an age of only 0.15 Myr (see also Penny et al. 1993) which is much less than the age of the next youngest star, HD 93250 with an age of 1.3 Myr. Although the uncertainties in the derived ages are very large, this finding is consistent with the fact that both stars have very similar spectra and parameters (T_{eff} and $\log g$), but almost one and a half magnitudes difference in brightness. It is also consistent with the fact that HD 93128 is a member of Trumpler 14, which has been argued to be significantly younger than Tr 16 to which HD 93250 belongs (see Walborn 1982a, 1995). (Aside: we would like to point out that also HD 93250 might be a binary (cf. Walborn 1982b, but also Walborn et al. 2002) which would additionally explain the rather low wind-momentum rate of this star compared to similar objects.)

From Fig. 4.18 we can also read off the masses predicted by the evolutionary tracks (i.e., the evolutionary masses) and compare them with those derived from the stellar parameters which were determined by spectral analysis (i.e., the spectroscopic masses). Note that both masses depend in a similar way on the adopted distance, and, therefore, their difference will not change unless we have to modify this distance dramatically.

Herrero et al. (1992) performed this comparison and found that the spectroscopic masses of giants and supergiants were systematically smaller than the evolutionary ones. At the same time, the spectroscopically determined helium *over*-abundances could not be explained by current theories of stellar structure and evolution. The correlation of the *mass discrepancy*, i.e., the difference between evolutionary and spectroscopic masses, and the distance to the Eddington limit indicated that the deduced discrepancy might have been related to the fact that Herrero et al. (1992) omitted sphericity and mass-loss in their analyses. However, even with the (approximate) inclusion of sphericity and mass-loss in the determination of stellar parameters as performed in Paper I, the actual problem could not be solved, but it could be improved.

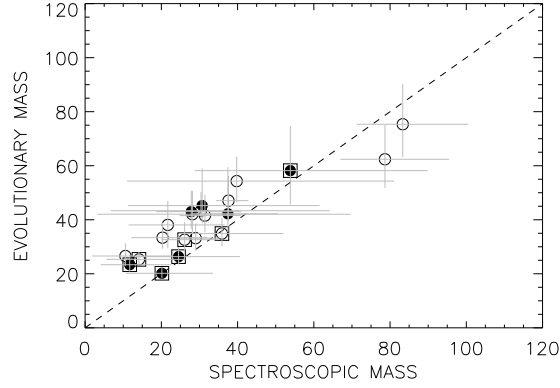


Figure 4.20: Spectroscopic and evolutionary masses of our sample stars with data from Table 4.1 and errors as discussed in Sect. 4.6. The binary components HD 93129A and HD 303308 have been discarded from the plot. Open squares denote rapid rotators with $V_r \sin i > 200 \text{ km s}^{-1}$, as in Fig. 4.18

From a recent analysis of seven Cyg OB2 supergiants including the effects of sphericity, mass-loss and line blanketing, Herrero et al. (2002) found no conclusive evidence for a mass discrepancy to be present. While the star with the lowest mass still showed a discrepancy, the other six stars were found to be evenly distributed on each side of the 1:1 line dividing spectroscopic and evolutionary mass, with the error bars crossing it.

In the present context and to illuminate the effects of line blocking/blanketing, it is now interesting to compare the evolutionary and spectroscopic masses from Paper I with the ones obtained in the present analysis, using the same absolute magnitudes. The result can be seen in Fig. 4.19. A distinct improvement of the general situation is obvious, especially for a number of stars in the “intermediate” mass range. Not surprisingly, these are stars for which the correction in effective temperature is very large.

The present situation (with respect to M_V and R_* from Table 4.1) is displayed in Fig. 4.20. We see that for almost all stars the corresponding error bars cross the 1:1 line with exception of those three objects with the lowest spectroscopic mass (which are *not* the three objects with the lowest luminosity in Fig. 4.18).

Although our new results are consistent with the ones found by Herrero et al. (2002), implying that the mass discrepancy seems to be limited to stars of less than $15 M_\odot$, there is still additional concern. Most stars with masses lower than $50 M_\odot$ (including those three objects with mass discrepancy) follow an imaginary line located parallel to the 1:1 line which is displaced by about $10 M_\odot$ in ordinates. We consider this finding as a milder form of the original mass discrepancy which still has to be explained.

Unfortunately, is not possible to perform a similar comparison using evolutionary calculations based on rotating models as presented by Meynet & Maeder (2000) and Heger & Langer (2000), since we do not know the initial rotational velocity of our objects. If we simply assume that all our objects had started with 300 km s^{-1} , the remaining discrepancies as discussed above would still have persisted. At least the derived range of He abundances could be explained, but not necessarily at the correct effective temperature, luminosity, and age as discussed by Herrero & Lennon (2003).

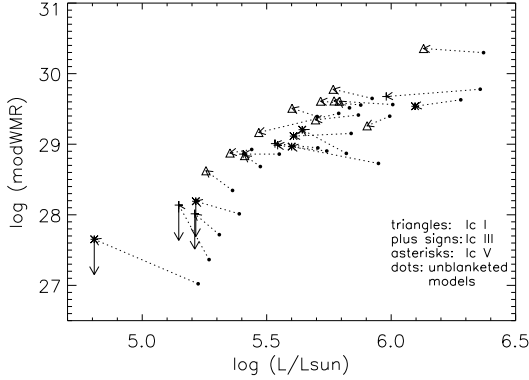


Figure 4.21: Logarithm of modified wind-momentum rate, $D_{\text{mom}} = \dot{M}v_{\infty}(R_{\star}/R_{\odot})^{0.5}$, vs. $\log(L/L_{\odot})$, for the values derived on the basis of R_{old} (i.e., assuming the same values for M_V as in Paper I), compared to the results from Paper I itself. For all stars in our sample, a shift towards lower luminosities has been found, whereas for most of the stars the modified wind-momentum rate remains roughly constant. Only for the stars with $\log(L/L_{\odot}) < 5.3$ the upper limit of the wind-momentum rate (indicated by arrows) has increased (see text).

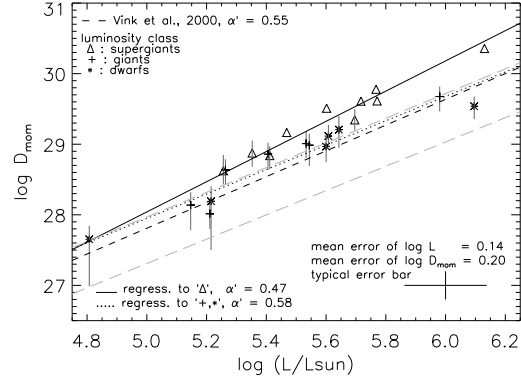


Figure 4.22: WLR for our sample, using the same M_V -values ($\rightarrow R_{\text{old}}$) as in Paper I. Denotation as written in the plot legend. The binary components HD 93129A (l.c.I, at $\log L = 6.13$ and $\log D_{\text{mom}} = 30.35$) and HD 303308 (l.c.V, at $\log L = 5.61$ and $\log D_{\text{mom}} = 29.12$) have been discarded from the regressions.

Error bars with respect to $\Delta \log D_{\text{mom}}$ are plotted only for objects with H_{α} in absorption. The regression was performed accounting for the errors in both directions and for their correlation (see text). Overplotted (in grey, long-dashed) are the regressions as obtained in Paper I using pure H/He-models. Note that the new regression for luminosity classes III/V (dotted) almost coincides with the “old” regression for supergiants, and that both agree well with the predictions by Vink et al. (2000, dashed).

4.7.5 Wind-momentum rates

Whereas the effective temperatures decrease significantly, mass-loss rates and stellar radii are hardly affected by line-blocking/blanketing and remain roughly at their “old” values (if the same values for distance/ M_V are used, of course). For the radii, this finding has already been explained in Sect 4.7.2 (increase of $T_{\text{rad}}/T_{\text{eff}}$ in the optical) and for the mass-loss rates the argument is similar: First, the H_{α} -emissivity increases only weakly due to the reduced electron temperature in the wind (at least for the hot stars considered here). Second, the underlying continuum, i.e., the radiation temperature close to H_{α} , remains comparable to or hotter than the continuum of an unblanketed model at its “older”, higher T_{eff} . The combined effect of the modified electron, radiation and effective temperature on \dot{M} can then be approximated by Eq. 49 in Paper I, and in most cases it turns out that we should expect a rather weak reduction in \dot{M} of the order of 10 to 20 %.

Comparison with previous results assuming identical M_V 's

This expectation has been checked in Fig. 4.21, where we have compared the modified wind-momentum rates as derived here with those resulting from Paper I. To avoid any confusion due to changes in R_* *because of differences in M_V* , this comparison has been performed on the basis of R_{old} (Table 4.1, last column), i.e., assuming the same values for M_V as in Paper I. With respect to the values for luminosity and D_{mom} as given in Tables 4.1 and 4.4, this means that both quantities have been scaled with $(R_{\text{old}}/R_*)^2$.

In contrast to our expectation from above, Fig. 4.21 shows that in some cases we actually encounter an increase in \dot{M} . The reason for this behaviour is twofold. The fitted value of β has decreased for a number of stars with emission lines, (e.g., for ζ Pup from 1.15 to 0.90), probably as a consequence of the somewhat modified run of $T_e(r)$. A decrease in β then translates into an increase in \dot{M} .

For objects with an almost purely photospheric H_α profile, on the other hand (the four low luminosity stars for which we could obtain only upper limits), this upper limit has increased due to the higher precision of the present analysis: The approximate approach used in Paper I becomes somewhat uncertain at (very) low mass-loss rates, mainly because it depends on an incident boundary condition based on results from hydrostatic, plane-parallel models. Additionally, all four objects are very fast rotators. In Paper I, we reduced the rotational velocity from its photospheric value to a somewhat lower, “effective” value in order to match the H_α profile. Again due to the higher precision of the present *unified* approach, it turned out that such a modification is no longer necessary, at least not for the three dwarfs (cf. Sects. 4.5 and 4.8). Keeping the nominal values of $V_r \sin i$ then increases the derived mass-loss rates.

Insofar, the dilemma discussed in Paper I (What is the reason that the modified wind-momentum rates of low-luminosity stars lie below the average relation?) finds its natural explanation: For the present results, this dilemma simply no longer exists, at least if we assume that the actual mass-loss rates lie at the obtained upper limits (where this assumption, admittedly, is rather bold.)

From our findings, we conclude that for most of our objects the *ratio* between mass-loss rate (and thus modified wind-momentum rate) and luminosity has become larger compared to previous results. This becomes particularly clear in Fig. 4.22, where we compare the average WLR for Galactic supergiants and giants/dwarfs obtained in Paper I (long-dashed, grey) with the corresponding regressions using the present data, again for the same values of M_V . Note that the latter have been performed accounting for the errors in both directions ($\Delta \log L$ and $\Delta \log D_{\text{mom}}$, cf. Table 4.4) and for their correlation (both quantities depend on R_*^2), as described in Markova et al. (2003).

The corresponding coefficients with respect to the WLR,

$$\log D_{\text{mom}} = x \log(L/L_\odot) + \log D_o, \quad x = \frac{1}{\alpha'}, \quad (4.16)$$

(with α' being the exponent of the line-strength distribution function, corrected for ionization effects) are given in Table 4.5. Interestingly, the new regression for luminosity classes III/V (dotted) almost coincides with the “old” regression for supergiants, whereas the new regression for the supergiants has become significantly steeper than previously determined. Taken literally, the new value of $\alpha'(\text{sg})$ is smaller than $\alpha'(\text{g/dw})$, in contrast to results from theoretical considerations (Puls et al., 2000). Let us point out, however, that the regression coefficients for supergiants are rather uncertain, since the minimum of χ^2 is extremely broad (in contrast to the lc III/V case).

Table 4.5: Coefficients of the WLR obtained in the present investigation (discarding HD 93129A and HD 303308 from the regression), compared to the results from Paper I and the theoretical prediction by Vink et al. (2000). Entry 4 and 5 correspond to values obtained by using the “old” absolute magnitudes ($\rightarrow R_{\text{old}}$), entry 6 and 7 correspond to the values derived from new ones including the results for seven Cyg OB2 stars by Herrero et al. (2002). The last entry corresponds to the regression performed in Fig 4.24. Present data has been analyzed by accounting for the errors in both directions and their correlation, whereas a standard least square fit has been performed for the data in Paper I (no errors available).

Sample	$\log D_o$	x	α'
Vink et al. (2000)	18.68 ± 0.26	1.83 ± 0.044	0.55 ± 0.013
sg (Paper I)	19.23 ± 0.98	1.75 ± 0.17	0.57 ± 0.055
g/d (Paper I)	18.90 ± 1.46	1.72 ± 0.25	0.58 ± 0.085
sg M_V (old)	17.34 ± 2.46	2.14 ± 0.44	0.47 ± 0.096
g/d M_V (old)	19.3 ± 1.22	1.73 ± 0.22	0.58 ± 0.074
sg (+CygOB2)	17.98 ± 1.88	2.00 ± 0.32	0.50 ± 0.080
g/d (+CygOB2)	18.70 ± 1.29	1.84 ± 0.23	0.54 ± 0.068
“unified”, cf. Fig. 4.24	18.92 ± 0.87	1.80 ± 0.16	0.56 ± 0.049

Although quantitatively different, both the results presented here and in Paper I indicate a clear separation between luminosity class I objects and the rest, although this separation seems to have decreased regarding our new data. The most obvious interpretation would be that the effective number of lines driving the wind (comprised in the quantity D_o from Eq. 4.16) is a function of luminosity class. A comparison with recent theoretical predictions (and even with older ones, cf. Fig. 25 in Paper I) obtained by *different independent* approaches (Vink et al., 2000; Pauldrach et al., 2003; Puls et al., 2003a) suggests that this is not probable, since these calculations predict a *unique* relation, almost coinciding with our present regression for class III/V objects (cf. Figs. 4.22, 4.23).

Clumping in the lower wind?

If we now use our preferred absolute magnitudes, i.e., the values given in Tables 4.1 and 4.4 and include the results obtained by Herrero et al. (2002) for seven Cyg OB2 stars¹¹ (which should be free of errors related to relative distances), the situation becomes even more confusing as shown in Fig. 4.23 (see also Puls et al. 2003a, Fig. 3). Although the Cyg OB2 sample consists almost exclusively of supergiants, only the two most extreme supergiants (CygOB2#7 and #11) follow the “upper” WLR from Fig. 4.22, whereas the derived wind-momenta for all other (five) objects are consistent with our present WLR for class III/V stars.

In order to clarify this confusion and on the basis of a preliminary analysis of the present data set, Puls et al. (2003a) have suggested a scenario which we would like to briefly summarize, because in the following we will present the corresponding outcome using *our* results.

When plotted not as a function of luminosity class but as a function of H_α *profile type* (Puls et al., 2003a, Fig. 4), it turned out that stars with H_α in emission and those with absorption profiles (only partly filled in by wind emission) form two distinct WLRs, respectively, where in this representation

¹¹Note that this analysis has been performed with the same code as applied by us, i.e., the results are at least in a differential sense of equal quality.

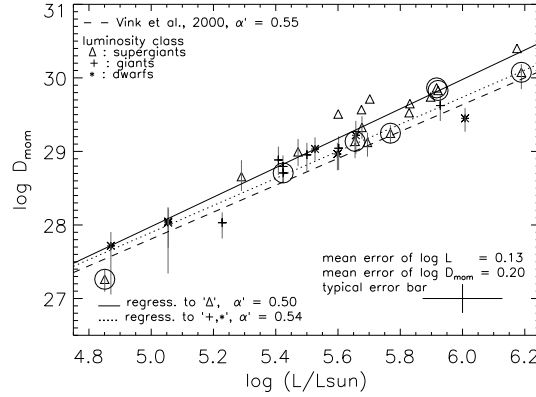


Figure 4.23: As Fig. 4.22, but with the actual absolute magnitudes from Table 4.1 including the results for seven Cyg OB2 stars analyzed by Herrero et al. (2002) (enclosed by circles).

the CygOB2 objects make no exception.

From these findings, Puls et al. (2003a) suggested that the different WLRs might be a consequence of wind-clumping: The contribution of wind emission to the total profile is significantly different for objects with H_α in absorption compared to object with H_α in emission, since for the former only contributions from the lowermost wind can be seen, whereas for the latter the emission is due to a significant wind volume. Thus, there is the possibility that for these objects we *see* the effects of a *clumped* wind which would mimic a higher mass-loss rate, as it is most probably the case for Wolf-Rayet winds (e.g., Moffat & Robert 1994). With this suggestion, we do not exclude the presence of clumping in the winds of objects with H_α in absorption; owing to the low optical depth, however, we simply cannot see it.

It should be mentioned that the principal presence of clumping has never been ruled out for O-star winds; however, at least from conventional spectrum analysis methods there was simply no indication that *the H_α forming region* was considerably clumped (see the discussion in Paper I). During the past years, this situation has somewhat changed. Apart from recent theoretical considerations (e.g., Feldmeier et al. 1997, Owocki & Puls 1999 and references therein) which do not prohibit such a relatively deep-seated clumped region, a number of additional evidence for such a scenario has been gathered.

First, note that time-series analyses of He II 4686 from ζ Pup by Eversberg et al. (1998) have revealed “outward moving inhomogeneities” from regions near the photosphere out to $2 R_\star$, i.e., just in the H_α forming region which extends typically out to 1.5 stellar radii. Although these features are most probably different from the clumps suggested here, these observations indicate that the lower wind is not as stationary as previously assumed.

Second, our hypothesis is supported by a number of UV-analyses. Based on FUSE-observations of (L)MC-stars, both Crowther et al. (2002), Massa et al. (2003) and Hillier et al. (2003, see below) found indications that the winds might be clumped, majorly from the behaviour of the PV resonance line (if phosphorus is not strongly under-abundant, as claimed by Pauldrach et al. 1994). By comparing the results from self-consistent wind models and UV line-synthesis, Puls et al. (2003a) found that the clumping scenario is also consistent with the behaviour of the SiIV resonance line.

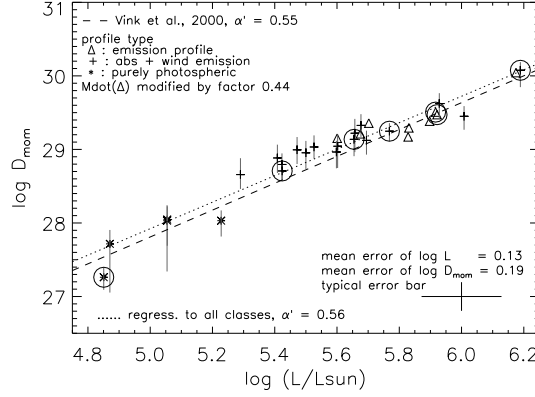


Figure 4.24: WLR of the combined sample from Fig. 4.23, \dot{M} for objects with H_α in emission reduced by a factor of 0.44. The resulting WLR follows closely the predictions by Vink et al. (2000) (see also Markova et al. 2003).

Most important in the present context, however, is the problem concerning the cores of the (blue) Balmer lines discussed in Sect. 4.4. At least for five out of the seven objects with H_α in emission, the synthetic H_γ H_δ (where present) and H_β lines formed in or close to the photosphere show too much wind emission in their cores, and would require at least a factor of 1.5 less mass-loss in order to be consistent with observations. Interestingly, this behaviour has also been found for the extreme objects of the Cyg OB2 sample analyzed by Herrero et al. (2002). This dilemma is not present for stars with H_α in absorption for which we anticipate that the derived mass-loss rates are *not* contaminated by clumping effects.

In Fig. 4.24 we have considered the following question: If the suggested scenario was correct, what (clumping) factor would be required to “unify” the different WLRs with each other and with the theoretical predictions, respectively? To this end, we have modified the mass-loss rates for all objects with H_α in emission (including the CygOB2 stars) in order to match the WLR of giants/dwarfs as close as possible. This approach, of course, assumes that either the clumping factor in the H_α emitting wind region is constant or that the H_α emitting volume is of similar size. The required factor with respect to \dot{M} turned out to be 0.44, corresponding to an (effective) clumping factor $\langle \rho^2 \rangle / \langle \rho \rangle^2 = 0.44^{-2} = 5.2$, which sounds reasonable and is somewhat lower than the values inferred from (the outer regions of) Wolf-Rayet winds.

With such a reduction we find an almost unique WLR consistent with theoretical simulations¹², where the corresponding parameters are given in Table 4.5. Recall that the quoted values have been “derived” on the basis of the *hypothesis* that the modified wind-momentum rate is a function of luminosity alone, independent of luminosity class. This hypothesis is strongly supported by theoretical predictions and simulations in those cases where the WLR is independent of stellar mass (which is the case for Galactic O-stars with α' close to 2/3). If this hypothesis is wrong, the derived clumping factors might be somewhat too large.

In any case and in summary, there are strong indications that mass-loss analyses of (at least) O-star

¹²For the “outliers” around $\log(L/L_\odot) \approx 5.8$, the deduced factor might be too large, indicating that these stars are affected by a smaller clumped wind volume than the rest.

winds utilizing H_α tend to overestimate the resulting values, unless clumping is accounted for or the winds are comparatively thin.

After finishing this investigation a very interesting paper by Hillier et al. (2003) appeared which gave additional support to our hypothesis. In this paper, two SMC O stars, AV83 (O7 Iaf⁺) and AV69 (OC7.5 III((f))) have been analyzed by means of CMFGEN. Although both objects are shown to be located at rather similar effective temperatures and luminosities ($\log(L/L_\odot) = 5.54$ and 5.62 , respectively), their spectra display quite different wind signatures, with H_α in emission for the supergiant and in absorption for the giant. Whereas for the supergiant the mass-loss rate could be determined precisely ($\dot{M} = 2.0 \cdot 10^{-6} M_\odot/\text{yr}$ for $\beta = 2$, neglecting clumping), the giant's mass-loss rate could not be derived unambiguously, due to the β -problem discussed in Sect. 4.6.2. For $\beta = 0.7, 1.0, 2.0$ mass-loss rates of $\dot{M} = 1.5, 0.92$ and $0.32 \cdot 10^{-6} M_\odot/\text{yr}$ are quoted, respectively. Accounting for the different terminal velocities (960 km s^{-1} vs. 1800 km s^{-1} – strongly related to the different gravities), the derived modified wind-momentum rates are quite similar if clumping is neglected. For an assumed value of, e.g., $\beta = 1.0$ for the giant, D_{mom} for the less luminous supergiant is slightly larger, by a factor of only 1.16.

On various evidence (including the behaviour of the PV line, see above), the authors then argue that the supergiant wind is probably clumped, and that the clumping should begin at the base of the wind! In this case, for a best simultaneous fit of all photospheric and wind lines the mass-loss rate becomes reduced by a factor of 0.37. Note that this number as well as the conclusion of *deep-seated* clumping agrees very well with our above hypothesis. Note also that no clumping correction has been applied to the giant, since clumping is (if at all) only weakly visible in a small number of UV wind lines (OIV and CIV), such that a correction of \dot{M} would be less than for the supergiant. Taking all numbers literally, a “unification” of the wind-momentum rates in the same spirit as above (i.e., claiming an equal value of D_o in Eq. 4.16) would yield a value of $\alpha' \approx 0.2$ for $\beta(\text{giant})=1.0$, which might be somewhat low for SMC O-(super)giants (cf. Puls et al. 2000; Vink et al. 2001). Note, however, that only a small reduction of the giant's mass-loss rate to a value of $0.58 \cdot 10^{-6} M_\odot/\text{yr}$ (corresponding to a $\beta \approx 1.5$ or/and a moderately clumping corrected mass-loss rate) would yield a much more typical value, i.e., $\alpha' \approx 0.4$.

4.8 Conclusions and summary

In this paper, we have re-analyzed the Galactic O-star sample from Paper I by means of line-blanketed NLTE model atmospheres in order to investigate the influence of line-blocking/blanketing on the derived stellar and wind parameters. For our analysis and in addition to the “conventional” strategic lines (e.g., Herrero et al. 1992), we have included a number of He lines neighboring H_α to provide complementary constraints on the fitting procedure.

The fit quality is generally good (or even very good), except for the following systematic inconsistencies:

- i) For five out of seven supergiants with H_α in emission, the line cores of the blue Balmer lines are too weak (i.e., too much filled in by wind emission) when the mass-loss rate was determined by matching H_α . This effect (in conjunction with the analysis of the WLR) might indicate an overestimate in mass-loss rate.
- ii) In a number of cases, He II 4541 turned out to be too weak, although He II 4200 (same lower level!) fitted perfectly. There are two possibilities to explain this deficiency: either the upper

level is too strongly populated, or the wind emission is too large (note, that He II 4541 is stronger than He II 4200, i.e., is formed further out in the wind). Since in most cases this problem occurred in parallel with the problem outlined in item i), a relation to an erroneous mass-loss rate cannot be excluded. Interestingly, Herrero et al. (1992) (using plane-parallel models) have reported a similar inconsistency, but in their case He II 4200 was too weak.

- iii) Although our models comprise the effects of mass-loss, sphericity and blanketing, with the present version of FASTWIND we were not able to get rid of the “generalized dilution effect” in He I 4471 emanating from both cooler supergiants and giants. The onset of this effect was found to be located around spectral type O6. For almost all affected stars the blue Balmer lines could perfectly be fitted, which makes a relation to an overestimated mass-loss rate rather unlikely.
- iv) If H_α appears with a P Cygni shape, we are not able to match the blue absorption component. This finding points either to an inconsistent treatment of the corresponding He II blend or to effects of stellar rotation disturbing the emergent profile.
- v) In Paper I, the nominal value of $V_r \sin i$ (from photospheric lines) was reduced for most of the objects with a large rotational velocity in order to match the observed H_α profiles. This was explained by the fact that the wind emission is formed in a differentially rotating medium with an “effective” rotational speed smaller than the *photospheric* one (see also Petrenz & Puls 1996). In our present analysis, we have encountered the same effect, but only in giants (and one supergiant), namely in HD 18409, HD 193682, HD 24912, HD 203064 and HD 191423 (cf. Sect. 4.5). For the fast-rotating dwarfs (HD 217086, HD 13268 and HD 149757), on the other hand, no discrepancy between H_α and the other lines was detected, in contrast to the results from Paper I. Actually, this finding is quite reassuring, since the wind-emission in those stars is so low that an influence of differential rotation in the wind ($V_{\text{rot}}(r) \propto V_{\text{rot}}(R_\star) R_\star/r$) is rather unlikely.

On the other hand, it should be noted that in most cases the notorious wind line He II 4686 could be reproduced in parallel with H_α , indicating that our (approximate) treatment of line-blocking around He II 303 is rather accurate.

Compared to pure H/He plane-parallel models, our new results display the following trend:

For a given spectral type, the effective temperatures become lower along with a reduction of either gravity or helium abundance. The reduction of T_{eff} is largest at earliest spectral types and for supergiants, and decreases towards later types. At O9.5, the differences to unblanketed analyses are small, at least for the objects from our sample. Recent work by Crowther et al. (2002), however, indicates that *extreme* O-supergiants of late spectral types have significantly lower values of T_{eff} than our objects.

The reduction of the effective temperature scale has been explained in Sect. 4.7.2 as the final consequence of UV line-blocking, increasing both the electron temperature by line-blanketing and the mean intensity by back-scattering in the outer photosphere where the strategic lines are formed. As a result, line-blanketed models of hot stars have photospheric He ionization fractions similar to those from unblanketed models at higher T_{eff} and higher $\log g$. Thus, any analysis based on the He ionization equilibrium results in lower values of T_{eff} , if line-blocking/blanketing is accounted for. In those cases, where a reduction of $\log g$ is prohibited by the Balmer line wings, the helium abundance has to be reduced instead in order to allow for a convincing fit.

On the other hand, stellar radii and mass-loss rates (and hence modified wind-momentum rates) remain roughly unaffected by line-blanketing, since the *optical* fluxes from line-blanketed models are similar to those from unblanketed models at their corresponding, higher effective temperatures due to flux-conservation.

After correcting for the centrifugal acceleration (where this correction and the corresponding error has been derived in Appendix A), we calculated the masses and compared them with previous results as well as with evolutionary masses. Although the former *mass discrepancy* (Herrero et al., 1992) becomes significantly reduced, it still seems to exist at the lowest masses ($M < 15 M_{\odot}$). For all stars with larger mass, at least the corresponding error bars do cross the 1:1 line. Nevertheless, a systematic trend seems to be present: For $15 M_{\odot} < M < 50 M_{\odot}$, the spectroscopically derived values are still lower than the masses derived from evolutionary calculations by roughly $10 M_{\odot}$.

In the case of the *helium discrepancy*, we could significantly reduce the He abundance for a number of objects, particularly for those where previous values were extremely large (e.g., for HD 193682 Y_{He} has decreased from 0.43 to 0.20). A significant fraction of our sample stars, however, still remains over-abundant in He. For these objects, at least the derived range in abundance is consistent with present evolutionary tracks when rotationally induced mixing is accounted for.

One of the major implications of reduced luminosities and almost unaltered wind-momentum rates affects the wind-momentum luminosity relation. Previous results for O-stars (Puls et al., 1996; Kudritzki & Puls, 2000) indicated a clear separation of the WLR as function of luminosity class, where the WLR for supergiants was found to be more or less consistent with recent theoretical simulations which do *not* predict any dependence on luminosity class. For giants and dwarfs, the WLR was located roughly 0.5 dex below that. In addition, it showed a kink towards even lower momentum rates for objects with $\log(L/L_{\odot}) < 5.3$ which could not be explained so far.

Regarding our new values, the separation of the WLR is still present with one decisive difference. Now, the WLR *for giants/dwarfs* is consistent with theoretical expectations and also the kink has vanished at least if we assume that the actual mass-loss rates lie at the obtained upper limits. On various evidence (including recent UV-analyses and the problematic line cores of the blue Balmer lines, see above, with additional support from a recent investigation by Hillier et al. (2003)) we have argued that the different WLRs can be unified on the basis of the following assumptions: For those stars with H_{α} in emission, the derived mass-loss rates are affected by clumping in the lower wind region. For stars with H_{α} in absorption, on the other hand, this line is formed very close to the photosphere so clumping effects cannot disturb the analysis. This kind of unification would then require a clumping factor of roughly 5, where the mass-loss rates of stars with H_{α} in emission would typically be overestimated by a factor of 2.3. As displayed in Fig. 4.24, the combined WLR is then consistent also with theory.

We have, of course, to be open to other possibilities which might explain the discrepancies found. A combined multi-spectral analysis (UV, optical, IR and radio) based on clumped wind-models and applied to large samples of stars of different spectral type should clarify these questions as well as others, e.g., the problem of wind-momenta from mid-type B-supergiants which appear to be much *lower* than expected (Kudritzki et al., 1999).

One of the major problems encountered in the present analysis is the uncertainty in stellar radius, which originates from uncertain distances and enters quadratically into the values for masses, luminosities and wind-momentum rates.

Since the distances to Galactic O-stars (which are important because of their “Galactic” abundances) will probably pose a problem for the next decade(s), there are only two possibilities to overcome this uncertainty (at least indirectly). Either we consider samples much larger than the present one (with the hope that better statistics will help to obtain better constraints), or we concentrate on the analysis of O-stars (definitely) belonging to distinct clusters (with the hope that the analysis is at least intrinsically consistent).

For recent progress into direction “one”, we refer the reader to Markova et al. (2003). Regarding the second possibility, a first step has been taken by Herrero et al. (2002), although the amount of analyzed objects (seven) is not enough to obtain representative results. Observational campaigns utilizing multi-object spectroscopy like the upcoming FLAMES-project, aiming at the analysis of samples of more than hundred Extragalactic and Galactic objects, will definitely lead to a dramatic increase of our knowledge of hot, massive stars.

Acknowledgements:

T.R. gratefully acknowledges financial support in form of a grant by the International Max-Planck Research School on Astrophysics (IMPRS), Garching. Many thanks especially to the anonymous referee of this paper as well as to Dr. Mark Neeser and Dr. Nevyana Markova for useful comments on the manuscript. We would also like to thank Dr. Nolan Walborn for his suggestions, especially for drawing our attention to the importance of the Lutz-Kelker effect. This work has been partially supported by the Spanish MCyT under project PNAYA 2001-0436.

4.9 Appendix: Centrifugal correction

The objective of this appendix is to derive an expression for the centrifugal correction which we will apply to the “effective” gravity, in order to obtain an approximation for the “true” value and the corresponding error (cf. Eqs 4.3, 4.4). Thus, we have to evaluate the average

$$\langle g_{\text{cent}} \rangle_{\text{disk}} = \frac{\langle (V_{\text{rot}} \sin \theta)^2 \rangle}{R_{\star}}, \quad (4.17)$$

where $\langle g_{\text{cent}} \rangle_{\text{disk}}$ is averaged is over the stellar *disk* and, thus, depends on the inclination $\sin i$. This quantity must not be mistaken for the centrifugal acceleration averaged over the stellar *sphere*,

$$\langle g_{\text{cent}} \rangle_{\text{sphere}} = \frac{\int_0^{2\pi} \int_0^{\pi} g_{\text{cent}}(\theta) R_{\star}^2 \sin \theta d\theta d\phi}{4\pi R_{\star}^2} = \frac{2}{3} \frac{V_{\text{rot}}^2}{R_{\star}}, \quad (4.18)$$

which, of course, is independent of the inclination. Here and in the following we neglect any distortion of the stellar radius due to centrifugal forces that might become relevant in the case of rotational velocities close to break-up.

The geometrical situation is sketched in Fig. 4.25. We consider two Cartesian co-ordinate systems, $(z_{\star}, p_{\star}, q_{\star})$ and (z, p, q) . The former refers to the stellar system with rotation axis q_{\star} , and the latter to the one of the observer. The z -axis is directed towards the observer, the “impact parameter” $p = p_{\star}$ is perpendicular to the (z, q) -plane (identical to the (z_{\star}, q_{\star}) -plane), and q is the “height” of the disk, perpendicular to both z and p . Thus, both planes are tilted with respect to one another in terms of inclination i (between q and q_{\star}).

The co-ordinates in the stellar system can be expressed in terms of stellar co-latitude θ , azimuthal angle ϕ and radius r . Any points, \vec{r} , *on the stellar surface* (and only those are needed for our calculation) can be described by the following relation:

$$\vec{r} = \begin{pmatrix} z_* \\ p_* \\ q_* \end{pmatrix} = \begin{pmatrix} R_* \sin \theta \cos \phi \\ R_* \sin \theta \sin \phi \\ R_* \cos \theta \end{pmatrix}. \quad (4.19)$$

For the integration over the stellar disk, on the other hand, we first employ a polar co-ordinate system with co-ordinates P and polar angle Φ . Any point \vec{d} situated *on the stellar disk* has then coordinates

$$\vec{d} = \begin{pmatrix} p \\ q \end{pmatrix} = \begin{pmatrix} P \cos \Phi \\ P \sin \Phi \end{pmatrix}, \quad P = \sqrt{p^2 + q^2}, \quad \Phi = \arctan(q/p). \quad (4.20)$$

In this representation the desired average of the centrifugal acceleration over the stellar disk is given by

$$\langle g_{\text{cent}} \rangle = \frac{\int_0^{2\pi} \int_0^{R_*} g_{\text{cent}} P dP d\Phi}{\pi R_*^2}. \quad (4.21)$$

However, since g_{cent} is dependent on the stellar co-latitude θ , an integration with respect to the spherical stellar co-ordinates is advantageous.

Before we consider the general case of arbitrary inclination, we will deal with the simpler case where $\sin i = 1$ (i.e., the star is observed equator-on). In this case, the stellar system (where θ is defined) and the system of the observer coincide, i.e., $q_* = q$, such that the transformation from (P, Φ) to (θ, ϕ) is the following: Any projected point on the stellar disk can be represented by the corresponding physical location on the stellar sphere via

$$\begin{aligned} \begin{pmatrix} p \\ q \end{pmatrix} &= \begin{pmatrix} P \cos \Phi \\ P \sin \Phi \end{pmatrix} = \begin{pmatrix} R_* \sin \theta \sin \phi \\ R_* \cos \theta \end{pmatrix}, \\ P^2 &= R_*^2 (\sin^2 \theta \sin^2 \phi + \cos^2 \theta) \\ \tan \Phi &= \frac{\cot \theta}{\sin \phi}. \end{aligned} \quad (4.22)$$

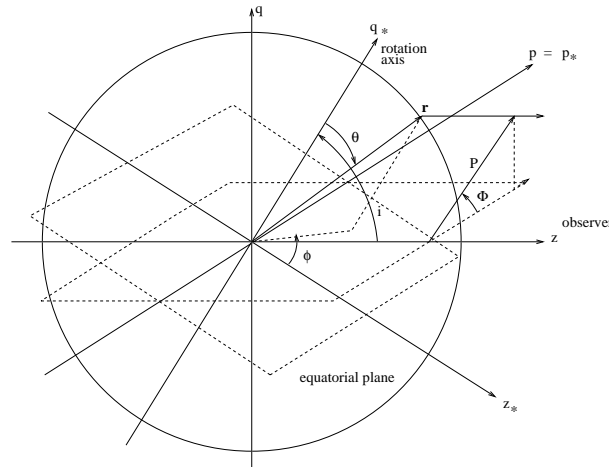


Figure 4.25: Geometry used for calculating the centrifugal correction (see text).

Note that we only have to consider the points on the half-sphere directed towards the observer, i.e., $z > 0$. Since the integral over PdP can alternatively be expressed by the integral over $1/2 dP^2$, the variable transformation inside the integrals, from $(dP^2, d\Phi)$ to $(d\theta, d\phi)$, is obtained by evaluating the determinant of the Jacobian of the transformation (4.22) which (after a number of operations) turns out to be

$$\det(J((P^2, \Phi), (\theta, \phi))) = 2R_\star^2 \sin^2 \theta \cos \phi. \quad (4.23)$$

Thus, for $\sin i = 1$, the integral over the stellar disk can be expressed as an integral over the front of the stellar sphere,

$$\begin{aligned} \frac{1}{2} \int_0^{2\pi} \int_0^{R_\star^2} f(P^2, \Phi) dP^2 d\Phi &= \\ &= R_\star^2 \int_{-\pi/2}^{\pi/2} \int_0^\pi f(\theta, \phi) \sin^2 \theta \cos \phi d\theta d\phi. \end{aligned} \quad (4.24)$$

One can readily convince oneself that for $f(\theta, \phi) = 1$ the correct result, $R_\star^2 \pi$, is obtained, whereas for $f(\theta, \phi) = g_{\text{cent}}(\theta)$ we find

$$\langle g_{\text{cent}} \rangle_{\text{disk}, \sin i=1} = \frac{3}{4} \frac{V_{\text{rot}}^2}{R_\star}. \quad (4.25)$$

For arbitrary inclinations the line of argument is similar. Note that the relation between stellar and observer's system can be represented by a rotation with respect to the common p -axis, i.e.,

$$\begin{pmatrix} z \\ p \\ q \end{pmatrix} = \begin{pmatrix} \sin i & 0 & \cos i \\ 0 & 1 & 0 \\ -\cos i & 0 & \sin i \end{pmatrix} \begin{pmatrix} z_\star \\ p_\star \\ q_\star \end{pmatrix} \quad (4.26)$$

and the generalization of (4.22) is

$$\begin{aligned} \begin{pmatrix} z \\ p \\ q \end{pmatrix} &= \begin{pmatrix} P \cos \Phi \\ P \sin \Phi \end{pmatrix} = \begin{pmatrix} R_\star (\sin \theta \cos \phi \sin i + \cos \theta \cos i) \\ R_\star \sin \theta \sin \phi \\ R_\star (-\sin \theta \cos \phi \cos i + \cos \theta \sin i) \end{pmatrix}, \\ P^2 &= R_\star^2 (\sin^2 \theta \sin^2 \phi + \sin^2 \theta \cos^2 \phi \cos^2 i + \cos^2 \theta \sin^2 i - \\ &\quad - 2 \sin \theta \cos \theta \cos \phi \sin i \cos i) \\ \tan \Phi &= \frac{-\cos \phi \cos i + \cot \theta \sin i}{\sin \phi}. \end{aligned} \quad (4.27)$$

The corresponding determinant of the Jacobian becomes (calculated with MATHEMATICA)

$$\det(J) = 2R_\star^2 \sin \theta (\cos \theta \cos i + \sin \theta \cos \phi \sin i), \quad (4.28)$$

and for $\sin i = 1$ we obtain the same result as above, whereas for $\sin i = 0$ (i.e., the star is observed pole-on) we find (using appropriate integration limits, see below)

$$\langle g_{\text{cent}} \rangle_{\text{disk}, \sin i=0} = \frac{R_\star^2 \int_0^{2\pi} \int_0^{\pi/2} g_{\text{cent}}(\theta) \sin \theta \cos \theta d\theta d\phi}{\pi R_\star^2} = \frac{1}{2} \frac{V_{\text{rot}}^2}{R_\star}. \quad (4.29)$$

In order to obtain the complete expression for arbitrary $\sin i$, we first have to calculate the integration limits. From the condition $z > 0$ (4.27) we find that

$$\begin{aligned} i < \frac{\pi}{2} & : \begin{cases} 0 < \phi < 2\pi, \\ 0 < \theta < \theta_{\max}, \end{cases} & \theta_{\max} = \frac{-\cos \phi \tan i}{\sqrt{1 + \cos^2 \phi \tan^2 i}} \\ i = \frac{\pi}{2} & : \begin{cases} -\pi/2 < \phi < \pi/2, \\ 0 < \theta < \pi. \end{cases} \end{aligned}$$

With these limits, we are able to calculate the first double integral ($\propto \cos i$, $i < \pi/2$, again with MATHEMATICA),

$$\cos i \int_0^{2\pi} \int_0^{\theta_{\max}} \sin^3 \theta \cos \theta d\theta d\phi = \frac{\pi}{8} \cos^2 i (4 - 2 \sin^2 i). \quad (4.30)$$

The second one ($\propto \sin i$, $i < \pi/2$) is given by

$$\sin i \int_0^{2\pi} \int_0^{\theta_{\max}} \sin^4 \theta \cos \phi d\theta d\phi = \frac{\pi}{8} \sin^2 i (8 - 2 \sin^2 i). \quad (4.31)$$

Finally, we obtain the rather simple result

$$\langle g_{\text{cent}} \rangle_{\text{disk}}(\sin i) = \frac{V_{\text{rot}}^2}{R_{\star}} \left(\frac{1}{2} + \frac{1}{4} \sin^2 i \right), \quad (4.32)$$

which includes the case $i = \pi/2$ (and, of course, the pole-on case $i = 0$).

In conclusion, the centrifugal acceleration averaged over the stellar disk depends on two terms. The first one, constituting a minimum value, depends on V_{rot}^2 alone (which *cannot* be measured) and a second term depends on $(V_{\text{r}} \sin i)^2$ (which *can* be measured).

In order to obtain a suitable approximation for the centrifugal correction based on the measurable quantity $(V_{\text{r}} \sin i)^2$, we will use appropriate means. Since the probability density function for the distribution of the inclination angle i is given by $\sin i$ itself (see, e.g., Chandrasekhar & Münch 1950), the mean and standard-deviation (i.e., square-root of the variance) of $\sin^2 i$ is given by

$$\langle \sin^2 i \rangle = \frac{2}{3} \left(1 \pm \frac{1}{\sqrt{5}} \right) \quad (4.33)$$

By approximating $(V_{\text{r}} \sin i)^2$ with $V_{\text{rot}}^2 \langle \sin^2 i \rangle$, we can express the centrifugal correction via

$$\begin{aligned} \langle g_{\text{cent}} \rangle & \approx \frac{(V_{\text{r}} \sin i)^2}{R_{\star}} \left(\frac{1}{2 \langle \sin^2 i \rangle} + \frac{1}{4} \right) = \frac{(V_{\text{r}} \sin i)^2}{R_{\star}} (1 + \Delta f) \\ \Delta f & = \frac{3}{4 \pm \sqrt{5} - 1} \approx \begin{matrix} +0.61 \\ -0.23 \end{matrix}. \end{aligned} \quad (4.34)$$

The larger error (i.e., an under-estimate of the centrifugal correction) occurs if $\sin^2 i < \langle \sin^2 i \rangle$ since V_{rot} is large, whereas $V_{\text{r}} \sin i$ is small. If $\sin^2 i \gtrsim \langle \sin^2 i \rangle$, the error is much lower because the estimator of V_{rot} is of the correct order. Thus, we encounter the (somewhat paradoxical) result that our approximate centrifugal correction is rather correct for fast rotators (except for the still missing correction concerning the deformation of the stellar radius), whereas for “slow” rotators the centrifugal correction might be too low.

Bibliography

- Abbott, D.C., Lucy, L.B. 1985, ApJ 288,679
- Bohannon, B., Voels, S.A., Hummer, D.G., Abbott, D.C. 1990, ApJ 365, 729
- Bromm, V., Kudritzki, R.P., Loeb, A. 2001, ApJ 552, 464
- Chandrasekhar, S., Münch, G. 1950, ApJ 111, 142
- Cranmer, S.R., Owocki, S.P. 1995, ApJ 440, 308
- Crowther, P.A., Hillier, D.J., Evans, C.J., et. al. 2002, ApJ 579, 774
- de Zeeuw, P.T., Hoogerwerf, R., de Bruijne, J.H.J., et al. 1999, AJ 117, 354
- ESA, 1997, The Hipparcos and Tycho Catalogues, ESA SP-1200
- Eversberg, T., Lepine, S., Moffat, A.F.J. 1998, ApJ 494, 799
- Feldmeier, A. 1995, A&A 299, 523
- Feldmeier, A., Puls, J., Pauldrach, A.W.A. 1997, A&A 322, 878
- Gabler, R., Gabler, A., Kudritzki, R.P., Puls, J., et. al. 1989, A&A 226, 162
- Garmany, C.D., Stencel, R.E. 1992, A&ASS 94, 211
- Gräfener, G., Koesterke, L., Hamann, W.-R. 2002, A&A 387, 244
- Harries, T.J., Howarth, I.D. 1996, A&A 310, 533
- Haser, S.M. 1995, Ph.D. Thesis, Universität München
- Heger, A., Langer, N. 2000, ApJ 544, 1016
- Herrero, A. 1993, SSRv 66, 137
- Herrero, A., Lennon, D.J. 2003, in: Proc. IAU Symp. 215, eds. A. Maeder & P. Eenens, ASP, in press
- Herrero, A., Kudritzki, R.P., Vílchez, J.M., et al. 1992, A&A 261, 209
- Herrero, A., Puls, J., Villamariz, M.R. 2000, A&A 354, 193
- Herrero, A., Puls, J., Najarro, F. 2002, A&A 396, 949

- Hillier, D.J., Miller, D.L. 1998, ApJ 496, 407
- Hillier, D.J., Lanz, T., Heap, S.R., et al. 2003, ApJ 588, 1039
- Hoogerwerf, R., de Bruijne, J.H.J., de Zeeuw, P.T. 2001, A&A 365, 49
- Howarth, I.D., Siebert, K.W., Hussain, G.A.J., et al. 1995, MNRAS 284, 265
- Hubeny, I., Lanz, T. 1995, ApJ 39, 875
- Hubeny, I., Heap, S.R., Lanz, T. 1998, ASP Conf. Series Vol. 131, 108
- Hummer, D.G. 1982, ApJ 257, 724
- Hummer, D.G., Abbott, D.C., Voels, S.A., Bohannon, B. 1988, ApJ 328, 704
- Humphreys, R.M. 1978, ApJSS 38, 309
- Koen, C. 1992, MNRAS 256, 65
- Kudritzki, R.P. 1980, A&A 85, 174
- Kudritzki, R.P., Puls, J. 2000, ARA&A 38, 613
- Kudritzki, R.P., Lennon, D.J., Puls, J. 1995, in: "Quantitative Spectroscopy of Luminous Blue Stars in Distant Galaxies". ESO Astrophysics Symposia, Science with the VLT, eds. J.R. Walsh & I.J. Danziger, Springer, Heidelberg, p. 246
- Kudritzki, R.P., Puls, J., Lennon, D.J., et al. 1999, A&A 350, 970
- Lennon, D.J., Dufton, P.L., Fitzsimmons, A. 1992, A&AS, 94, 569
- Lennon, D.J., Dufton, P.L., Fitzsimmons, A. 1993, A&AS 97, 559
- Leitherer, C., Heckman T.M. 1995, ApJS 96, 9
- Lutz, T.E., Kelker, D.H. 1973, PASP 85, 573
- Maeder, A., Meynet, G. 2000, ARA&A 38, 143
- Maeder, A., Meynet, G. 2000, A&A 361, 159
- Markova, N., Puls, J., Repolust, T.M., Markov, H. 2004, A&A 413, 693
- Martins, F., Schaerer, D., Hillier, D.J. 2002, A&A 382, 999
- Massa, D., Fullerton, A.W., Sonneborn, G., et al. 2003, ApJ 586, 996
- Massey, P. 1998, *VIII IAC Winter School of Astrophysics: Stellar Astrophysics for the Local Group*, eds. A. Aparicio, A. Herrero & F. Sanchez, CUP, p. 95
- Meynet, G., Maeder, A. 2000, A&A 361, 101
- Moffat, A.F.J., Robert, C. 1994, ApJ 421, 310

- Nelan, E., et. al. 2003, in prep.
- Oey, S. 2003, in: Proc. IAU Symp 212, eds. K.A. van der Hucht, A. Herrero & C. Esteban, ASP, p. 620
- Oudmajier, R.D., Groenewegen, M.A.T., Schrijver, H. 1998, MNRAS 294, L41
- Owocki, 1999, in: Proc. IAU Coll. 169, eds. B. Wolf, O. Stahl & A. W. Fullerton, p. 294
- Owocki, S.P., Puls, J. 1999, ApJ 510, 355
- Owocki, S.P., Castor, J.I., Rybicki, G.B. 1988, ApJ 335, 914
- Pauldrach, A.W.A., Puls, J., Kudritzki, R.P. 1986, A&A 164, 86
- Pauldrach, A.W.A., Kudritzki, R.P., Puls, J., et al. 1994, A&A 283, 525
- Pauldrach, A.W.A., Hoffmann, T.L., Lennon, M. 2001, A&A 375, 161
- Pauldrach, A.W.A., Hoffmann, T.L., Méndez, R. 2003, in Proc. IAU Symp. 209, eds. S.Kwok & M.Dopita, in press
- Penny, L.R. 1996, ApJ 463, 737
- Penny, L.R., Gies, D.R., Hartkopf W.I., et al. 1993, PASP 105, 588
- Petrenz, P., Puls, J. 1996, A&A 312, 195
- Petrenz, P., Puls, J. 2000, A&A 358, 956
- Pettini, M., Steidel, C.C., Adelberger, K.L., et al. 2000, ApJ 528, 96
- Puls, J., Kudritzki, R.P., Herrero, A., et al. 1996, A&A 305, 171 (Paper I)
- Puls, J., Springmann, U., Lennon, M. 2000, A&A 141,23
- Puls, J., et al. 2003, in: Proc. IAU Symp 212, eds. K.A. van der Hucht, A. Herrero & C. Esteban, ASP, p. 61
- Puls, J., et al. 2003, in prep.
- Repolust, T., Puls, J., Herrero, A. 2004, A&A 415, 349
- Santolaya-Rey, A.E., Puls, J., Herrero, A. 1997, A&A 323, 488
- Silich, S., Tenorio-Tagle, G. 2001, ApJ, 552, 9
- Schaerer, D., Schmutz, W. 1994, A&A 288, 231
- Schaller, G., Schaerer, D., Meynet, G., Maeder, A. 1992, A&AS 96, 269
- Schmutz, W., 1991, in: Stellar Atmospheres: Beyond Classical Models, eds. Crivellari, L., Hubeny, I., and Hummer, D.G., NATO ASI Series C Vol.341, Kluwer, Dordrecht, p.191

- Schmutz, W. 1997, A&A 321, 268
- Shortridge, K 1987, FIGARO user manual
- Smith, K.C., Howarth, I.D. 1998, MNRAS 299, 1146
- Steidel, C.C., Giavalisco, M., Pettini, M., et al. 1996, ApJL 462, L17
- Urbaneja, M.A., Herrero, A., Bresolin, F., et al. 2003, ApJL 584, 73
- Vacca, W.D., Garmany, C.D., Shull, M. 1996, ApJ 460, 914
- Villamariz, M.R., Herrero, A. 2000, A&A 357, 597
- Villamariz, M.R., Herrero, A., Butler, K., Becker, S.R. 2002, A&A 388, 940
- Vink, J.S., de Koter, A., Lamers, H.J.G.L.M. 2000, A&A, 362, 295
- Vink, J.S., de Koter, A., Lamers, H.J.G.L.M. 2001, A&A, 369, 574
- Voels, S.A., Bohannon, B., Abbott, D.C. 1989, ApJ 340, 1073
- Walborn, N.R. 1972, AJ 77, 312
- Walborn, N.R. 1973, AJ 78, 1067
- Walborn, N.R. 1982a, AJ 87, 1300
- Walborn, N.R. 1982b, ApJ 254, L15
- Walborn, N.R. 1995, RMxAC 2, 51
- Walborn, N.R., Howarth, I.D., Lennon, D.J., et al. 2002, AJ 123, 2754

Chapter 5

Mass-loss and wind-momentum rates of O-type stars: A pure H_α analysis accounting for line-blanketing

N. Markova, J. Puls, T. Repolust, H. Markov, A&A 413, 693

Abstract. We study mass-loss and wind momentum rates of 29 Galactic O-type stars with luminosity classes I, III and V by means of a pure H_α profile analysis and investigate to what extent the results compare to those originating from a state-of-the-art, complete spectral analysis. Our investigation relies on the approximate method developed by Puls et al. (1996) which we have modified to account for the effects of line-blanketing. Effective temperatures and gravities needed to obtain *quantitative* results from such a simplified approach have been derived by means of calibrations based on most recent spectroscopic NLTE analyses and models of Galactic stars by Repolust et al. (2004) and Martins et al. (2002). Comparing (i) the derived wind-densities to those determined by Repolust et al. (2004) for eleven stars in common and (ii) the Wind-momentum Luminosity Relationship (WLR) for our sample stars to those derived by other investigations, we conclude that our approximate approach is actually able to provide consistent results. Additionally, we studied the consequences of “fine tuning” some of the direct and indirect parameters entering the WLR, especially by accounting for different possible values of stellar reddening and distances. Combining our data set with the corresponding data provided by Herrero et al. (2002) and Repolust et al. (2004) we finally study the WLR for the largest sample of Galactic O-type stars gathered so far, including an elaborate error treatment. The established disagreement between the theoretical predictions and the “observed” WLRs being a function of luminosity class is suggested to be a result of wind clumping. Different strategies to check this hypothesis are discussed, particularly by comparing the H_α mass-loss rates with the ones derived from radio observations.

5.1 Introduction

The evolution of the Universe, since the time when the first stars were formed, is a central topic of present-day astrophysical research. Massive stars are the main engines which drive this cosmic evolution. Although rotation may also play an important role, mass-loss is still considered to be the dominant process for the evolution of these stars. As shown in numerous stellar evolution calculations, a change in mass-loss rates of massive stars by even a factor of 2 has a dramatic effect on their evolution (Meynet et al., 1994). Indeed, the nature of the eventual supernova explosion may depend critically on the precursor's mass-loss history, in particular during the poorly understood post main-sequence phases of evolution (Woosley, Heger & Weaver, 2002).

Thus, accurate mass-loss rates are crucial for both our knowledge of the nature and evolution of massive stars and our understanding of the Universe as a whole. Accurate mass-loss rates are also important with respect to the so-called Wind-momentum Luminosity Relationship (WLR, cf. Kudritzki & Puls 2000 and references therein) which will provide an alternative possibility to determine extragalactic distances by means of purely spectroscopic tools. There are several physical processes that may effect and significantly modify the observed mass-loss rates, of which the most important are metallicity, wind clumping, spectral variability and rotation.

During the recent years new model atmosphere codes have been developed which can provide accurate and consistent stellar and wind parameters for O-type stars. These codes take the effects of NLTE and winds properly into account, in particular the presence of metal line-blocking/blanketing (Hillier & Miller, 1998; Pauldrach et al., 2001; Herrero et al., 2002). The inclusion of these processes has a strong impact on the derived effective temperatures and leads to lower values, compared to results from unblanketed models (Martins et al., 2002; Herrero et al., 2002; Crowther et al., 2002; Bianchi & Garcia, 2002; Repolust et al., 2004), see also Hubeny & Lanz (1995). This temperature reduction leads to a downward revision of stellar luminosities (and, to a lesser extent, of gravities, radii and mass-loss rates) for O-type stars.

The application of the new codes, in particular to far-UV and UV spectra, indicated that O-star winds might be clumped (Crowther et al., 2002; Bianchi & Garcia, 2002; Massa et al., 2003), which is in agreement with predictions from time-dependent hydrodynamical simulations (Owocki, Castor & Rybicki, 1988; Feldmeier, 1995; Owocki & Puls, 1999). Additional evidence in support of the clumped nature of O-star winds has been found by Repolust et al. (2004, henceforth “RPH”) who studied the corresponding WLR using optical spectra. These authors confirmed the clear separation between the WLRs for luminosity class I (Ic I) and luminosity class III/V (Ic III/V) stars, already detected by means of unblanketed analyses (Puls et al., 1996). Note that such a separation is in contrast to present-day theoretical simulations of line-driven winds, predicting a unique relation instead (Vink et al., 2000; Pauldrach et al., 2002; Puls et al., 2003).

The effect of clumping may be the key to resolve this discrepancy. In particular, Puls et al. (2003) suggested that there might be no separation at all, but that one can “see” the effects of clumping in objects with H_α in emission (i.e., with a large contributing wind volume), which then mimics a higher mass-loss rate (and thus wind-momentum) than actually present. In objects with H_α in absorption, on the other hand, only contributions from the innermost (not clumped) wind are present and, thus, \dot{M} is observed at its actual value.

The possibility to use the WLR of O-stars as an indicator of wind clumping is very exciting but still needs to be proven. One way to check this possibility is to compare mass-loss rates derived from wind diagnostics relying on different density dependences, e.g., from H_α and UV resonance

lines. In fact, a coarse comparison of observed and synthetic UV spectra performed by Puls et al. (2003) revealed that for those objects where the H_α mass-loss rates did not agree with the theoretical predictions, SiIV (which is ρ^2 -dependent) favoured the “observed”, i.e., larger mass-loss rate. Those lines, however, which form close to the photosphere seemed to be consistent with a lower value. Hence, a (re-)analysis of UV spectra aiming at an independent \dot{M} determination for those stars with H_α in emission might be worthwhile.

Another possibility to check for clumping in O-star winds is to compare H_α and radio mass-loss rates. In the case of completely clumped winds and owing to the suggested radial stratification of the clumping factor (Owocki et al., 2000), radio and H_α mass-loss rates might differ significantly. The comparisons performed so far do not give evidence of any systematic difference (Lamers & Leitherer, 1993; Scuderi & Panagia, 2000). Note, however, that in view of the interpretation by Puls et al. (2003) also this result needs to be re-investigated (cf. Sect. 6).

Following the outlined reasoning, we have started a project to address the questions of wind clumping in O-type stars (beginning with Galactic objects), by comparison of optical data with radio (and IR) mass-loss rates. Such a project requires a (very) large sample of stars to be analyzed, because of the rather large error bars in \dot{M} -estimates for individual objects (at least in our Galaxy, due to uncertain distances). It must be noted, however, that the computational effort to analyze the spectra of even *one* star is extremely large, so that the application of the codes mentioned above becomes rather problematic.

In order to find a suitable resolution to this problem, we decided to investigate the following question: To what extent can the analysis of the H_α profile *alone* provide results consistent with those originating from a complete spectral analysis? In case of reasonable agreement, such an analysis can be used at least in two ways: First, valuable information can be added to complement smaller samples which have been analyzed in a detailed way by using already available H_α spectra (or spectra with missing strategic lines). Second, from such an analysis targets for follow-up observations (and analyses) can be selected, particularly for investigations in the radio and IR band.

The results of this investigation are presented in the following. In Section 2 and 3 we describe the observational material and the stellar sample; in Section 4 we outline the method, determine mass-loss rates and compare with results from complete analyses. Based on these data and as a first application we derive the corresponding WLR and compare it with similar studies as shown in Sect. 5. Having convinced ourselves that the simplified approach gives consistent results, we finally combine our data with alternative data sets, namely those from RPH and Herrero et al. (2002), to obtain the largest sample of Galactic O-stars used so far for a study of the WLR. In Section 6 we discuss the implications and present our (preliminary) conclusions.

5.2 Spectral observations

The H_α spectra analyzed in the present work have been obtained as part of a three year observation program to study wind variability of luminous early type stars in our Galaxy. We used the Coudé spectrograph of the 2m RCC telescope at the National Astronomical Observatory, Bulgaria. The project started in 1997 with an ELECTRON CCD with 520 x 580 pixels of 22 x 24 μ as detector. Beginning in the fall of 1998, we used a PHOTOMETRIC CCD with a pixel area of 1024 x 1024 and a pixel size of 24 μ . With the former configuration approximately 115 Å can be observed in one exposure with a resolution of $R = 15\,000$, while with the latter one the spectrum coverage is approximately 200 Å, again

with a resolution of 15 000. Spectra taken in April 1998 were obtained using a SBIG ST6 Thomson CCD with an area of 375×242 pixels and a pixel size of $23 \times 27 \mu$. The resolution of these spectra is 15 000 over a spectral range of 72 \AA .

While the observational material derived throughout this program has been/will be used as a basis for a series of investigations dealing with wind variability itself, in the present study we have considered only one (the most “representative”) spectrum per star.

We followed a standard procedure for data reduction, including bias subtraction, flat-fielding, cosmic ray hits removal, wavelength calibration and correction for heliocentric radial velocity. The spectra were normalized by a polynomial fit to the continuum, specified by carefully selected continuum windows, and re-binned to a step-size of 0.2 \AA per pixel. The atmospheric water vapour lines were removed by dividing each spectrum of each target with a specially constructed “telluric spectrum”. All steps in the reduction procedure were performed using a series of modules written in IDL. More information about the observations and the reduction procedure can be found in Markova & Valchev (2000).

5.3 Sample stars

Our sample consists of 29 stars with spectral classes ranging from O4 to O9.7 including 22 supergiants of luminosity class If, Ia, Ib and Iab, one bright giant, 3 normal giants and 3 dwarfs. The stars are listed in Table 5.1 together with the adopted spectral types and luminosity classes (Column 2), clusters or association membership (Column 3), visual magnitudes and $(B - V)$ colours (Columns 4 and 5), extinction ratio R and distances (Column 6 and 7) and absolute magnitudes, M_V (Column 8).

Twenty one of the targets have been selected by means of the following criteria:

1. To be brighter than 9^m in order to allow spectra with a signal-to-noise ratio of approximately 200 to be obtained with the available instruments in less than 15 min.
2. To be spectroscopically single stars (see below)
3. To be members of clusters or associations, i.e., to have “known” distances.

The remaining eight targets (displayed in the lower part of Table 5.1) satisfy the first two criteria but are not members of clusters or associations. Nevertheless, we have included these stars into our sample because, first, they have never been analyzed with respect to mass-loss rates using H_α (except for HD 188 209). Second, a part of them has recently been observed as radio sources (Scuderi et al., 2003), whereas the other part has good chances to be detected in the radio band as their H_α profiles appear mainly in emission. In particular, we intend to use these additional objects in order to derive constraints on the clumpiness of their winds.

Spectral types and luminosity classes for the majority of the stars are taken from the work of Walborn (1971, 1972, 1973). For HD 24 912, however, we adopt a luminosity class I instead of III as assigned by Walborn, in agreement with Herrero et al. (1992) who found that even with the correction for the effects of centrifugal forces the gravity of this star is much lower than for typical luminosity class III objects. For the two stars without a classification by Walborn, BD+56739 and HD 338 926, spectral types and luminosity classes originate from Hiltner (1956) and from Hiltner & Iriarte (1955), respectively.

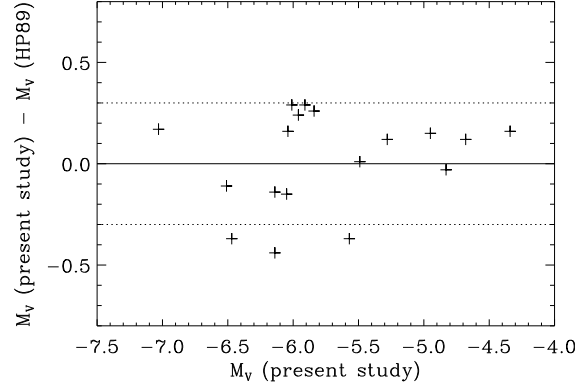


Figure 5.1: Difference in absolute magnitude between our recalculations (using photometry by *Hipparcos*) and the values reproduced by Howarth & Prinja (1989), for those stars of our sample which belong to an association or cluster. The three outliers at the bottom correspond, from left to right, to HD 30 614, HD 209 975 and HD 36 861 (see text).

Cluster and association membership are from Humphreys (1978), from Garmany & Stencel (1992) and from Lennon et al. (1992, HD 30 614). For all but two stars, HD 66 811 and HD 30 614, distances adopted by Humphreys (1978) have been used. In these two exceptional cases, distances are taken from the Galactic O Stars Catalogue (Cruz-Gonzalez et al., 1974). To check the stars for spectroscopic binarity we consulted the list of Gies (1987).

To avoid possible inconsistencies when adopting absolute magnitudes from different sources we recalculated the M_V of our targets using photometry and colours from *Hipparcos* (given in columns 4 and 5 of Table 5.1) combined with a mean intrinsic colour $(B - V)_0 = -0^m31$ and -0^m28 for stars of luminosity classes V/III and I, respectively (FitzGerald, 1970; Wegner, 1994) and an extinction law with $R = 3.1$, again, with the distances as mentioned above.

However, since the extinction can change significantly depending on the line of sight and since individual estimates of R for stars in several associations are available in the literature (Cardelli, 1988; Clayton & Cardelli, 1988; Cardelli et al., 1989), we decided to use these estimates as a second entry to determine absolute magnitudes. In particular, for objects in Cep OB2, in Per OB1 and in Ori OB1 the second entry for R is the average of more than one member.

As shown in Fig 5.1, the obtained M_V values agree within $\pm 0^m3$ with those published by Howarth & Prinja (1989) for all stars in common, except for HD 209 975, HD 36 861 and HD 30 614.¹ In the first two cases, the larger differences in M_V are due to relatively large differences between the *Hipparcos* photometry and the one used by Howarth & Prinja (1989). HD 30 614, on the other hand, is marked as a field star in Howarth & Prinja (1989) ($M_V = -6^m0$), while in the present work we consider it as a member of the globular cluster NGC 1502.

For several stars more than one entry is given in Table 5.1. This has been done to account for the “distance” problem inherent to *Galactic* objects mentioned in the introduction and to address the effects of using different radii on the resulting mass-loss and wind-momentum rates. The entry superscribed with number (1) accounts for the individual values of R as discussed above while the

¹Note that with regard to absolute magnitudes the work of Howarth & Prinja (1989) is not a primary source, because the authors adopted these values from an unpublished catalogue by K. Garmany.

Table 5.1: Spectral types and photometric data of the studied stars. For objects with more than one entry, see caption below and text.

Star HD	Spec. type	Assoc.	m_V mag	B-V mag	R	d kpc	M_V mag
HD 190 429A	O4If+	CygOB3	6.62	0.148	3.1	2.29	-6.51
HD 66 811	O4I(n)f	Gum Nebula	2.21	-0.269	3.1	0.46	-6.14
HD 66 811 ²⁾		field			3.1		-6.40*
HD 66 811 ⁴⁾		runaway			3.1	0.73	-7.14
HD 16 691	O4If	PerOB1	8.69	0.411	3.1	2.29	-5.25
HD 16 691 ¹⁾		PerOB1			2.8	2.29	-5.04
HD 16 691 ³⁾		runaway			3.1		-6.40*
HD 14 947	O5If+	PerOB1	8.03	0.389	3.1	2.29	-5.84
HD 14 947 ¹⁾		PerOB1			2.8	2.29	-5.64
HD 14 947 ²⁾		field			3.1		-6.90*
HD 210 839	O6I(n)f	CepOB2	5.05	0.192	3.1	0.83	-6.01
HD 210 839 ¹⁾		CepOB2			2.76	0.83	-5.85
HD 210 839 ²⁾		runaway			3.1		-6.60*
HD 42 088	O6.5V	GemOB1	7.55	0.014	3.1	1.51	-4.35
HD 42 088 ⁵⁾		GemOB1			3.1	2.00	-4.96
HD 54 662	O6.5V	CMaOB1	6.23	-0.018	3.1	1.32	-5.28
HD 192 639	O7Ib(f)	CygOB1	7.12	0.279	3.1	1.82	-5.91
HD 193 514	O7Ib(f)	CygOB1	7.42	0.392	3.1	1.82	-5.96
HD 34 656	O7II(f)	AurOB1	6.79	0.00	3.1	1.32	-4.68
HD 34 656 ⁶⁾		AurOB2			3.1	3.02	-6.64
HD 47 839	O7V((f))	MonOB1	4.66	-0.233	3.1	0.71	-4.83
HD 24 912	O7.5I(n)((f))	PerOB2	3.98	0.016	3.1	0.40	-4.95
HD 24 912 ¹⁾		PerOB2	3.98		3.24	0.40	-4.99
HD 24 912 ²⁾		runaway			3.1		-6.70*
HD 36 861	O8III((f))	OriOB1	3.39	-0.160	3.1	0.50	-5.57
HD 36 861 ¹⁾		OriOB1			5.0	0.50	-5.85
HD 210 809	O9Iab	CepOB1	7.56	0.010	3.1	3.47	-6.04
HD 207 198	O9Ib/II	CepOB2	5.94	0.312	3.1	0.83	-5.49
HD 207 198 ¹⁾		CepOB2			2.76	0.83	-5.29
HD 37 043	O9III	OriOB1	2.75	-0.210	3.1	0.50	-6.05
HD 37 043 ¹⁾		OriOB1			5.0	0.50	-6.24
HD 24 431	O9III	CamOB1	6.74	0.349	3.1	1.00	-5.30
HD 24 431 ¹⁾		CamOB1			3.51	1.00	-5.57
HD 16 429	O9.5I/II	CasOB6	7.70	0.530	3.1	2.19	-6.51
HD 30 614	O9.5Ia	NGC1502	4.26	-0.008	3.1	0.95	-6.47
HD 30 614 ²⁾		runaway			3.1		-6.00*
HD 209 975	O9.5Ib	CepOB2	5.07	0.240	3.1	0.83	-6.14
HD 209 975 ¹⁾		CepOB2			2.76	0.83	-5.96
HD 18 409	O9.7Ibe	CasOB6	8.37	0.419	3.1	2.19	-5.50
HD 17 603	O7.5Ib(f)	field	8.49	0.551	3.1		-6.70*
HD 225 160	O8Ib(f)	field	8.19	0.260	3.1		-6.40*
HD 338 926	O8.5Ib(e?)	field	9.52	1.207	3.1		-6.60*
HD 188 209	O9.5Iab	field	5.60	-0.078	3.1		-6.00*
HD 202 124	O9.5Iab	field	7.74	0.209	3.1		-6.00*
HD 218 915	O9.5Iab	runaway	7.23	-0.026	3.1		-6.00*
BD +56 739	O9.5Ib	field	9.95	0.991	3.1		-6.00*
HD 47 432	O9.7Ib	field	6.23	0.086	3.1		-6.00*

* data corresponding to Garmany's spectral type- M_V calibration reproduced by Howarth & Prinja (1989).

¹⁾ M_V computed with individual values for R (see text).

²⁾ suggested to be a field/runaway star by Gies (1987).

³⁾ suggested to be a runaway star by Stone (1979).

⁴⁾ suggested to be a runaway star by Sahu & Blaauw (1993).

⁵⁾ distance (as a member of NGC 2175 in GemOB1) given by Felli et al. (1977).

⁶⁾ distance as a member of AurOB2 (Tovmassian et al., 1994).

one superscribed with number (2) takes into account those stars which have been suggested by Gies (1987) to be field or runaway stars, in contrast to the work by Humphreys (1978). In the latter case as well as for the stars listed in the lower part of Table 5.1 (i.e., field stars), absolute magnitudes derived with the same spectral type – M_V relation as used by Howarth & Prinja (1989) have been adopted. Entry number (3) relates to the work of Stone (1979) who suggested that HD 16 691 is a runaway star originating in the Galactic plane. Entry (4) refers to the work by Sahu & Blaauw (1993) who suggested, based on proper motion and radial velocity data, that the supergiant ζ Pup is a runaway star originating in the Vela Molecular Ridge close to the Vela R2 association. With a distance of 730 pc, ζ Pup would become the most luminous star in our sample. Entry (5) and (6) refer to comments given in Sect. 5.1.

5.4 H_α mass-loss rates

As noted in the introduction, one of the major goals of the present study is to check to what extent the analysis of H_α profiles alone can provide results consistent with those originating from a complete spectral analysis. To this end, we employed the approximate method developed by Puls et al. (1996) which we have modified to account for the effects of line-blocking and blanketing. This method uses H and HeII departure coefficients from unified model atmospheres parameterized in a simple way as a function of wind velocity together with photospheric NLTE line profiles as an inner boundary condition in order to obtain an “exact” (i.e., non-Sobolev) radiative transfer solution to synthesize the wind contaminated H_α -profile.

Detailed information about the actual fit procedure can be found in Puls et al. (1996). In the following, we will discuss how we obtain (i.e., approximate) those input parameters which are *not* varied throughout the fit, and how we account for line-blocking/blanketing effects.

5.4.1 Input parameters

Since we are going to use “only” H_α all stellar parameters including v_∞ have to be provided either from different sources or from calibrations.

Effective temperatures and surface gravities (Columns 3 and 5 of Table 5.2) are determined from spectral types using own calibrations based on data obtained by RPH via line profile fitting to a number of strategic (hydrogen and helium) lines in the spectral range between 4 000 and 6 700 Å using NLTE atmosphere models with mass-loss, sphericity and an approximative treatment of metal line-blocking/blanketing.

Actually, not all of the stars studied by RPH have been included to derive the spectral type – T_{eff} relation: close binaries (HD 93 129A and HD 303 308, Nelan et al. 2003) as well as fast rotators (e.g., HD 217 086 with $v \sin i = 350 \text{ km s}^{-1}$ and HD 13 268 with $v \sin i = 300 \text{ km s}^{-1}$) were excluded. The former due to a possible influence of the secondary on the “observed” temperatures and the latter because of the effects of stellar rotation on the surface temperature distribution (gravity darkening).

Since there was only a small number of luminosity class V stars left after the reduction of the Repolust sample we incorporated data presented by Martins et al. (2002) in a comparable investigation. (With respect to $\log g$, we used the Repolust sample alone). Fig 5.2 shows the temperature (left panel) and $\log g$ (right panel) calibrations for luminosity classes I, III and V derived and used in the present study.

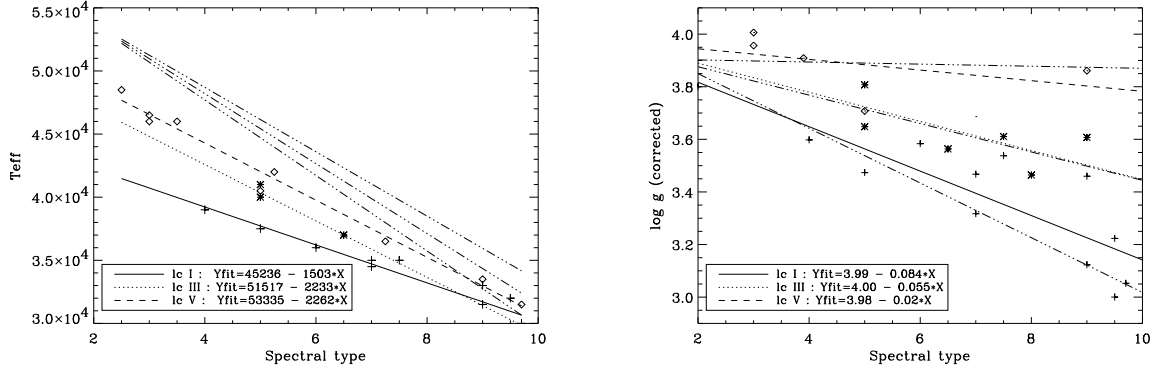


Figure 5.2: Spectral type– T_{eff} (left panel) and spectral type– $\log g$ relations for luminosity class I (bold), III (dotted) and V (dashed) derived and used in the present study. Overplotted are the corresponding data from RPH and for lc V objects in the left panel also from Martins et al. (2002): crosses – lc I, asterisks – lc III, diamonds – lc V. The dotted-dashed lines represent the empirical calibrations obtained by Vacca et al. (1996) using data derived by means of pure H/He, non-LTE, plane-parallel, hydrostatic model atmospheres.

One can see that the scatter of the T_{eff} data around the regression lines is relatively small ($\sigma = 950$, 360 and 793 K, for lc I, III and V, respectively), while in the case of the spectral type– $\log g$ relations it is somewhat larger ($\sigma = 0.12$, 0.17 and 0.20). On the other hand, the reader may note that the T_{eff} calibration for late spectral types (later than O7) remains somewhat uncertain due to the strong influence of the specific wind-density on T_{eff} . The dotted-dashed lines overplotted in each panel represent the empirical calibrations obtained by Vacca et al. (1996) using data derived by means of pure H/He, non-LTE, plane-parallel, hydrostatic model atmospheres.

Our results indicate that the differences between the blanketed and the unblanketed temperature scale decrease with decreasing T_{eff} , being largest ($\max(\Delta T_{\text{eff}}) \sim 10\,000$ K) for luminosity class I and smallest ($\max(\Delta T_{\text{eff}}) \sim 5\,000$ K) for luminosity class V stars due to the additional wind blanketing present in supergiant atmospheres.

On the other hand, the $\log g$ regressions for luminosity classes III and V based on blanketed models are almost identical to the calibration by Vacca et al., while for (late) supergiants an increase of less than 0.15 dex is found, in agreement with what might be expected from theory (different density stratification in hydrostatic vs. mass-losing atmospheres in those regions where the Balmer line wings are formed, cf. Puls et al. (1996)). All gravities displayed in Fig. 5.2 have been corrected for the effects of centrifugal forces (similarly to the procedure applied by Herrero et al. 1992, Vacca et al. 1996 and particularly RPH), since many of the stars from the Repolust sample have projected rotational speeds exceeding of 200 km s^{-1} . For the faster rotators in our sample, we have finally re-corrected the derived $\log g$ values in order to use photospheric input profiles with appropriate *effective* gravities in our H_α line-profile fitting procedure.

We are aware of the fact that the spectral type – T_{eff} relationship may not be linear, e.g. Crowther (1998). Note, however, that the data used here do not give any evidence of significant deviations from a linear approximation, at least not in the covered range of spectral subclasses. In particular, using a cubic, instead of a linear regression for stars with stronger (lc I) and weaker (lc V) winds improves the fit quality by less than 100 K, which is much smaller than the typical error in T_{eff} ($\pm 1\,000 \dots 1\,500$ K) derived from complete spectral analyses (e.g., Herrero et al. 1992; RPH). Admittedly, our calibration

might be somewhat unrealistic for the earliest spectral types at luminosity class III. Note, however, that our sample does not comprise any objects in this range, and therefore our analysis is not affected by this uncertainty.

Stellar radii (Column 4 of Table 5.2) have been derived from de-reddened absolute magnitudes and theoretical fluxes in the V-band using the procedure outlined by Kudritzki (1980), cf. Eqs. 1 and 2 in RPH. The theoretical fluxes have been approximated by using a radiation temperature of $T_{\text{rad}} \approx 0.9 T_{\text{eff}}$ (V-band!), where this approximation results from an analysis of line-blanketed O-star model atmospheres. The typical accuracy of this approximation (which translates almost linearly into the derived radii) is of the order of 5% in the O-star domain.

Helium abundance. For those stars in common with the sample by Repolust et al. we have adopted their helium abundance. For the remainder, we have used a “normal” abundance of $Y_{\text{He}} = N(\text{He})/N(\text{H}) = 0.1$ as a first guess. Subsequently, this value was increased, if necessary, to obtain a better fit (with respect to the HeII blend), accounting also for the evolutionary phase (dwarf/supergiant) of the objects. Therefore, these values can be considered only as rough estimates.

Radial and rotational velocities. Puls et al. (1996) noted that the accuracy of the adopted radial velocity, v_r , should be better than 20 km s^{-1} in order to obtain reliable fit results. In the present study, radial velocities (not listed in Table 5.2) and projected rotational velocities $v \sin i$ (Column 7 of Table 5.2) of the sample stars hotter than 35 500 K are taken from the General Catalogue of Mean Radial Velocity (GCMRV, Barbier-Brossat & Figon, 2000) and from Penny (1996), respectively, except for HD 16 691, for which we have used our own estimate of $v \sin i$ (see below).

For stars cooler than 35 500 K, with the exception of HD 36 861, HD 338 926 and HD 188 209, we obtained own estimates for $v \sin i$ and v_r by means of fitting the HeI $\lambda 6678$ absorption line. The reliability of our determinations has been checked by comparison with data from other investigations. In particular, our set of $v \sin i$ estimates conforms quite well (within $\pm 10 \text{ km s}^{-1}$) with those from Penny (1996) for 9 out of 11 objects in common. In the exceptional cases of HD 36 861 and HD 188 209 our estimates of $v \sin i$ turned out to be larger (by $\sim 30\%$) than those from Penny, and the estimates of Penny have been adopted.

Good agreement was also found between our set of v_r data and that of Conti et al. (1977) (within $\pm 20 \text{ km s}^{-1}$) for 13 stars in common. The H_α spectrum of HD 338 926 does not include HeI $\lambda 6678$. Hence, no estimates of either $v \sin i$ or v_r could be derived. We adopted v_r from the SIMBAD Catalogue and a typical value of 80 km s^{-1} for $v \sin i$.

Wind terminal velocities (Column 9 of Table 5.2) have been derived by interpolating various estimates available in the literature (Haser, 1995; Howarth et al., 1997; Lamers et al., 1995; Groenewegen et al., 1989), except for HD 16 691, HD 225 160, HD 17 603, HD 338 926, BD+56 739 and HD 18 409. For the first two of the latter stars we derived a v_∞ - estimated by means of line-profile fitting of UV lines available from the Jnes IUE archive, while for the remaining four objects we used the calibration provided by Kudritzki & Puls (2000).

Radiation temperatures at H_α and photospheric profiles. To account for the effects of line blanketing, we have used a value of $T_{\text{rad}} = 0.91 T_{\text{eff}}$ for luminosity class I objects and $T_{\text{rad}} = 0.86 T_{\text{eff}}$ for

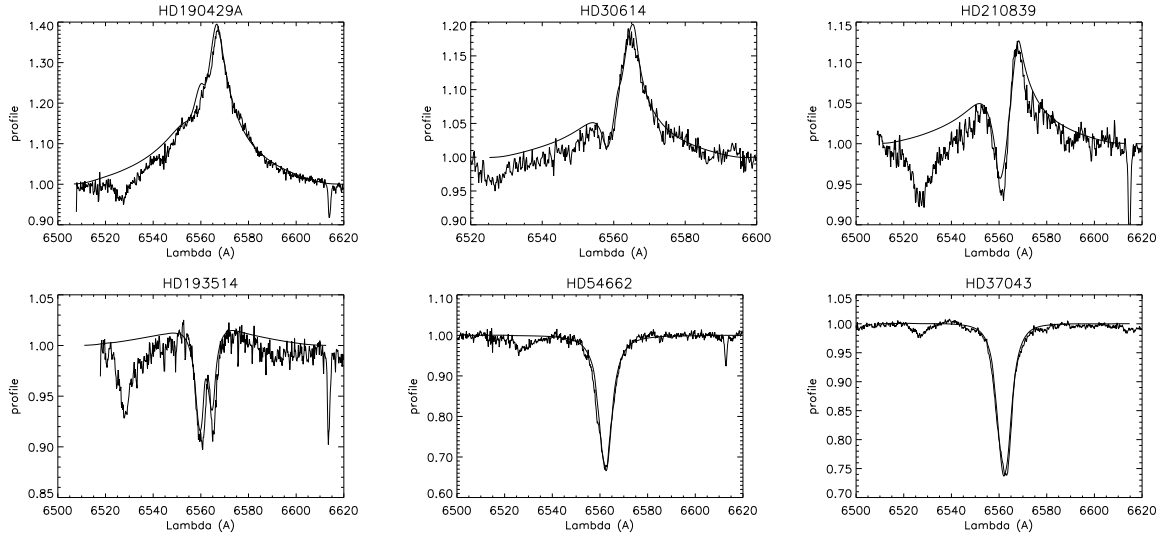


Figure 5.3: Examples of differently shaped H_α profiles from stars of our sample together with the corresponding model fits

the other luminosity classes, where these values originate from a calibration of a large grid of (line-blanketed) model fluxes calculated by J. Puls and co-workers. Note that for unblanketed model atmospheres this value is much lower, i.e., of the order of $0.77 T_{\text{eff}}$ (cf. Puls et al., 1996).

In principle, the photospheric input profiles have to be recalculated as well. Because of the insensitivity of the Balmer lines to changes in T_{eff} in the *O*-star domain (differences up to 5,000 K result only in marginal changes), however, we employed the same (unblanketed) grid of line profiles as described in Puls et al. (1996), evaluated at the “new” effective temperatures, of course.

The only quantities left to be specified are the wind minimum velocity v_{min} and the electron temperature T_e . Following Puls et al., we adopt $v_{\text{min}} = 1 \text{ km s}^{-1}$ and $T_e = 0.75 T_{\text{eff}}$, which are the values consistent with the parameterized run of the H/He departure coefficients. A comparison with H_α profiles from the consistent analysis performed by RPH convinced ourselves finally that this parameterization remains roughly unaffected by blanketing effects, at least if the values of T_{rad} as cited above were used.

5.4.2 Results

General remarks

When performing the individual profile fits, it turned out that most of the supergiants exhibit H_α profiles with a blue wing that cannot be fitted with the adopted “standard” parameterization of the HeII departure coefficients. To fit these profiles, we were forced to increase the He-opacity in the inner wind part - corresponding to an increase in the departure coefficient b_4^{in} typically by a factor $r_4^{\text{in}} = 1.3$ - and, in a few cases, to reduce the emissivity outside, i.e., to lower b_6^∞ (a typical factor here is $r_6^\infty \approx 0.8$). The same problem was noted by Puls et al. (1996) who attributed this to the neglect of the effects of (EUV) line blocking which become particularly important in dense winds. Our results indicate a similar trend (remember, that we use the “standard” parameterization derived

from unblocked models) with a somewhat smaller correction though compared to the results by Puls et al., which most probably is due to the increased ratio of $T_{\text{rad}} / T_{\text{eff}}$ in our modified approach.

Concerning the run of the hydrogen departure coefficients, we found that the adopted “standard” parameterization does not pose any problems when used to fit the lines of the observed profiles. In general, an almost perfect fit to any kind of profile (emission, absorption, P Cygni type) was obtained.

The only problems we have found so far are related to the following profile types in supergiants:

- i) profiles exhibiting a strong decline from the emission maximum towards the absorption minimum, e.g., from HD 66 811, HD 14 947 and HD 47 432.
- ii) profiles showing H_α in absorption with a central emission, e.g., from HD 193 514, HD 209 975, HD 188 209, HD 218 915 and BD+56 739.

To fit these profiles, in all but two of the above cases we were forced to enhance the H_α emissivity, i.e., to increase b_3^{in} (typically, from the “standard” value 1.2 to a value of 1.4). For HD 66 811 and HD 47 432, the H_α emissivity in the inner wind part had to be reduced (typically, $b_3^{\text{in}} \approx 1.05$). Finally, in the case of HD 210 839, we had to increase the H_α opacity in the inner wind part. Let us point out that all these modifications are more or less “cosmetic”, i.e., they lead “only” to an optically almost perfect fit. The decisive parameters obtained from the fit, however, \dot{M} and β (see below), remain at the same value as if one uses the “standard” parameterization. Typical examples of differently shaped profiles together with the corresponding model fits are shown in Fig. 5.3.

As noted by Puls et al. (1996), objects with H_α in emission allow to derive the velocity parameter β in parallel with the mass-loss rate. For these objects (with β given as italic numbers in Table 5.2), we find an average value of $\beta = 1.02 \pm 0.09$. For objects with H_α in absorption, we used $\beta = 0.8$ (expected from theory for thin winds) as a starting value and improved this value from the line fit, where possible. In these cases, of course, the uncertainty in β and, thus, in \dot{M} (c.f. Kudritzki & Puls, 2000; Puls et al., 1996) is much larger than in the cases where β can be derived unambiguously (at least with respect to the “standard model” of winds) and will, therefore, be considered separately in our error analysis.

It is worth noting that for ζ Pup - for which a fit using unblanketed models resulted in $\beta = 1.15$ (Puls et al., 1996) - we find $\beta = 0.92$, in agreement with the recent optical analysis by RPH, and much closer to the results from UV line-profile fits, $\beta_{\text{UV}} = 0.7 \dots 0.8$, see Groenewegen & Lamers (1989) and Haser (1995).

For one star in our sample, HD 202 124, we have obtained a rather large value, $\beta = 1.25$. This object is a supergiant of spectral type O9.5 which shows, in contrast to the other supergiants of the same spectral type in our sample, a P Cygni-like profile with an absorption dip that seems too strong to be solely due to absorption from the HeII blend. In particular, this absorption feature cannot be fitted by simply “playing” with the H/He departure coefficients.

Finally, we like to point out that the last two plots of Fig. 5.3 allow to assess the quality of our $\log g$ calibration (Sect. 5.4.1). Since we did *not* vary the gravity during our fit procedure but always used the value derived by means of our calibration, the almost perfect agreement between observed and modeled line wings indicates a rather high precision of this calibration.

Error analysis

In the following, we briefly describe our error analysis which will become important in the next section when deriving the wind-momentum luminosity relation for our sample.

Table 5.2: Stellar and wind parameters of the O-star sample, derived from calibrations discussed in Sect 5.4.1 and by H_α line fitting. Stars with more than one entry correspond to the entries in Table 5.1 and differ mainly in the adopted stellar radius and in the dependent quantities. Spectral types abbreviated, cf. Table 5.1.

Bold face numbers for $\log L$ and D_{mom} indicate the preferred solution that is used in our final analysis of the WLR (“case C”, cf. Sect. 5.5.1) while italics for β mark values *derived* from emission type profiles. Modifications of departure coefficients for HeII given as *multipliers* $r_{4,6}$ to standard values from Puls et al. (1996). Modifications of departure coefficients for hydrogen are given by absolute numbers, $b_2^{\text{in}}/b_3^{\text{in}}$. “pt” indicates whether H_α is in absorption or emission.

Luminosity L in L_\odot , $v \sin i$ and v_∞ in units of km s^{-1} , \dot{M} in $10^{-6} M_\odot/\text{yr}$, modified wind-momentum rate $D_{\text{mom}} = \dot{M} v_\infty (R_\star/R_\odot)^{0.5}$ in cgs and $Q = \dot{M}/(R_\star/R_\odot)^{1.5}$ in units of M_\odot/yr .

Object	Sp	M_V	T_{eff}	R_\star	$\log g$	Y_{He}	$v \sin i$	$\log L$	v_∞	\dot{M}	β	$r_4^{\text{in}}/r_6^\infty$	$b_2^{\text{in}}/b_3^{\text{in}}$	$\log D_m$	$\log Q$	pt
HD 190429A	O4I	-6.51	39 200	20.8	3.65	0.14	135	5.97	2400	14.2	0.95	1.05/		29.99	-6.82	e
HD 66 811	O4I	-6.14	39 200	17.5	3.65	0.20	203	5.82	2300	6.4	0.92		/1.05	29.59	-7.06	e
HD 66 811 ⁽²⁾		-6.40		19.8				5.92		7.6			/1.05	29.69	-7.06	
HD 66 811 ⁽⁴⁾		-7.14		27.8				6.22		12.8			/1.05	29.99	-7.06	
HD 16 691	O4I	-5.25	39 200	11.6	3.65	0.10	140	5.46	2300	5.6	0.96			29.46	-6.85	e
HD 16 691 ⁽¹⁾		-5.04		10.6				5.38		4.9				29.38	-6.85	
HD 16 691 ⁽³⁾		-6.40		19.8				5.92		12.5				29.92	-6.85	
HD 14 947	O5I	-5.84	37 700	15.7	3.56	0.20	133	5.65	2300	7.7	0.98	1.15/	/1.45	29.65	-6.91	e
HD 14 947 ⁽¹⁾		-5.64		14.3				5.57		6.67		1.15/	/1.45	29.56	-6.91	
HD 14 947 ⁽²⁾		-6.90		25.6				6.08		16.0		1.15/	/1.45	30.07	-6.91	
HD 210 839	O6I	-6.01	36 200	17.5	3.48	0.10	214	5.68	2200	5.1	1.00	1.05/	2./	29.47	-7.16	e
HD 210 839 ⁽¹⁾		-5.85		16.3				5.62		4.6		1.05/	2./	29.41	-7.16	
HD 210 839 ⁽²⁾		-6.60		23.0				5.91		7.7		1.05/	2./	29.71	-7.16	
HD 42 088	O6.5V	-4.35	38 600	7.7	3.85	0.12	62	5.08	2200	0.38	0.85	1.3/		28.17	-7.75	a
HD 42 088 ⁽⁵⁾		-4.96		10.7				5.36		0.62		1.3/		28.45	-7.75	
HD 54 662	O6.5V	-5.28	38 600	11.9	3.85	0.12	85	5.45	2450	0.6	0.80			28.50	-7.84	a
HD 192 639	O7Ib	-5.91	34 700	17.2	3.39	0.20	110	5.59	2150	5.3	1.09	1.25/80		29.47	-7.13	e
HD 193 514	O7Ib	-5.96	34 700	17.6	3.39	0.10	95	5.61	2200	2.7	0.80		/1.48	29.20	-7.44	a
HD 34 656	O7II	-4.68	34 700	9.8	3.50	0.12	85	5.10	2150	0.62	1.09	1.5/		28.42	-7.69	a
HD 34 656 ⁽⁶⁾		-6.64		24.1				5.88		2.40		1.5/		29.20	-7.69	
HD 47 839	O7V	-4.83	37 500	9.9	3.84	0.10	62	5.24	2200	1.2	0.75			28.72	-7.41	a
HD 24 912	O7.5I	-4.95	34 000	11.2	3.35	0.15	204	5.18	2400	1.19	0.78	1.3/85		28.78	-7.50	a
HD 24 912 ⁽¹⁾		-4.99		11.5				5.20		1.23		1.3/85		28.80	-7.50	
HD 24 912 ⁽²⁾		-6.70		25.2				5.88		4.0		1.3/85		29.48	-7.50	
HD 36 861	O8III	-5.57	33 600	15.1	3.56	0.10	66	5.42	2400	0.8	0.80			28.67	-7.87	a
HD 36 861 ⁽¹⁾		-5.85		17.2				5.53		0.97				28.78	-7.87	
HD 210 809	O9Iab	-6.04	31 700	19.6	3.23	0.14	100	5.54	2100	4.5	0.91	1.1/		29.42	-7.29	e
HD 207 198	O9Ib/II	-5.49	31 700	15.2	3.23	0.12	85	5.32	2100	0.9	0.97	1.3/		28.67	-7.82	a
HD 207 198 ⁽¹⁾		-5.29		13.9				5.25		0.79		1.3/		28.59	-7.82	
HD 37 043	O9III	-6.05	31 400	19.8	3.50	0.12	120	5.54	2300	1.2	0.85	1.6/		28.89	-7.87	a
HD 37 043 ⁽¹⁾		-6.24		21.6				5.61		1.37		1.6/		28.97	-7.86	
HD 24 431	O9III	-5.30	31 400	14.0	3.50	0.12	90	5.24	2150	0.3	0.95	1.3/		28.18	-8.24	a
HD 24 431 ⁽¹⁾		-5.57		15.9				5.35		0.36		1.3/		28.29	-8.25	
HD 16 429	O9.5I/II	-6.51	31 000	24.8	3.19	0.10	80	5.71	1600	1.4	0.85	1.3/9		28.85	-7.95	a
HD 30 614	O9.5Ia	-6.47	31 000	24.9	3.19	0.10	100	5.71	1550	4.2	1.05	1.3/		29.31	-7.47	e
HD 30 614 ⁽²⁾		-6.00		19.6				5.51		2.9		1.3/		29.10	-7.48	
HD 209 975	O9.5Ib	-6.14	31 000	20.9	3.19	0.10	90	5.56	2050	1.8	0.80	1.3/	/1.42	29.03	-7.72	a
HD 209 975 ⁽¹⁾		-5.96		19.2				5.49		1.58		1.3/	/1.42	28.95	-7.73	
HD 18 409	O9.7Ib	-5.50	30 600	15.7	3.17	0.14	110	5.29	1750	1.5	0.70			28.82	-7.62	a
HD 17 603	O7.5Ib	-6.70	34 000	25.2	3.35	0.12	110	5.88	1900	5.90	1.05	1.1/		29.55	-7.33	e
HD 225 160	O8Ib	-6.40	33 000	22.4	3.31	0.12	125	5.73	1600	5.3	0.85	1.5/9		29.40	-7.30	e
HD 338 926	O8.5Ib	-6.60	32 500	22.7	3.27	0.12	80	5.72	2000	5.7	1.00			29.53	-7.28	e
HD 188 209	O9.5Iab	-6.00	31 000	19.6	3.19	0.12	87	5.51	1650	1.6	0.90	1.4/	/1.47	28.87	-7.73	a
HD 202 124	O9.5Iab	-6.00	31 000	19.6	3.19	0.12	140	5.51	1700	3.2	1.25	1.4/7		29.18	-7.43	e
HD 218 915	O9.5Iab	-6.00	31 000	19.6	3.19	0.12	80	5.51	2000	1.7	0.95	1.2/	/1.54	28.98	-7.71	a
BD+56 739	O9.5Ib	-6.00	31 000	19.6	3.19	0.12	80	5.51	2000	2.3	0.85	1.35/	/1.33	29.02	-7.61	a
HD 47 432	O9.7Ib	-6.00	30 500	18.9	3.17	0.12	95	5.45	1600	1.9	1.03	1.4/8	/1.07	28.92	-7.64	e

In order to assess the errors in $\log L$ and $\log D_{\text{mom}}$ we followed the philosophy outlined in detail by RPH. To estimate the uncertainty in the stellar radius, we applied their Eq. 8 with $\Delta M_V = \pm 0.3$ and $\Delta T_{\text{eff}} = \pm 1500$ K. The former value is in accordance with the results displayed in our Fig. 5.1, while the latter reflects the uncertainties in our spectral type – T_{eff} calibration and in the underlying data base, cf. Fig. 5.2. With these estimates, the error in the stellar radius is dominated by the uncertainty in M_V and is of the order of $\Delta \log R_\star \approx \pm 0.06$, i.e., roughly 15 %.

Specified in this way, the error in luminosity is given by

$$\Delta \log L \approx \sqrt{(4 \Delta \log T_{\text{eff}})^2 + (2 \Delta \log R_\star)^2} \quad (5.1)$$

and results in $\Delta \log L \approx \pm 0.15$, i.e., the error due to ΔR_\star is somewhat larger than due to ΔT_{eff} .

To assess the errors in the wind-momentum rate, let us first analyze the errors in \dot{M} inherent to our analysis. Actually, any line-fit to H α does not specify \dot{M} itself, but only the quantity Q introduced by Puls et al. (1996),

$$Q = \frac{\dot{M}}{R_\star^{1.5}}. \quad (5.2)$$

In particular, any change in R_\star leads to an identical fit if \dot{M} is adapted in such a way that Q remains constant (compare Table 5.2 for those objects with more than one entry). Thus, Q is the quantity for which the error has to be evaluated.

For emission profiles, where also β can be constrained from the fit, we estimate the precision of the derived Q as $\pm 20\%$ (from the fit quality). For absorption profiles, we have varied β typically by ± 0.1 (or more, if necessary), and obtained the corresponding upper and lower boundaries of \dot{M} (actually, of Q) from additional fits to the observed profiles. The results of this procedure are displayed in Table 5.3. When these error estimates were smaller than the adopted error from above (i.e., $\pm 20\%$), the latter value was chosen as a conservative minimum. Note that the maximum errors in Q can reach factors of almost two (for absorption profiles)!

From the error in Q , the uncertainty in the derived wind-momentum rate, $D_{\text{mom}} = Q v_\infty R_\star^2$, can be calculated via

$$\Delta \log D_{\text{mom}} \approx \sqrt{(\Delta \log Q)^2 + (2 \Delta \log R_\star)^2 + (\Delta \log v_\infty)^2}. \quad (5.3)$$

Note that the error in R_\star enters again quadratically. The errors in v_∞ have been assumed to be ± 150 km s $^{-1}$ or larger, if either the different sources for v_∞ do not coincide or v_∞ has been obtained from calibrations. Thus, in most cases the resulting error in $\log D_{\text{mom}}$ is of the order of ± 0.15 , i.e., similar to the error in $\log L$.

5.4.3 Comparison with results from a complete analysis

The basic outcome of our approximate analysis, namely the Q -value, is listed in Table 5.2. Before we discuss further consequences and as outlined in the introduction, we have to convince ourselves that the estimates derived for this quantity are consistent with the results of the complete analysis. That way, we particularly verify our modifications concerning the effects of line-blocking/blanketing.

Any Q -value derived from H α profiles should be almost independent of stellar parameters if in the underlying models the same terminal velocities were used and if the influence of different effective temperatures were considered by applying the temperature correction given in Puls et al. (their Eqs. 48

Table 5.3: Objects with H_α in absorption: variation in derived \dot{M} , if β is modified within the typical uncertainties, $\beta^- < \beta < \beta^+$, with $\Delta\beta$ of order 0.1. \dot{M} in units of $10^{-6} M_\odot/\text{yr}$.

Object	β	\dot{M}	β^-	\dot{M}^+	β^+	\dot{M}^-
HD42088	0.85	0.38	0.75	0.46	0.95	0.30
HD54662	0.80	0.60	0.70	0.90	0.90	0.40
HD193514	0.80	2.70	0.70	3.24	0.90	2.05
HD34656	1.09	0.62	0.80	0.95	1.20	0.50
HD47839	0.75	1.20	0.65	1.50	0.90	0.95
HD24912 ⁽²⁾	0.78	4.00	0.65	5.00	0.90	3.00
HD36861	0.80	0.80	0.70	1.40	0.90	0.64
HD207198	0.97	0.90	0.80	1.25	1.10	0.70
HD37043	0.85	1.20	0.75	1.50	0.95	0.96
HD24431	0.95	0.30	0.80	0.60	1.05	0.24
HD16429	0.85	1.40	0.75	1.70	0.95	1.12
HD209975	0.80	1.80	0.70	2.16	0.90	1.44
HD18409	0.70	1.50	0.65	1.80	0.90	0.90
<hr/>						
HD188209	0.90	1.60	0.80	1.92	1.00	1.28
HD218915	0.95	1.70	0.80	2.04	1.05	1.30
BD+56739	0.80	2.15	0.70	2.58	0.90	1.72

and 49). In our comparison with the Repolust sample for 11 stars in common (Fig. 5.4) we have performed such a correction.

This figure shows that at higher values of $\log Q$, i.e., denser winds, the agreement is excellent (within 0.06 dex). On the other hand, at lower values the differences can become significant, e.g., for HD 207 198, HD 18 409 and HD 24 912. From Table 5.2, last column, we see that the H_α profiles of these stars all appear in absorption. Insofar, the above mentioned β -problem might be a reason of this discrepancy, and a closer inspection of the corresponding errors (see Table 5.3) reveals that this actually is the major source of disagreement.

The remaining disagreement of < 0.1 dex (in those cases where the formal errors are still too low) more likely reflects real variability in the strength of the studied winds. Note, e.g., that mass-loss variations of up to $\sim 45\%$ have been suggested by Markova & Scuderi (2003) to explain the variability of the H_α emissivity observed in our sample stars over a 2 year period. Interpreted in this way, the disagreement found here would indicate variations of the same order.

Finally, let us explicitly state that the discrepancy found at low wind densities is *not* related to the problems we have partly met when fitting H_α profiles in absorption, (i.e., to the required modifications of departure coefficients), since the final values of \dot{M} are only weakly affected by this procedure: The line opacity scales with \dot{M}^2 but only linearly with the b_i 's.

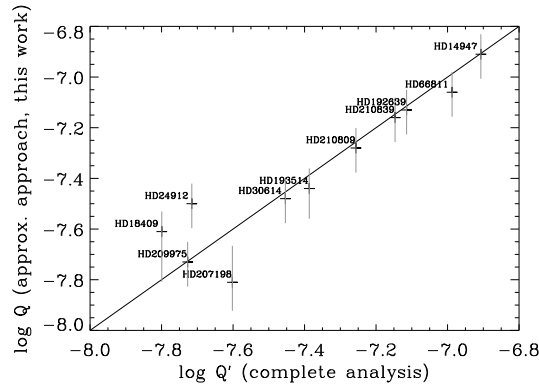


Figure 5.4: Comparison of derived Q -values from our analysis with corresponding data from RPH, for eleven stars in common. The Q -values of the complete analysis have been corrected for differences in effective temperature. Overplotted are the individual error bars calculated according to Sect. 5.4.2. For a discussion concerning the outliers, see text.

5.5 Wind-momentum rates and WLR

Table 5.2 summarizes all stellar and wind parameters derived (and adopted) for our sample stars as described in the previous section. Before we proceed towards an analysis of the corresponding WLR, let us give some

Remarks on individual objects. A closer inspection of the available data reveals that at least in three cases, HD 16 619, HD 24 912 and HD 34 656, the derived values for M_V , and accordingly R_* , seem to be inconsistent with the adopted spectral type /luminosity class and the available spectroscopy.

The estimates of R_* for HD 16 619 (as a member of the Double Cluster χ and ξ Persei), derived with the standard and the individual extinction ratio are both a factor of two lower than the radii of the other two sample stars of same spectral type.

The reason for this discrepancy is most likely related to the fact that the distance to this star is very uncertain (Stone, 1979; Walborn, 2002). Thus, in the following we will preferentially use the parameters resulting from a calibration of M_V , i.e., entry (3).

The second star with doubtful parameters is HD 24 912. If one follows the plausible arguments given by Herrero et al. (1992) that this star is a supergiant, then its radius cannot be of the order of $11 R_\odot$. On the other hand, if one believes that it is a normal giant, then its wind-momentum is too high for a luminosity class III object. The situation does not improve if the individual extinction ratio is adopted. The possibility that HD 24 912 is not a member of PerOB2 but a runaway star (Gies, 1987) seems to resolve the problem, and also for this star we will use the parameters resulting from a calibration of M_V (entry (2)).

Humphreys (1978) has listed HD 34 656 as a member of Aur OB1 ($d=1.32$ kps). However, the R_* derived when adopting this distance is rather low, a factor of two lower than the radii of the other two supergiants of same spectral type. On the other hand, Tovmassian et al. (1994) argue that HD 34 656 is a member of a small group of stars located at the distance of AurOB2 ($d=3$ kpc). Although the values for M_V and R_* resulting from this distance seem a bit too large for the adopted spectral type/luminosity class, we will use these parameters (entry (6)) until further notice.

Two other objects deserve special attention as well. HD 42 088 is listed as a member of GemOB1 ($d=1.5$ kpc) by Humphreys (1978). However, Felli et al. (1977) identified this object as a member of NGC 2175 for which several independent distance determinations exist, ranging from 1.91 to 2.87 kpc. Thus, a distance of 2 kpc as adopted by Felli et al. (1977) seems to be a good compromise for HD 42 088, also with respect to its radius, and we will use this value in the following (entry (5)).

For ζ Pup (HD 66 811), the values resulting from both its “conventional” distance of 460 pc and a calibration of M_V (entry (2)) overlap within the adopted errors, and we will preferentially use the “standard” values for this star. In addition, we will follow the suggestion by Sahu & Blaauw (1993) that this star is a runaway star originating from the Vela Molecular Ridge and has a distance of 730 pc. With this value and adopting a standard reddening, the radius of ζ Pup becomes $28 R_\odot$ which is rather large for its spectral type. Interestingly, a present investigation by Pauldrach and co-workers (in prep. for A&A) seems to favour such a large value in terms of both a self-consistent hydrodynamical wind model and the corresponding synthetical UV spectrum, when compared to observations. In what follows we will use this entry (4) as a second choice in order to consider its possible relevance within the wind-momentum luminosity relation.

Hereafter, we will denote HD 16 691, HD 24 912, HD 34 656 and HD 42 088 as “peculiar objects”.

5.5.1 WLR as function of luminosity class

From now on, we will concentrate on the second major objective of the present investigation, namely on the wind-momentum luminosity relation (WLR) for Galactic O-type stars. We begin with considering the consequences of “fine tuning” direct and indirect parameters entering the WLR.

Let us first comment on the influence of using different values for the total to selective extinction, R . The larger R , the brighter the star is in the visual, and the larger the stellar radius. Since we are fitting for \dot{Q} , also the mass-loss and the wind-momentum rate increases, as well as the (bolometric) luminosity. Even in cases of an “extreme” extinction ratio of 5.0, however, the resulting differences in R_* and \dot{M} are small, roughly 10-14% of the values derived with $R = 3.1$. (Hereafter all data obtained using $R = 3.1$ will be referred to as “standard” values). The corresponding variations in $\log L$ and D_{mom} are 0.11 dex and 0.08 dex, respectively, as shown in Fig. 5.5, and are (much) smaller than the individual uncertainties for these quantities. Moreover, the corresponding shifts are almost in parallel to any expected wind-momentum luminosity relationship (for comparison, we have overplotted the theoretical relation provided by Vink et al. 2000), so that any uncertainty in R should be of minor influence on the results discussed below.

In addition to the effect caused by using different redding laws, there is also the distance problem, which, taken together, forced us to deal with more than one entry for many of our sample objects (cf. Sect. 5.3). Consequently, various combinations have to be accounted for, and we decided to consider the following different cases (A to C without field stars):

- Case A includes those entries without any superscript (standard, i.e., (almost) all distances from Humphreys (1978) and $R = 3.1$) plus the specific values adopted for “peculiar objects” as discussed above.
- Case B refers to entries with superscript 1 (individual reddening) plus “peculiar objects” + data without superscript for the rest of the stars.

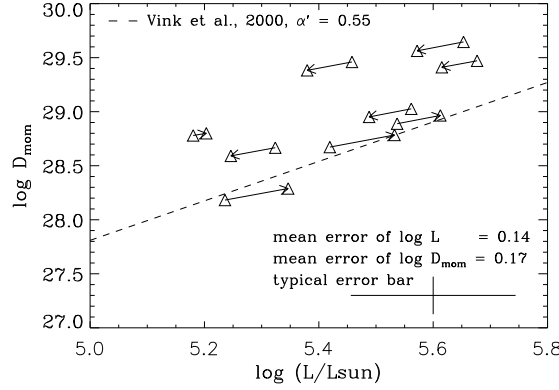


Figure 5.5: Influence of uncertainty in reddening on modified wind-momenta and luminosities. Arrows point from positions resulting from standard reddening, $R = 3.1$, to positions resulting from adopting individual values for R (entries with superscript (1) in Tables 5.1 and 5.2). Dashed: theoretical WLR predicted by Vink et al. (2000).

- Case C combines data with superscript 2 plus “peculiar objects” plus data with superscript 1 (if no entry with superscript 2 available) plus standard values for the rest.
- Case D comprises case C plus field stars.

In Fig. 5.6 we have displayed the WLRs based on the data-sets corresponding to case A, which is the starting point of our investigation, and case D, which is the ending point. Numbers correspond to luminosity classes.

Linear regressions, obtained by means of χ^2 minimization accounting for the individual errors (calculated as described in Sect. 5.4.2) in *both* directions, are shown as solid (l.c. I/II) and dotted (l.c. III/V) lines. We have used the conventional formulation

$$\log D_{\text{mom}} = x \log(L/L_{\odot}) + D_0 \quad (5.4)$$

with exponent x being the inverse of α' , which corresponds to the slope of the line-strength distribution function corrected for ionization effects (Puls et al., 2000; Kudritzki & Puls, 2000).

To our knowledge, this investigation together with that of RPH are the first to account for errors in both directions. Our approach follows the principle arguments given by Press et al. (1992, Sect. 15.3 and references therein), i.e., the parameters of the regression follow from minimizing

$$\chi^2(x, D_0) = \sum_i \frac{(\log D_{\text{mom},i} - x \log L_i/L_{\odot} - D_0)^2}{\text{Var}_{\text{tot},i}} \quad (5.5)$$

with *total* variance Var_{tot} ,

$$\text{Var}_{\text{tot},i} = \text{Var}(\log D_{\text{mom},i} - x \log L_i/L_{\odot} - D_0). \quad (5.6)$$

Since $\log D_{\text{mom}}$ and $\log L$ are statistically dependent (via R_{\star}^2 , a case not considered by Press et al.),

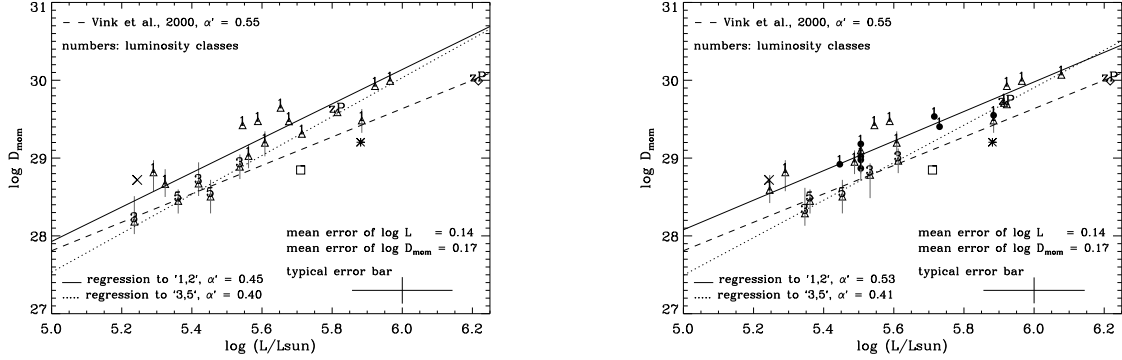


Figure 5.6: WLR for our sample of Galactic O-type stars. Case A (left) and case D (right) as discussed in the text. Error bars with respect to $\Delta \log D_{\text{mom}}$ are displayed for all stars with H_α in absorption. The errors for the remaining objects with H_α in emission and the errors for $\Delta \log L$ roughly agree with the typical error bars displayed in the figures. Regressions obtained from χ^2 minimization with individual errors in both co-ordinates, accounting for the covariance between luminosity and modified wind-momentum rate.

Numbers 1, 3 and 5 correspond to luminosity classes I, III and V, respectively. Special symbols: “zP” corresponds to ζ Pup as used for the regression (either standard or entry 2) and additionally to entry 4 (upper right). The “x” denotes HD 47839 (15 Mon, Ic V), the open square HD 16429 (Ic I) and the asterisk HD 34656; all three objects have been discarded from the corresponding regressions. The filled circles denote the field stars of our sample included for case D.

one has to account for the covariance between both terms. Thus, we have

$$\begin{aligned} \text{Var}_{\text{tot},i} &= \text{Var}(\log D_{\text{mom},i}) + x^2 \text{Var}(\log L_i/L_\odot) - \\ &- 2x \text{Covar}(\log D_{\text{mom},i}, \log L_i/L_\odot). \end{aligned} \quad (5.7)$$

with

$$\text{Covar}(\log D_{\text{mom},i}, \log L_i/L_\odot) \approx 4\text{Var}(\log R_i/R_\odot) \quad (5.8)$$

if we neglect the weak dependence of R_\star on T_{eff} .

We consider this type of regression as essential, since the errors in $\log L$ are of the same order as those in $\log D_{\text{mom}}$, and they *are* correlated indeed. E.g., if we assume that the momentum rate is lower because of a smaller radius, we also have to assume that the luminosity is smaller (and vice versa), a fact not accounted for in the standard type of regression.

Actually, by comparing with results from a conventional least square fit (even accounting for the specific errors in $\log D_{\text{mom}}$), we sometimes find significant differences in the regression coefficients. Only when the errors in $\log L$ are small, both methods yield similar results. Insofar, the more simple method might be justified in cases where the (relative) uncertainty in distance is small, e.g., in investigations of extra-galactic sources or specific associations, as performed by Herrero et al. (2002).

In Fig. 5.6 one can see that *normal giants and dwarfs show lower wind momenta (roughly by 0.3...0.5 dex) than supergiants at the same bolometric luminosity*, and that they are in good agreement with the theoretical predictions by Vink et al. (2000, dashed line). Note that because of the short interval in $\log L$ covered by giants and dwarfs, the regressions for luminosity III/V objects cannot be

regarded as significant. Thus, in Table 5.5 only the regression coefficients for the luminosity class I objects obtained for the different samples (A, B, C and D) are listed.

There are three stars that deviate strongly from the above “rule”: HD 47 839 (15 Mon, denoted by an “x”), HD 16 429 (denoted by an open square) and HD 34 656 (denoted with an asterisk). Interestingly, all these stars have been recognized as “blue stragglers” (Schild & Berthet, 1986), among which the rate of double/multiple systems seems to be exceptionally high (Bellazzini et al., 2002; Carney et al., 2001). Actually, the former two objects were proven to be a double (Gies et al., 1993, and references therein) and a triple (Gies, private communication) system, respectively - a result that might explain their “erroneous” position (compared to the theoretical predictions). Accordingly, one might speculate that the excess luminosity of HD 34 656 might also be due to the influence of (a) possible companion(s). In view of these uncertainties, we have discarded all three objects from the regression.

In addition, we like to mention that ζ Pup with parameters from entry(4), i.e., assuming the “large” radius, lies well below the regression of the other lc I objects, whereas with the “conventional” radius its location is just slightly below the mean. This result might be used to favour the lower radius. Note, however, that ζ Pup is a “bona fide” runaway star, i.e., its parent association, Vela R2, has been identified, and hence it is quite probable that the star has not reached its present status through single star evolution. In particular, Vanbeveren, de Loore & Rensbergen (1998) have argued that ζ Pup could not have become a single runaway as a consequence of close encounters with other stars in a very dense cluster, but is more likely to originate from a supernova explosion in a massive close binary. In view of this scenario, the “peculiar” characteristics of ζ Pup, such as enhanced He and N abundances at the stellar surface, higher peculiar and rotational velocities and overluminosity might all find their natural explanation.

Our analysis indicates that the regression somewhat improves, i.e., the errors of the parameters decrease (and move towards those predicted by theory, cf. Table 5.5), when individual values of R (case B) are used instead of the standard ones. This improvement becomes even larger by adopting those parameters resulting from a calibration of M_V for objects suspected to be runaway stars (Case C). The final inclusion of the definite field stars (lower part of Table 5.1) has a minor influence on the corresponding regression coefficients (Case D), although the statistics further improves. Accounting for the fact that the positions of these stars remain somewhat uncertain since they strongly depend on the accuracy of the empirical M_V -calibration, we will concentrate now on sample C, since it appears to be the most relevant, in terms of both statistics and underlying physical assumptions.

Comparison with other investigations. Apart from the work by RPH mentioned in the introduction, there are a number of other investigations which have previously tried to derive wind-momentum rates as function of luminosity. In particular, Kudritzki & Puls (2000) and Herrero et al. (2002) provided corresponding coefficients for Galactic O-type supergiants, which have been included in Table 5.5 for comparison. Note that the values quoted by Kudritzki & Puls (2000) refer to the analysis of Puls et al. (1996), i.e., have been derived by means of *unblocked* model atmospheres, and that all coefficients except those from RPH refer to conventional least square fitting. Additionally, we quote the coefficients of the theoretical relation for stars with $T_{\text{eff}} > 30\,000$ K as calculated by Vink et al. (2000), which is predicted to be independent of luminosity class (see below) and compares well with the position of our lc III/V objects.

Except for the data from Kudritzki & Puls (2000), the remaining “observational” results are rather similar. On the one hand, this is not too astonishing, since all three investigations either use or rely on the same (line-blanketed) model atmosphere code, FASTWIND. On the other hand, however,

Table 5.4: Coefficients of the WLR obtained for the supergiants of our sample cases A, B, C and D in comparison to results from other investigations. The values of the minimized χ^2 (not displayed here) indicate an acceptable fit in all four cases. Regression accounting for errors in both co-ordinates for case A to D and the analysis by Repolust et al.; standard least square fit for remaining entries.

Sample	$\log D_o$	x	α'
Case A	16.88 ± 2.53	2.21 ± 0.45	0.45 ± 0.09
Case B	17.53 ± 2.18	2.10 ± 0.38	0.48 ± 0.09
Case C	19.00 ± 1.37	1.83 ± 0.24	0.55 ± 0.08
Case D	18.58 ± 1.25	1.90 ± 0.22	0.53 ± 0.06
Herrero et al.	19.27 ± 1.37	1.74 ± 0.24	0.58 ± 0.08
Repolust et al.	18.30 ± 2.12	1.97 ± 0.38	0.51 ± 0.10
Kudritzki & Puls	20.69 ± 1.04	1.51 ± 0.18	0.66 ± 0.08
Vink et al. (2000)	18.68 ± 0.26	1.83 ± 0.044	0.55 ± 0.013

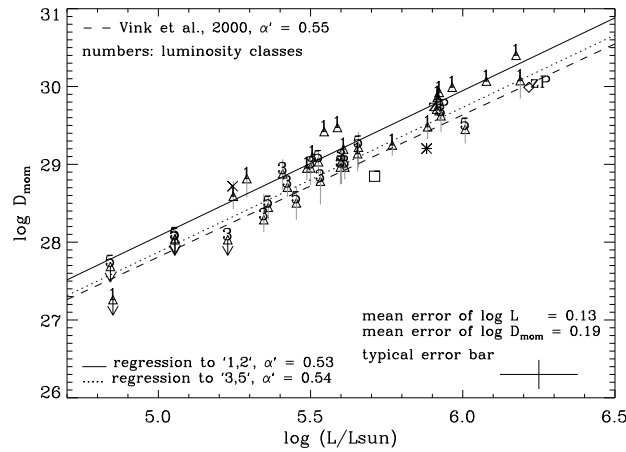


Figure 5.7: WLR for Galactic O-type stars. Sample includes our sample case C, the sample by RPH for objects *not* in common and the sample by Herrero et al. (2002). Regression accounting for errors in both directions and appropriate correlations; errors corresponding to respective publications. All symbols as in Fig. 5.6; arrows indicate upper limits for objects with almost purely photospheric profiles which have been discarded from the regression.

the fairly good agreement between our results (in particular, Case D) and those from the complete spectral analysis RPH indicates that the approximate approach followed by us actually can provide compatible results in terms of both mass-loss rates (Sect. 6.5) and WLR, not only qualitatively, but also quantitatively.

5.5.2 Enlarging the sample

The latter conclusion allows us to proceed in the spirit as outlined in the introduction, namely to combine our data with the data-sets from RPH for stars not in common and Herrero et al. (2002), in order to improve the statistics and to study the WLR of Galactic O stars by means of the largest sample

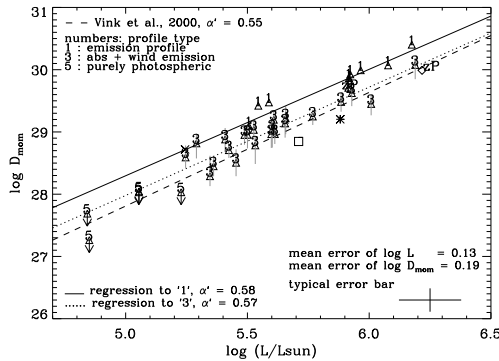


Figure 5.8: As Fig. 5.7, but with regression in dependence of profile type (see text).

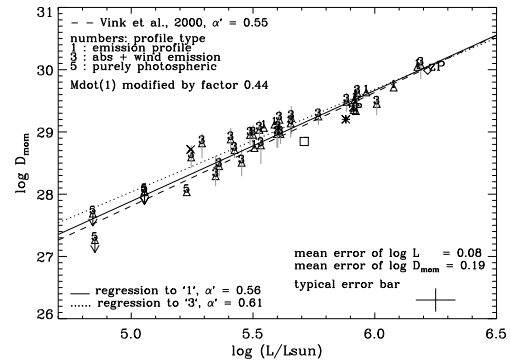


Figure 5.9: As Fig. 5.8; \dot{M} of class 1 objects (H_α in emission) decreased by a factor of 0.48.

of stars used so far. In total, this sample comprises 19 supergiants and 15 lc III/V objects entering the regression. Again, we have accounted for the errors in both directions, with errors taken from the respective investigations. Note that the errors in the sample from Repolust et al. are dominated by the uncertainty in radius, similar to the objects from our sample. In contrast, the errors in the sample from Herrero et al. are somewhat lower, since these authors have investigated objects from *one* association only, i.e. CyOB2, which reduces the scatter.

The results obtained in Fig. 5.7 confirm those presented in the previous section as well as the ones reported by RPH: The WLR for luminosity class III/V objects strictly follows the theoretical predictions while the relation for the supergiants shows a vertical offset, corresponding now to an average factor of roughly 0.25 dex.

Note that with respect to lc III/V objects, the “unified” sample covers a much larger range in $\log L$. Thus a more precise determination of the corresponding regression coefficients than before is possible. Note in addition that even those stars with only upper limits for D_{mom} (those with an arrow), which have *not* been included into the regression, follow the continuation of lc III/V objects - a finding that has already been discussed by RPH.

The results of the regression analysis for our “unified” sample and for the “unified” sample of RPH are summarized in Table 5.5. Note in particular that the coefficients for lc I objects derived by us are closer to the values predicted by theory and affected by smaller errors (due to the improved statistics) than those obtained by RPH. Note also that because of the inclusion of giants and dwarfs from our investigation, the “unified” lc III/V sample now shows a better coverage along the $\log L$ axis (with no gaps in between). The corresponding regression coefficients, however, deviate stronger from the values predicted by theory and have a somewhat larger error than those derived by RPH. This finding (for weak winds) again points to the β problem discussed in Sect. 6.5 and may also indicate a higher sensitivity of the results on the approximations used by our method.

5.5.3 WLR as function of profile type

The clear separation between the WLRs for luminosity class I objects and those of luminosity class III/V might in principle be explained by a different number of effective lines driving the wind, since the coefficient D_o depends on this quantity via $D_o \propto N_0^{1/\alpha'}$ (c.f. Kudritzki & Puls, 2000, their

Table 5.5: Coefficients of the WLR obtained for Galactic O-stars, by combining our sample case C with the results from Herrero et al. (2002) and RPH for objects not in common. Regression accounting for errors in both co-ordinates. $\chi^2/(N - 2)$ gives the “average” value of the minimized χ^2 per degree of freedom, when N is the number of objects included in the sample. “lc” denotes regression as function of luminosity class, “pt” as function of profile type, respectively. Asterisks mark corresponding data from RPH.

Sample	$\log D_o$	x	α'	$\chi^2/(N - 2)$
lc I	18.73 ± 1.13	1.87 ± 0.20	0.53 ± 0.06	0.77
lc I*	18.24 ± 1.76	1.96 ± 0.30	0.51 ± 0.08	
lc III/V	18.57 ± 1.98	1.86 ± 0.36	0.54 ± 0.10	0.66
lc III/V*	18.64 ± 1.29	1.85 ± 0.23	0.54 ± 0.07	
pt 1	19.75 ± 1.85	1.71 ± 0.32	0.58 ± 0.11	0.50
pt 3	19.28 ± 1.15	1.74 ± 0.21	0.57 ± 0.07	0.64

Eq. 18). However, such a difference is rather unlikely since present theoretical simulations of line-driven winds (on the basis of completely different approaches) do not find such a separation, but predict a unique relation instead (Vink et al., 2000; Pauldrach et al., 2002; Puls et al., 2003).

Although the separation between supergiants and the rest is fairly obvious, there are certain outliers that are much more consistent with the regression for lc III/V stars. Among them are three supergiants from the sample of Herrero et al. with well-defined positions due to their membership to CygOB2. Interestingly, all these outliers show H_α in absorption. Note that this confusing situation has already been noted by Puls et al. (2003).

Subsequently, these authors suggested to plot the WLR in a slightly different manner, namely as a function of profile type instead of luminosity class. Class 1 corresponds to objects with H_α in emission, class 3 to objects with H_α in absorption and class 5 to objects with an almost purely photospheric profile, i.e., with very thin winds. In this way, these authors found a much closer correlation without any outliers.

In Fig. 5.8, we have repeated this exercise for our “unified” sample. The corresponding coefficients are displayed in Table 5.5. Our conclusion for the enlarged sample is not as clear as for the data used by Puls et al. (2003), but similar to that reported by RPH. In fact, the situation for emission type objects has improved, and the fit quality (expressed by the minimized χ^2) for class 1 objects is lower than for lc I objects. Also, for class 3 objects the scatter in the regression coefficients has decreased compared to lc III stars. A closer inspection of Fig 5.8, however, reveals a new problem: At $\log L/L_\odot < 5.4$, we find at least two class 3 stars located considerably above the corresponding regression curve.

Both of these objects are supergiants, HD 18 409 and HD 207 198; neither of them is a fast rotator or suspected binary. Certainly one could find reasons to exclude them from the regression, but we regard their positions as reliable within the error bars. Although there are certain discrepancies with respect to the derived Q -values (cf. Sect. 6.5), they cover similar positions in the investigation by Repolust et al., i.e., they lie in the continuation of class 1 stars.

Thus, we encounter the following situation: at larger luminosities, $\log L/L_\odot > 5.5$, the *separation* of the WLR seems to be more a function of profile type than of luminosity class (which might indicate that the present classification scheme is simply too coarse). For lower luminosities, the opposite might be true, or the clear relationship between D_{mom} and $\log L$ vanishes at all. Before a final

statement can be given, however, a complete NLTE analysis has to be awaited for, at least for the critical objects with low momentum rates, since in this case the errors bars are particularly large.

Following the suggestion of Puls et al. (2003, see also RPH) that there might be no separation at all, but that for objects with emission lines one observes the effects of clumping², we shifted the WLR of class 1 stars onto the WLR for class 3 stars by reducing \dot{M} by a factor of 0.48 (cf. Fig. 5.9). The corresponding (effective) clumping factor equals 4.3 ($\langle \rho^2 \rangle / \langle \rho \rangle^2 = 0.48^{-2}$)

5.6 Summary, discussion and conclusions

The first objective of the present paper was to investigate the potential of a pure H_α profile analysis to provide mass-loss and wind-momentum rates for O-type stars, compatible to those from a state-of-the-art complete spectral analysis. This goal has been attained in two ways: (i) by comparing the derived mass-loss rates (actually, the corresponding Q -values) to those determined by RPH via a complete NLTE spectral analysis for stars in common and (ii) by comparing the Wind-momentum Luminosity Relationship for our sample stars to those derived by other investigators (Kudritzki & Puls, 2000; Herrero et al. , 2002, RPH) Additionally, we studied the consequences of “fine tuning” direct and indirect parameters entering the WLR, e.g., by taking different values for stellar reddening and distance into account.

To determine \dot{M} and velocity field exponents β , we applied the approximate method developed by Puls et al. (1996) which has been modified by us to account for the effects of metal line-blocking/blanketing. Effective temperatures and gravities needed to perform the H_α profile fitting have been obtained via spectral type – T_{eff} and spectral type – $\log g$ calibrations for O stars of luminosity classes I, III and V. These calibrations are based on results of recent spectroscopic analyses of individual Galactic stars derived via NLTE atmospheric models with mass-loss, sphericity and metal line blocking/blanketing (RPH, Martins et al. 2002).

It must be noted that in our regression we have assumed a linear relation between spectral type and T_{eff} , a fact that might raise some suspicion concerning the reliability of the derived temperatures (see, e.g., Crowther 1998). Note, however, that the data underlying our calibrations did not give any evidence of significant deviations from a linear approach. This is particularly true for the case of dwarfs and supergiants where the available data cover a relatively wide range of subclasses. Admittedly, at spectral types earlier than O5 our calibration for luminosity class III might be somewhat unrealistic due to the lack of appropriate data. However, since our sample does not comprise any objects in this range, our analysis is not affected by this uncertainty. One word of warning: Caution is well-advised when using the provided calibrations for supergiants, since they refer to “typical” representatives as considered in the present investigation, but *not* to extreme objects. In the latter case (which is visible, e.g., from the strength of the H_α line itself), the uniqueness of a spectral type – T_{eff} relation is no longer guaranteed.

On the basis of these calibrations, we have analyzed H_α by means of the approximate method cited above. The major modification to include the effects of line-blanketing concerns the change of radiation temperature in the neighbouring continuum. A comparison of our Q -values with those from RPH (see above) for 11 stars in common indicates that both methods give excellent agreement in those cases where the wind-emission is significant, whereas for (very) low wind-densities discrepancies may arise, which are mostly related to the problem of uncertain velocity exponents, β .

²This mimics a higher mass-loss rate than actually present, in analogy to the case of WR-stars, cf. also Sect. 5.1.

Based on the complete set of stellar and wind parameters we derived the corresponding WLR for the sample stars accounting for different combinations of stellar reddening and distances available in the literature. In particular, this analysis indicates that using individual instead of mean values for stellar reddening causes variations in $\log L$ and D_{mom} , which are (much) smaller than the individual uncertainties for these quantities.

Our analysis showed that not only the Q -values but also the WLR derived by means of our approximate approach are in good agreement to the results originating from a complete spectral analysis. In particular, we confirm the result published by RPH that the WLR for lc III/V strictly follows the theoretical predictions of Vink et al. (2000), while the relation for lc I shows a vertical offset.

Following the idea of Puls et al. (2003), this offset may reflect the effects of clumping in the innermost part of the wind. For the combination of our sample with data from comparable investigations, we find that with an enhancement factor of ~ 2 for stars with H_α in emission the differences in the corresponding WLRs almost vanish and a unique relation can be obtained (though some problems at lower luminosities still exist admittedly). This enhancement factor corresponds to an effective clumping factor of 4.3, which is somewhat lower than in WR winds and in agreement with the value provided by RPH.

The possibility to use the WLR as an indicator of wind clumping in O star winds is very exciting but needs to be proven independently. One way to check this possibility is to compare H_α and radio mass-loss rates. In particular, and if the assumption of Puls et al. was correct, one might expect larger H_α mass-loss rates for stars with stronger winds, i.e. H_α in emission, whereas the opposite, i.e., similar or even higher radio mass-loss rates, might be expected for stars with weaker winds (H_α in absorption). Guided by this perspective we compared mass-loss rates derived from H_α with such derived from radio free – free emission (Lamers & Leitherer, 1993; Scuderi et al., 1998) for stars in common. In total, these are seven stars, but only for four stars we have information concerning the distance (for the other three we have calibrated M_V): HD 190 429A, HD 66 811, HD 192 639 and HD 36 861. The results obtained indicate perfect agreement between the \dot{M} -estimates for the lc III star HD 36 861 with H_α in absorption ($\log \dot{M}(H_\alpha) / \dot{M}(\text{radio}) = 0.03$), while for the three supergiants with H_α in emission the radio mass-loss rates are lower than those from H_α (by an average factor of ~ 2). In particular, we found $\log \dot{M}(H_\alpha) / \dot{M}(\text{radio})$ equal to 0.29 for HD 190 429 ($d=2.3$ kpc), equal to 0.36 for HD 192 639 ($d=1.82$ kpc) and equal to 0.40 for HD 66 811 ($d=0.7$ kpc). This finding is consistent with both the presence of a stratified clumping factor and our assumption that clumping is “observable” only in the H_α emission of stronger winds.

The results outlined above indicate that the approximate method employed can provide results which are not only quantitatively but also qualitatively consistent to those from a complete spectral analysis. Therefore, this method can be used to solve the statistical problem mentioned in the introduction when studying wind properties of Galactic O-stars and especially when addressing the problem of wind clumping by comparing optical and radio observations. Note in particular that the *ratio* of H_α and radio mass-loss rate remains almost unaffected by any uncertainty in distance, if both values are derived using the *same* value for d : since both mass-loss rates (as function of Q and of flux, respectively) depend on $d^{-1.5}$, the distance cancels almost out, except for the effects of reddening. This means that field stars can also be used as targets for studying wind clumping, a fact that will allow to additionally improve the statistics.

Although the uncertainties in distance cause many problems when studying radii and wind parameters of Galactic stars, we finally like to emphasize that we cannot refrain from such an investigation because of the need to establish a reference base for the behaviour of stars with the corresponding

metallicity.

5.6.1 Future work

While considerable progress has been obtained with respect to the WLR for (Galactic) O-type stars, also a number of questions became evident. In our opinion, one of the most important problems is the following: Presently, we do not know (at least with confidence) the H_α -wind-momentum rates of low luminosity supergiants ($\log L/L_\odot < 5.5$) due to the lack of a significant number of objects in our present sample. In particular, for objects with H_α in absorption we have to answer the question whether the momentum rate is similar or higher than theoretically predicted.³

In the former case our assumption concerning the behaviour of H_α (“actual” \dot{M} , if profile in absorption) still works, while in the latter case it becomes questionable. To clarify this point we have started a new observational program that focuses on lc I objects with $\log L \leq 5.5$. The question concerning the behaviour of B and A supergiants is obvious, and should also be answered in a follow-up investigation.

Even if there is clumping, the question concerning its radial stratification still remains and introduces a number of additional parameters concerning the model atmospheres. The only way to derive reliable constraints is via a multi-wavelength campaign, where the radio and IR domain are particularly important, since the effective stellar radius (i.e., the region where the optical depth reaches unity) is increasing with wavelength. In this regard and as a next step, we plan to perform and analyze radio observations at least for those stars of our sample which can be detected at radio wavelengths.

Acknowledgements:

We like to thank our anonymous referee for very useful suggestions and comments. NM highly appreciates financial support from the German DFG under grants 436 BUL 112/21/01 and 436 BUL 112/34/02. This work is supported in part by NSF to MES (Bulgaria) through grant F-813/98.

³Remember that for the only two supergiants at low L in our sample we found higher values, however not at a statistically significant level.

Bibliography

- Abbott, D.C., Bieging, J.H. & Churchwell, E. 1981, ApJ, 250, 645
- Barbier-Brossat, M., Figon, P. 2000, A&AS, 142, 217
- Bellazzini, M., Fusi Pecci, F., Messineo, M., et al. 2002, AJ, 123, 1509
- Bianchi, L. & Garcia, M. 2002, ApJ, 581, 610
- Cardelli, J.A. 1988, ApJ 335, 177
- Cardelli, J.A., Clayton, G.C., Mathis, J.C. 1989 ApJ, 345, 245
- Clayton, G.C., Cardelli, J.A. 1988, AJ, 96, 695
- Carney, B.W., Latham, D.W., Laird, J.B., et al. 2001, AJ, 122, 3419
- Conti, P.S., Leep, E.M., Lorre, J.J. 1977, ApJ, 214, 759
- Crowther, P.A. 1998, in: Proc IAU Symp. No. 189, eds. T.R. Bedding, A.J. Booth & J. Davis, Kluwer, Dordrecht, p. 137.
- Crowther, P.A., Hillier, D.J., Evans, C.J., et al. 2002, ApJ, 579, 774
- Crowther, P.A., Hillier, D.J., Fullerton, A.W., et al. 2001, A&AS 199, 130
- Cruz-Gonzalez, C., Recillaz-Cruz, E., Costero, R., et al. 1974, RMxAA, 1, 211
- Eversberg, Th., Lepine, S. & Moffat, A.F.J. 1998, ApJ, 494, 799
- Feldmeier, A. 1995, A&A, 299, 523
- Feldmeier, A, Pauldrach, A. & Puls, J. 1997, A&A, 322, 878
- Felli, M., Habing, H.J., Israel, F.P. 1977, A&A, 59, 43
- FitzGerald, M.P. 1970, A&A, 4, 234
- Garmany, C.D., Stencel, R.E. 1992, A&AS, 94, 221
- Gies, D.R. 1987, ApJS, 64, 545
- Gies, D.R. & Bolton, C.T. 1986, ApJS, 61, 419

- Gies, D.R., Mason, B.D., Hartkopf, W.I., et al. 1993, AJ, 106, 2027
- Groenewegen, M.A.T., Lamers, H.J.G.M.L. 1989, A&AS, 79, 359
- Groenewegen, M.A.T., Lamers, H.J.G.M.L., Pauldrach, A.W.A. 1989, A&A, 221, 78
- Haser, S.M. 1995, PhD thesis, University of Munich
- Herrero, A., Kudritzki, R.-P., Vilchez, J.M., et al. 1992, A&A, 261, 209
- Herrero, A., Puls, J., Najarro, F. 2002, A&A, 396, 949
- Hillier, D.J., Miller, D.L. 1998, ApJ, 496, 407
- Hiltner, W.A. 1956, ApJS 2, 389
- Hiltner, W.A., Iriarte, B. 1955, ApJ, 122, 185
- Howarth, I.D., Prinja, R.K. 1989, ApJS, 69, 527
- Howarth, I.D., Siebert, K.W., Hussain, G.A., et al. 1997, MNRAS, 284, 265
- Hubeny, I., Lanz, T. 1995, ApJ 39, 875
- Humphreys, R. 1978, ApJS, 38, 309
- Kudritzki, R.-P. 1980, A&A, 85, 174
- Kudritzki, R.-P., Puls, J. 2000, ARA&A, 38, 613
- Lamers, H.J.G.M.L., Leitherer, C. 1993, ApJ, 412, 771
- Lamers, H.J.G.M.L., Snow, T., Lindholm, D.M. 1995, ApJ, 455, 269
- Lamers, H.J.G.M.L., Haser, S., de Koter, A., et al. 1999, ApJ, 516, 872
- Lennon, D.J., Dufton, P.L. & Fitzsimmons, A. 1992, A&AS, 94, 569
- Markova, N. & Scuderi, S. 2003, in preparation
- Markova, N., Valchev, T. 2000, A&A, 363, 995
- Markova, N., Puls, J., Repolust, T.M., Markov, H. 2004, A&A, 413, 693
- Martins, F., Schaerer, D. & Hillier, D.J. 2002, A&A, 382, 999
- Massa, D., Fullerton, A.W., Sonneborn, G., et al. 2003, ApJ 586, 996
- Meynet, D et al. 1994, A&AS, 103, 97
- Moffat, A.F.J., Robert, C. 1994, ApJ, 421, 310
- Nelan, E., et. al. 2003, in prep.
- Owocki, S.P. & Puls, J. 1999, ApJ, 510, 355

- Owocki, S.P., Castor, J.I. & Rybicki, G.B. 1988, *ApJ*, 335, 914
- Owocki, S.P., Runacres, M.C. & Cohen, D.H. 2000, in *ASP Conf. Ser. 204, Thermal and Ionization Aspects of Flows from Hot Stars: Observations and Theory*, eds. H.J.G.L.M. Lamers & A. Sagar, 183
- Pauldrach, A.W.A., Hoffmann, T.L., Lennon, M. 2001, *A&A*, 375, 161
- Pauldrach, A.W.A., Hoffmann, T.L., Mendéz, R.H. 2002, in *Proc. IAU Symp. No. 209*, eds. S.Kwok & M.Dopita, in press
- Penny, L.R. 1996, *ApJ*, 463, 737
- Puls, J., Kudritzki, R.-P., Herrero, A., et al. 1996, *A&A*, 305, 171
- Puls, J., Springmann, U., Lennon, M. 2000, *A&AS*, 141, 23
- Puls, J., Repolust, T., Hofmann, T., et al. 2002, in *Proc. IAU Symp. No. 212*, eds. K.A. van der Hucht, A. Herrero & C. Esteban, *ASP Conf. Ser.*, p. 61
- Press, W.H., Teukolsky, S.A., Vetterling, W.T., et al. 1992, *Numerical Recipes in Fortran*, 2nd edition, Cambridge University Press
- Repolust, T., Puls, J., Herrero, A. 2004, *A&A* 415, 349
- Sahu, M., Blaauw, A. 1993, in *ASP Conf. Ser. 35, Massive Stars: Their Lives in the Interstellar Medium*, eds. J.P. Cassinelli & E.B. Churchwell, 278
- Schild, H. & Berthet, S. 1986, *A&A* 162, 369
- Scuderi, S., Panagia, N. 2000, in *ASP Conf. Ser. 204, Thermal and Ionization Aspects of Flows from Hot Stars: Observations and Theory*, eds. H.J.G.L.M. Lamers & A. Sagar, 419
- Scuderi, S., Panagia, N., Stanghellini, C., et al. 1998, *A&A*, 332, 251
- Scuderi, S., Panagia, N., Stanghellini, C., et al., 2003, in prep. for *A&A*
- Stone, R.C. 1979, *ApJ*, 232, 520
- Tovmassian, H.M., Hovhannessian, R.Kh., Epremian, R.A., et al. 1994 *MNRAS*, 266, 337
- Vacca, W.D., Garmany, C.D., Shull, J.M. 1996, *ApJ*, 460, 914
- Vanbeveren, D., de Loore, C. & van Rensbergen, W. 1998, *A&A Rev*, 9, 63
- Vink, J.S., de Koter, A., Lamers, H.J.G.L.M. 2000, *A&A*, 362, 295
- Wegner, W. 1994, *MNRAS*, 270, 229
- Walborn, N.R. 1971, *ApJS*, 23, 257
- Walborn, N.R. 1972, *AJ*, 77, 312

Walborn, N.R. 1973, AJ, 78, 1067

Walborn, N.R. 2002, AJ, 124, 507

Woosley, S.E., Heger, E. & Weaver, T.A. 2002, Rev.Mod.Phys. 74, 1015

Chapter 6

Quantitative H and K band spectroscopy of Galactic OB-stars at medium resolution

T. Repolust, J. Puls, M. M. Hanson, R.-P. Kudritzki, M. R. Makiem, A&A submitted

Abstract. In this paper we have analyzed 25 Galactic O and early B-stars by means of *H* and *K* band spectroscopy, with the primary goal to investigate to what extent a lone near-IR spectroscopy is able to recover stellar and wind parameters derived in the optical. Most of the spectra have been taken with SUBARU-IRCS, at an intermediate resolution of 12,000, and with a very high S/N, mostly on the order of 200 or better. In order to synthesize the strategic H/He lines, we have used our recent, line-blanketed version of FASTWIND (Puls et al. 2005). In total, seven lines have been investigated, where for two stars we could make additional use of the He I 2.05 singlet which has been observed with IRTF-CSHELL. Apart from Br γ and He II 2.18, the other lines are predominately formed in the stellar photosphere, and thus remain fairly uncontaminated from more complex physical processes, particularly clumping.

First we investigated the predicted behaviour of the strategic lines. In contradiction to what one expects from the optical in the O-star regime, almost all photospheric H/He I/He II *H/K* band lines *become stronger if the gravity decreases*. Concerning H and He II, this finding is related to the behaviour of Stark broadening as a function of electron density, which in the line cores is different for members of lower (optical) and higher (IR) series. Regarding He I, the predicted behaviour is due to some subtle NLTE effects resulting in a stronger overpopulation of the lower level when the gravity decreases.

We have compared our calculations with results from the alternative NLTE model atmosphere code CMFGEN (Hillier & Miller 1998). In most cases, we found reasonable or nearly perfect agreement. Only the He I 2.05 singlet for mid O-types suffers from some discrepancy, analogous with findings for the optical He I singlets.

For most of our objects, we obtained good fits, except for the line cores of Br γ in early O-stars with significant mass-loss. Whereas the observations show Br γ mostly as rather symmetric emission lines, the models predict a P Cygni type profile with strong absorption. This discrepancy (which also appears in lines synthesized by CMFGEN) might be an indirect effect of clumping.

After having derived the stellar and wind parameters from the IR, we have compared them to results from previous optical analyses. Overall, the IR results coincide in most cases with the optical ones within the typical errors usually quoted for the corresponding parameters, i.e., an uncertainty in T_{eff} of 5%, in $\log g$ of 0.1 dex and in \dot{M} of 0.2 dex, with lower errors at higher wind densities. Outliers above the 1- σ level were found in four cases with respect to $\log g$ and in two cases for \dot{M} .

6.1 Introduction

Although rare by number, massive stars dominate the life cycle of gas and dust in star forming regions. They are responsible for the chemical enrichment of the ISM, which in turn has a significant impact on the chemical evolution of the parent galaxy. The main reason for this is that due to their large masses, each physical stage evolves on much shorter timescales and more violently, compared to low-mass stars, which provides a very efficient recycling of elements. Moreover, the large amount of momentum and energy input of these objects into the ISM controls the dynamical evolution of the ISM and, in turn, the evolution of the parent galaxy (e.g., Leitherer & Heckman 1995; Silich & Tenorio-Tagle 2001; Oey 2003).

Presently, high mass star formation is still poorly understood. This is due in part to the molecular gas and dust found in star forming regions allowing little or no light to escape at optical wavelengths. The dust, however, becomes more transparent in the infrared (IR) regime. Observations at such wavelengths reveal the hot stellar content of these dust-enshrouded environments like young HII regions in dense molecular clouds, the Galactic centre or massive clusters.

Following the substantial progress in ground-based IR instrumentation in the past decade, IR spectroscopy has become a powerful diagnostics for the investigation of hot stars and the stellar winds surrounding them. The first systematic *observational* studies of OB stars in the *H* and *K* band have been performed by e.g., Hanson et al. (1996), Morris et al. (1996) and Fullerton & Najarro (1998) providing an important basis for quantitative spectral analysis of early type stars. With the use of satellites (e.g., the Infrared Space Observatory (ISO) in 1995 and the Spitzer Space Telescope in 2003) a larger spectral window became accessible, completing the IR regime already observed from the ground.

Modeling of the near-infrared, on the other hand, has been performed mostly for early-type stars with dense winds, i.e., for Wolf-Rayet Stars (Hillier 1982), Galactic centre objects (Najarro et al. 1994), Of/WN stars (Crowther et al. 1995, 1998) and Luminous Blue Variables (Najarro et al. 1997, 1998). For objects with thinner winds (which are of particular interest when aiming at the youngest objects emerging from Ultra-Compact HII (UCHII) regions), no results are available so far, except from a pilot study by Lenorzer et al. (2004). In this study, various *synthetic* H/He IR-profiles, located in the *J* to *L* band, are presented for a comprehensive grid of O-type stars (from dwarfs to supergiants), and their diagnostic potential and value is discussed.

The reader may note that most of the available datasets of IR-spectra have been observed at relatively low resolution (typically, at $R \approx 2,000$, though Fullerton & Najarro (1998) present a few spectra with $R \approx 10,000$), which compromises a precise spectroscopic analysis, since many decisive spectral features remain unresolved. Meanwhile, however, Hanson et al. (2005) have re-observed a large sample of Galactic O-type “standards” with much higher resolution, typically at $R \approx 12,000$. The objects were chosen in such a way that they both largely overlap with stars which have been analyzed before in the optical (e.g., Herrero et al. 2002; Repolust et al. 2004), and cover a wide range in spectral type and luminosity class. Therefore, the present paper has the following objectives:

- We carry out a spectral analysis for this sample in the near infrared regime and compare it with results already obtained in the optical. This will allow us to check the extent to which the data derived from the IR is consistent with results obtained from alternative studies in different wavelength bands. As an ultimate goal, we plan to use solely the infrared regime to provide accurate constraints to the characteristics of stars which can only be observed at these wavelengths.

- We test our model atmosphere code FASTWIND (Santolaya-Rey et al. 1997; Herrero et al. 2002; Puls et al. 2005) for OB stars in the near infrared, hence extending its usage to these wavelength ranges.
- We give special attention to those lines which are located in the *H* and *K* band, i.e., which can be accessed by *ground-based* instrumentation alone. Note that these lines are mainly formed close to the photosphere, i.e., remain uncontaminated by additional effects such as clumping and X-rays and, thus, should provide rather robust estimates for effective temperatures and gravities.

The remainder of this paper is organized as follows. In Sect. 6.2 we briefly describe the observations and the lines used in our analysis. In Sect. 6.3 we summarize our model calculations and comment on our treatment of line-broadening for the hydrogen lines. Sect. 6.4 outlines some theoretical predictions concerning the behaviour of strategic lines, and Sect. 6.5 compares our results with those obtained by Lenorzer et al. (2004) by means of the alternative wind-code CMFGEN (Hillier & Miller 1998). In Sect. 6.6, we discuss the analysis of the individual objects of our sample, and Sect. 6.7 compares the results with those from the corresponding optical data. In Sect. 6.8, finally, we present our summary and conclusions.

6.2 Observations, targets and strategic lines

For our analysis we use a subset of stars given by Hanson et al. (2005). Detailed information about the observation dates, resolution, spectrometers and data reduction can be found there. We selected the spectra from that sample which were obtained with the Infrared Camera and Spectrograph (IRCS) mounted at the Cassegrain focus of the 8.2m Subaru Telescope at Mauna Kea, Hawaii. This totaled in 29 stars out of the 37 targets collected by Hanson et al. (2005).

The targets had been selected i) to fairly cover the complete OB star range down to B2/B3 at all luminosity classes, and ii) that most of them have already been analyzed in the optical (for details, see Hanson et al. 2005). According to the purpose of our analysis, we have exclusively used the data from the Subaru Telescope and not the VLT data (comprising the remaining 8 objects), since we did not possess complementary optical spectra for the latter dataset. In the following, we will define four different sub-samples denoted by I to IV in order to distinguish between objects analyzed in the optical by different authors. Sample I comprises those stars discussed by Repolust et al. (2004), sample II corresponds to objects analyzed by Herrero et al. (2000, 2002)¹, sample III (B-supergiants) has been analyzed by Kudritzki et al. (1999, only with respect to wind-parameters), and sample IV consists of the few remaining objects considered by various authors or not at all. In particular, HD 46150 has been investigated by Herrero et al. (1992, plane-parallel, unblanketed models) and τ Sco (HD 149438) by Kilian et al. (1991, plane-parallel NLTE analysis with underlying Kurucz models) and by Przybilla & Butler (2004) with respect to optical and IR hydrogen lines. Table 6.1 indicates to which individual sub-sample the various objects belong.

The Subaru/IRCS *H* band and *K* band spectral resolution is $R \approx 12000$. The typical signal-to-noise ratios obtained with these spectra were $S/N \approx 200-300$, with areas as high as $S/N \approx 500$, and as low as $S/N \approx 100$, depending on the telluric contamination. The spectra were obtained over two separate runs, the first in November 2001 and the second in July 2002. Due to poor weather condition, the

¹Note that the first of the two investigations has been performed by unblanketed models.

Table 6.1: Sample stars and observing data in the H and K band. In sub-samples I to III we have grouped those objects which have been previously analyzed in the optical (sub-sample I: Repolust et al. 2004; sub-sample II: Herrero et al. 2000, 2002; sub-sample III: Kudritzki et al. 1999). Subsample IV comprises those objects covered by various authors or not analyzed at all.

Star	Sp.Type	SUBARU-IRCS	sample
Cyg OB2 #7	O3 If*	Nov 01	II
Cyg OB2 #8A	O5.5 I(f)	July 02	II
Cyg OB2 #8C	O5 If	July 02	II
HD 5689	O6 V	Nov 01/July 02	II
HD 13268	ON8 V	Nov 01	I
HD 13854	B1 Iab	Nov 01	III
HD 13866	B2 Ib	July 02	III
HD 14134	B3 Ia	July 02	III
HD 14947	O5 If+	Nov 01	I
HD 15570	O4 If+	Nov 01	II
HD 15558 ¹⁾	O5 III(f)	July 02	I
HD 15629	O5 V((f))	July 02	I
HD 30614	O9.5 Ia	Nov 01	I
HD 36166	B2 V	Nov 01	IV
HD 37128	B0 Ia	Nov 01	III
HD 37468	O9.5 V	Nov 01	IV
HD 46150	O5 V((f))	Nov 01	IV
HD 46223	O4 V((f))	Nov 01	IV
HD 64568	O3 V((f))	Nov 01	IV
HD 66811	O4 I(n)f	Nov 01	I
HD 149438 ^{1,2)}	B0.2 V	July 02	IV
HD 149757	O9 V	July 02	I
HD 190864 ²⁾	O6.5 III(f)	July 02	I
HD 191423	O9 III:n*	July 02	I
HD 192639	O7 Ib	July 02	I
HD 203064	O7.5 III:n ((f))	July 02	I
HD 209975	O9.5 Ib	July 02	I
HD 210809	O9 Iab	July 02	I
HD 217086	O7 Vn	Nov 01	I

¹⁾ only K band available.

²⁾ Additional IRTF-CSHELL spectra covering He I2.05 available.

telluric corrections for some of the spectra proved to be difficult. This can be seen in the *H* band spectra of HD 217086, HD 149757, HD 66811, HD 5689 and HD 15629. Furthermore, there were no *H* band spectra of HD 15558 and τ Sco available, weakening the significance of their analyses. The reduction of the data was performed using IRAF routines and Perl IDL including standard procedures such as bias subtraction, flat field division, spectrum extraction, wavelength calibration and continuum rectification. Table 6.1 summarizes all observational runs obtained with IRCS. In the following, all wavelengths of NIR lines are given in microns (μ).

The data for the He I λ 2.05 line, which had not been observed by SUBARU were taken at the Infrared Telescope Facility (IRTF) in March, June and July of 2003. The CSHELL echelle spectrograph (Greene et al. 1993) was used with a slit of 1.0 arcseconds. The instrumental spectral resolving power as measured by a Gaussian fit to the OH night sky emission lines was 4.0 pixels FWHM, or 12.1 km s⁻¹, corresponding to a resolution of 24,000. The spectra were reduced using IRAF routines and the subsequent analysis was done using routines written in Perl IDL. For all spectra, dark frames and flat field frames were averaged together to form a master dark and flat frame. Unfortunately, He I λ 2.05 lies within a region where the telluric absorption is extremely large, degrading the signal significantly (Kenworthy & Hanson 2004). After the reduction, it turned out that most of our spectra did not possess sufficient quality (only moderate S/N), and we could use only the spectra obtained for two of the stars (HD 190864 and τ Sco) for our analysis. Nevertheless, in all cases we have included the *synthesized* line for the sake of completeness.

The spectral classification of sample I is the one adopted by Herrero et al. (1992), based mostly on the work by Walborn (1972, 1973), the unpublished catalogue of OB stars by C. Garmany and by Mathys (1989). As for samples II to IV, the spectral classification used by Hanson et al. (2005) has been retained. The classifications were based mostly on Walborn classifications, except for the Cyg OB2 stars, which relied on Massey & Thompson (1991).

In total the sample consists of 29 Galactic O and early B type stars as listed in Table 6.1 ranging from O3 to B3 and covering luminosity class Ia/Iab, Ib/II, III, and V objects, where 4 stars (of the latest spectral types) have been discarded later in the study. The strategic lines used in our analysis are (all wavelengths in air)

- *H* band

- H I λ 1.68 ($n = 4 \rightarrow 11$, Br11),
- H I λ 1.74 ($n = 4 \rightarrow 10$, Br10),
- He I λ 1.70 ($3p^3P^o - 4d^3D$, triplet)
- He II λ 1.69 ($n = 7 \rightarrow 12$).

- *K* band

- H I λ 2.166 ($n = 4 \rightarrow 7$, Br $_{\gamma}$),
- He I λ 2.058 ($2s^1S - 2p^1P^o$, singlet), where available,
- He I λ 2.11 (comprising the He I triplet λ 2.1120 ($3p^3P^o - 4s^3S$) and the He I singlet λ 2.1132 ($3p^1P^o - 4s^1S$)),
- He II λ 2.188 ($n = 7 \rightarrow 10$).

Note that Br $_{\gamma}$ overlaps with the He I triplet $\lambda 2.1607$ ($4d\ ^3D - 7f\ ^3F^o$), the He I singlet $\lambda 2.1616$ ($4d\ ^1D - 7f\ ^1F^o$) and He II $\lambda 2.1647$ ($n = 8 \rightarrow 14$). Whereas the singlet is not included in our formal solution, the He I triplet, in particular, has been used to check the consistency of our results. Note that the influence of the He II lines overlapping with Br10 and Br11 is marginal.

6.3 Model calculations

The calculations presented in this paper have been performed by means of our present version of FASTWIND, as described by Puls et al. (2005). In addition to the features summarized in Repolust et al. (2004), this code meanwhile allows for the calculation of a consistent² temperature, utilizing a flux-correction method in the lower atmosphere and the thermal balance of electrons in the outer one. As has been discussed, e.g., by Kubát et al. (1999), the latter method is advantageous compared to exploiting the condition of radiative equilibrium in those regions where the radiation field becomes almost independent on T_e . Particularly for IR-spectroscopy, such a consistent T-stratification is of importance, since the IR is formed above the stellar photosphere in most cases and depends (sometimes critically) on the run of T_e . We have convinced ourselves that our previous results concerning optical lines remain (almost) unaffected by this modification.

Puls et al. (2005) present a thorough comparison with models from alternative “wind-codes” (WM-basic, Pauldrach et al. 2001 and CMFGEN, Hillier & Miller 1998). Some differences were seen in the OII continuum at and below 350 Å (FASTWIND predicts a higher degree of line-blocking in this region), which might have some influence on the helium ionization balance, due to a different illumination of the He II resonance lines. Also, CMFGEN predicted weaker optical He I singlets in the temperature range between 36,000 to 41,000 K for dwarfs and between 31,000 to 35,000 K for supergiants. Otherwise, the comparison resulted in very good agreement.

6.3.1 Atomic data and line broadening

In order to obtain reliable results in the IR, our present H and He II models consist of 20 levels each, and He I includes levels until $n = 10$, where levels with $n = 8, 9, 10$ have been packed. Further information concerning cross-sections etc. can be found in Jokuthy (2002).

The hydrogen bound-bound collision strengths require some special remarks. The atomic data on *radiative* line processes in H I are very accurate because they can be obtained analytically due to the two-body nature of the hydrogen atom. However, for excitation/de-excitation processes, these involve a colliding particle, making the situation much more complex. In most cases only approximation formulae are available.

Note that the “choice” of the collisional data is an especially important factor for the line formation in the IR. Although the effect of different collisional data will not be apparent for the ground state, higher levels display a significant sensitivity, reaching its maximum for levels with intermediate n at line formation depth. Recently, Przybilla & Butler (2004) have emphasized the differences in the collisional cross section from approximation formulae and ab initio computations for transitions up to $n = 7$. Particularly, the frequently used approximations by Mihalas et al. (1975) and by Johnson (1972) show a different behaviour and fail to simultaneously reproduce the optical and IR spectra over a wide parameter range. However, the collisional data provided by Przybilla & Butler (in combination

²Note, however, that non-radiative heating processes might be of importance.

with the approximation formulae by Percival & Richards (1978) and Mihalas et al. (1975)) are able to reproduce the observed line profiles in those cases which have been checked. Note, however, that these checks did not cover O-type supergiants, cf. Sect. 6.7.1!

The standard implementation of the corresponding cross sections in FASTWIND, on the other hand, is based on data presented by Giovanardi et al. (1987). Although affected by similar problems as described above, the differences to the ab initio calculations are smaller but still worrisome. As detailed later on, a comparison of simulations using both data-sets alternatively revealed that *for our O-star sample* we find better agreement with corresponding optical results if our standard implementation is used. Consequently, all calculations described in the following are based on these data, whereas further comments concerning the effect of incorporating the data by Przybilla & Butler (2004) are given in Sect. 6.7.1.

Since we are concentrating on those lines which are formed close to the photosphere, line-broadening is particularly important (and leads to a number of interesting effects, shown below). Unfortunately, calculations as “exact” as for optical lines do not yet exist for their IR counterparts, leaving us to use reasonable approximations.

Actually, Lemke (1997) has published extended Stark broadening tables (based on the approach by Vidal, Cooper & Smith 1973, “VCS”) for the hydrogen Lyman to Brackett series. In a first step, we have used his dataset for the calculation of the Brackett lines. However, we immediately realized that at least Br11 must be erroneous by virtue of a comparison with observed mid-resolution B-type NIR spectra which revealed no problems if approximate broadening functions are used (see Hanson et al. 2003, Fig. 4). After a careful investigation by K. Butler (priv. comm.), it turned out that not only Br11 but also other transitions, i.e., predominantly members of the higher series, are affected by a number of (numerical) problems in the code used by Lemke.

Thus, Stark-broadening of hydrogen needs to be approximated as well. We follow the method by Griem (1967) as outlined in Auer & Mihalas (1972, Appendix), based on a corrected asymptotic Holtsmark formula. Due to comparisons with VCS calculations for optical transitions from Schöning & Butler (1989), which are used by FASTWIND anyway, we have convinced ourselves that the Griem approximation recovers the more exact VCS results with very high precision, if the upper and lower level of the transition lie not too closely together (e.g., H_α is badly approximated, whereas for H_γ no differences are visible). The results obtained by using either the (erroneous) data by Lemke or the Griem approximation are given by means of a detailed comparison later on, cf. Fig. 6.6. Griem-broadening is also applied to He II (1.69, 2.18 μ), whereas for He I (1.70, 2.05, 2.11 μ) we have used Voigt functions only, with damping parameters accounting for natural and collisional broadening. The comparison to observations suggests that this approximation describes reality sufficiently well.

6.4 Predicted behaviour of strategic lines

Before we describe the results of our analysis, we will investigate the behaviour of our synthesized lines in some detail, particularly because their dependence on gravity seems to be somewhat strange, at least if one extrapolates the knowledge accumulated in the optical. Although a related investigation has already been performed by Lenorzer et al. (2004), they have only discussed the behaviour of the equivalent widths. Moreover, their model grid is rather restricted and does not allow the investigation of changes in synthesized profiles if only *one* atmospheric parameter is altered. On the other hand, we have calculated a rather large grid of models in the parameter range $20,000 < T_{\text{eff}} < 50,000$ with a

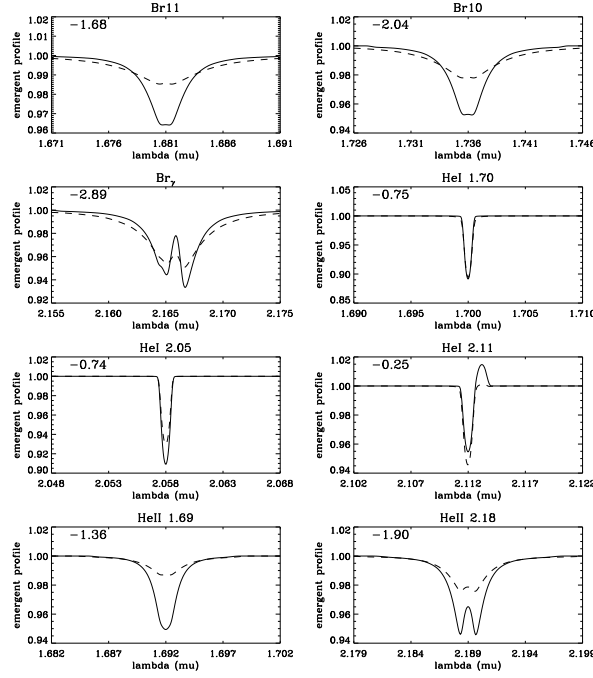


Figure 6.1: Comparison of strategic NIR lines for two atmospheric models at $T_{\text{eff}} = 40,000$ K and different gravities, $\log g = 3.7$ (solid) and $\log g = 4.5$ (dashed), respectively. Both models have a negligible wind, with $\log Q = -14$. The number in the upper left corner gives the equivalent width (in Å) of the low-gravity model, where, in agreement with previous papers, negative numbers indicate net-absorption. All profiles are displayed on the same horizontal scale (of width 0.02μ), and the profiles have been rotationally convolved with $V_r \sin i = 80 \text{ km s}^{-1}$.

typical variation in $\log g$ over two dex, and wind strengths varying from negligible to very large (cf. Puls et al. 2005), allowing us to inspect this kind of reaction in more detail. In the next section we will, of course, compare our results also to those obtained by Lenorzer et al. (2004).

As a prototypical example, in Fig 6.1 we compare the strategic H/He NIR lines for a model at $T_{\text{eff}} = 40000$ K, with $\log g = 3.7$ (solid) and 4.5 (dashed). Both models have a vanishing wind density, corresponding to $\log Q = -14$, where Q is a suitable measure to compare the influence of different wind strengths in recombination lines (see Puls et al. (1996)). Throughout this paper, we have defined

$$Q = \frac{\dot{M}[\text{M}_{\odot}/\text{yr}]}{((R_{\star}/R_{\odot})v_{\infty}[\text{kms}^{-1}])^{1.5}}. \quad (6.1)$$

Most interestingly, almost all NIR features *become deeper and their equivalent width increases if the gravity decreases*. In contrast to the Balmer lines, the cores of Br10, Br11, and (and of He II 1.69/2.18) are significantly anti-correlated with gravity. This behaviour is completely opposite to what one expects from the optical. Only the far wings of the hydrogen lines bear resemblance to the optical, which become shallower when the gravity decreases.

Although the reaction of He I on $\log g$ is only moderate, at lower temperatures (with more He I present) we observe the same trend, i.e., the equivalent width (e.w.) increases with decreasing gravity, as shown in the e.w. iso-contour plots in Fig. 6.3. For comparison, this plot also shows the extremely

“well-behaved” He I4471 line, which decreases in strength with decreasing gravity in all regions of the $T_{\text{eff}}\text{-}\log g$ -plane.

Before we will further discuss the origin of this peculiar behaviour of NIR-lines, let us point out that these trends do *not* depend on specific details of the atmospheric model, particularly not on the presence or absence of a temperature inversion in the upper photospheric layers. The same relations (not quantitatively, but qualitatively) were also found in models with a monotonically decreasing temperature structure in the inner part ($\log \tau_{\text{Ross}} > -2$) and a constant minimum temperature in the outer wind.

6.4.1 Hydrogen and He II lines: Influence of Stark broadening

The peculiar behaviour of the line cores of the hydrogen Brackett lines and He II 1.69/2.18 can be understood from the reaction of the core of the corresponding Stark-profiles as a function of electron density. Fig. 6.2 shows the Stark-profiles for H_γ and Br10 as a function of frequency displacement from the line centre in units of thermal Doppler-width, calculated in the Griem approximation. Both profiles have been calculated for typical line-forming parameters, $T_e = 40,000$ K and $\log n_e = 11.5, 12.5$ and 13.5 , respectively. The corresponding pure Doppler profile is overplotted (in grey). The decisive point is, that for H_γ , with relatively low upper principal quantum number, the Stark width is not considerably large, and the core of the profile is dominated by Doppler-broadening, independent of electron density. Only in the far wings does the well known dependence on n_e become visible. On the other hand, for Br10 the Stark width becomes substantial (being proportional to the fourth power of upper principal quantum number), and even the Stark-core becomes extremely density dependent. Only at lowest densities, the profile coincides with the pure Doppler profile, whereas for larger densities the profile function (and thus the frequential line opacity) decreases with increasing density. In the far cores, finally, the conventional result ($\phi(\nu)$ correlated with n_e) is recovered. Thus, as a consequence of the dependence of Stark-broadening on density, the line cores of the hydrogen lines with large upper principal quantum number become weaker with increasing gravity. Br $_\gamma$ (with upper quantum number $n=7$) is less sensitive to this effect, cf. Fig 6.1.

In Fig. 6.4, we demonstrate the different reactions of the Stark profiles on electron density (gravity) by comparing the synthesized *emergent* profiles of the high- and low-gravity model at $T_{\text{eff}}=40,000$ K, as described above. In particular, we compare these profiles with the corresponding profiles calculated with pure Doppler-broadening. For H_γ , the core of the Stark-broadened profile agrees well with the Doppler-broadened one (dashed) in both cases. The major difference is found in the far wings, which become wider and deeper as a function of (electron-) density, thus, being the most useful indicators for the effective gravity. For Br10, on the other hand, the pure Doppler profile is much deeper than the Stark-broadened core, where the differences are more pronounced for the high gravity model. Note particularly that the (absolute) e.w. is larger for the low gravity model (although the high gravity model has more extended wings), since the major part of the profile is dominated by the core which is deeper for lower gravities!

Actually, the same effect is already visible in the optical, namely for the prominent He II lines at 4200\AA (transition 4-11) and 4541\AA (transition 4-9, not shown here). The increase in absolute e.w. as a function of gravity is solely due to the wings. In accordance with Br10/Br11, however, the cores of the lines become shallower with increasing gravity, *not because of an effect of less absorbers, but because of less frequential opacity due to a strongly decreased broadening function.*

Let us allude to an interesting by-product of our investigation. A comparison of our synthetic NIR

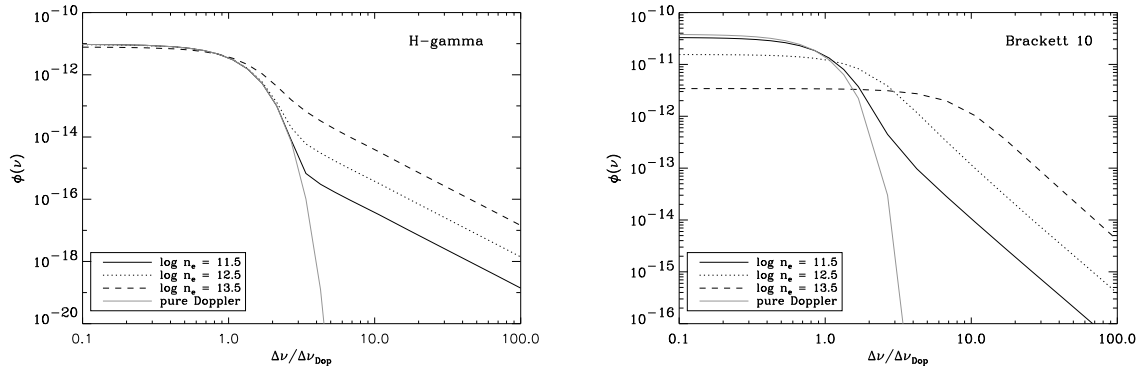


Figure 6.2: Line broadening profile functions (convolution of Doppler with Stark profiles, in $[s^{-1}]$) for H_γ and Br10, as a function of frequency displacement from the line centre in units of thermal Doppler-width. Both profiles have been calculated in Griem approximation, for an electron temperature $T_e = 40,000$ K and three different electron densities typical for the line forming region. The grey line corresponds to a pure Doppler profile. Note that for H_γ the core of the Stark profile is identical with the pure Doppler profile, whereas for Br10 the Stark core is extremely density dependent and coincides with the Doppler profile only at lowest densities (see text).

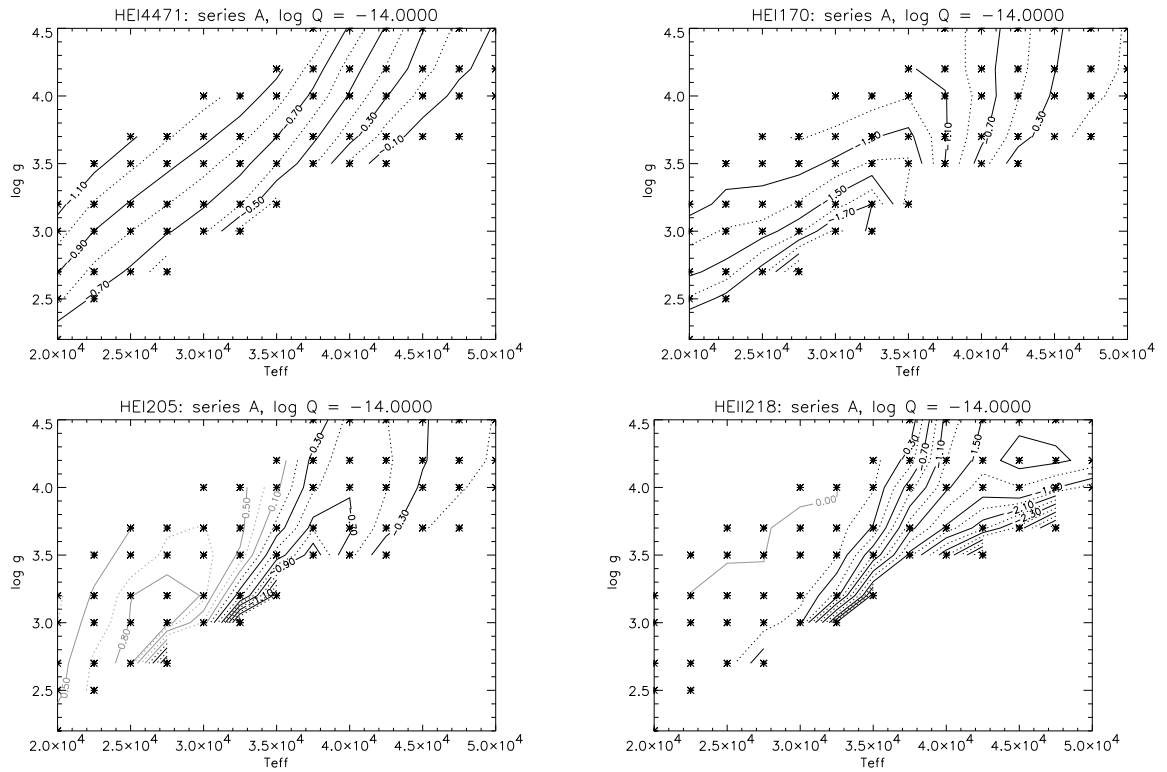


Figure 6.3: Iso-contours of equivalent widths for He I and He II lines using a model-grid with values for T_{eff} and $\log g$ as indicated, and negligible wind densities, $\log Q = -14$. Curves in grey color (left-hand side of HeI205 iso-contours) indicate net emission. Note that for the optical transition (HeI4471) the absorption increases as function of gravity, whereas for the NIR lines this behaviour is mostly reversed. Asterisks denote the position of the calculated models (see also Puls et al. 2005).

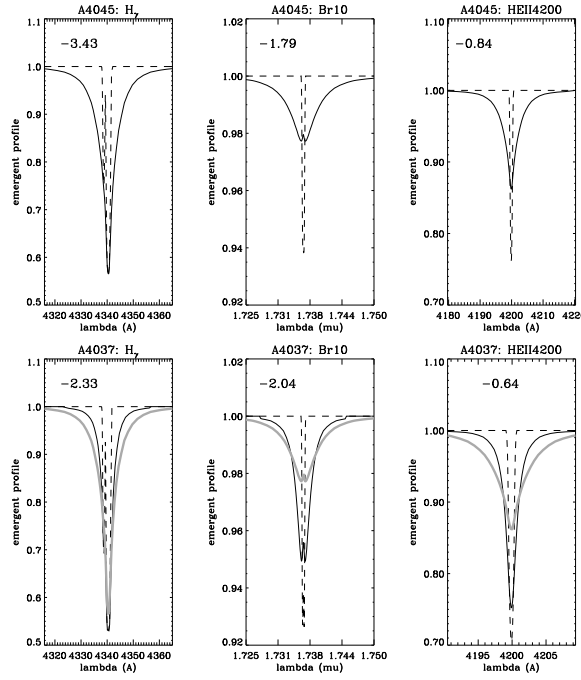


Figure 6.4: Influence of Stark-broadening for lines with low- and high-lying upper level as a function of gravity. Upper level, solid lines: Synthetic spectra of $H\gamma$, Br10 and He II 4200 ($n=4 \rightarrow 11$) for an atmospheric model with $T_{\text{eff}} = 40,000$ K, $\log g = 4.5$ and $\log Q = -14$ (cf. dashed lines in Fig. 6.1). Overplotted (dashed) are the corresponding profiles with pure Doppler-broadening. Lower panel: As the upper panel, but for an atmosphere with $\log g = 3.7$ (solid lines in Fig. 6.1). For comparison, the results for the Stark-broadened profiles from the upper panel are overplotted in grey. Note the similarity in effects between Br10 and He II 4200.

profiles with the observations will show that in a number of cases the observed Br10/Br11 profiles cannot be fitted in parallel. In this case the line formation is well understood and the profiles from CMFGEN are identical (note that also the optical hydrogen lines agree well, see Repolust et al. 2004), giving us confidence that our occupation numbers are reasonable and that the obvious differences are due to inadequate broadening functions.

On the other hand, since He II 4200/4541 is affected by almost identical line broadening, we would like to suggest a solution for a long standing problem in the *optical* spectroscopy of hot stars: It is well known that for a wide range of O-star parameters the theoretical simulations of these lines (by means of both plane-parallel and extended atmospheres) have never been able to reproduce the observations in parallel (e.g., Herrero et al. 2002), where the largest discrepancies have been found in the line cores. The origin of this discrepancy is still unknown.³ Due to the similarity of this problem to the one shown by Br10/11 and accounting for the similar physics, we suggest that also in this case we suffer from an insufficient description of presently available broadening functions (which are described within the VCS-approach, see Schöning & Butler 1989). Thus, a re-investigation of line broadening for transitions with high lying upper levels seems to be urgently required.

In summary, due to their tight coupling with electron density, the cores of Br10/11 and

³Note that this problem is most probably not related to the presence of the N III blend in He II 4200, since it occurs also in hot objects.

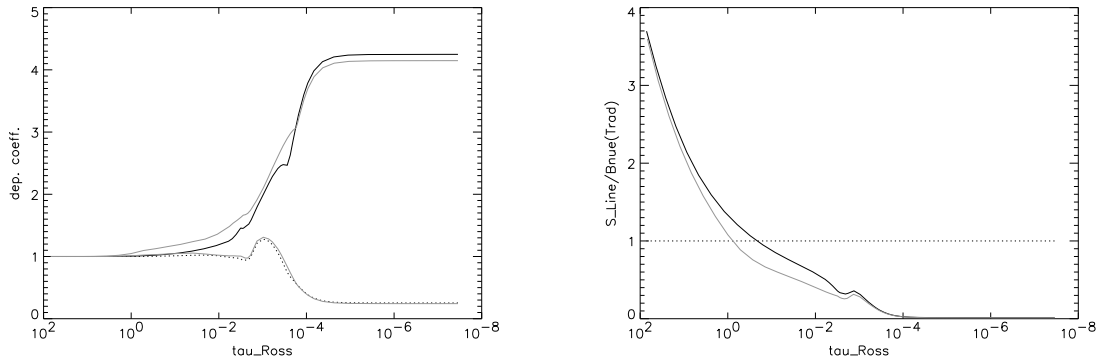


Figure 6.5: Left panel: NLTE-departure coefficients for the lower (solid) and upper (dotted) levels of He II 1.70 for a model with $T_{\text{eff}} = 30,000$ K, $\log g = 3.4$ and negligible wind. Overplotted in grey are the corresponding values for a similar model, but with lower gravity, $\log g = 3.0$.

Right panel: As the left panel, but for the corresponding line source functions in units of the emergent continuum at 1.70μ .

He II 1.69/2.18 are excellent indicators of gravity, where deeper cores indicate lower gravities (if the (projected) rotational velocities are similar).

6.4.2 He I lines: Influence of NLTE effects

The peculiar behaviour of the hydrogenic lines could be traced down to the influence of the profile-functions, whereas the formation of most of the NIR He I lines is dominated by NLTE-effects. As has been extensively discussed by Mihalas (1978), Kudritzki (1979), Najarro et al. (1998), Przybilla & Butler (2004) and Lenorzer et al. (2004), the low value of $h\nu/kT$ leads to the fact that even small departures from LTE become substantially amplified in the IR (in contrast to the situation in the UV and optical). A typical example is given by the behaviour of He II 1.70 at temperatures below $T_{\text{eff}} \approx 35,000$ K, cf. Fig. 6.3 (note, that CMFGEN gives identical predictions). Again, this line becomes stronger for lower gravity, in contrast to the well known behaviour of optical lines (compare with the He I 4471 iso-contours).

Fig. 6.5 gives a first explanation, by means of two atmospheric models with $T_{\text{eff}} = 30,000$ K, $\log g = 3.4$ and 3.0 , respectively, and (almost) no wind. The departure coefficient of the upper level, b_u , of this transition ($4d^3D$) is independent of gravity and has, in the line forming region, a value of roughly unity (strong coupling to the He II ground-state), whereas the lower level ($3p^3P^o$) is quite sensitive to the different densities, i.e., being stronger overpopulated in the low-gravity model. Consequently, the line source function, being roughly proportional to b_u/b_l , is considerably lower throughout the photosphere (right panel of Fig. 6.5), and thus the profile is deeper, even if the formation depth is reached at larger values of τ_{Ross} .

The reason for this stronger overpopulation at lower $\log g$ -values is explained by considering the most important processes which populate the $3p$ -level. First, the influence of collisions is larger at higher densities, which drives the departure coefficient into LTE. Second, the level is strongly coupled to the triplet “ground state” (i.e., the lowest meta-stable state) which, in the photosphere, is overpopulated as an inverse function of the predominant density. The overpopulation (with the consequence of over-populating the $3p$ -level) is triggered by the strength of the corresponding ionizing

fluxes. These are located in the near UV (roughly at 2,600 Å) and are larger for high gravity models than for low gravity ones. This is because the stronger Lyman-jump and the stronger EUV flux-blocking (higher densities \rightarrow lower metal ionization stages \rightarrow more lines) have to be compensated for on the red side of the flux-maximum to achieve flux conservation.

If the ionization/recombination rates are dominating, the (photospheric) departure coefficients inversely scale with the flux at the corresponding edge (for similar electron temperatures, cf. Mihalas 1978), and for higher gravities we obtain lower departure coefficients (more ionization) than for lower gravities. Thus, the increase of the He I 1.70 line flux with gravity is a final consequence of the different near UV radiation temperatures as a function of gravity.

One might wonder why the strength of He I 4471 is “well” behaved, since this line has the same upper level as He I 1.70, and the lower level ($2p^3P^o$) is strongly coupled to the triplet ground-state as well. Actually, a simple simulation shows that for this transition the same effect as for the He I 1.70 line would be present *if the transition were situated in the IR*. Only because the transition is located in the optical ($h\nu/kT \gg 1$), the corresponding source functions are much less dependent on gravity (the non-linear response discussed above is largely suppressed). The profiles react almost only on the opacity, which is lower for lower gravity due to the lower number of available He I ions.

In summary, the He I line formation *in the optical* is primarily controlled by different formation regions, since the source functions do not strongly depend on gravity, whereas *in the IR* the deviations from LTE become decisive. In particular, the influence of considerably different source-functions is stronger than the different formation depths, where these source functions are larger for high-gravity models due to a less overpopulated lower level.

With respect to the singlet transitions (He I 2.05, reacting inversely to the red component of He I 2.11), we refer the reader to the discussion by Najarro et al. (1994) and Lenorzer et al. (2004). But we would like to mention that for a large range of parameters He I 2.05 reacts similar to the way described above, simply because the ionization/recombination rates (over-)populating the lower level ($2s^1S$, again a meta-stable level, located at roughly 3,100 Å) remain the decisive ingredients controlling the corresponding source functions.

6.5 Comparison with results by Lenorzer et al.

As already mentioned, recently Lenorzer et al. (2004) presented a first calibration of the spectral properties of normal OB stars using near infrared lines. The analysis was based on a grid of 30 line-blanketed unified atmospheres computed with CMFGEN, with 10 models per luminosity class I, III, and V, where wind-properties according to the predictions by Vink et al. (2000) have been used, and T_{eff} ranges from 24,000 K up to 49,000 K (cf. Fig. 6.7). Emphasis was put on the behaviour of the equivalent widths of the 20 strongest lines of H and He in the *J*, *H*, *K* and *L* band. For detailed information on procedure and results see Lenorzer et al. (2004). In order to check our results obtained by means of FASTWIND, we have calculated models with identical parameters and synthesized the same set of NIR lines (see also Puls et al. 2005). Note that CMFGEN uses a constant photospheric scale height (in contrast to FASTWIND), so that the photospheric density structures are somewhat different, particularly for low gravity models where the influence of the photospheric line pressure becomes decisive.

Since Lenorzer et al. calculated their hydrogenic profiles with the erroneous broadening functions provided by Lemke (1997), the *H* and *K* band profiles have been recalculated by means of the Griem

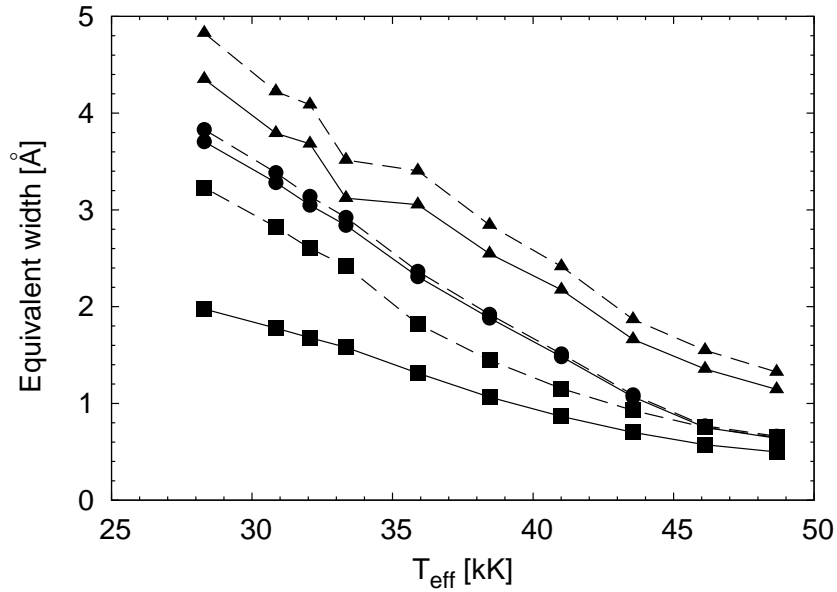


Figure 6.6: Comparison of equivalent widths (defined here in the conventional way) for NIR hydrogen lines of O-type dwarfs (Lenorzer et al. 2004) using the (erroneous) broadening functions by Lemke (1997) with results using broadening functions in the Griem approximation (dashed). Squares, circles and triangles correspond to Br11, Br10 and Br γ , respectively. Note that in all cases the equivalent width becomes larger and that the most significant differences occur for Br11 at lower temperatures.

approximation by one of us (R.M.). The differences in the equivalent widths for the dwarf grid are shown in Fig. 6.6. In all cases the equivalent widths became larger, mainly because of increased line wings, and the most significant changes occurred for Br11 at lower temperatures. Note, however, that also Br γ has become stronger throughout the complete grid.

In Fig. 6.7 we now compare the detailed profiles of the strategic lines located in the *H* and *K* band of the present investigation (results from CMFGEN in grey). The agreement between the results for the (almost purely photospheric) lines in the *H* band (Br10/11, He II1.70 and He II1.69) is nearly perfect. The only differences occur in the cores of Br10, where CMFGEN predicts some emission for hotter objects, and some marginal differences in the far wings of the supergiants, which we attribute to the somewhat different density stratification in the photosphere. Additionally, CMFGEN predicts slightly stronger He II1.69 lines for the hottest objects (models “1V” and “1Ia”) and for the supergiant model “6Ia”.

Concerning the *K* band, the comparison is also rather satisfactory, except for He II2.05 at intermediate spectral type (see below). Concerning Br γ , the dwarf models give rather similar results, with the exception of intermediate spectral types, where FASTWIND produces some central emission. We have convinced ourselves that this prediction is very stable (and not depending on any temperature inversion), resulting from some intermediate layers where the population of the hydrogen levels is similar to the nebular case. Here the departure coefficients of the individual levels increase as a function of quantum number. In such a situation, a central emission owing to a strong source function is inevitable. For the supergiants, the major differences regard, again, the line cores, with CMFGEN predicting more refilling.

Somewhat larger differences are found for He II2.18, again (cf. He II1.69) for the hottest models

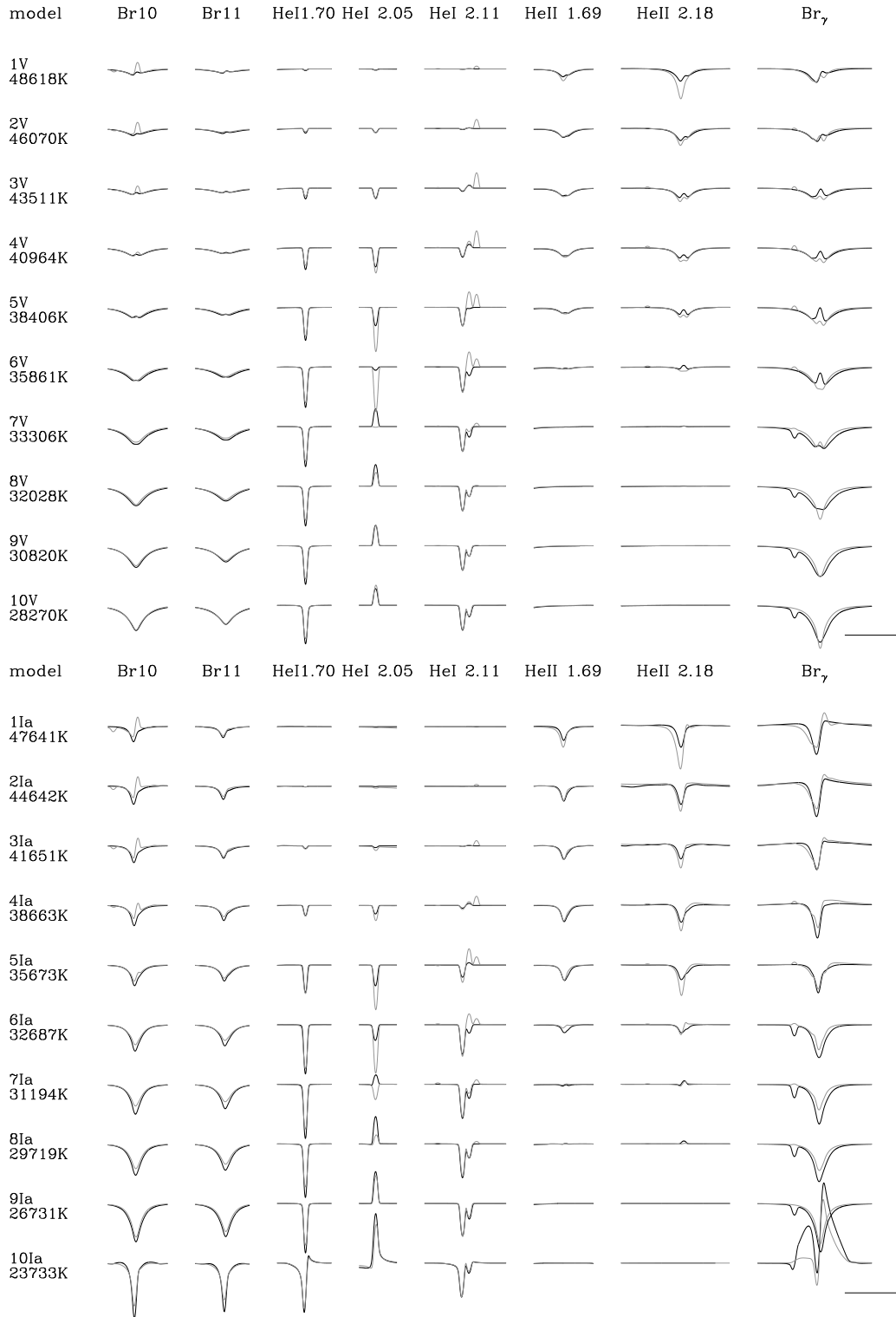


Figure 6.7: Comparison of synthetic NIR lines for the grid of O-type dwarfs (upper panel) and supergiants (lower panel) described by Lenorzer et al. (2004), as calculated by FASTWIND and CMFGEN (in grey). For hydrogen and He II, the results reported by Lenorzer et al. have been recalculated using the Griem approximation. The horizontal and vertical lines in the bottom right corner indicate the scale used and correspond to 0.01μ in wavelength and 0.1 in units of the continuum, respectively. To simplify the comparison, the synthetic profiles have been convolved with a rotational profile corresponding to $V_r \sin i = 80 \text{ km s}^{-1}$ and degraded to a typical resolution of 10,000.

where CMFGEN predicts significantly more absorption.

Concerning He I, the situation for the triplet line (blue component of He I2.11) is as perfect as for He I1.70. The differences for the He I (triplet) component located at the blue of Br $_{\gamma}$ are quite interesting. CMFGEN predicts an emission for hot stars but “nothing” for cooler objects, whereas FASTWIND predicts a rather strong absorption at cooler temperatures. To our present knowledge, this is the only discrepancy we have found so far (including the optical range) for a *triplet* line.

The only *important* discrepancies concern the He I singlets (He I2.05 and the red component of He I2.11) of the supergiant *and* dwarf models in the range between models 5 to 7. Starting from the hotter side, CMFGEN predicts strong absorption, which abruptly switches into emission at models no. 7, whereas FASTWIND predicts a smooth transition from strong absorption at model 4 to strong emission at model 8. Reassuring is the fact that at least the inverse behaviour between He I2.05 and He I2.11(red) (as discussed in Najarro et al. 1994 and Lenorzer et al. 2004) is always present.

Analogous comparisons performed in the optical (Puls et al. 2005) have revealed that the strongest discrepancies are found in the same range of spectral types. The triplets agree perfectly, whereas the singlets disagree, because they are predicted to be much shallower by CMFGEN than the ones resulting from FASTWIND. Again, the transition from shallow to deep profiles (at late spectral type) occurs abruptly in CMFGEN.

Puls et al. (2005) have discussed a number of possibilities which might be responsible for the obvious discrepancy, but at present the situation remains unclear, and further conclusions concerning the origin of the “singlet problem” are not possible. We will, of course, continue in our effort to clarify this inconsistency regarding the He I singlets.

In addition to the detailed comparison performed in the *H* and *K* band, we have also compared the resulting e.w.’s of some other important lines in the *J* and *L* band. Most important is the comparison for Br $_{\alpha}$, which is a primary indicator of mass-loss, as already discussed in Lenorzer et al. (2004). Fig. 6.8 compares the corresponding e.w.’s, as a function of “equivalent width invariant” Q' (see Lenorzer et al.). Generally, the comparison is satisfactory, and particularly the differences at large mass-loss rates are not worrying, since in this range the net-emission reacts strongly on small changes in \dot{M} . Real differences are found only for the weakest winds, probably related to “uncorrected” broadening functions used by Lenorzer et al.

As we have found for He II2.18, also the differences for the other He II lines are significant. Note that we can only compare the e.w.’s and that the broadening as calculated by Lenorzer et al. suffers from erroneous line broadening. For He II5-7 the behaviour compared to Lenorzer et al. (2004) is the same, but our lines are twice as strong in absorption in the case of giants and dwarfs. For the supergiants we obtain the strongest absorption at 36 kK, in contrast to 42 kK in the comparison models. The only difference found for He II6-11 concerns the behaviour of supergiant and dwarf line trends. The supergiants in the comparison models show stronger absorption lines than the dwarfs, whereas in our case the situation is reversed.

At high T_{eff} , the models for He II7-13 display a monotonic behaviour with the hottest models showing the strongest absorption. Our hottest models display weaker absorption profiles (as was found in the detailed comparison of He II1.69 (7-12)), partly due to emission in the line cores. Finally, our emission lines obtained for He II6-7 are twice as strong in the case of supergiants and giants compared to Lenorzer et al. (2004).

In summary we conclude that at least from a theoretical point of view, all *H/K* band lines synthesized by FASTWIND can be trusted, except for He I2.05 at intermediate spectral type and maybe He II2.18, where certain discrepancies are found in comparison with CMFGEN, mostly at hottest tem-

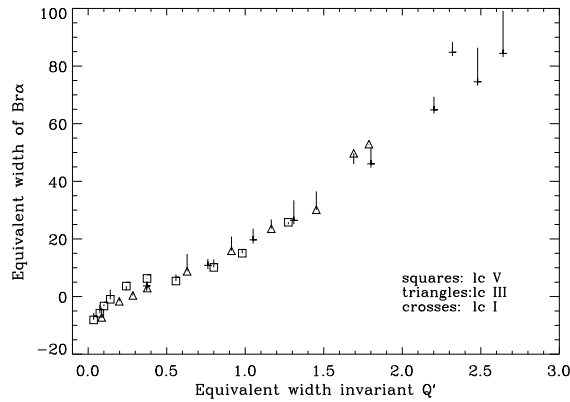


Figure 6.8: Equivalent width of Br_α as a function of equivalent width invariant $Q' = \frac{\dot{M}}{R_{*}^{1.5} T_{\text{eff}}^2 v_\infty}$ (see Lenorzer et al. 2004). The dwarf, giant and supergiant models are denoted by squares, triangles and crosses, respectively. Corresponding values from Lenorzer et al. (2004, their Fig. 7) are given by the end-points of the vertical lines (see text).

peratures. Concerning the discrepancies of He II in other bands, we have to clarify the influence of correct broadening functions, whereas for the He I singlet problem work is already in progress.

6.6 Analysis

6.6.1 General remarks

It might be questioned to what extent all decisive stellar and wind parameters can be obtained from a lone IR-analysis in the H and K band. In view of the available number of strategic lines, however, in most cases we are able to obtain the full parameter set, except for

- i) the terminal velocity, which in most cases cannot be derived from the optical either, and has been taken from UV-measurements. For our analysis, we have used the values given in the publications corresponding to sample I to III. The terminal velocities of sample IV have been adopted from Howarth et al. (1997). If no information is (or will be) present, calibrations of v_∞ as a function of spectral type have to be used, e.g., Kudritzki & Puls (2000).
- ii) the stellar radius, which can be inferred from M_V and the theoretical fluxes (Kudritzki 1980), and has been taken from the optical analyses in the present work. In future investigations when no optical data will be available, a similar strategy exploiting infrared colors can certainly be established.

In particular, Br10 and Br11 give clues on the gravity (if T_{eff} is known), He I and He II define temperature and helium content, and Br_γ can serve as an \dot{M} indicator, at least in principle. In those cases, where only one ionization stage of helium is visible, the determination of Y_{He} becomes problematic, and also the uncertainty for T_{eff} increases (see below). Due to the high quality of our spectra, however, both He II lines are visible for most spectral types.

Only for the coolest objects He II vanishes, which occurs for spectral types later than O9 for dwarfs, about B0 for giants, and again B0 for supergiants (cf. Figs. 6.9 to 6.11). In those cases

it still should be possible to derive (somewhat more inaccurate) estimates for T_{eff} , at least if some guess for Y_{He} is present. This possibility is due to the behaviour of He I 1.70 vs. He I 2.05 (Fig. 6.3), since the former line is almost only dependent on $\log g$, whereas the latter depends strongly on T_{eff} . Unfortunately, the data for He I 2.05 are not of sufficient quality (except for HD 190864 and τ Sco, where the latter just lies in the critical domain) that we could exploit this behaviour only once and had to refrain from an analysis of the remaining coolest objects (four in total).

Because of the independence of He I 1.70 on T_{eff} and the fact that Br 10/11 can *always* be fitted for certain combinations of $T_{\text{eff}}/\log g$, a perfect fit in combination with completely erroneous parameters would result if He I 2.05 had to be discarded. This is indicated in Fig. 6.11 for HD 14134, being a B3Ia supergiant (with T_{eff} roughly at 18,000 K, see Kudritzki et al. 1999), which could be fitted with $T_{\text{eff}} = 25,000$ K. If, on the other hand, He I 2.05 had been available, the appropriate parameters should have been obtained, at least when the helium content could have been guessed. Such a guess of the helium abundance should always be possible for objects we are eventually aiming at in our project (cf. Sect. 6.1), i.e., for very young, unevolved stars with unprocessed helium.

Micro-turbulence. In agreement with the findings by Repolust et al. (2004), we have adopted a micro-turbulence of $v_{\text{turb}} = 10 \text{ km s}^{-1}$ for all stars with spectral type O7 or later regardless of their luminosity class, whereas for hotter O-type stars the micro-turbulent velocity has almost no effect on the analysis and we have neglected it. At spectral type O6.5, our IR-analysis of HD 190864 (O6.5 III) indicated that a micro-turbulence is still needed, whereas from O7 onwards v_{turb} did not play any role, e.g., for HD 192639 (O7 Ib). Since the former and the latter stars have $T_{\text{eff}} = 37$ and 35 kK, respectively, we conclude that at roughly $T_{\text{eff}} = 36$ kK the influence of v_{turb} on the H/He lines is vanishing, in agreement with our previous findings from the optical.

Rotational velocities. For the (projected) rotational velocities, we have, as a first guess, used the values provided by Repolust et al. (2004), Herrero et al. (2000, 2002) and Howarth et al. (1997) for sample I, II and III/IV, respectively. In our spirit to rely on IR data alone, we have subsequently inferred the rotational velocity from the (narrow) He lines, with most emphasis on He I. Concerning sample I, the results from our IR-analysis are consistent with the velocities derived from the optical, except for HD 190864 and HD 192639, where the profiles indicated slightly lower values (10% and 20%, respectively), which have been used instead of the “original” ones.

For sample II stars, in 3 out of 5 cases the “optical” values derived by Herrero et al. (2000, 2002) were inconsistent with our IR-data. In particular, for HD 5689 we found a velocity of 220 km s^{-1} (instead of 250 km s^{-1}), for HD 15570 a velocity of 120 km s^{-1} (instead of 105 km s^{-1}) and for Cyg OB2#7 our analysis produced the largest differences, namely $V_r \sin i = 145 \text{ km s}^{-1}$, compared to a value of 105 km s^{-1} provided by Herrero et al. (2002) (30% difference!).

The values taken from Howarth et al. (1997) for the remaining sample III/IV objects, finally, agree fairly well with our IR data, and are also consistent with the values derived by Kudritzki et al. (1999) in their analysis of sample III objects.

Let us finally mention that in those cases when Br $_{\gamma}$ does not show emission wings, a statement concerning the velocity field parameter, β , is not possible, as is true for the optical analysis. In order to allow for a meaningful comparison with respect to optical determinations of \dot{M} , we have used the corresponding values derived or adopted from the optical. In future analyses, of course, this possibility will no longer be present, and we have to rely on our accumulated knowledge, i.e., we will have to

adopt “reasonable” values for β , with all related problems concerning the accuracy of \dot{M} (cf. Puls et al. 1996; Markova et al. 2004).

6.6.2 Fitting strategy and line trends

In order to obtain reliable fits, we applied the following strategy. At first, we searched for a coarse determination of the relevant sub-volume in parameter space by comparing the observed profiles with our large grid of synthetic profiles as described by Puls et al. (2005), which has a typical resolution of 2,500 K in T_{eff} , 0.3 in $\log g$, and 0.25 in $\log Q$. A subsequent fine fit is obtained by modifying the parameters by hand (using the “actual” values for R_* and v_∞ to obtain information on \dot{M} additionally to $\log Q$), where typically 10 trials are enough to provide a best compromise. In those cases, where at present no information about R_* is available (which concerns the three objects presented in Table 6.3), “only” $\log Q$ can be derived. For the actual fits of these three objects we have, of course, used prototypical parameters for R_* and v_∞ .

Most weight has been given to the fits of the He lines (which are rather uncontaminated from errors in both broadening functions and reduction of the observed material) followed by the photospheric hydrogen lines, Br10/11, which sometimes strongly suffer from both defects. Least weight has been given to Br $_\gamma$, because of the number of problems inherent to this line, as recently described by Lenorzer et al. (2004) and independently found by Jokuthy (2002). Particularly, the synthetic profiles for larger wind densities, predicted by both FASTWIND and CMFGEN, are of P Cygni type, whereas the observations show an almost pure emission profile. Moreover, from a comparison of equivalent widths, it has turned out that in a lot of cases the predicted e.w. is much larger than the observed one, which would indicate that the models underestimate the wind-emission (remember, that Br $_\gamma$ forms inside the H $_\alpha$ sphere). Often, however, this larger e.w. is due to the predicted P Cygni absorption component which is missing in the observations, and we tried to concentrate on the Br $_\gamma$ line wings in our fits ignoring any discrepancy concerning the predicted P Cygni troughs. If the synthetic lines actually predicted too few wind emission, this problem would become severe for lines where pure absorption lines are observed, and should lead to an overestimate of \dot{M} . We will come back to this point in the discussion of our analysis.

Another important point to make concerns the He I $\lambda 2.11$ line (comprising the He I triplet $\lambda 2.1120$ and the He I singlet $\lambda 2.1132$). Close to its central frequency, a broad emission feature can be seen (at $\lambda 2.115$) in the spectra of hot stars. This line can either be identified as NIII ($n = 7 \rightarrow 8$) or as CIII ($n = 7 \rightarrow 8$) or maybe both (Hanson et al. 1996; Najarro et al. 1997a, 2004).⁴ This feature is seen in stars of all luminosity classes, for stars hotter than and including spectral type O8 in the case of dwarfs and giants and O9 in the case of supergiants (though its designation is somewhat unclear, as He I2.11 appears as a P Cygni profile in late-O supergiants, possibly mimicking this feature). Since our present version of FASTWIND synthesizes “only” H/He lines and their analysis is the scope of the present paper, we are not able to fit this feature, but have to consider the fact that this feature significantly contaminates He I2.11.

Due to the well-resolved spectra, the two He I lines overlapping with Br $_\gamma$ as mentioned in Sect. 6.2, i.e., the He I triplet $\lambda 2.1607$ and the He I singlet $\lambda 2.1616$, are also visible in certain domains. For

⁴Due to the rather similar structure and the fact that these transitions occur between high lying levels, the predicted transition frequencies are almost equal. Since most of the stars in the OIf phase will have depleted C and enhanced N, however, the major contribution should be due to NIII and possibly also due to Nv2.105 ($10 \rightarrow 11$) for the hottest objects (F. Najarro, priv. comm.). CIII will be contributing if CIV at 2.07-2.08 μ is strong.

supergiants later than O5, He I 2.1607 begins to appear in the blue wings of Br γ , and in two stars, HD 30614 and HD 37128 the He I 2.1616 singlet seems to be present, even if difficult to see. In the giant spectra, He I 2.1607 can be seen from spectral type O9 onwards, and in the dwarf spectra this line appears in spectral types later than O8.

The strength of the Brackett lines in supergiants (Fig. 6.11) show a smooth behaviour as a function of spectral type, apart from certain fluctuations such as blends in the late O- and early B-type stars. As one moves from early B-type to mid O-type (i.e., O5), the Br γ absorption weakens, and from mid to the earliest O-types the line profiles switch into emission, where the emission at the blue wings of Br γ is much more pronounced (except for HD 15570), presumably due to the overlapping He II blend.

As for the photospheric Br10/11 lines, we can see that these absorption profiles show an extremely continuous behaviour, being rather weak for early O-type stars and increasing in strength towards early B-types. Hence, the cooler supergiants show the most prominent and sharpest absorption features. The emission features visible at the blue side of Br10 in the hottest supergiants are due to an unidentified feature.

Fig. 6.11 shows that the observed Br10/11 profiles are mostly well reproduced by the theoretical predictions, although at hotter temperatures certain inconsistencies arise, particularly with respect to the line cores. Most interestingly, in a number of cases we could not fit both profiles in parallel, and typically Br11 is then of better quality. Since we have convinced ourselves that the differences most probably are not exclusively due to reduction problems, we repeat our hypothesis that the broadening functions are somewhat erroneous, cf. Sect. 6.4.1. Again, for the theoretical profiles for Br γ , we would like to mention that for emission lines the wings are fairly well reproduced in contrast to the line cores.

The He I 1.70 line shows a very smooth behaviour, being absent in the hottest and most luminous star, Cyg OB2 #7, and successively increasing towards late O-type and early B-type stars. This also applies to the sharpness of the profiles. As has been stressed earlier on, He II 1.69 and He II 2.18 vanish in supergiants of spectral type B0 (being still detectable for α Cam, O9.5Ia)

The situation is similar in the case of giants (Fig. 6.10) and dwarfs (Fig. 6.9). All hydrogen and He I lines show the systematic variations expected, namely, an increase in strength from early O-types to early B-types. The model predictions do agree well with the observed profiles, again, except for certain discrepancies between Br10 vs. Br 11. Since Br γ remains in absorption throughout the entire spectral range, it can be reasonably fitted in most cases (whether at the “correct” value, will be clarified in Sect. 6.7). Particularly, the He II profiles give almost perfect fits except for very few outliers, and vanishes at O9 for dwarfs and about B0 for giants.

6.6.3 Comments on the individual objects

In the following, we will comment on the fits for the individual objects where necessary. Further information on the objects can be found in the corresponding publications concerning the optical analyses, see Tab. 6.1. A summary of all derived values can be found in Tables 6.2 and 6.3.

Dwarfs

HD 64568. The fit quality of the lines is generally good except for Br γ . The theoretical profile displays a central emission which is more due to an overpopulated upper level than due to wind effects (cf. Sect. 6.5) and, thus, cannot be removed by adopting a lower \dot{M} . Moreover, the theoretical

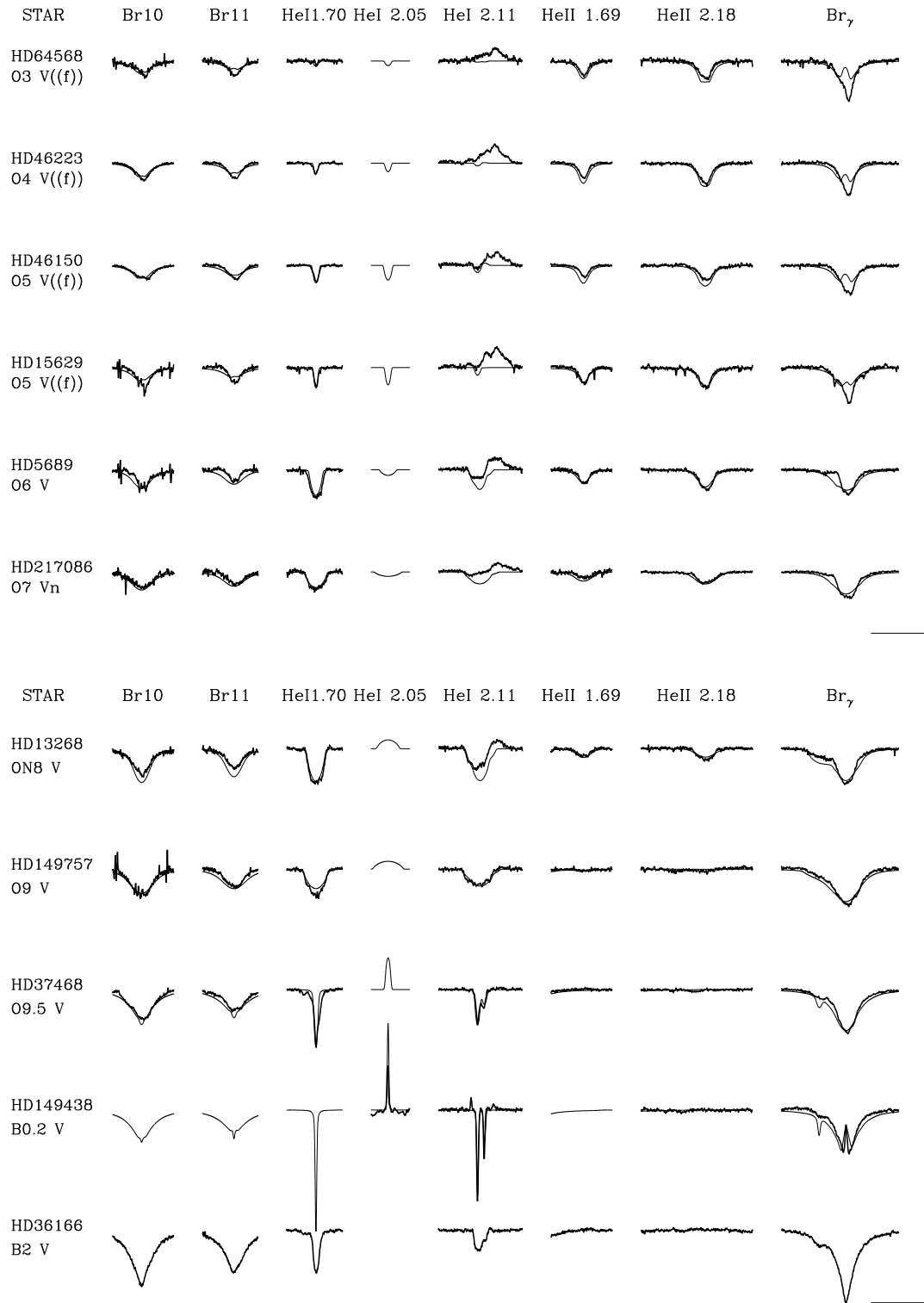


Figure 6.9: Line fits for hot dwarfs with spectral types ranging from O3 to O7 (upper panel) and cool dwarfs with spectral types ranging from O8 to B2 (lower panel). The lowermost object (HD 36166, B2V) has not been analyzed due to missing He II and He I 2.05 (see text). The horizontal and vertical lines in the bottom right corner indicate the scale used and correspond to 0.01 microns in wavelength and 0.10 in units of the continuum, respectively.

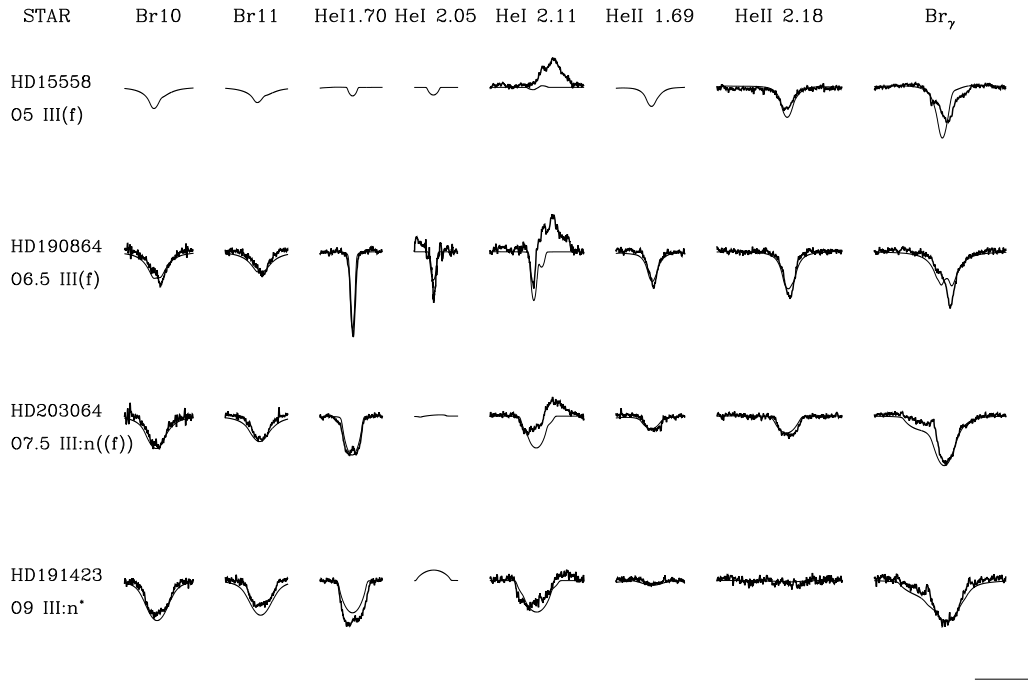


Figure 6.10: As Fig. 6.9, but for giants with spectral types ranging from O5 to B9. Concerning HD 15558 (only H band available), see text.

He II line would become too strong if a lower \dot{M} were used. Insofar, the present fits display the best compromise. Since no radius information is available, only the optical depth invariant $\log Q$ is presented.

HD 46223 and HD 46150. For both objects, the fit quality is satisfying, except for the He II lines (particularly in HD 46150) and Br_{γ} , where the former lines are predicted to be too strong and for the latter there is, again, too much central emission present. It is, however, not possible to reduce the temperature in order to fit the He II line, since this would adversely affect He I. A further reduction of Y_{He} (adopted here to be “solar”, i.e., 0.1) is implausible, so that the presented line fits reveal the best fit quality possible. For HD 46223 we can derive only the optical depth invariant $\log Q$ due to missing radius information.

HD 15629. The fit quality for the He lines is very good, and we confirm the helium deficiency to be $Y_{\text{He}} = 0.08$ as determined in the optical, see Repolust et al. (2004). Br_{γ} , again, suffers from too much central emission, and the cores of Br10/11 are much narrower than predicted (at least partly, as some of the narrowness might be due to reduction problems). The mass-loss rate is moderate with a value of $\dot{M} \approx 1.3 \cdot 10^{-6} M_{\odot}/\text{yr}$ which represents the same value as determined in the optical, whereas $\log g$ is found to be larger by 0.1 dex.

HD 5689. Again, moderate mismatches for the H lines are found, whereas the He lines provide a good fit. Br_γ does not show a central emission anymore, but the theoretical profile seems to be too broad. The same problem (very steep increase on the blue side, almost perfect fit on the red side) seems to be present also in HD 217086 (and, to a lesser extent, in HD 203064 and HD 191423), and we attribute some of this disagreement to reduction errors, although an underestimate of the He II blend (which is in emission in this parameter range) might be possible as well. Since all four stars are very fast rotators, effects from differential rotation in combination with a non-spherical wind (cf. Puls et al. 1996; Repolust et al. 2004 and references therein) cannot be excluded, see below.

In the case of Br10/11, on the other hand, problems in the broadening functions might explain the disagreement, as already discussed. Finally, the absorption trough of the theoretical profile for He I2.11 seems to be too strong, but might be contaminated by the bluewards NIII/CIII complex.

HD 217086. A very similar fit quality to HD 5689 has been obtained for this star, although Br10/11 are now in better agreement. The parameters determined are comparable to the ones obtained from the optical, including the overabundance of He ($Y_{\text{He}} = 0.15$). An upper limit for the mass-loss rate has been derived, which is less than half the value obtained from the optical.

HD 13268. The theoretical prediction reproduces the observation quite well, especially in the case of He I1.70 and both He II lines. As for the hydrogen lines, the two photospheric lines Br10 and Br11 show too much absorption in the line cores, whereas He I2.11 shows the same trend as already discussed for HD 5689. The fit quality for Br_γ , however, is much better, and even the He I2.1607 (triplet) blend is reasonably reproduced, although slightly too strong. For the mass-loss rate only an upper limit of $0.17 \cdot 10^{-6} \text{M}_\odot/\text{yr}$ can be given, for an adopted value of $\beta = 0.80$. The enhanced helium abundance $Y_{\text{He}} = 0.25$, as found in the optical, could be confirmed, giving the best compromise regarding all He lines.

HD 149757 and HD 37468. The very good fit quality makes further comments unnecessary.

HD 149438. τ Sco is probably one of the most interesting stars of the sample analyzed, since it is a *very* slow rotator and all features become visible at the obtained resolution. Although only the *K* band observation is available, it can be seen that we obtain a very good fit quality for all H and He lines present (He II is absent at these temperatures). As discussed before, in those cases where only one ionization stage of helium is visible, the determination of Y_{He} becomes problematic, and also the uncertainty for T_{eff} increases. Since in the case of τ Sco we could make use of the He I2.05 line, we could still determine the effective temperature (resulting in a similar value as in the optical), on the basis of an adopted value $Y_{\text{He}} = 0.1$. Also the mass-loss rate is well constrained from the *resolved* central emission feature in Br_γ , having a value of $0.02 \cdot 10^{-6} \text{M}_\odot/\text{yr}$. From a similar investigation by Przybilla & Butler (2004), exploiting the central emissions of Pf_γ , Pf_β and Br_α as well, they derived a value of $0.009 \cdot 10^{-6} \text{M}_\odot/\text{yr}$ (factor two lower) as a compromise, but have adopted a different velocity-field exponent ($\beta = 2.4$ instead of $\beta = 1.0$ used here) and utilized the “canonical” value for $\log g = 4.25$ which fits H_γ . In our case, however, and in the spirit to rely on a lone IR analysis, we preferred a lower value, $\log g = 4.0$, since in this case the emission feature is better reproduced (much narrower) than for a higher gravity, whereas the differences in He I2.05 (and concerning the line wings of Br_γ !)

are almost negligible. If we have had the information on Br10/11, this dichotomy could have been solved.

Having finished our investigation, one of us (R.M.) has analyzed the *optical* spectrum of τ Sco, also by means of FASTWIND. Details will be published elsewhere. Most interestingly, he obtained perfect line fits, at parameters $T_{\text{eff}} = 31,500$ K, $\log g = 4.0!$, $Y_{\text{He}} = 0.14$ and $\dot{M} = 0.017 \dots 0.047 \cdot 10^{-6} M_{\odot}/\text{yr}$ (for velocity exponents $\beta = 2.4 \dots 0.8$, respectively). We like to stress that this analysis has *not* been biased by our present results from the IR, since it was performed by an “automatic” line fitting procedure based on a genetic algorithm. After all, this consistency with the parameters derived by our IR-analysis is certainly reassuring.

HD 36166. This object has not been analyzed, due to missing He II *and* He I2.05 lines.

Giants

HD 15558. Also for this star, only the *K* band observation is available, and because of the high temperature and rather large \dot{M} no independent information concerning T_{eff} and $\log g$ can be derived. Thus, we adopted the effective temperature at its “optical” value, $T_{\text{eff}} = 41,000$ K. With this value, a simultaneous “fit” of $\log g$, Y_{He} and \dot{M} resulted in the synthetic spectrum displayed. \dot{M} was constrained by the wings of Br $_{\gamma}$, and $Y_{\text{He}} = 0.08$ derived on the basis that at this value He II is still somewhat too strong. $\log g$ is rather badly defined, since a variation by ± 0.2 dex gives only small differences in all three observed lines. In conclusion, the fit obtained allows to reliably constrain the mass-loss rate alone, and this only *if* the temperature actually has the adopted value. Note, however, that a (much) lower value is excluded since the predicted He II2.18 line would become too weak (cf. Fig 6.3, lower right panel).

HD 190864. The analysis gives a consistent fit for all lines (including He I2.05!) except for Br $_{\gamma}$, where the theoretical profile of Br $_{\gamma}$ shows too much central emission. The parameters remained almost the same compared to the optical except for the helium abundance, Y_{He} , which has been increased from 0.15 to 0.20.

HD 203064 and HD 191423. The analysis for HD 203064 yields a consistent fit for all lines, except for He I2.11 which displays a similar problem as described for HD 5689. We recovered the same values for T_{eff} and $\log g$ as in the optical, though the helium abundance had to be doubled and also the mass-loss rate increased by roughly 80%. The theoretical profile of Br $_{\gamma}$ for both stars is slightly broader than observed, although the effect is weaker than found for HD 5689 and HD 217086. Note in particular that for both giants also H $_{\alpha}$ turned out to be narrower than predicted, with “emission humps” present on both sides of the absorption trough (Repolust et al. 2004, Fig. 6). Summarizing and considering their extreme rotation velocities ($V_{\text{r}} \sin i$ being 300 km s^{-1} and 400 km s^{-1} for HD 203064 and HD 191423, respectively), our above hypothesis of rotational distortion is the most probable solution for the apparent dilemma in these cases.

Also for all other lines, HD 191423 behaves very similarly to HD 203064, although a better fit quality for He I2.11 is found, whereas He I1.70 has become worse (we aimed at a compromise between both lines).

Supergiants

Cyg OB2 #7. This star, being the hottest one in the sample, shows an enormous discrepancy in the Br_γ line, due to the observed central emission, which is not predicted by our simulations. It is the only star in our sample where we find the same problem in He II2.18, i.e., where the theoretical predictions with respect to its morphology could not be confirmed. In order to determine a fairly reliable mass-loss rate, we have concentrated exclusively on the wings of Br_γ . The parameters derived agree with their values from the optical, except for the helium abundance. The determination of this quantity is problematic due to missing He I. In contrast to the optical value, $Y_{\text{He}} = 0.3$ (Herrero et al. 2002), our best fit favoured $Y_{\text{He}} = 0.1$, whereas simulations using the optical value have adversely affected the H lines. Moreover, to preserve the good fit quality of He II1.69, we would have to lower T_{eff} significantly if $Y_{\text{He}} = 0.3$ were the correct value. (Actually, a temperature already lower by 1,500 K compared to the optical has been used to achieve the displayed fit). Interestingly, a re-analysis of Cyg OB2 #7 in the optical performed by one of us (R.M.) resulted in a value just in between, namely $Y_{\text{He}} = 0.20$ (at $T_{\text{eff}} = 46,000$ K). The emission on the blue side of Br10 is due to an unknown feature, as discussed in Sect. 6.6.2.

HD 66811. The fit quality is generally good, except for Br_γ , which again shows much more central emission than predicted. The wings, on the other hand, could well be fitted and gave a mass-loss rate of $8.8 \cdot 10^{-6} M_\odot/\text{yr}$, in agreement with the optical value. Br10 is contaminated on the blue side, but to a lesser extent than in Cyg OB2 #7.

HD 15570 and HD 14947. show very similar profiles, and could be reasonably well fitted. Note the prominent emission in Br_γ , which could not be matched, so that we had to concentrate on the wings. In both cases He II2.18 gives an additional constraint on \dot{M} , since at higher values the (theoretical) wings would show too much emission.

Cyg OB2 #8C and Cyg OB2 #8A. These stars, being of rather similar type and displaying rather similar profiles (with the noticeable difference of He II1.70, immediately indicating that 8A is somewhat cooler than 8C), have been carefully analyzed in the optical (and, again, reanalyzed by R.M.). From the optical, both stars have significantly different gravities (well constrained from the Balmer line wings), where object 8C with $\log g = 3.8$ has a rather large gravity for its type, cf. Herrero et al. (2002). The values derived from the IR, on the other hand, are much closer to each other, namely 3.62 and 3.41, respectively. According to the observed shape of the profiles and their corresponding theoretical fits, a higher $\log g$ would lead to severe inconsistencies. Apart from gravity, however, the other parameters derived are comparable to their optical counterparts, including the differences in \dot{M} , although the fit quality of Br_γ is dissatisfying.

HD 192639. For this star, we found a reasonable compromise concerning the fit quality of the lines present. We derived a $\log g$ value of 3.3 compared to 3.45 in the optical, because of the wings Br10/11 (note the different degree of inconsistency in the lines cores!) and due to the shape of He II2.18. With a value of $\log g = 3.45$ He II2.18 becomes even narrower, with a more pronounced P-Cygni type profile. The helium abundance was raised to 0.3 (from 0.2 in the optical) in order to fit the He I and He II lines appropriately in combination with the derived T_{eff} . Also in this case, the observed Br_γ

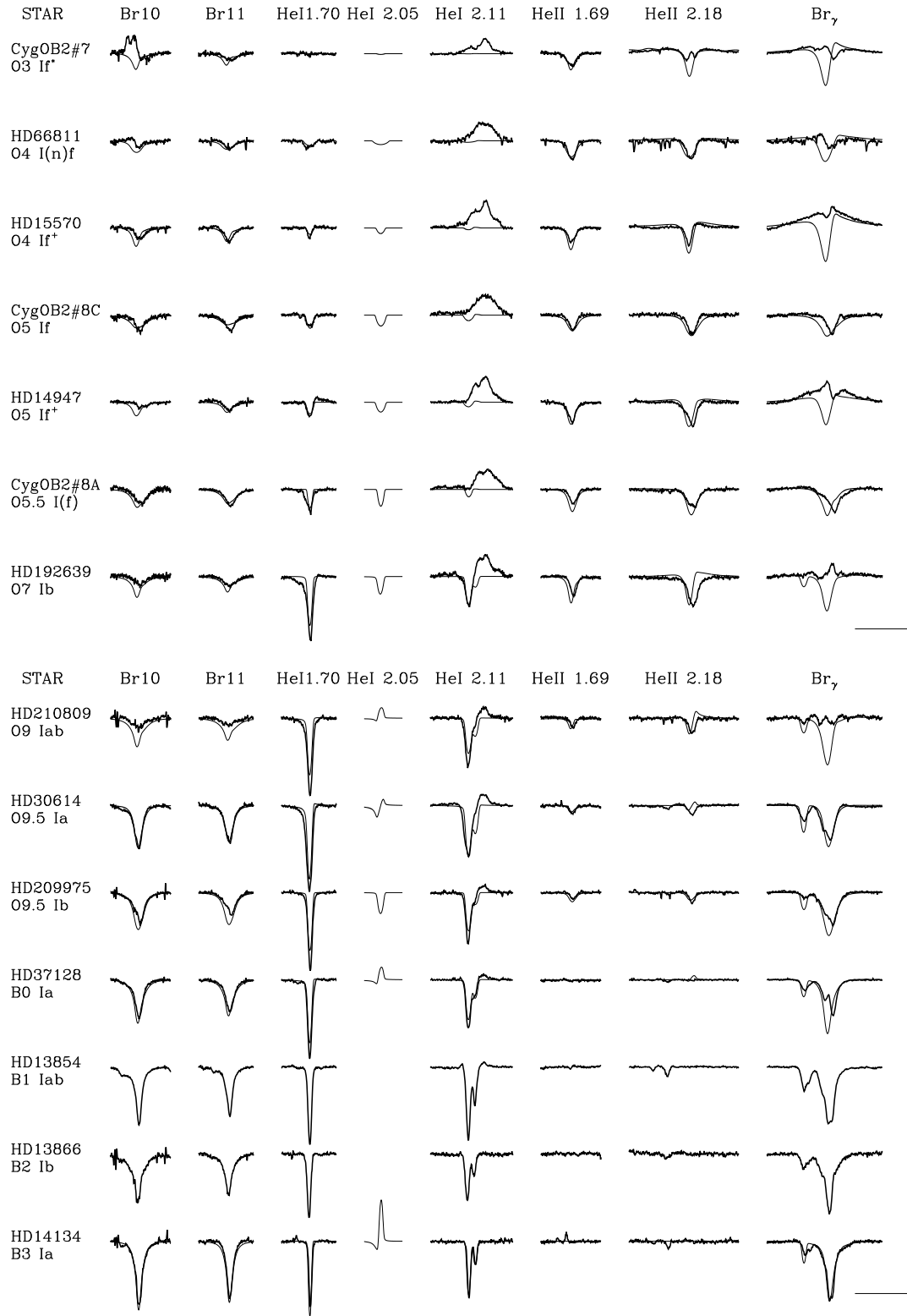


Figure 6.11: As Fig. 6.9, but for hot supergiants of spectral type O3 to O7 (upper panel) and cool supergiants (O9 to B3, lower panel). The three lowermost objects (HD 13854, B1Iab, HD 13866, B2Ib and HD 14134, B3Ia) have not been analyzed. The synthetic profiles overplotted for HD 14134 show a perfect fit for completely wrong parameters ($T_{\text{eff}} = 25,000$ K, $\log g = 2.7$), indicating that a spectroscopic H/K band analysis is impossible if He II and/or He I 2.05 are missing (see text).

line shows a central emission which could by no means be reproduced. The He II 12.1607 triplet blend showing up in the theoretical prediction is not yet present in the observation.

HD 210809. Part of the observed discrepancy in Br γ might be attributed to intrinsic variations in the notoriously variable wind of this star (Markova et al. 2005), though it is also possible that some (though not all) of the mismatch arises from errors in the removal of the Br γ feature in the telluric standard. Fortunately, the line wings could fairly well be fitted, resulting in a mass-loss rate of $5.80 \cdot 10^{-6} M_{\odot}/\text{yr}$ compared to $5.30 \cdot 10^{-6} M_{\odot}/\text{yr}$ in the optical. The major difficulty encountered was to fit the He I and He II lines simultaneously. In fact, a decrease in T_{eff} leads to an even more pronounced P-Cygni type profile for He II 2.18 for the given mass-loss rate, as was already true for HD 192639. We regard our solution as the best compromise possible, accounting for the fact that by a reduction in T_{eff} we would also increase the apparent dilemma in Br10/11 and the He I component in Br γ . The helium abundance was raised by 0.06 to 0.2 in order to find a compromise for the He lines.

HD 30614. For these stars a very good fit quality was obtained making further comments unnecessary.

HD 209975. The stellar profiles are fairly well reproduced and represent the best compromise possible. All hydrogen features predicted are a little too strong, with some contamination on the blue side of the profiles. The parameters obtained are comparable to the optical ones, except for $\log g$, where we determined a smaller value (0.15 dex).

HD 37128 (ϵ Ori). Almost perfect fit. Let us only point out that the derived value for T_{eff} represents an upper limit, since from this star onwards He II is no longer present and He I becomes rather insensitive to T_{eff} , so that without He II 2.05 further conclusions are almost impossible.

HD 13854 and HD 13866. have not been analyzed, due to missing He II and He II 2.05.

HD 14134. As above. The “theoretical” spectrum displayed in Fig 6.11 shows the insensitivity of the He II 1.70 and He II 2.11 lines to T_{eff} for temperatures below 30,000 K. Although a virtually perfect fit has been obtained, the synthetic model ($T_{\text{eff}} = 25,000$ K, $\log g = 2.70$) is located far away from realistic values (roughly at $T_{\text{eff}} = 18,000$ K, $\log g = 2.20$, cf. Kudritzki et al. 1999).

6.7 Comparison with optical data

In this section, we can answer the question to what extent a lone near IR analysis is suitable to recover the parameters from an analogous optical analysis. The corresponding data can be found in Tab. 6.2.

In contrast, Tab. 6.3 summarizes the parameters derived for those stars which have not yet been analyzed in the optical, i.e., constitute a “by-product” of our investigations. Since at present no radius information is available for the latter objects, we present the corresponding values for the optical depth invariant, $\log Q$, instead of the mass-loss rate \dot{M} . In the following, we will no longer comment on these stars, but would like to point out that all derived parameters appear to be fairly reasonable, except for the gravity of HD 46223, which is rather low for a dwarf of spectral type O4.

Table 6.2: Comparison of stellar and wind parameters in the optical and the near infrared derived using FASTWIND. T_{eff} in kK, R_* in R_\odot , \dot{M} in $10^{-6}M_\odot/\text{yr}$. $\log g$ values are corrected for centrifugal acceleration. If not explicitly indicated, the optical parameters have been taken from Repolust et al. (2004).

Star	Sp.Type	R_*	$T_{\text{eff}}^{\text{opt}}$	$T_{\text{eff}}^{\text{ir}}$	$\log g_{\text{true}}^{\text{opt}}$	$\log g_{\text{true}}^{\text{ir}}$	$Y_{\text{He}}^{\text{opt}}$	$Y_{\text{He}}^{\text{ir}}$	\dot{M}^{opt}	\dot{M}^{ir}
Cyg OB2 #7 ¹⁾	O3 If*	14.6	45.5	44.0	3.71	3.71	0.20 ^{a)} -0.30	0.10	9.86	10.00
HD 66811	O4 I(n)f	19.4	39.0	39.0	3.59	3.59	0.20	0.17	8.80	8.77
HD 15570 ²⁾	O4 If+	22.0	42.0	38.0	3.81	3.51	0.18	0.15	17.8	15.20
Cyg OB2 #8C ¹⁾	O5 If	13.3	41.0	39.0	3.81	3.62	0.09	0.10	2.25	2.00
HD 14947	O5 If+	16.8	37.5	37.5	3.48	3.48	0.20	0.20	8.52	7.46
Cyg OB2 #8A ¹⁾	O5.5 I(f)	27.9	38.5	37.0	3.51	3.41	0.10	0.10	13.5	11.50
HD 192639	O7 Ib	18.7	35.0	34.0	3.47	3.32	0.20	0.30	6.32	6.32
HD 210809	O9 Iab	21.2	31.5	32.0	3.12	3.31	0.14	0.20	5.30	5.80
HD 30614	O9.5 Ia	32.5	29.0	29.0	2.99	2.88	0.10	0.20	6.04	6.04
HD 209975	O9.5 Ib	22.9	32.0	31.0	3.22	3.07	0.10	0.10	2.15	3.30
HD 37128 ³⁾	B0 Ia	35.0	28.5	29.0 ^{b)}	3.00	3.01	0.10	0.10	2.40	5.25
HD 15558	O5 III(f)	18.2	41.0	41.0 ^{c)}	3.81	3.81	0.10	0.08	5.58	7.10
HD 190864	O6.5 III	12.3	37.0	36.5	3.57	3.61	0.15	0.20	1.39	0.98
HD 203064	O7.5 III	15.7	34.5	34.5	3.60	3.60	0.10	0.20	1.41	2.58
HD 191423	O9 III	12.9	32.5	32.0	3.60	3.56	0.20	0.20	≤ 0.41	≤ 0.39
HD 46150 ⁴⁾	O5 V((f))	13.1	43.0	40.0	3.71	3.71	0.10	0.10	N/A	1.38
HD 15629	O5 V((f))	12.8	40.5	40.5	3.71	3.81	0.08	0.08	1.28	1.28
HD 5689 ²⁾	O6 V	7.7	37.0	36.0	3.57	3.66	0.33	0.20	0.16	0.17
HD 217086	O7 Vn	8.6	36.0	36.0	3.72	3.78	0.15	0.15	≤ 0.23	≤ 0.09
HD 13268	ON8 V	10.3	33.0	33.0	3.48	3.48	0.25	0.25	≤ 0.26	≤ 0.17
HD 149757	O9 V	8.9	32.0	33.5	3.85	3.85	0.17	0.17	≤ 0.18	≤ 0.15
HD 149438 ⁵⁾	B0.2 V	5.3	31.4 31.5	31.0	4.24 4.00	4.00	0.10 0.14	0.10	0.009 0.017...0.047	0.020

Optical parameters taken from

¹⁾ Herrero et al. (2002) ²⁾ Herrero et al. (2000) (unblanketed FASTWIND models) ³⁾ Kudritzki et al. (1999)

⁴⁾ Herrero et al. (1992) (unblanketed plane-parallel H/He models)

⁵⁾ Kilian et al. (1991) and from Przybilla & Butler (2004) with respect to wind properties (upper entries) and from R.M. (FASTWIND, lower entries); the limits of \dot{M} correspond to velocity field exponents $\beta = 2.4 \dots 0.8$.

^{a)} from a re-analysis by R.M.(FASTWIND)

^{b)} upper limit

^{c)} taken from optical analysis

Table 6.3: Adopted and derived stellar and wind parameters obtained from spectra in the infrared for sample IV objects *not* analyzed in the optical. Since no radius information is available, only the optical depth invariant, $\log Q$, can be derived (Eq. 6.1). T_{eff} in kK, $V_r \sin i$ in km s^{-1} . Centrifugal correction assuming a typical radius.

Star	Sp.Type	T_{eff}	$\log g$	$\log g_{\text{true}}^{2)}$	Y_{He}	$V_r \sin i$	$\log Q$	β
HD 64568	O3 V((f))	45.0	3.85	3.86	0.10	150	-13.00	0.90
HD 46223	O4 V((f))	42.0	3.70	3.71	0.10	100	-12.70	0.90
HD 37468	O9.5 V	30.0	4.00	4.00	0.10	80	-14.10	1.00

Figs. 6.12 and 6.13 compare the results for T_{eff} , $\log g$ and \dot{M} for all stars which have been analyzed in the optical. In each figure, we have indicated error bars usually quoted for the corresponding “optical” quantity. In particular, the *maximum* errors for effective temperature are on the order of $\pm 5\%$ (corresponding to $\pm 2,000 \text{ K}$ at $T_{\text{eff}} = 40,000 \text{ K}^5$) and *typical* errors for $\log g$ are ± 0.1 . The “error bars” for the mass-loss rates, indicated as ± 0.2 dex, correspond to *mean* values attributed to \dot{M} measurements from H_α . Note, however, that the actual precision is an increasing function of \dot{M} , being higher than 0.2 dex for low \dot{M} and lower for larger values (e.g., Puls et al. 1996). Remember also that all our simulations (both in the IR and the optical) have been performed with *unclumped* models, i.e., the derived mass-loss rates represent upper limits and may need to be corrected.

From the three figures, it can immediately be seen that the majority of IR-values are in reasonable agreement with the corresponding optical data. Most importantly, no *obvious* trend is visible, neither as a function of the parameter itself nor as a function of luminosity class (“lc”), although a weak trend in T_{eff} cannot be excluded: From $T_{\text{eff}} = 35,000 \text{ K}$ on, the IR data are distributed more towards lower values (than derived from the optical).

In the following, we will briefly discuss the outliers, i.e., those objects which are located beyond the indicated error bars and thus must be interpreted as severe mismatches.

With respect to T_{eff} , only two objects behave “peculiarly”, at least at first glance, namely HD 46150 (lc V, being 3000 K cooler) and HD 15570 (lc I, 4000 K cooler). Actually, both objects do not pose any problem, since the corresponding optical analyses has been performed by *unblanketed* models, so that the obtained differences are just of the expected order of blanketing effects at $T_{\text{eff}} = 42,000 \text{ K}$, i.e., roughly $\Delta T_{\text{eff}} \approx -3,500 \text{ K}$ (e.g., Martins et al. 2002; Repolust et al. 2004). New positions corrected for blanketing effects of this amount have been indicated by arrows.

Blanketing effects do not only affect effective temperatures, but also gravities. Unfortunately, the corresponding corrections depend strongly on the specific situation, and corrections towards significantly lower values and of negligible amount have been found in parallel, see Repolust et al. (2004, Fig. 16). We have indicated the two stars by circles in Fig. 6.12, right panel. HD 15550, on the one hand, may be actually affected by such a strong effect, being responsible for the most severe discrepancy with $\Delta \log g = -0.3$. HD 46150, on the other hand, poses no problem with respect to gravity, consistent with the second possibility as described above. For the comparison concerning $\tau \text{ Sco}$, we have used the optical parameters derived by R.M. (cf. Sect. 6.6.3). Consequently, no differences are visible for this object. Remember, however, the actual dilemma regarding $\tau \text{ Sco}$. Since no pho-

⁵This uncertainty is also consistent with the uncertainty related to the He I singlet problem possibly affecting our optical analyses, cf. Puls et al. (2005, Sect. 10).

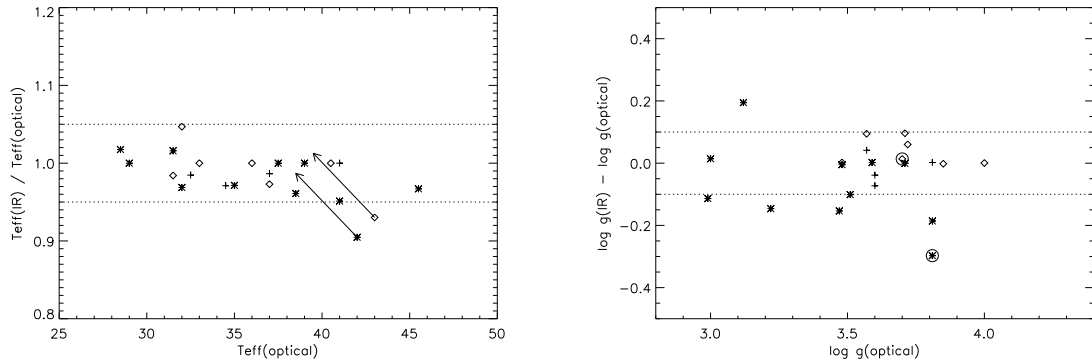


Figure 6.12: Comparison of T_{eff} and $\log g$ derived from the optical and the near-IR. Asterisks, crosses and diamonds correspond to luminosity classes I, III and V, respectively. The displayed “error bars” correspond to maximum uncertainties claimed in optical analyses, namely $\pm 5\%$ in T_{eff} and ± 0.1 in $\log g$. The two arrows in the left panel correspond to the objects HD 15570 and HD 46150 (analyzed by means of unblanketed models in the optical) and indicate the average shift in position if blanketing effects would have been accounted for. The same objects are indicated by circles on the right. The “optical” gravity of τ Sco has been adopted as $\log g = 4.0$, in accordance with the analysis by R.M. Concerning the remaining outliers, see text.

ospheric hydrogen lines have been observed, its gravity is almost unconstrained with respect to our NIR analysis, and we have favoured the lower value alone because of the shape of the central emission in $\text{Br}\gamma$, which constitutes the only difference between a $\log g = 4.0$ and $\log g = 4.25$ model, given the observed lines. In future analyses with only IR spectra available we would favour this fit under the same circumstances anyway.

Thus, in total we have four “real” outliers (i.e., above the $1\text{-}\sigma$ level), namely HD 192639 and HD 209975, which both appear to be lower in gravity by -0.15 dex when compared to the optical, and the record holders, Cyg OB2 #8C and HD 210809, which give differences of -0.2 and $+0.2$ dex, respectively. In this sample, we might also include HD 46223 from Tab. 6.3, since the derived gravity is probably too low by a similar amount.

Concerning mass-loss rates, the situation is as satisfying as described above. First note that Fig. 6.13 also displays those stars for which we can only provide upper limits of \dot{M} , and which we have compared. The only star missing in this comparison is τ Sco, however a comparison with both the “optical” mass-loss rate and the value cited in Tab. 6.2 (which has been derived from an alternative IR analysis, cf. Sect. 6.6.3) reveals a disagreement of a factor of two (smaller and larger, respectively). Such a difference is not too bad, taken the intrinsic uncertainties at such low wind densities. We will come back to this problem later on, though.

As expected from the non-linear increase of wind-emission as a function of \dot{M} , the disagreement between optical and near IR mass-loss rates becomes smaller for larger wind-densities. For $\log \dot{M}^{\text{opt}} \gtrsim -5.3$, these differences are lower than 0.1 dex, which indicates the sensitivity of the $\text{Br}\gamma$ line wings (remember that only the wings could be fitted in high \dot{M} objects) and partly of He II on this parameter. The differences obtained for the corresponding equivalent widths (observations vs. theory, cf. Lenorzer et al. 2004 and Sect. 6.6.2) are thus almost exclusively due to the differences with respect to the line cores, which cannot be explained at present. For the low \dot{M} stars, on the other hand, no trend (particularly not towards considerably larger \dot{M}) is visible, so that the above problem might

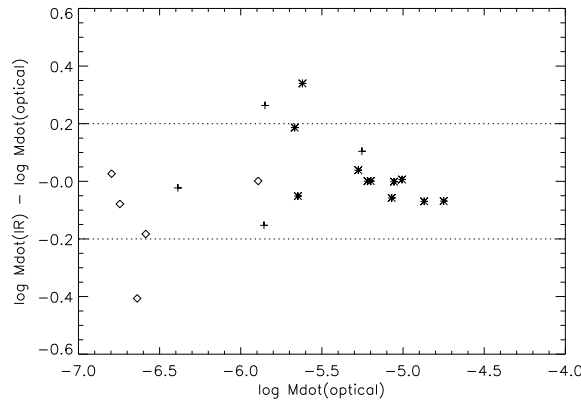


Figure 6.13: As Fig. 6.12, but for mass-loss rate \dot{M} . Upper limits have been treated at their nominal values. The “error bars” correspond to mean uncertainties of ± 0.2 dex quoted for H_α measurements. τ Sco has not been included in this comparison (see text).

be related to the physical conditions in the outer wind, whereas in the lowermost wind no obvious differences between the formation of H_α and Br_γ seems to be present.

With respect to the outliers, we find the most prominent differences for HD 37128 (ϵ Ori), $\Delta \log \dot{M} = 0.33$, which might partly be related to the fact that the optical mass-loss rate has been derived from unblanketed models. The differences found in HD 203064, $\Delta \log \dot{M} = 0.26$, have to be considered as “real”, since all other parameters derived do agree (except for Y_{He} , which has only marginal influence on the derived mass-loss rate). For HD 217086, finally, differences occur only with respect to an upper limit, e.g., the IR analysis predicts a lower limit than the optical one.

Concerning the helium abundance (not plotted), there are only two problematic cases. Cyg OB2 #7 has been discussed already in Sect. 6.6.3, and both the optical abundance ($Y_{He} = 0.2 \dots 0.3$) and the corresponding IR value ($Y_{He} = 0.1$) are uncertain, the latter due to the missing He I lines (although we would derive a significantly lower T_{eff} if the high abundance were true). The second outlier is HD 5689 with $Y_{He}(\text{optical}) = 0.33$ and $Y_{He}(\text{IR}) = 0.20$. Again, this discrepancy is probably irrelevant, since the optical analysis has been performed by means of unblanketed atmospheres, which are well-known to overestimate the helium abundance in a number of cases (cf. Repolust et al. 2004, particularly Sect. 7.2).

6.7.1 Comments on hydrogen collisional cross sections

In Sect. 6.3.1 we briefly discussed the importance of consistent collisional data for the resulting IR line profiles. We outlined recent calculations performed by Przybilla & Butler (2004) and references therein. These authors provide a recipe for an “optimum” choice of collisional data, based on a number of comparisons with observations, comprising mostly BA-type dwarfs (including τ Sco) and supergiants, whereas only one test has been presented for an O-star, the O3.5 dwarf HD 93250.

After incorporating their data into our version of FASTWIND⁶, we have subsequently tried to analyze our observed dataset. First let us mention that this modification gave rise to changes in the

⁶Note that Przybilla & Butler have used a similar version to check part of their calculations.

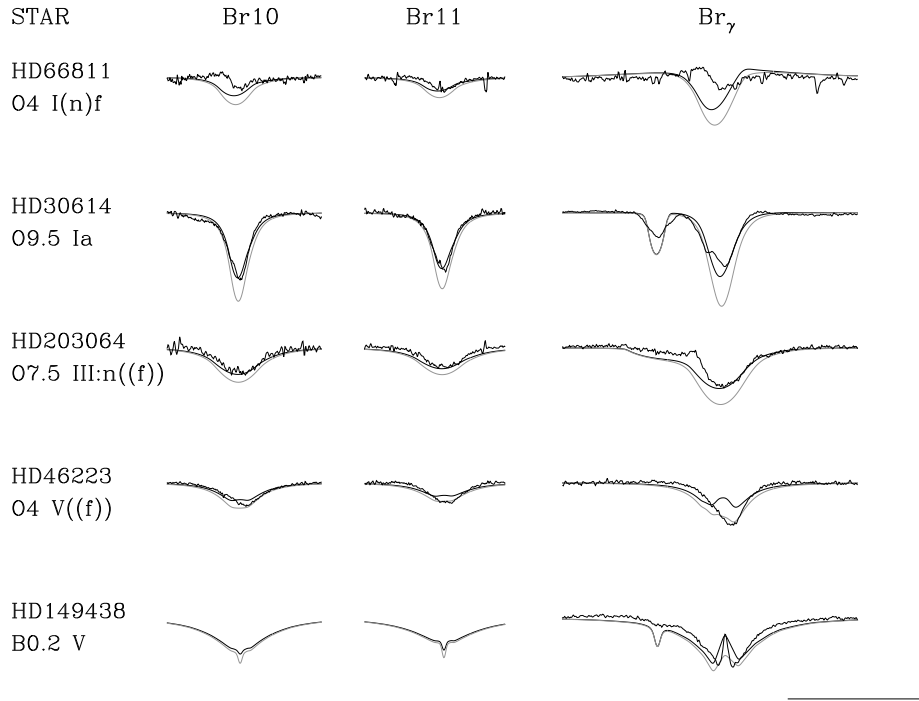


Figure 6.14: Influence of different collisional cross sections for hydrogen: Some prototypical examples. Solid: Best fit with cross sections from Giovanardi et al. (1987), as in Figs. 6.9 to 6.11. Grey: Models with *identical parameters*, but cross sections calculated according to Przybilla & Butler (2004) as described in the text.

hydrogen lines alone, since in all cases the temperature structure (being dependent on the collisional bound-bound rates) remained almost unaffected, with maximum changes on the order of 100 Kelvin.

Unfortunately, however, it turned also out that, again in *all cases*, the hydrogen line cores became stronger (in agreement with the findings by Przybilla & Butler), whereas the line wings are barely affected, as shown in Fig. 6.14 for some prototypical examples taken from the fits in Figs. 6.9 to 6.11. In a few cases this might actually lead to an improvement of the situation, e.g., for HD 46223 or Cyg OB2 #8C, which actually need gravities higher than those derived above. (Remember that increasing the gravity results in shallower line cores, cf. Sect. 6.4.1). Since, however, the IR-gravities based on our standard collisional data from Giovanardi et al. (1987) were found to be consistent with the optical ones in the *majority* of cases, models based on the alternative data by Przybilla & Butler would consequently lead to an overestimate of gravities.

The same would be true for the mass-loss rates. Using the new data would sometimes improve the situation, e.g., any central emission inside Br γ (if present) becomes reduced, cf. HD 46233 and τ Sco in Fig. 6.14. Actually, this reduction is the origin of the lower mass-loss rate of τ Sco as derived by Przybilla & Butler (2004): If \dot{M} is decreased, the strength of this feature increases again, at least if the winds are very weak, due to subtle NLTE effects and unrelated to any direct wind emission.

For “normal” winds, on the other hand, where wind emission plays the primary role, the deeper cores predicted by the “new” models would necessitate higher mass-loss rates. Thus, the present situation would get worse, at least in those cases where \dot{M} is no longer derived exclusively from

the wings. As an example, consider HD 203064 in Fig. 6.14, which presently has an IR mass-loss rate which is a factor of two larger already. Using the new dataset would further deteriorate this discrepancy.

Insofar, the preference for our standard set of collisional data is triggered solely from the results described above, namely from the generally satisfying agreement between the IR and optical analyses *for those objects analyzed in the present investigation*. We do not argue that one set or the other is better, but point out that in these cases our standard dataset gives results which are more consistent with the optical.

Of course, we have also looked into some of the details responsible for the differences obtained. It turned out that the NLTE departure coefficients are astonishingly similar, when comparing the results from both collisional datasets. There are only (very) subtle differences in those regions where the line cores are formed giving rise to the deeper profiles if the dataset by Przybilla & Butler is used. Either the lower level of the transition is slightly more populated, or the upper one is slightly less populated. The obvious discrepancies are then induced by the extreme sensitivity of the IR line formation on such subtle differences. As has already been argued about the formation of He I lines (Sect. 6.4.2), this discrepancy would barely be visible if the lines were situated in the optical. Insofar, not only the data but also the numerical treatment plays a crucial role. In any case it is quite astonishing how well the observed profiles can be simulated.

6.8 Summary and conclusions

In this paper, we have analyzed 25 Galactic O and early B-stars by means of H and K band spectroscopy. The primary goal of this investigation was to check to what extent a lone near-IR spectroscopy is able to recover stellar and wind parameters derived in the optical. This is critical to our desire to precisely analyze the hot, massive stars, deep within the disk of our galaxy, and in particular the very young, massive stars just emanating from their birth places.

Most of the spectra have been taken with SUBARU-IRCS, at an intermediate resolution of 12,000. In order to synthesize the strategic H/He lines present in the H/K band, we have used our recent, line-blanketed version of FASTWIND. In total, seven lines have been investigated, three from hydrogen, including Br_γ serving as a diagnostic tool to derive wind-densities, two He I and two He II lines. For two stars, we could make additional use of He II 2.05 (singlet) which has been observed with IRTF-CSHELL. Apart from Br_γ and He II 2.18, the other lines are predominately formed in the stellar photosphere, and thus remain fairly uncontaminated from more complex physical processes, particularly clumping.

In our attempt to prepare all required broadening functions, it turned out that at present we have to rely on the Griem approximation for Stark broadening (important for hydrogen and He II), since the corresponding published data (based on the more exact VCS approach) suffer from numerical problems, particularly for the members of higher series.

First we investigated the predicted behaviour of the strategic lines, by means of a large model grid described in Puls et al. (2005). Interestingly and in contradiction to what one expects from the optical, almost all photospheric lines in the H and K band (from H, He I and He II) *become stronger if the gravity decreases*. In Sect. 6.4, we have carefully investigated the origin of this rather unexpected behaviour.

Concerning H and He II, it is related to the particular behaviour of Stark broadening as a function

of electron density, which in the line cores is somewhat different for members of lower and higher series. For the latter, the cores become deeper when the density decreases, and contribute more to the total line strength than in the optical.

Regarding He I, on the other hand, the predicted behaviour is due to some subtle NLTE effects resulting in a stronger overpopulation of the lower level when the gravity decreases, so that the source function becomes weaker and the profile deeper, i.e., stronger. This strong dependence of the profile on the source function is a direct consequence of the IR line formation with $h\nu/kT \ll 1$. If those lines were situated in the optical, on the other hand, optical depth effects would dominate, leading to a decrease of line strength due to a lower number of He I absorbers. This explains the different (and “normal”) behaviour of, e.g., He I4471.

In Sect. 6.5, we have compared our calculations with results presented recently by Lenorzer et al. (2004), utilizing the alternative NLTE model atmosphere code CMFGEN. In most cases, we found reasonable and partly perfect agreement. Only the He I2.05 singlet for mid O-types suffers from some discrepancy, in agreement with our analogous findings for optical He I singlets (Puls et al. 2005).

After carrying out the analysis for our sample described above (and in agreement with the predictions from our model grid), we find that an *H/K* band analysis is able to derive constraints on the same set of stellar and wind parameters as it is known from the optical, e.g., T_{eff} , $\log g$, Y_{He} and optical depth invariant Q , where the latter yields the mass-loss rate \dot{M} if stellar radius and terminal velocity are known. For cooler objects, when He II is missing, a similar analysis might be possible if He I2.05 is available (due to the almost orthogonal reaction of He I2.05 and He I2.11 on T_{eff} and $\log g$) and the helium content can be adopted, which should be possible for very young objects containing unprocessed material.

For future purposes, when no UV observations will be available, the terminal velocity v_{∞} has to be taken from calibrations, as it is true for the velocity field exponent β , at least in those cases when no emission wings in Br_{γ} are visible. Concerning the determination of R_{\star} , a similar strategy as in the optical might be developed, utilizing infrared colours and distances.

For most of our objects, we obtained good fits, except for the line cores of Br_{γ} in early O-stars with significant mass-loss (see below), and except for the fact that particularly at mid O-types Br10/11 could not be fitted in parallel. We have argued that this discrepancy is similar to the problem in the optical, concerning He II4200/4541 (e.g., Herrero et al. 2002). Due to the similarity in the involved levels and broadening functions, we have speculated about a possible defect of these broadening functions for transitions between members of higher series. The largest discrepancy, however, was found for the line cores of Br_{γ} . First note that this problem is not particularly related to our code, since also CMFGEN exhibits the same shortcoming. Whereas the observations show Br_{γ} mostly as rather symmetric emission lines, the models predict a P Cygni type line, with a comparably deep core which is never observed. Note that this type of profile can only be created if the *ratio* of departure coefficients for the involved levels ($n = 4 \rightarrow 7$) deviates strongly from unity (cf. Puls et al. 1996), whereas a ratio close to unity would just give the observed symmetric emission profile. One might speculate that this can be achieved due to a stronger influence of collisional bound-bound processes, which, e.g., might be possible in a strongly clumped medium. Remember, however, that Br_{γ} typically forms inside the H_{α} -“sphere” (Lenorzer et al. 2004), where the degree of clumping is usually thought to be moderate (e.g., Markova et al. 2004; Repolust et al. 2004), though a recent investigation by Bouret et al. (2005) strongly indicates the opposite.

After having derived the stellar and wind parameters from the IR, we have compared them to results from previous optical analyses, in an almost strictly differential way, since most of these results

have been obtained also on the basis of FASTWIND. Overall, the IR results coincide in most cases with the optical ones within the typical errors usually quoted for the corresponding parameters, i.e., an uncertainty in T_{eff} of 5%, in $\log g$ of 0.1 dex and in \dot{M} of 0.2 dex, with lower errors at higher wind densities. In most of the cases where we have found discrepancies beyond these errors, their origin could be easily identified. Outliers above the $1\text{-}\sigma$ level were found in four cases with respect to $\log g$ and in two cases for \dot{M} .

As a by-product of our investigation, we could determine the (IR-) stellar parameters and the $\log Q$ value for three dwarfs, which have not been analyzed in the optical so far. Of course, these objects need to be checked in this spectral range.

Let us highlight one additional “bonus” obtained from the infrared. In those cases when a star has an extremely weak wind and the core of Br_γ can be resolved (requiring a very low rotational speed), the central emission will give us a clue about the actual mass-loss rate and not only an upper limit, as is true for the optical. An example of this kind of diagnostics is τ Sco. Particularly with respect to recent investigations of young dwarfs with surprisingly weak winds (Martins et al. 2004), this will turn out as an invaluable source of information (even more, if coupled with observations of Br_α , e.g. Najarro et al. 1998; Przybilla & Butler 2004).

After finishing this investigation, we are now able to constrain the observational requirements to perform such an IR-analysis. Most important is a (very) high S/N, because most of the lines to be investigated are extremely shallow, at least for the hotter objects, and a very good resolution, similar to the one used here (of order 10,000). Only then is it possible to disentangle the line cores from the wings (particularly important for Br_γ) and to obtain reasonable clues about any contamination due to reduction problems. As for the required set of lines, almost all lines analyzed in the present paper are necessary to obtain useful constraints, maybe except for $\text{Br}10$, since $\text{Br}11$ seems to be less contaminated. Since both He II lines behave very similarly and show the same degree of consistency or disagreement (if present), one of those two lines might be discarded as well.

In the last section of this paper, we have argued that our standard implementation of hydrogen collisional cross sections seems to give results which are in better agreement with the optical results for our sample of *hot* objects, compared to the data suggested recently by Przybilla & Butler (2004). In view of their findings, namely that for cooler stars their prescription gives more consistent results, this discrepancy has to be clarified in future work. The same of course is true regarding the severe mismatch of the Br_γ cores. A first step will require to include clumping and to investigate to what extent this process might improve the situation.

The value of a reliable quantitative analysis for hot, massive stars based entirely in the infrared cannot be overstated. Most obvious, it will allow the evaluation of massive star characteristics at an evolutionary stage significantly earlier than has ever been possible before. The influence of disk emission may render the photosphere of some very young massive stars inaccessible. We suspect, however, that among the most massive stars, around mid-O or hotter, the disk will be destroyed well before even near-infrared studies would be feasible due to the very short disk lifetime (Watson & Hanson 1997).

More broadly, nearly every O star within our galaxy now becomes accessible to a quantitative analysis, provided the extinction is not extreme ($A_V < 50$). One of the powers of quantitative analysis is its ability to determine absolute magnitudes. When OB stars are in clusters, those cluster distances will be robust, giving us clues to the structure and nature of the presently, poorly understood, inner Milky Way. OB stars serve as secondaries to massive compact objects. Because the extinction is typically high for such systems found in the inner galaxy, a NIR analysis of the OB companion provides

the only means for making critical measurements to constrain these fascinating systems. In truth, because many more O stars within our galaxy are visible in the NIR than the optical *by almost two orders of magnitude*, the development of a robust quantitative analysis in the infrared will stimulate entirely new, important results on massive stars, their formation and evolution and numerous valuable insights into the inner workings of our Milky Way galaxy.

Acknowledgements:

We like to thank Dr. Keith Butler for stimulating discussion and assistance. We are grateful to Dr. Alan Tokunaga for his expertise and guidance in the use of the Subaru and IRTF telescopes.

T.R. appreciates financial support in the form of a grant by the International Max-Planck Research School on Astrophysics (IMPRS), Garching. M.M.H. was supported by the National Science Foundation under Grant No. 0094050 to the University of Cincinnati, and J.P. gratefully acknowledges support by NATO Collaborative Linkage Grant No. PST/CLG 980007.

Bibliography

- Auer, L.H., Mihalas, D. 1974, ApJS 24, 193
- Bouret, J.-C., Lanz, T., Hillier, D.J. 2005, A&A, accepted
- Crowther, P.A., Hillier, D.J., Smith, L.J. 1995, A&A 293, 172
- Crowther P.A., Bohannan, B., Pasquali, A. 1998, in: Boulder-Munich II, eds. I.D. Howarth, ASP 131, p.38
- Fullerton, A.W., Najarro, F. 1998, in: Boulder-Munich II, eds. I.D. Howarth, ASP 131, p.47
- Giovanardi, C., Natta, A., Palla, F. 1987, A&AS, 70, 269
- Greene, T.P., Tokunaga, A.T., et al. 1993, in: Proc. SPIE, 1946, 313
- Griem, H. 1967, ApJ 147, 1092
- Hanson, M.M., Conti, P.S. , Rieke, M.J. 1996, ApJS 107, 311
- Hanson, M.M., Rieke, G.H., Luhman, K.L. 1998, ApJ 116, 1915
- Hanson, M.M., Kaper, L., Bik, A., et al. 2003, in: Proc. IAU Symp 212, eds. K.A. van der Hucht, A.Herrero & C. Esteban, ASP, p. 467
- Hanson, M.M., Kenworthy, M.A., Puls, J., et al. 2005, in prep.
- Herrero, A., Kudritzki, R.P., Vilchez, J.M., et al. 1992, A&A 261, 209
- Herrero, A., Puls, J., Villamariz, M. R. 2000, A&A 354, 193
- Herrero, A., Puls, J., Najarro, F. 2002, A&A 396, 949
- Hillier, D.J. 1982, in: IAUS 99, eds. C.H. de Loore & A.J. Willis, Reidel, Dordrecht, p. 225
- Hillier, D.J., Miller, D.L. 1998, ApJ 496, 407
- Howarth, I. D., Siebert, K. W., Hussain, G. A. J., Prinja, R. K. 1997, MNRAS 284, 265
- Johnson, L.C. 1972, ApJ, 174, 227
- Jokuthy, A. 2002, "Infrared spectrum analysis of hot stars", Diploma thesis, University Munich

- Kilian, J., Becker, S. R., Gehren, T., et al. 1991, A&A 244, 419
- Kenworthy, M.A., Hanson, M.M. 2004, PASP 116, 97
- Kubat, J., Puls, J., Pauldrach, A.W.A. 1999, A&A 341, 587
- Kudritzki, R.P. 1979, in: Proc. 22nd Liege International Symposium, 295
- Kudritzki, R.P. 1980, A&A 85, 174
- Kudritzki, R.P., Puls, J., Lennon, D.J., et al. 1999, A&A 350, 970
- Kudritzki, R.P., Puls, J. 2000, AARev 38, 613
- Leitherer, C., Heckman T.M. 1995, ApJS 96, 9
- Lemke, M. 1997 A&AS 122, 285
- Lenorzer, A., Mokiem, M.R., de Koter, A., Puls, J. 2004, A&A 422, 275
- Markova, N., Puls, J., Repolust, T., Markov, H. 2004, A&A 413, 693
- Markova, N., Puls, J., Scuderi, S, et al. 2005, A&A, submitted
- Martins, F., Schaerer, D., Hillier, D.J. 2002, A&A 382, 999
- Martins, F., Schaerer, D., Hillier, D.J., et al. 2004, A&A 420, 1087
- Massey, P., Thompson, A.B. 1991, AJ 101, 1408
- Mathys, G. 1989 A&AS 81, 237
- Mihalas, D. 1978, in: Stellar Atmospheres. 2nd Edition. Freeman: San Francisco
- Mihalas, D., Heasley, J.N., Auer, L.H. 1975, in: A Non-LTE Model Stellar Atmospheres Computer Program, NCAR-TN/STR 104
- Morris, P.W., Eenens P.R.J., et al. 1996, ApJ 470, 597
- Najarro, F., Hillier, D.J., Kudritzki, R.P. et al. 1994, A&A 285, 573
- Najarro, F., Hillier, D.J., Stahl, O. 1997, A&A 326, 111
- Najarro, F., Krabbe, A., Genezel, R., et al. 1997, A&A 325, 700
- Najarro, F., Kudritzki, R.P., Hillier, D.J., et al. 1998, in: Boulder-Munich II, eds. I.D. Howarth, ASP 131, p.57
- Najarro, F., Figer, D.F., Hillier, D.J., et al. 2004, ApJL 611, L105
- Oey, S. 2003, in: Proc. IAU Symp 212, eds. K.A. van der Hucht, A. Herrero & C. Esteban, ASP, p. 620
- Pauldrach, A.W.A., Hoffmann, T.L., Lennon, M. 2001, A&A 375, 161

- Percival, I.C., Richards, D. 1978, MNRAS, 183, 329
- Puls, J., Kudritzki, R.P., Herrero, A., et al. 1996, A&A 305, 171 (Paper I)
- Puls, J., Springmann, U., Lennon, M. 2000, A&A 141,23
- Puls, J., et al. 2003, in: Proc. IAU Symp 212, eds. K.A. van der Hucht, A. Herrero & C. Esteban, ASP, p. 61
- Puls, J., Urbaneja, M.A., Venero, R., et al. 2005, A&A, accepted
- Przybilla, N., Butler, K. 2004, ApJ 609, 1181
- Repolust, T., Puls, J., Herrero, A. 2004, A&A 415, 349
- Repolust, T., Puls, J., Hanson, M.M. 2005, submitted
- Santolaya-Rey, A.E., Puls, J., Herrero, A. 1997, A&A 323, 488
- Schöning, T., Butler, K. 1989, A&AS 78, 51
- Silich, S., Tenorio-Tagle, G. 2001, ApJ, 552, 9
- Smith, K.C., Howarth, I.D. 1998, MNRAS 299, 1146
- Vidal, C.R., Cooper, J., Smith, E. W. 1973, ApJS 25, 37, "VCS"
- Vink, J., de Koter, A., Lamers, H.J.G.L.M. 2000, A&A 362, 295
- Walborn, N.R. 1972, AJ 77, 312
- Walborn, N.R. 1973, AJ 78, 1067
- Watson, A.M., Hanson, M.M. 1997, ApJL 490, 165

Bibliography

- Crowther, P.A., Hillier, D.J., Evans, C.J., et. al. 2002, ApJ 579, 774
- Feldmeier, A., Puls, J., Pauldrach, A.W.A. 1997, A&A 322, 878
- Eversberg, T., Lepine, S., Moffat, A.F.J. 1998, ApJ 494, 799
- Herrero, A., Kudritzki, R.P., Vílchez, J.M., et al. 1992, A&A 261, 209
- Herrero, A., Puls, J., Najarro, F. 2002, A&A 396, 949
- Hillier, D.J., Miller, D.L. 1998, ApJ 496, 407
- Hubeny, I., Lanz, T. 1995, ApJ 39, 875
- Kudritzki, R.P., Puls, J. 2000, ARA&A 38, 613
- Kudritzki, R.P., Puls, J., Lennon, D.J., et al. 1999, A&A 350, 970
- Martins, F., Schaerer, D., Hillier, D.J. 2002, A&A 382, 999
- Owocki, S.P., Puls, J. 1999, ApJ 510, 355
- Pauldrach, A.W.A., Hoffmann, T.L., Lennon, M. 2001, A&A 375, 161
- Pauldrach, A.W.A., Hoffmann, T.L., Méndez, R. 2003, in Proc. IAU Symp. 209, eds. S.Kwok & M.Dopita, in press
- Puls, J., Kudritzki, R.P., Herrero, A., et al. 1996, A&A 305, 171
- Puls, J., et al. 2003, in: Proc. IAU Symp 212, eds. K.A. van der Hucht, A. Herrero & C. Esteban, ASP, p. 61
- Santolaya-Rey, A.E., Puls, J., Herrero, A. 1997, A&A 323, 488
- Vacca, W.D., Garmany, C.D., Shull, M. 1996, ApJ 460, 914
- Vink, J.S., de Koter, A., Lamers, H.J.G.L.M. 2000, A&A, 362, 295
- Abbott, D.C., Lucy, L.B. 1985, ApJ 288, 679
- Bohannon, B., Voels, S.A., Hummer, D.G., Abbott, D.C. 1990, ApJ 365, 729

- Bromm, V., Kudritzki, R.P., Loeb, A. 2001, *ApJ* 552, 464
- Chandrasekhar, S., Münch, G. 1950, *ApJ* 111, 142
- Cranmer, S.R., Owocki, S.P. 1995, *ApJ* 440, 308
- Crowther, P.A., Hillier, D.J., Evans, C.J., et. al. 2002, *ApJ* 579, 774
- de Zeeuw, P.T., Hoogerwerf, R., de Bruijne, J.H.J., et al. 1999, *AJ* 117, 354
- ESA, 1997, *The Hipparcos and Tycho Catalogues*, ESA SP-1200
- Eversberg, T., Lepine, S., Moffat, A.F.J. 1998, *ApJ* 494, 799
- Feldmeier, A. 1995, *A&A* 299, 523
- Feldmeier, A., Puls, J., Pauldrach, A.W.A. 1997, *A&A* 322, 878
- Gabler, R., Gabler, A., Kudritzki, R.P., Puls, J., et. al. 1989, *A&A* 226, 162
- Garmany, C.D., Stencel, R.E. 1992, *A&ASS* 94, 211
- Gräfener, G., Koesterke, L., Hamann, W.-R. 2002, *A&A* 387, 244
- Harries, T.J., Howarth, I.D. 1996, *A&A* 310, 533
- Haser, S.M. 1995, Ph.D. Thesis, Universität München
- Heger, A., Langer, N. 2000, *ApJ* 544, 1016
- Herrero, A. 1993, *SSRv* 66, 137
- Herrero, A., Lennon, D.J. 2003, in: *Proc. IAU Symp.* 215, eds. A. Maeder & P. Eenens, ASP, in press
- Herrero, A., Kudritzki, R.P., Vílchez, J.M., et al. 1992, *A&A* 261, 209
- Herrero, A., Puls, J., Villamariz, M.R. 2000, *A&A* 354, 193
- Herrero, A., Puls, J., Najarro, F. 2002, *A&A* 396, 949
- Hillier, D.J., Miller, D.L. 1998, *ApJ* 496, 407
- Hillier, D.J., Lanz, T., Heap, S.R., et al. 2003, *ApJ* 588, 1039
- Hoogerwerf, R., de Bruijne, J.H.J., de Zeeuw, P.T. 2001, *A&A* 365, 49
- Howarth, I.D., Siebert, K.W., Hussain, G.A.J., et al. 1995, *MNRAS* 284, 265
- Hubeny, I., Lanz, T. 1995, *ApJ* 39, 875
- Hubeny, I., Heap, S.R., Lanz, T. 1998, *ASP Conf. Series* Vol. 131, 108
- Hummer, D.G. 1982, *ApJ* 257, 724
- Hummer, D.G., Abbott, D.C., Voels, S.A., Bohannon, B. 1988, *ApJ* 328, 704

- Humphreys, R.M. 1978, ApJSS 38, 309
- Koen, C. 1992, MNRAS 256, 65
- Kudritzki, R.P. 1980, A&A 85, 174
- Kudritzki, R.P., Puls, J. 2000, ARA&A 38, 613
- Kudritzki, R.P., Lennon, D.J., Puls, J. 1995, in: "Quantitative Spectroscopy of Luminous Blue Stars in Distant Galaxies". ESO Astrophysics Symposia, Science with the VLT, eds. J.R. Walsh & I.J. Danziger, Springer, Heidelberg, p. 246
- Kudritzki, R.P., Puls, J., Lennon, D.J., et al. 1999, A&A 350, 970
- Lennon, D.J., Dufton, P.L., Fitzsimmons, A. 1992, A&AS, 94, 569
- Lennon, D.J., Dufton, P.L., Fitzsimmons, A. 1993, A&AS 97, 559
- Leitherer, C., Heckman T.M. 1995, ApJS 96, 9
- Lutz, T.E., Kelker, D.H. 1973, PASP 85, 573
- Maeder, A., Meynet, G. 2000, ARA&A 38, 143
- Maeder, A., Meynet, G. 2000, A&A 361, 159
- Markova, N., Puls, J., Repolust, T.M., Markov, H. 2003, in press.
- Martins, F., Schaerer, D., Hillier, D.J. 2002, A&A 382, 999
- Massa, D., Fullerton, A.W., Sonneborn, G., et al. 2003, ApJ 586, 996
- Massey, P. 1998, *VIII IAC Winter School of Astrophysics: Stellar Astrophysics for the Local Group*, eds. A. Aparicio, A. Herrero & F. Sanchez, CUP, p. 95
- Meynet, G., Maeder, A. 2000, A&A 361, 101
- Moffat, A.F.J., Robert, C. 1994, ApJ 421, 310
- Nelan, E., et. al. 2003, in prep.
- Oey, S. 2003, in: Proc. IAU Symp 212, eds. K.A. van der Hucht, A. Herrero & C. Esteban, ASP, p. 620
- Oudmajier, R.D., Groenewegen, M.A.T., Schrijver, H. 1998, MNRAS 294, L41
- Owocki, 1999, in: Proc. IAU Coll. 169, eds. B. Wolf, O. Stahl & A. W. Fullerton, p. 294
- Owocki, S.P., Puls, J. 1999, ApJ 510, 355
- Owocki, S.P., Castor, J.I., Rybicki, G.B. 1988, ApJ 335, 914
- Pauldrach, A.W.A., Puls, J., Kudritzki, R.P. 1986, A&A 164, 86

- Pauldrach, A.W.A., Kudritzki, R.P., Puls, J., et al. 1994, A&A 283, 525
- Pauldrach, A.W.A., Hoffmann, T.L., Lennon, M. 2001, A&A 375, 161
- Pauldrach, A.W.A., Hoffmann, T.L., Méndez, R. 2003, in Proc. IAU Symp. 209, eds. S.Kwok & M.Dopita, in press
- Penny, L.R. 1996, ApJ 463, 737
- Penny, L.R., Gies, D.R., Hartkopf W.I., et al. 1993, PASP 105, 588
- Petrenz, P., Puls, J. 1996, A&A 312, 195
- Petrenz, P., Puls, J. 2000, A&A 358, 956
- Pettini, M., Steidel, C.C., Adelberger, K.L., et al. 2000, ApJ 528, 96
- Puls, J., Kudritzki, R.P., Herrero, A., et al. 1996, A&A 305, 171 (Paper I)
- Puls, J., Springmann, U., Lennon, M. 2000, A&A 141,23
- Puls, J., et al. 2003, in: Proc. IAU Symp 212, eds. K.A. van der Hucht, A. Herrero & C. Esteban, ASP, p. 61
- Puls, J., et al. 2003, in prep.
- Repolust, T., Puls, J., Herrero, A. 2004, A&A 415, 349
- Santolaya-Rey, A.E., Puls, J., Herrero, A. 1997, A&A 323, 488
- Silich, S., Tenorio-Tagle, G. 2001, ApJ, 552, 9
- Schaerer, D., Schmutz, W. 1994, A&A 288, 231
- Schaller, G., Schaerer, D., Meynet, G., Maeder, A. 1992, A&AS 96, 269
- Schmutz, W., 1991, in: Stellar Atmospheres: Beyond Classical Models, eds. Crivellari, L., Hubeny, I., and Hummer, D.G., NATO ASI Series C Vol.341, Kluwer, Dordrecht, p.191
- Schmutz, W. 1997, A&A 321, 268
- Shortridge, K 1987, FIGARO user manual
- Smith, K.C., Howarth, I.D. 1998, MNRAS 299, 1146
- Steidel, C.C., Giavalisco, M., Pettini, M., et al. 1996, ApJL 462, L17
- Urbaneja, M.A., Herrero, A., Bresolin, F., et al. 2003, ApJL 584, 73
- Vacca, W.D., Garmany, C.D., Shull, M. 1996, ApJ 460, 914
- Villamariz, M.R., Herrero, A. 2000, A&A 357, 597
- Villamariz, M.R., Herrero, A., Butler, K., Becker, S.R. 2002, A&A 388, 940

- Vink, J.S., de Koter, A., Lamers, H.J.G.L.M. 2000, A&A, 362, 295
- Vink, J.S., de Koter, A., Lamers, H.J.G.L.M. 2001, A&A, 369, 574
- Voels, S.A., Bohannan, B., Abbott, D.C. 1989, ApJ 340, 1073
- Walborn, N.R. 1972, AJ 77, 312
- Walborn, N.R. 1973, AJ 78, 1067
- Walborn, N.R. 1982a, AJ 87, 1300
- Walborn, N.R. 1982b, ApJ 254, L15
- Walborn, N.R. 1995, RMxAC 2, 51
- Walborn, N.R., Howarth, I.D., Lennon, D.J., et al. 2002, AJ 123, 2754
- Abbott, D.C., Biegging, J.H. & Churchwell, E. 1981, ApJ, 250, 645
- Barbier-Brossat, M., Figon, P. 2000, A&AS, 142, 217
- Bellazzini, M., Fusi Pecci, F., Messineo, M., et al. 2002, AJ, 123, 1509
- Bianchi, L. & Garcia, M. 2002, ApJ, 581, 610
- Cardelli, J.A. 1988, ApJ 335, 177
- Cardelli, J.A., Clayton, G.C., Mathis, J.C. 1989 ApJ, 345, 245
- Clayton, G.C., Cardelli, J.A. 1988, AJ, 96, 695
- Carney, B.W., Latham, D.W., Laird, J.B., et al. 2001, AJ, 122, 3419
- Conti, P.S., Leep, E.M., Lorre, J.J. 1977, ApJ, 214, 759
- Crowther, P.A. 1998, in: Proc IAU Symp. No. 189, eds. T.R. Bedding, A.J. Booth & J. Davis, Kluwer, Dordrecht, p. 137.
- Crowther, P.A., Hillier, D.J., Evans, C.J., et al. 2002, ApJ, 579, 774
- Crowther, P.A., Hillier, D.J., Fullerton, A.W., et al. 2001, A&AS 199, 130
- Cruz-Gonzalez, C., Recillaz-Cruz, E., Costero, R., et al. 1974, RMxAA, 1, 211
- Eversberg, Th., Lepine, S. & Moffat, A.F.J. 1998, ApJ, 494, 799
- Feldmeier, A. 1995, A&A, 299, 523
- Feldmeier, A., Pauldrach, A. & Puls, J. 1997, A&A, 322, 878
- Felli, M., Habing, H.J., Israel, F.P. 1977, A&A, 59, 43
- FitzGerald, M.P. 1970, A&A, 4, 234

- Garmany, C.D., Stencel, R.E. 1992, A&AS, 94, 221
- Gies, D.R. 1987, ApJS, 64, 545
- Gies, D.R. & Bolton, C.T. 1986, ApJS, 61, 419
- Gies, D.R., Mason, B.D., Hartkopf, W.I., et al. 1993, AJ, 106, 2027
- Groenewegen, M.A.T., Lamers, H.J.G.M.L. 1989, A&AS, 79, 359
- Groenewegen, M.A.T., Lamers, H.J.G.M.L., Pauldrach, A.W.A. 1989, A&A, 221, 78
- Haser, S.M. 1995, PhD thesis, University of Munich
- Herrero, A., Kudritzki, R.-P., Vilchez, J.M., et al. 1992, A&A, 261, 209
- Herrero, A., Puls, J., Najarro, F. 2002, A&A, 396, 949
- Hillier, D.J., Miller, D.L. 1998, ApJ, 496, 407
- Hiltner, W.A. 1956, ApJS 2, 389
- Hiltner, W.A., Iriarte, B. 1955, ApJ, 122, 185
- Howarth, I.D., Prinja, R.K. 1989, ApJS, 69, 527
- Howarth, I.D., Siebert, K.W., Hussain, G.A., et al. 1997, MNRAS, 284, 265
- Hubeny, I., Lanz, T. 1995, ApJ 39, 875
- Humphreys, R. 1978, ApJS, 38, 309
- Kudritzki, R.-P. 1980, A&A, 85, 174
- Kudritzki, R.-P., Puls, J. 2000, ARA&A, 38, 613
- Lamers, H.J.G.M.L., Leitherer, C. 1993, ApJ, 412, 771
- Lamers, H.J.G.M.L., Snow, T., Lindholm, D.M. 1995, ApJ, 455, 269
- Lamers, H.J.G.M.L., Haser, S., de Koter, A., et al. 1999, ApJ, 516, 872
- Lennon, D.J., Dufton, P.L. & Fitzsimmons, A. 1992, A&AS, 94, 569
- Markova, N. & Scuderi, S. 2003, in preparation
- Markova, N., Valchev, T. 2000, A&A, 363, 995
- Markova, N., Puls, J., Repolust, T.M., Markov, H. 2004, A&A, 413, 693
- Martins, F., Schaerer, D. & Hillier, D.J. 2002, A&A, 382, 999
- Massa, D., Fullerton, A.W., Sonneborn, G., et al. 2003, ApJ 586, 996
- Meynet, D et al. 1994, A&AS, 103,97

- Moffat, A.F.J., Robert, C. 1994, *ApJ*, 421, 310
- Nelan, E., et. al. 2003, in prep.
- Owocki, S.P. & Puls, J. 1999, *ApJ*, 510, 355
- Owocki, S.P., Castor, J.I. & Rybicki, G.B. 1988, *ApJ*, 335, 914
- Owocki, S.P., Runacres, M.C. & Cohen, D.H. 2000, in ASP Conf. Ser. 204, Thermal and Ionization Aspects of Flows from Hot Stars: Observations and Theory, eds. H.J.G.L.M. Lamers & A. Sapar, 183
- Pauldrach, A.W.A., Hoffmann, T.L., Lennon, M. 2001, *A&A*, 375, 161
- Pauldrach, A.W.A., Hoffmann, T.L., Mendéz, R.H. 2002, in Proc. IAU Symp. No. 209, eds. S.Kwok & M.Dopita, in press
- Penny, L.R. 1996, *ApJ*, 463, 737
- Puls, J., Kudritzki, R.-P., Herrero, A., et al. 1996, *A&A*, 305, 171
- Puls, J., Springmann, U., Lennon, M. 2000, *A&AS*, 141, 23
- Puls, J., Repolust, T., Hofmann, T., et al. 2002, in Proc. IAU Symp. No. 212, eds. K.A. van der Hucht, A. Herrero & C. Esteban, ASP Conf. Ser. p. 61
- Press, W.H., Teukolsky, S.A., Vetterling, W.T., et al. 1992, Numerical Recipes in Fortran, 2nd edition, Cambridge University Press
- Repolust, T., Puls, J., Herrero, A. 2004, *A&A* 415, 349
- Sahu, M., Blaauw, A. 1993, in ASP Conf. Ser. 35, Massive Stars: Their Lives in the Interstellar Medium, eds. J.P. Cassinelli & E.B. Churchwell, 278
- Schild, H. & Berthet, S. 1986, *A&A* 162, 369
- Scuderi, S., Panagia, N. 2000, in ASP Conf. Ser. 204, Thermal and Ionization Aspects of Flows from Hot Stars: Observations and Theory, eds. H.J.G.L.M. Lamers & A. Sapar, 419
- Scuderi, S., Panagia, N., Stanghellini, C., et al. 1998, *A&A*, 332, 251
- Scuderi, S., Panagia, N., Stanghellini, C., et al., 2003, in prep. for *A&A*
- Stone, R.C. 1979, *ApJ*, 232, 520
- Tovmassian, H.M., Hovhannessian, R.Kh., Epemian, R.A., et al. 1994 *MNRAS*, 266, 337
- Vacca, W.D., Garmany, C.D., Shull, J.M. 1996, *ApJ*, 460, 914
- Vanbeveren, D., de Loore, C. & van Rensbergen, W. 1998, *A&A Rev*, 9, 63
- Vink, J.S., de Koter, A., Lamers, H.J.G.L.M. 2000, *A&A*, 362, 295

- Wegner, W. 1994, MNRAS, 270, 229
- Walborn, N.R. 1971, ApJS, 23, 257
- Walborn, N.R. 1972, AJ, 77, 312
- Walborn, N.R. 1973, AJ, 78, 1067
- Walborn, N.R. 2002, AJ, 124, 507
- Woosley, S.E., Heger, E. & Weaver, T.A. 2002, Rev.Mod.Phys. 74, 1015
- Abbott, D.C. 1982, ApJ 259, 282
- Abbott, D.C., Lucy, L.B. 1985, ApJ 288, 679
- Aufdenberg, J. P., Hauschildt, P. H., Baron, E., et al. 2002, ApJ 570, 344
- Baschek, B., v. Waldenfels, W., Wehrse, R. 2001, A&A 371, 1084
- Bianchi, L., Garcia, M. 2002, ApJ 581, 610
- Bouret, J.-C., Lanz, T., Hillier, D. J., et al. 2003, ApJ 595, 1182
- Butler K., Giddings J.R., 1985, Coll. Comp. Project No. 7 (CCP7), Newsletter 9, London, p. 7
- Castor, J., Abbott, D.C., Klein, R.I. 1975, ApJ 195, 157
- Crowther, P.A., Hillier, D.J., Evans, C.J., et. al. 2002, ApJ 579, 774
- de Koter, A., Schmutz, W., Lamers, H.J.G.L.M. 1993, A&A 277, 561
- de Koter, A., Heap, S.R., Hubeny, I. 1998, ApJ 509, 879
- Drew, J. 1985, MNRAS 217, 867
- Drew, J. 1985, ApJS 71, 267
- Feldmeier, A., Puls, J., Pauldrach, A.W.A. 1997, A&A 322, 878
- Fullerton, A.W., Crowther, P.A., De Marco, O., et al. 2000, ApJ 538 L43
- Gabler, R., Gabler, A., Kudritzki, R.P., Puls, J., et. al. 1989, A&A 226, 162
- Garcia, M., Bianchi, L. 2004, ApJ 606, 497
- Gräfener, G., Koesterke, L., Hamann, W.-R. 2002, A&A 387, 244
- Grevesse, N., Sauval, A.J. 1998, SSR 85, 161
- Hamann, W.-R. 1981, A&A 100, 169
- Hauschildt, P.H., Baron, E. 1999, J. Comp. Appl. Math. 109, 41
- Herrero, A., Puls, J., Najarro, F. 2002, A&A 396, 949

- Hillier, D.J., Miller, D.L. 1998, ApJ 496, 407
- Hillier, D.J., Lanz, T., Heap, S.R., et al. 2003, ApJ 588, 1039
- Hubeny, I. 1992, in “The Atmospheres of Early-Type Stars”, eds. U. Heber & C.S. Jeffery, Springer, Berlin, p. 377
- Hubeny, I., Lanz, T. 1995, ApJ 39, 875
- Hummer, D.G., Rybicky, G.B. 1985, ApJ 293, 258
- Jokuthy, A. 2002, “Infrared spectrum analysis of hot stars”, Diploma thesis, University Munich
- Kramer, R.H., Cohen, D.H., Owocki, S.P. 2003, ApJ 592, 532
- Kubát, J., Puls, J., Pauldrach, A.W.A. 1999, A&A 341, 587
- Kudritzki, R.P., Puls, J. 2000, ARA&A 38, 613
- Lenorzer, A., Mokiem, M.R., de Koter, A., Puls, J. 2004, A&A 422, 275
- Lucy, L.B. 1999, A&A 345, 211
- Lucy, L.B., Abbott, D.C. 1993, ApJ 405, 738
- Martins, F., Schaerer, D., Hillier, D.J. 2002, A&A 382, 999
- Martins, F., Schaerer, D., Hillier, D.J., et al. 2004, A&A 420, 1087
- Massey, P., Kudritzki, R.P., Bresolin, F., et al. 2004, ApJ 608, 1001
- Massey, P., Puls, J., Pauldrach, A.W.A., et al. 2005, in prep. for ApJ
- Mazzali, P.A., Lucy, L.B. 1993, A&A 279, 447
- Mazzali, P.A. 2000, A&A 363, 705
- Mihalas, D. 1975, “Stellar atmospheres”, 2nd edition, Freeman, San Francisco
- Mihalas, D., Kunasz, P.B., Hummer, D.G. 1975, ApJ 202, 465
- Oskinova, L.M., Feldmeier, A., Hamann, W.-R. 2004, A&A 422, 675
- Pauldrach, A.W.A., Puls, J., Kudritzki, R.P. 1986, A&A 164, 86
- Pauldrach, A.W.A., Lennon, M., Hoffmann, T.L., et al. 1998, in: Boulder-Munich Workshop II, PASP conf. series 131, ed. I. Howarth, p. 258
- Pauldrach, A.W.A., Hoffmann, T.L., Lennon, M. 2001, A&A 375, 161
- Przybilla, N., Butler, K. 2004, ApJ 609, 1181
- Puls, J., Hummer, D.G. 1988, A&A 191, 87

- Puls, J., Kudritzki, R.P., Herrero, A., et al. 1996, A&A 305, 171
- Puls, J., Pauldrach, A.W.A. 1990, in: Proc. Boulder Munich Workshop, ed. C. Garmany, PASPC 7, p. 202
- Puls, J., Springmann, U., Lennon, M. 2000, A&A 141, 23
- Repolust, T., Puls, J., Herrero, A. 2004, A&A 415, 349
- Rybicki, G.B., Hummer, D.G. 1991, A&A 245, 171
- Santolaya-Rey, A.E., Puls, J., Herrero, A. 1997, A&A 323, 488 (Paper I)
- Schaerer, D., Schmutz, W. 1994, A&A 288, 231
- Schaerer, D., de Koter, A. 1997, A&A 322, 598
- Schaerer, D., Meynet, G., Maeder, A., Schaller, G. 1993, A&AS 98, 523
- Schmutz, W., 1991, in: Stellar Atmospheres: Beyond Classical Models, eds. Crivellari, L., Hubeny, I., and Hummer, D.G., NATO ASI Series C Vol.341, Kluwer, Dordrecht, p.191
- Schmutz, W., Hamann, W.-R., Wessolowski, U. 1989, A&A 210, 236
- Seaton, M. 1958, MNRAS 118, 504
- Springmann, U. 1997, “On the theory of radiation driven winds of Wolf-Rayet stars”, thesis, University Munich
- Taresch, G., Kudritzki, R.P., Hurwitz, M., et al. 1999, A&A 321, 531
- Trundle, C., Lennon, D.J., Puls, J., et al. 2004, A&A 417, 217
- Urbaneja, M.A. 2004, “B Supergiants in the Milky Way and nearby galaxies: models and quantitative spectroscopy”, thesis, University of La Laguna
- Urbaneja, M.A., Herrero, A., Bresolin, F., et al. 2003, ApJL 584, 73
- Wehrse, R., von Waldenfels, W., Baschek, B. 1998, JQSRT 60, 963

Acknowledgements

A lot of people were involved in the realisation of this thesis, but above all I want to thank my supervisor Joachim Puls for his constant support, continuous encouragement and patience throughout the last 3 years. He provided the direction to accomplish the work by conveying an invaluable amount of knowledge, answering all the questions which I never actually asked, but by simply interpreting the puzzled look on my face. He patiently taught me, not always successfully, to work in a consistent manner, not to take things for granted, and to always question physical interpretations, statements and results. I very much appreciate his straightforwardness and, in particular, his genuine "human-ness" (although he consistently tries to conceal this trait).

I want to thank Harald Lesch for being my wailing wall and for all his advice in matters pertaining to anything. I'm grateful for his financial support after the expiration of the scholarship and for his initiative concerning "life after astronomy". I also want to thank Adi Pauldrach for not casting my feet in concrete and for stopping to convince me of the benefits of soccer. I will always remember him saying: "Don't study... think!"

It was a pleasure to meet numerous devoted and excellent astronomers, and especially to work with some of them. I would like to thank Margaret Hanson for providing valuable observational data and for proofreading the manuscript, and A. Herrero, N. Markova, M.A. Urbaneja, R. Venero, A. Jokuthy, M.R. Mokiem, H. Markov, and R.-P. Kudritzki for all their hard work, comments and suggestions. I benefited enormously from their experience. I also want to express my gratitude to Paul Crowther, who answered countless questions concerning the topic of my diploma thesis. Without his help I would probably never have come this far.

Among my fellow students, I especially want to thank my dear friend, Pamela Fon Sing, for explaining complex mathematical concepts and proofs over and over again. She is an excellent teacher and it was a great pleasure studying with her. I also want to thank Dugan Witherick, Dawn Leslie, Xavier König, Yvonne Ho, and Barry Cross for being such good friends and for making me feel at home. Without these guys, life in London and at UCL would not have been so much fun. I'm very grateful to have met Christoph Safferling and Billy Swan, my dearest friends, who were always there for me, successfully distracting me from studying. Together we explored every single pub in Camden Town, discussing the facts and the meaning of life. Moving from the past to the present, special thanks go to my fellow students at USM, in particular, to my office mates Philip Hultsch and Matthias Stehle, Andre Nickel, Michael Wegner, Tadziu Hoffmann, Mark Neeser, Arno Riffeser, Andreas Korn, Thomas Puzia, Norbert Przybilla, Claus Jaroschek, Christoph Nodes, Guido Birk, Andre Crusius and, of course, to all the others I have forgotten to mention - extragalactic, plasmatic, hot and cool, etc.

I'm indebted to my new boss Dr. Pfau and my colleagues in the field of intellectual property law for their support and endurance during the past few months. Not only did they all readily provide assistance with any work-related problems, but they also constantly encouraged me to carry on, despite the double workload.

I want to thank my parents, my brother, and Oma for their confidence and encouragement, and my boyfriend, Olaf, who had to put up with all of this.

Last, but not least, I also gratefully acknowledge financial support in form of a grant by the International Max-Planck Research School on Astrophysics (IMPRS), Garching.

Curriculum Vitae

Angaben zur Person:

Name: Repolust
Vorname: Tamara Maria
Geburtsdatum: 16. November 1969
Geburtsort: Graz, Österreich
Staatsangehörigkeit: Österreichisch

Aus- und Weiterbildung:

seit Okt.2004 Grünecker, Kinkeldey, Stockmair & Schwanhäusser
Patentingenieur

2001 - 2005 Ludwig-Maximilians-Universität, Scheinerstraße 1, 81679 München
Promotionsstudium der Astronomie an der
LMU - Ludwig-Maximilians-Universität München und
IMPRS - International Max-Planck Research School on Astrophysics
University of Munich, Garching

1997 - 2001 University College London, Gower Street, London WC1E 6BT
Studienfach Astrophysik, Abschluss Master of Science, MSci

1996 - 1997 University College London, Gower Street, London WC1E 6BT
Physical Sciences

1991 - 1993 Handelsakademie, 8010 Graz
Abendschule, Abschluss Matura

1990 - 1995 Volksbank Graz-Bruck, Hofgasse 9, 8010 Graz
Privatkundenbetreuer

1980 - 1989 Neusprachliches Gymnasium, 8430 Leibnitz
Abschluss Matura

1976 - 1980 Volksschule, 8410 Wildon